Production of the excited charm mesons D_1 and D_2^* at HERA

Dissertation
zur Erlangung des Doktorgrades
des Department Physik
der Universität Hamburg

Vorgelegt von

Andrii Verbytskyi

aus Hmilnyk/Kiew

Hamburg
2013

Gutachter der Dissertation: Dr. Olaf Behnke
Prof. Dr. Brian Foster
Gutachter der Disputation: Dr. Achim Geiser
Prof. Dr. Johannes Haller
Datum der Disputation: 19.02.2013
Vorsitzender des Prüfungsausschusses: Dr. Georg Steinbrück
Vorsitzender des Promitionsausschusses: Prof. Dr. Peter Hausschild
Dekan der MIN Fakultät: Prof. Dr. Heinrich Graener
Leiterin des Fachbereichs Physik: Prof. Dr. Daniela Pfannkuche

Abstract

The production of the excited charm mesons D_1, D_2^* and D_{s1}^+ in ep collisions has been measured with the ZEUS detector at HERA. The data sample taken by the ZEUS detector in the years 2003-2007, corresponding to an integrated luminosity of $373\,\mathrm{pb}^{-1}$ has been used. The masses of the neutral, charged and strange states, the widths of the neutral states, the helicity parameters of D_1^0 and D_{s1}^+ were determined and compared with other measurements and with theoretical expectations. The measured helicity parameters of the D_1^0 and D_{s1}^+ allows for some mixing of S- and D-waves in their decays to $D^{*\pm}\pi^{\mp}$ and $D^{*\pm}K^0$ respectively. The measured value of the D_1^0 helicity parameter is also consistent with a pure D-wave decay. Ratios of branching fractions of the two decay modes of the D_2^{*0}, $D_2^{*\pm}$ and D_{s1}^+ states were measured and compared with previous measurements. The fractions of charm quarks hadronising into D_1, D_2^* and D_{s1}^+ were measured and are consistent with those obtained in e^+e^- annihilations.

The Grid computing technology has a high importance for modern High Energy Physics. This technology has been successfully used in ZEUS experiment for the MC simulations and data analysis. The dedicated infrastructure has been maintained by the author since 2010. In addition to continuous support, the author has upgraded and improved the performance of the Grid MC simulations and contributed to the ZEUS data preservation project.

Kurzfassung

Die Produktion der angeregten Charm-Mesonen D_1, D_2^* und D_{s1}^+ in ep-Kollisionen wurde mit dem Detektor ZEUS in HERA gemessen. Ein vom ZEUS Detector in den Jahren 2003-2007 aufgenommener Datensatz, entsprechend einer Luminosität von $373\,\mathrm{pb}^{-1}$, wird in dieser Arbeit verwendet.

Die Massen der neutralen, geladenen und "strange" Zustände und die Breiten der neutralen Zustände, die Helizitätsparameter von D_1^0 und D_{s1}^+ wurden bestimmt und mit anderen Experimenten sowie mit theoretischen Erwartungen verglichen. Die gemessenen Helizitätsparameter von D_1^0 und D_{s1}^+ sind in Überstimmung mit einer Mischung der S- und D-Wellen in ihrem Zerfall zu $D^{*\pm}\pi^{\mp}$ und $D^{*\pm}K^0$. Der gemessene Wert des Helizitätsparameters von D_1^0 ist außerdem konsistent mit einem reinen D-Wellen Zerfall. Die Verhältnisse der Verzweigungsverhältnisse zweier Zerfallsmodi der Zustände D_2^{*0}, D_{s1}^+ und $D_2^{*\pm}$ wurden gemessen und mit früheren Messungen verglichen. Die Anteile von Charm-Quarks, die in D_1, D_2^* und D_{s1}^+ hadronisieren, wurden gemessen und sind mit jenen, die in e^+e^--Anihilationen beobachten wurden, konsistent.

Die Grid-Technologie ist für die moderne Hochenergiephysik außerordentlich wichtig. Diese Technologie wurde mit Erfolg im ZEUS Experiment für Monte-Carlo Simulationen und Datenanalyse benutzt. Die dazugehörige Infrastruktur wurde von dem Verfasser seit 2010 administriert. Zusätzlich zum andauernden Support hat der Verfasser die Performance der Monte-Carlo-Simulationen auf dem Grid ausgebaut und verbessert, und hat zu dem Datensicherungsprojekt von ZEUS beigetragen.

Introduction

For the last 2500 years, humankind put major efforts towards understanding the basic principles of the surrounding world. The key to this understanding is the answer to question *"What is the content and the origin of matter?"*. The ideas of atomism and cosmogony, have been invented in the IV century BC[1]; the existence of molecules/atoms has been confirmed only in the XIX and early XX centuries[2]. A bit later, in 1911, Ernest Rutherford conducted his famous experiments on α-particle scattering and revealed the existence of finer structure in the atom. The structure included nuclei and electrons and has been explained by Niels Bohr in 1913 using the ideas of electromagnetic interaction. Since that time the interactions in physics were coupled with matter. The later discoveries of isotopes[3], proton[4] and neutron[5] were clear evidence for an even finer and more complicated structure of matter. For the next decades, the physics community made major efforts to develop a theory that will explain the matter.

In the middle of 1970s the basic skeleton of a novel theory of matter, the Standard Model, was assembled. This was one of the biggest advances in physics since the beginning of XX century when quantum mechanics and general relativity theory were developed. The theory describes all known particles and interactions with the exception of gravity and includes a number of sub-atomic particles: quarks, leptons and bosons.

In the context of this thesis the most relevant interaction is the strong force, as described by the theory of Quantum Chromodynamics (QCD). The strong force occurs between quarks and gluons and has distinct properties: at small distances and large transferred momenta the force is weak and one can calculate scattering of interacting objects. On the other hand at large distances and low transferred momenta the calculations of interactions are not possible. Both cases are interesting for the understanding of QCD. However, the second one requires a special approach, which is called effective theory. The effective theory operates with approximate fields and makes QCD calculations at large distances/low energies possible. One of effective theories is HQET (Heavy Quark Effective Theory),

---

[1] Democritus, ca. 400 BC

[2] Jonh Dalton, 1800; Amedeo Avogadro, 1811; Robert Brown, 1827; Albert Einstein, 1905; Jean Perrin, 1908

[3] Frederick Soddy, 1913

[4] Ernest Rutherford, 1920

[5] Ernest Rutherford, 1920; James Chadwick, 1932

which successfully describes the bound states of heavy quark hadrons and their decays. From this perspective, the experimental study of bound charm states can improve the understanding of low energy QCD. One of the experimental facilities in which such studies can be carried out is HERA, the accelerator complex for *ep* collisions. The primary goal of HERA was to study the structure of the proton, however the data taken at HERA contains millions of events with heavy charm quarks, which makes it a wonderful facility for charm-quark physics. The ground charm-meson states were studied quite well before, so higher, poorly known states of charm mesons have a bigger interest. This work presents the studies of the excited charm mesons D_1^+, D_2^{*+}, D_1^0, D_2^{*0} and D_{s1}^+ at HERA.

The first section of this thesis contains a brief description of the Standard Model and a motivation for the effective theories in the context of heavy-quark physics. One of those, the Heavy Quark Effective Theory, as well as some derived predictions, is explained Section 2. The section ends with an overview of the charm quark production at HERA. Section 3 describes the experimental set-up: the HERA accelerating complex, the general properties of the ZEUS detector and the sub-detectors which are most relevant for this analysis. The same section also describes ZEUS trigger and detector simulation. Section 4 is devoted to the reconstruction of tracks, vertices and related topics. The particle identification with dE/dx information is described. This section also introduces vertexing-related quantities used in the analysis. Section 5 contains the description of the data-analysis procedure: the event and candidates selection, the reconstructed mass spectra and the description of the reconstructed spectra content. The results of the fits, namely the values of masses, widths and helicity parameters are discussed in Section 6. In the same section a comparison to the results of other experiments and the theoretical expectations is done. Section 7 provides formulae and explanations for the calculations of the charm-quark fragmentation fractions and the branching ratios of the excited charm mesons. The obtained results are discussed and compared to other measurements and theoretical expectations in Section 8. Section 9 contains an overview of systematic checks conducted for this analysis. The important technical information on the spectra fit procedure and signal extraction is given in Appendix 11. The other appendices describe the studies conducted in parallel to the main physics analysis. The technical task of the author, the Grid infrastructure maintenance for the ZEUS experiment is described in Appendix 12. The results of studies of relative (data to MC) tracking efficiency are given in the Appendix 13.

Contents

1 An overview of modern HEP

1.1 Standard Model

According to the Standard Model, all the matter in the Universe consists of a limited set of elementary particles, which interact with each other via different types of forces. The first group of those particles are twelve elementary particles-fermions[6], which carry spin 1/2. Those particles are six quarks and six leptons (see Tabs. 1.1, 1.2). The second group of elementary particles in the Standard Model are the gauge bosons listed in Tab. 1.3. Those particles are mediators of fundamental interactions. Four of them – W^+, W^-, Z^0 and γ correspond to the electroweak interaction and one, the gluon, g – to the strong interaction. The hypothetical mediator that corresponds to gravity is called a graviton. The experimental discovery of a single graviton is not foreseen in the near future, as the energies sufficient for its detection are too high for modern accelerators and the cross section for the interaction of gravitons with matter is too low. Other particles, such as mesons and baryons, contain quarks and anti-quarks, mesons contain a quark-anti-quark pair, baryons – three (anti)quarks.

Charge	Particle and mass		
$+2/3\|e\|$	$u, 2.3^{+0.7}_{-0.5}\,\mathrm{MeV}$	$c, 1275 \pm 25\,\mathrm{MeV}$	$t, 173.5 \pm 0.6 \pm 0.8\,\mathrm{GeV}$
$-1/3\|e\|$	$d, 4.8^{+0.7}_{-0.3}\,\mathrm{MeV}$	$s, 95 \pm 5\,\mathrm{MeV}$	$b, 4.18 \pm 0.03\,\mathrm{GeV}$

Table 1.1: *Quarks and their properties [1].*

Charge	Particle and mass		
$-\|e\|$	$e, 0.511\,\mathrm{MeV}$	$\mu, 105.66\,\mathrm{MeV}$	$\tau, 1776.82 \pm 0.16\,\mathrm{MeV}$
0	$\nu_e, < 2\,\mathrm{eV}$	$\nu_\mu, < 1.9\,\mathrm{MeV}$	$\nu_\tau, < 18\,\mathrm{MeV}$

Table 1.2: *Leptons and their properties [1].*

---

[6] Corresponding to those particles, there is an associated antiparticle with the same mass and opposite electric charge.

Charge	Particle and mass
$+\lvert e\rvert$	$W, 80.385 \pm 0.015\,\mathrm{GeV}$
0	$Z^0, 91.1876 \pm 0.0021\,\mathrm{GeV}$
0	$\gamma, 0$
0	$g, 0$

Table 1.3: *Fundamental bosons and their properties [1].*

All particles in the theory, except gluons, interact **electroweakly**.

At low energies the electroweak interaction is mediated dominantly by gamma quanta and thus essentially identical to the electromagnetic interaction, which deals with electric charges. This interaction was the first in which special of relativity and quantum physics were unified. The resulting theory, Quantum Electrodynamics, served as a template for the development of more complicated theories for other kinds of fundamental forces explained below.

The electrical charges of all elementary particles are quoted in Tabs. 1.1, 1.2, 1.3. Using the charges of quarks and their estimated masses the quarks are grouped into three groups (generations), which are shown in different columns of Tab. 1.1. A similar division to three groups (generations) is done for leptons in the Tab. 1.2. The neutral leptons are grouped in pairs with charged ones via the idea of conserved[7] “lepton number” that is unique for each lepton generation.

The **strong** interaction involves only quarks and gluons. It occurs between coloured objects and is mediated by gluons. Colour is a property of an object with three possible components. In the early studies these components(charges) were named after three colours: red, green, blue[8]. The theory of strong interactions is correspondingly called Quantum Chromodynamics (QCD).

The fact that gluons themselves carry a colour charge makes things more complicated. The strong force amplifies itself on long distances and makes impossible an observation of free coloured objects – quarks and gluons. All observable objects – mesons, baryons and leptons, are colourless, i.e. the sum of all colour charges totals to zero. This behaviour of coloured objects is called **confinement**.

---

[7] not strictly, as neutrino oscillations exist, see Ref. [1]

[8] This also implies an existence of anti-charges: anti-red, anti-green and anti-blue.

Confinement is also reflected in the dependence of running the QCD coupling constant, which decreases with momentum transferred between interacting particles, Q^2:

$$\alpha_s(Q^2) = \frac{12\pi}{(33 - 2n_f)ln(Q^2/\Lambda^2_{\mathrm{QCD}})}.$$

Here n_f stands for the number of involved flavours and $\Lambda_{\mathrm{QCD}} \approx 200\,\mathrm{MeV}$ is the so-called "QCD energy scale".

The other important property of coloured objects is that at short distances colour objects will not interact with each other and will behave as free particles. This property is called **asymptotic freedom**.

The ideas of confinement and asymptotic freedom are essential for the theory: it helps to perform calculations at high Q^2 (e.g. jet cross sections) and makes them impossible at low (e.g. hadronic transitions), where they become non-perturbative[9]. For the latter case, effective theories like HQET (Heavy Quark Effective Theory) [2] and ChPT (Chiral perturbation theory) [3] are used.

---

[9] not for every particular energy of interacting system exist a well defined parameter that could be used for expansion of motion-equations solution

2 QCD and heavy quark effective theory (HQET)

This section provides an overview of modern effective QCD theories, models and lists the derived predictions of the heavy meson properties.

2.1 The principles of HQET

As was mentioned above, the most recognised and developed theory of strong interactions is QCD. It has been extremely successful in the description of known phenomena and predictions of new ones. The key to this success is the exploitation of the asymptotic freedom, which allows perturbative calculations for various processes: deep-inelastic scattering, Drell-Yan processes [4] and many others. However, that is not always possible. This leads to the development of effective theories for the cases when the perturbative calculations are not possible. The description of heavy-light mesons $Q\bar{q}$ (one heavy and one light quarks) and baryons Qq_1q_2 (one heavy and two light quark) is one such case. An approach known as heavy quark effective theory (HQET) [2, 5, 6] has emerged for analysing those systems. This section presents some basic ideas of HQET as is given in Ref. [6].

A simple estimation shows that the heavy quark in a heavy-light hadron moves non-relativistically. In this case the hadron should have a momentum of order Λ_{QCD}:

$$p_Q = p_{\text{light}} \sim \Lambda_{\text{QCD}},$$

where Λ_{QCD} is the QCD energy scale (see Sec. 1.1). This momentum corresponds to the velocity of the heavy quark

$$v_Q = \frac{p_Q}{m_Q} \sim \frac{\Lambda_{\text{QCD}}}{m_Q}$$

For heavy quarks, $m_{c,b,t} \gg \Lambda_{\text{QCD}}$, $v_Q \ll 1$ and the heavy quark is essentially a stationary source of a colour field. In this case the actual mass of the heavy quark becomes irrelevant and the spin interaction decouples from the rest of the meson dynamics. This means that the heavy quark $Q(v, s)$ (e.g. charm) with velocity v and spin s in the description can be replaced with another one $Q'(v, s)$ (e.g. beauty) with the same velocity and spin. This property is important for the description of a real system of heavy-light mesons and baryons and provides a valid expansion parameter: E/m_Q, where E is the kinetic energy of the heavy quark. As the colour magnet interaction strength is proportional to $1/m_Q$, in the limit of infinite mass, $m_Q \to \infty$, in leading order the properties of the hadron will depend only on the light quarks. This causes a two-fold spin degeneracy of $Q\bar{q}$ states and allows the spin of the heavy quark to be neglected for leading-order calculations. For more precise calculations, the higher order corrections to $1/m_Q$ should be taken into account.

The $1/m_Q$ terms for s quark are too large, so the s quark cannot be treated as "heavy enough". Practically the theory can be applied to c and b quarks; however the t quark decays too fast to hadronize. The HQET in this form might be applied for studies of charm and beauty meson masses, widths and to decays with heavy quarks in initial and final states: $D_2^{*+} \to D^0\pi^+$, $B^0 \to D^{*+}\pi^-$ etc. It does not improve the understanding of the dynamics, but the new symmetries of the effective theory provide a lot of predictions.

2.2 Excited charm meson mass spectra and mixing

The lowest-mass states of the $c\bar{u}$, $c\bar{d}$ and $c\bar{s}$ systems with orbital angular momentum[10] $L = 0$ and spin $S = 0$ (D^0, D^+, D_s^+) and $S = 1$ $(D^{*0}, D^{*+}, D_s^{*+})$ are well established [1]. For higher states with $L = 1$[11], four states are expected for each $c\bar{q}$ system: one state with $S = 0$ and three states with $S = 1$. This makes one state with $J^P = 0^+$, one with $J^P = 2^+$ and two with $J^P = 1^+$. The $L = 1$ mesons can decay via the strong interaction to charm mesons with $L = 0$ by emitting one or more pions or kaons. According to HQET predictions [2, 7], the properties of

---

[10] In this section and below the following quantities are used:

- S, the spin of the system;
- J, the total angular momentum of the system;
- M, the component of J along the $\widehat{z}$ axis;
- L, the orbital angular momentum;
- n, the number associated with the radial excitations;
- ℓ, the orbital angular momentum of the light quark;
- j, the total angular momentum of the light quark;
- m, the component of j along the $\widehat{z}$ axis.

The state of a system is described by the wave-function $\psi_{n,\ell,j,m}(r, \theta, \varphi)$ with an energy $E_{n,\ell,j,J}$.

[11] These states are called excited (charm) mesons and often denoted by D^{**} in this thesis.

the $L = 1$ mesons are determined mainly by the total angular momentum of the light quark, $j = \ell + s$, where s denotes the spin of the light quark. On this basis, the four states are grouped in doublets with $j = 3/2$ and $j = 1/2$.

The HQET predicts different properties for those doublets. The $j = 3/2$ mesons are allowed to decay only via D-wave decays and $j = 1/2$ mesons are allowed to decay only via S-wave decays. As the kinematic space for both cases are similar, the $j = 1/2$ doublet members are expected to be wider [8, 9].

However, the general Hamiltonian of the heavy-light quark system might contain terms which can mix any states with the same total angular momentum, J, and parity, P [10]. The mixing terms are supposed to be of order $1/m_Q$. The prediction [10] states only two types of sizable mixing. Large mixing can occur for pairs of states $\psi_{n,\ell,j,J,M}$ and $\psi_{n',\ell',j',J,M}$ with:

- $n = n'$, $\ell = \ell'$ and $j + \frac{1}{2} = j' - \frac{1}{2} = \ell = J$ (i.e. mixing within a given n and l multiplet);
- $n+1 = n'$, $\ell+2 = \ell'$ and $j+\frac{1}{2} = j'-\frac{1}{2} = \ell = J$ (e.g. S-D mixing of states).

The mixing in the wave-functions and in the energy levels could be estimated from a perturbation theory with an expansion of the Hamiltonian in powers of $(1/m_Q)$

$$\mathcal{H} = \mathcal{H}^{(0)} + \frac{1}{m_Q}\mathcal{H}^{(1)} + \frac{1}{m_Q^2}\mathcal{H}^{(2)} + ...,$$

where the $\mathcal{H}^{(0)}$ is the Hamiltonian of system without an interaction and higher-order terms are responsible for the interaction. In this approach the mixing changes the physical wave-functions and energy levels of the system to:

$$\begin{pmatrix} \psi_{n,\ell,j,m} \\ \psi_{n',\ell',j',m} \end{pmatrix}^{\text{phys.}} = \begin{pmatrix} 1 & +\frac{\epsilon}{2\Delta} \\ -\frac{\epsilon}{2\Delta} & 1 \end{pmatrix} \begin{pmatrix} \psi_{n,\ell,j,m} \\ \psi_{n',\ell',j',m} \end{pmatrix} + \mathcal{O}(\epsilon^2)$$

$$\begin{pmatrix} E_{n,\ell,j,J} \\ E_{n',\ell',j',J} \end{pmatrix}^{\text{phys.}} = \begin{pmatrix} E_{n,\ell,j,J} + \frac{\epsilon^2}{2\Delta} \\ E_{n',\ell',j',J} - \frac{\epsilon^2}{2\Delta} \end{pmatrix} + \mathcal{O}(\epsilon^2)$$

with $\Delta = (E_{n,\ell,j,J} - E_{n',\ell',j',J})/2$ and

$$\epsilon = \frac{1}{m_Q} \sum_M \int \Psi^\dagger_{n,\ell,j,J,M}(x)\mathcal{H}^{(1)}\Psi_{n',\ell',j',J,M}(x)\mathrm{d}^3x.$$

$H\ (n^jL_J)$	M [10]	ω [10]	M [11]	ω [11]	M [12]
$D\ (1^{\frac{1}{2}}S_0)$	1.868		1.871		1.869
$D\ (1^{\frac{1}{2}}S_1)$	2.005		2.010		2.011
$D\ (1^{\frac{1}{2}}P_0)$	2.377		2.406		2.308
$D\ (1^{\frac{3}{2}}P_1)$	2.417	-0.1092	2.426	0.62	2.425
$D\ (1^{\frac{3}{2}}P_2)$	2.460		2.460		2.468
$D\ (1^{\frac{1}{2}}P_1)$	2.490	0.1092	2.469	0.62	2.421
$D\ (2^{\frac{1}{2}}S_0)$	2.589		2.581		
$D\ (2^{\frac{1}{2}}S_1)$	2.692	0.0217	2.632		
$D\ (1^{\frac{5}{2}}D_2)$	2.775	-0.0541			
$D\ (1^{\frac{3}{2}}D_1)$	2.795	-0.0217			
$D\ (1^{\frac{5}{2}}D_3)$	2.799				
$D\ (1^{\frac{3}{2}}D_2)$	2.833	0.0541			
$D_s\ (1^{\frac{1}{2}}S_0)$	1.965		1.969		1.969
$D_s\ (1^{\frac{1}{2}}S_1)$	2.113		2.111		2.110
$D_s\ (1^{\frac{1}{2}}P_0)$	2.487		2.509		2.325
$D_s\ (1^{\frac{3}{2}}P_1)$	2.535	-0.1162	2.536	0.60	2.467
$D_s\ (1^{\frac{3}{2}}P_2)$	2.581		2.571		2.568
$D_s\ (1^{\frac{1}{2}}P_1)$	2.605	0.1162	2.574	0.60	2.525
$D_s\ (2^{\frac{1}{2}}S_0)$	2.700		2.688		
$D_s\ (2^{\frac{1}{2}}S_1)$	2.806	0.0197			
$D_s\ (1^{\frac{5}{2}}D_2)$	2.900	-0.0611			
$D_s\ (1^{\frac{3}{2}}D_1)$	2.913	-0.0197			
$D_s\ (1^{\frac{5}{2}}D_3)$	2.925				
$D_s\ (1^{\frac{3}{2}}D_2)$	2.953	0.0611			

Table 2.1: *The predictions for masses $M[\,GeV]$ and state mixing angle (ω) of D and D_s mesons based on HQET.*

The expressions above provide a recipe for the calculations of the heavy meson masses and mixing angles. Unfortunately the explicit form of the wave functions and $\mathcal{H}^{(1)}$ is not known, but considering confinement and asymptotic freedom, some general conclusions can be made: this should be an interaction potential that is close to linear at large distances and more Coulomb-like at short distances. Every prediction scheme has its own splitting between vector and scalar parts of the interaction potentials, in many cases requiring a good description of $L = 0$ states. The angular part of $\Psi^{\dagger}_{n,\ell,j,J,M}(x)$ is known from general considerations and the angular part of the functions is arbitrary and is chosen "reasonably" to satisfy boundary conditions.

The described approach was studied in Ref. [10–12] and used for predictions of masses and mixing angles of heavy-light mesons based on lattice simulations. The results are listed in Tab. 2.1. The predicted heavy-light meson spectra should be compared to the spectra of established states (see Fig. 2.1). According to the PDG [1] the narrow excited charm mesons, $D_1(2420)^0$, $D_1(2420)^{\pm}$, $D_{s1}(2536)^{\pm}$ and $D_2^*(2460)^0$, $D_2^*(2460)^{\pm}$, $D_{s2}(2573)^{\pm}$ are tentatively identified as the members of the $j = 3/2$ doublets with $J^P = 1^+$ and 2^+. The HQET expectations were supported by the measurements of the broad non-strange excited charm mesons: neutral and charged $D_0^*(2400)^{0,\pm}$ with $J^P = 0^+$ [13,14], and $D_1(2430)^0$ with $J^P = 1^+$ [15]. At the same time the predicted broad non-strange charged excited charm meson with $J^P = 1^+$ has not yet been observed. The two charm-strange excited mesons, $D_{s0}^*(2317)^{\pm}$ [16] with $J^P = 0^+$ and $D_{s1}(2460)^{\pm}$ [17] with $J^P = 1^+$ revealed their surprisingly small masses and as a result narrow widths [1] (the small mass values forbid their decay into $D^{(*)}K$ final states). The case of mixing among $J^P = 1^+$ states is the only sizable predicted mixing (see Tab. 2.1) and hereby is the most important one for the tests of HQET. The pairs of states with $J^P = 1^+$, $D_1(2420)^0, D_1(2430)^0$ $D_1(2420)^+, D_1(2430)^+$ and $D_{s1}(2460)^{\pm}, D_{s1}(2536)^{\pm}$ can be a mixture of states with $j = 3/2$ and $j = 1/2$ with corresponding mixture in the $D_1 \to D^*\pi$ decays (S-wave and D-wave decay mixture). The angular distributions of the decay products of $J^P = 1^+$ mesons decay products will depend on the widths of S-wave and D-wave channels, the mixing among states and the mixing among decay waves. A brief explanation on this topic is given below. The differential width of the decay is by definition

$$d\Gamma_{D_1} \propto |\psi_{D_1}\widehat{M}\psi^*_{D^*\pi}|^2 dV,$$

where $\widehat{M}$ is a matrix element of transition between ψ_{D_1} and $\psi_{D^*\pi}$ states and dV

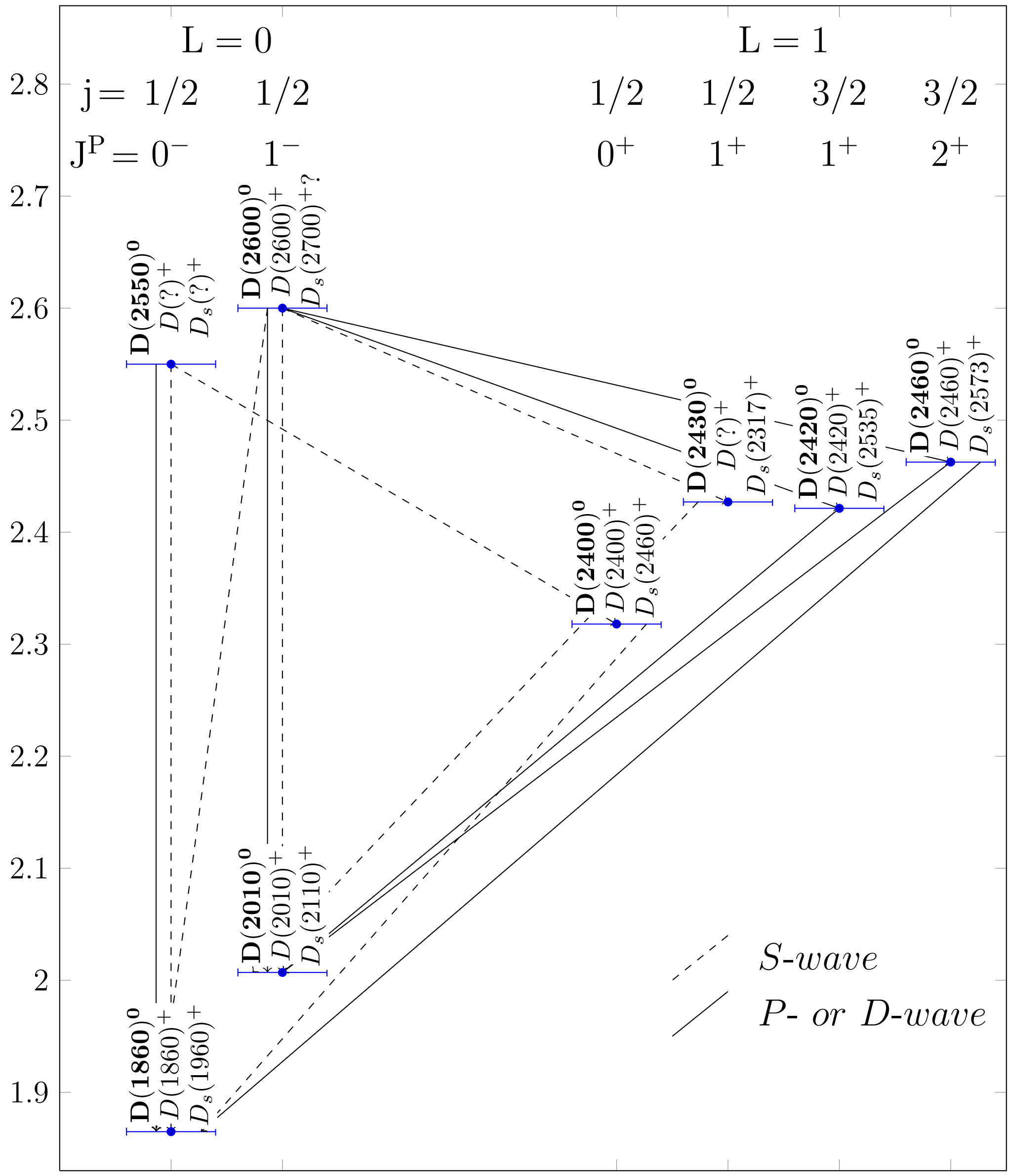

Figure 2.1: *Charm meson spectra and one particle transitions [1]. The levels (masses) are shown for neutral states (bold labels). The corresponding charged and strange states are given with neutral states with the same quantum numbers. The transitions occur with an emission of* $\pi^{0,\pm}$, $K^{0,\pm}$, $\rho^{0,\pm}$ *or* γ, *see details in Ref. [1].*

denotes an element of phase space. We assume that the D_1 state is a mixture of two states with $j = 3/2$ and $j = 1/2$:

$$\psi_{D_1} = \psi_{D_1,1/2} \sin\omega + \psi_{D_1,3/2} \cos\omega,$$

where $\omega = \arctan(2\epsilon/\Delta)$ is the state mixing angle. In this case the differential width is

$$\begin{aligned} d\Gamma_{D_1} \propto (|(\psi_{D_1,1/2} \sin\omega + \psi_{D_1,3/2} \cos\omega)(\widehat{M}_{D_1\to D^*\pi,S} + e^{i\phi}\widehat{M}_{D_1\to D^*\pi,D})\times \\ \times(\psi^*_{D^*\pi,1/2} \sin\omega + \psi^*_{D^*\pi,3/2} \cos\omega)|^2)dV, \end{aligned} \tag{2.1}$$

where ϕ is the relative phase between the two matrix elements of S- and D-wave transitions, $\widehat{M}_{D_1\to D^*\pi,S}$ and $\widehat{M}_{D_1\to D^*\pi,D}$. After transformation of Eq. (2.1) and omitting terms like $\psi_{D_1,1/2}\widehat{M}_{D_1\to D^*\pi,D}\psi^*_{D^*\pi,1/2} \sin^2\omega$ (the $D_1, 1/2$ state is not allowed to decay through D-wave) we have:

$$d\Gamma_{D_1} \propto |\psi_{D_1,1/2}\widehat{M}_{D_1\to D^*\pi,S}\psi^*_{D^*\pi,1/2} \sin^2\omega + e^{i\phi}\psi_{D_1,3/2}\widehat{M}_{D_1\to D^*\pi,D}\psi^*_{D^*\pi,3/2} \cos^2\omega|^2 dV,$$

or

$$\begin{aligned} d\Gamma_{D_1} \propto (|\psi_{D_1,1/2}\widehat{M}_{D_1\to D^*\pi,S}\psi^*_{D^*\pi,1/2} \sin^2\omega|^2 + |\psi_{D_1,3/2}\widehat{M}_{D_1\to D^*\pi,D}\psi^*_{D^*\pi,3/2} \cos^2\omega|^2 + \\ +2\cos\phi|\psi_{D_1,1/2}\widehat{M}_{D_1\to D^*\pi,S}\psi^*_{D^*\pi,1/2} \cos^2\omega||\psi_{D_1,3/2}\widehat{M}_{D_1\to D^*\pi,D}\psi^*_{D^*\pi,3/2} \sin^2\omega|)dV. \end{aligned}$$

Defining

$$\int |\psi_{D_1,1/2}\widehat{M}_{D_1\to D^*\pi,S}\psi^*_{D^*\pi,1/2} \sin^2\omega|^2 dV = \Gamma_S,$$

$$\int |\psi_{D_1,3/2}\widehat{M}_{D_1\to D^*\pi,D}\psi^*_{D^*\pi,3/2} \cos^2\omega|^2 dV = \Gamma_D$$

and taking into account the angular dependence of matrix elements on the azimuthal angle θ and on α, the angle between the pion from the D^* and the pion from the D_1 (see details in Ref. [5])

$$\widehat{M}_{D_1\to D^*\pi,D} \propto (\sin\theta \sin\alpha + 2\cos\theta\cos\alpha),$$

$$\widehat{M}_{D_1\to D^*\pi,S} \propto (\sin\theta \sin\alpha - \cos\theta\cos\alpha),$$

we have

$$\frac{d\Gamma_{D_1}}{d\cos\alpha d\cos\theta} \propto \Gamma_S(\sin\theta\sin\alpha - \cos\theta\cos\alpha)^2 + \Gamma_D(\sin\theta\sin\alpha + 2\cos\theta\cos\alpha)^2 +$$

$$+2\cos\phi\sqrt{\Gamma_S\Gamma_D}(\sin\theta\sin\alpha\cos\theta\cos\alpha)(\sin\theta\sin\alpha + 2\cos\theta\cos\alpha),$$

or, after integration over $\cos\theta$

$$\frac{d\Gamma_{D_1}}{d\cos\alpha} \propto \Gamma_S + \Gamma_D(1 + 3\cos^2\alpha)/2 + \sqrt{2\Gamma_S\Gamma_D}\cos\phi(1 - 3\cos^2\alpha).$$

Using the substitution $r = \Gamma_S/(\Gamma_S + \Gamma_D)$ leads to

$$\frac{d\Gamma_{D_1}}{d\cos\alpha} \propto r + (1-r)(1 + 3\cos^2\alpha)/2 + \sqrt{2r(1-r)}\cos\phi(1 - 3\cos^2\alpha).$$

The latter can be parametrised for the experimental measurements as

$$\frac{d\Gamma_{D_1}}{d\cos\alpha} \propto 1 + h\cos^2\alpha, \tag{2.2}$$

where $h = \frac{3(1-r-2\sqrt{2r(1-r)}\cos\phi)}{1+r+2\sqrt{2r(1-r)}\cos\phi}$. The relation between h, r and ϕ is given by

$$\cos\phi = \frac{(3-h)/(3+h) - r}{2\sqrt{2r(1-r)}}.$$

The parameter h is called helicity. The leading-order prediction of HQET without mixing gives $r = 0$ and $h = 3$ for D_1 states.

As it was mentioned above, the D_2 states can mix only with higher states, so it is expected that $D_2 \to D^*\pi$ decays are pure D-wave decays and $\Gamma = \Gamma_D$. The angular distribution of $\widehat{M}_{D_2\to D^*\pi,D}$ is

$$\widehat{M}_{D_2\to D^*\pi,D} \propto \sin\theta\cos\theta\sin\alpha,$$

which gives

$$\frac{d\Gamma_{D_2}}{d\cos\alpha} \propto \sin^2\alpha = 1 - \cos^2\alpha.$$

This angular distribution corresponds to helicity $h = -1$.

2.3 Excited charm meson widths and branching ratios

In addition to the mass spectra and decay properties, the HQET tries to predict the branching ratio of different decay modes. To predict the full width of the resonance, a sum over partial widths of decay should be taken. This approach requires taking into account all decay modes, thus an accurate prediction is not always possible. Typically within the same prediction scheme at least one of the widths of $L = 1$ D-mesons is quite away from the measured values [18] [19]. The typical predictions on widths are between 15 MeV and 27 MeV for $D_1^{+,0}$ and between 50 MeV and 65 MeV for $D_2^{*0,+}$ (see Ref. [18]).

On the other hand, the ratio of two branching ratios might be predicted more precisely.

- According to the general theory of pion transitions between heavy hadrons [5, 8] the rate for the pion transition from a heavy hadron with light degrees of freedom with spin j to a heavy hadron with light degrees of freedom freedom of spin j' depends on the total spins J, J' of the initial and final hadrons according to the factor

  $$(2j+1)(2J'+1)\left|\begin{Bmatrix} j' & j & L \\ J & J' & \frac{1}{2} \end{Bmatrix}\right|^2 \cdot p_\pi^{2L+1}.$$

  In this equation, L is the pion orbital angular momentum, the bracket denotes a 6-j symbol, and p_π is the pion 3-momentum. For the transitions from (D_1, D_2^*) to (D, D^*), $L = 2$ [5]. The last factor is the kinematic suppression factor for emitting pions of large L, which may vary significantly over the heavy multiplets even if their splitting is small. This approach gives [5]

  $$\Gamma(D_1 \to D\pi) \div \Gamma(D_1 \to D^*\pi) \div \Gamma(D_2^* \to D\pi) \div \Gamma(D_2^* \to D^*\pi) =$$

  $$= (0 \times 4.5) \div (1 \times 0.9) \div (2/5 \times 6.2) \div (3/5 \times 1.4)$$

  and

  $$\frac{\Gamma(D_2^* \to D\pi)}{\Gamma(D_2^* \to D^*\pi)} \approx 3.0.$$

- Using a chiral perturbation theory approach, in Ref. [20] it was predicted:
$$\frac{\Gamma(D_2^{*0} \to D^+\pi^-)}{\Gamma(D_2^{*0} \to D^{*+}\pi^-)} = 2.7.$$

- Calculations similar to that used for the mass-spectrum prediction [21] give the ratio of branching ratios:
$$\frac{\Gamma(D_2^{*+} \to D^0\pi^+)}{\Gamma(D_2^{*+} \to D^{*0}\pi^+)} = 2.266 \pm 0.015,$$
$$\frac{\Gamma(D_2^{*0} \to D^+\pi^-)}{\Gamma(D_2^{*0} \to D^{*+}\pi^-)} = 2.280 \pm 0.007.$$

- The estimated ratio of branching ratios for the excited charm-strange meson D_{s1}^+ [18] is:
$$\frac{\Gamma(D_{s1}^+ \to D^{*0}K^+)}{\Gamma(D_{s1}^+ \to D^{*+}K^0)} = 1.2 - 1.7.$$

The given predictions can be tested experimentally.

2.4 Charm quark fragmentation fractions from theoretical expectations

Hadron production in *ep* collisions at high energy is generally believed to be the result of a two-stage process: a parton shower generated by the qq pair and a fragmentation of the partons into observable hadrons. The former process is hard and can be described by perturbative QCD, whereas the latter is soft and not calculable with a perturbative approach. Therefore, several phenomenological models aimed at describing quantitatively the fragmentation process have been developed.

In one of those the production of a quark pair in the colour string field can be considered as a tunnelling process. In this approach [22] the probability to produce a qq pair is proportional to $\exp(-m_q^2/k)$, where m_q is the constituent quark mass, and k the string constant. In this approach the probability of quarks recombined to form a hadron with mass M_h is proportional to $\exp(-E_{\text{bind}}/T)$, where $E_{\text{bind}} = M_h - \Sigma q_i$ is the hadron binding energy, and T the effective temperature in hadronisation. The production rates of light flavoured mesons and baryons from fragmentation can be described as

$$f(q \to h) = C\frac{2J+1}{C_B}(\gamma_s)^{N_s}\exp(-E_{\mathrm{bind}}/T), \tag{2.3}$$

where $\gamma_s = \exp(-\pi(m_s^2 - m_u^2))$ is the strangeness suppression factor, N_s is the number of strange quarks contained in the hadron and C_B is the relative normalisation factor between mesons and baryons (for mesons $C_B = 1$), which should be independent of the centre-of-mass energy. In this model, parameters γ_s, $\delta m = m_s - m_u$, T, C and C_B are free and should be extracted from data. The obtained predictions are listed in Tab. 2.2.

The other approach, the thermodynamical model [23, 24], implies postulating the existence of a hadron gas in thermodynamical equilibrium before the hadrons decouple. A more detailed overview of this model is given elsewhere [23]. The thermodynamical approach was used in Ref. [24] for calculation of charm fragmentation fractions of charm mesons. The obtained predictions are listed in Tab. 2.2.

Fraction	Prediction,% [24]	Prediction,% [22]
$f(c \to D_1^+)$	-	-
$f(c \to D_1^0)$	3.5	-
$f(c \to D_2^{*+})$	-	-
$f(c \to D_2^{*0})$	4.7	-
$f(c \to D_{1s}^+)$	0.54	-
$f(c \to D_1^+) + f(c \to D_2^{*+})$	-	8.5
$f(c \to D_1^0) + f(c \to D_2^{*0})$	-	8.5
$f(c \to D_{1s}^+) + f(c \to D_{2s}^{*+})$	-	1.4

Table 2.2: *The predictions for charm quark fragmentation fractions to $L = 1$ mesons according to different models.*

2.5 Heavy flavour production at HERA

In the general case the scattering at an *ep* collider can be described as a process

$$ep \to l'X,$$

where the l' is a scattered lepton, and X denotes the hadronic system. In first order this interaction is mediated by γ and Z^0 bosons (this is called neutral current), or $W^\pm$ (this is called charged current). The general view of this process is shown in Fig. 2.2. The kinematics of this process is described with a set of variables:

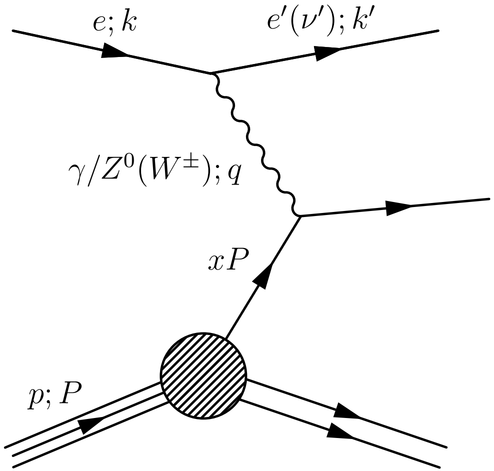

Figure 2.2: *The general Feynman diagram for the ep scattering.*

- incoming and scattered lepton momentum k and k';
- incoming proton with momentum P;
- $s = (k + P)^2$, the squared centre-of-mass energy;
- $Q^2 = -q^2 = -(k - k')^2$ the squared exchanged four momentum at the interaction point;
- $x = \frac{Q^2}{2Pq}$, the Bjorken scale variable;
- $y = \frac{Pq}{Pk}$ inelasticity;

- $W^2 = (P + q)^2$, the squared centre-of-mass energy of the boson-proton system.

For sufficiently large Q^2, the masses of proton and electron can be neglected and with a good approximation

$$Q^2 = sxy.$$

As the s is fixed for HERA, only two variables are needed to describe the kinematics of the process. On the basis of Q^2 the events are divided in two groups: photoproduction events (PHP) with almost real photons, $Q^2 \approx 0$ and deep inelastic scattering (DIS) events with Q^2 higher than a few GeV^2. The main mechanism of heavy flavour production at HERA is the leading order boson-gluon fusion (BGF) illustrated in Fig. 2.3(a). Some fraction of charm quarks will be produced in resolved events, when the photon fluctuates hadronically and a parton from the fluctuation (mostly gluon) then participates in the hard interaction (see Fig. 2.3(b)). Other types of events are events with an excitation in proton or photon, when the interaction occurs with intrinsic charm or beauty inside the proton or photon (see Fig. 2.3(d,e,f)). More illustrations for the charm production are shown in Fig. 2.3. The produced heavy quarks c, b in the end fragment to different hadrons.

The mechanism of charm meson production in HERA described above differs from the production mechanism in other experiments (e.g. beauty factories). At the beauty factories the charm mesons are born in the decays of beauty mesons (e.g. $e^+e^- \to \Upsilon, \Upsilon \to BB, B \to DX$) or from the fragmentation of low-energy charm quarks produced in pairs (e.g. $e^+e^- \to c\bar{c}, c \to D$). HERA thereby provides a unique opportunity for the measurements of charm-quark fragmentation fractions even if the number of produced charm mesons is lower than at beauty factories.

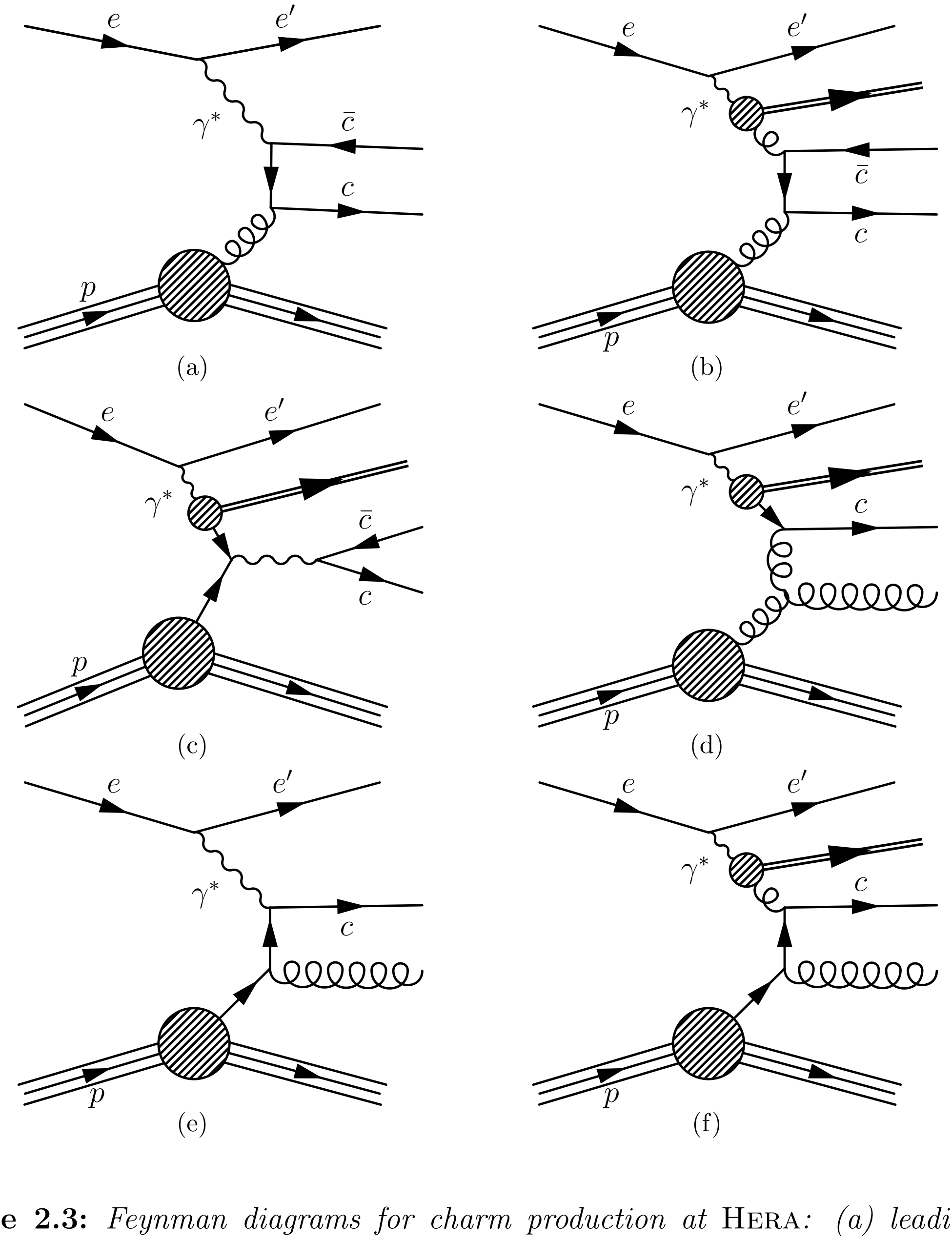

Figure 2.3: *Feynman diagrams for charm production at* HERA*: (a) leading-order boson-gluon fusion; (b) resolved boson-gluon fusion; (c) Drell-Yan process; (d) charm excitation in photon; (e) charm excitation in proton; (f) (another) charm excitation in proton.*

3 Experimental set-up

This section describes the experimental set-up. After a short introduction devoted to DESY a brief description of the accelerator facilities follows. Then, after a general description of the ZEUS detector, the parts relevant to this study are described with more details.

3.1 HERA ring

The Deutsches Electronen Synchrotron (DESY) is one of the largest HEP research centres in the world. The Hadron Electron Ring Anlage (HERA) is a ring accelerator at DESY in Hamburg [26]. It is a unique electron-proton collider in the world[12]. The ring tunnel has a circumference of approximately 6336 m. It is

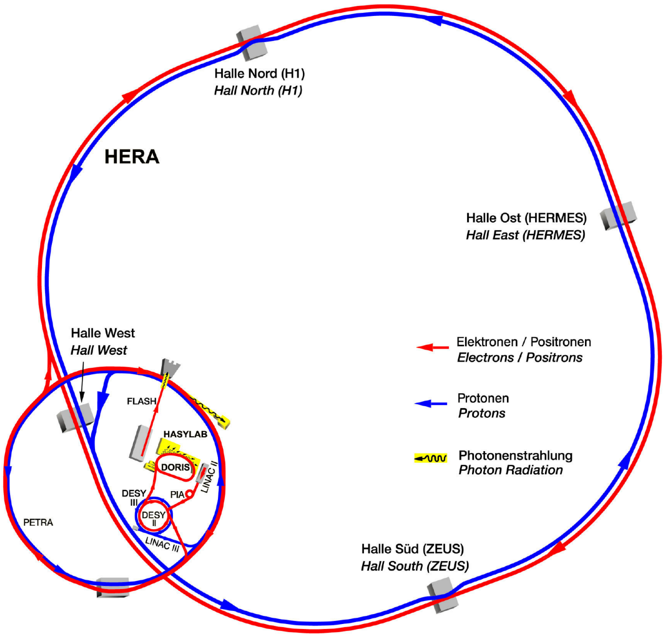

Figure 3.1: *Schematic view of* HERA *accelerating ring, preacceleration facilities and experimental holes [25].*

---

[12] Here and below the particle (e.g. electron) will refer to both – particle and antiparticle unless it is stated explicitly.

divided in four straight sections with acceleration facilities and four arcs that connect straight sections. The HERA tunnel is simultaneously used for acceleration of protons and electrons with the electron ring placed on top of the proton ring. The magnets of the electron ring operate at normal (room) temperature, while the magnets of the proton ring are build using superconducting technology and operate at 4.2 K, creating a magnetic field of 4.7 T. The tunnel is located between fifteen and twenty meters underground. The four experimental halls are located in the centres of straight sections. A schematic overview of the accelerator ring is given in Fig. 3.1.

Although HERA was build as an electron-proton collider, only two of its experimental holes (Hall North and Hall South) were used for electron-proton collisions in H1 and ZEUS experiments respectively. The other two halls (Hall North and Hall South) were used by fixed target experiments: HERMES, which studied the spin structure of the proton with electron beams and HERA-B, which was intended to study beauty production with proton beams. The storage rings were designed for energies of 820 GeV for protons and 30 GeV for electrons. The operational energy for electrons was 27.5 GeV, while for protons it was 820 GeV before 1997 and 920 GeVafterwards. The most important characteristics of the HERA acceleration complex are listed in Tab. 3.1.

The acceleration process starts in the preacceleration complex of HERA. [27] The injection of protons starts with acceleration of negative charged hydrogen ions (H) to 50 MeV in Proton Linac. Then, the proton beams were transmitted to the proton synchrotron Desy-III and accelerated there to 7.5 GeV. At the next stage the protons were transferred to PETRA and to HERA. The circumference of HERA is 11/4 times bigger than the circumference of PETRA. Thus, up to three full PETRA injections were needed to fill HERA with protons. The electrons are pre-accelerated in the linear accelerators Linac-I or Linac-II with corresponding energies 220 MeV and 450 MeV [27]. From there electrons were transferred to Desy-II and accelerated to 7.5 GeV. Finally, after further acceleration in PETRA to 14 GeV they are transmitted to HERA. To fill HERA, the electrons were transmitted from PETRA to HERA up to five times.

During the 2001-2002 break the HERA ring was upgraded: the luminosity was increased and electron polarisation systems were installed [28]. The time of break was also used to install new detector – HERMES and upgrade existing ZEUS, H1 and HERA-B. Before decommissioning, in 2007, a two special data taking periods with lower proton energy took place. For the first data taking period,

The HERA tunnel	Value	
Commissioning	1991	
Circumference of the HERA tunnel	6336 m	
Depth underground	10 – 25 m	
Inner diameter of the tunnel	5.2 m	
Thickness of the tunnel walls	30 cm	
Number of pre-accelerators for HERA	6	
Number of experimental halls	4	
Size of the experimental halls	25 m × 43 m	
Number of experiments (1st stage)	2 (H1 and ZEUS)	
Beginning of the experiments	April 1992	
Number of interaction points	3	
The HERA Beams	Electron	Proton
Nominal energy	30 GeV	820 GeV
Centre of mass energy	314 GeV	
Injection energy	14 GeV	40 GeV
Luminosity per int. point	1.5×10^{31} cm$^{-2}s^{-1}$	
Particle current	60 mA	160 mA
Particles per bunch	3.5×10^{10}	10^{11}
Number of bunch buckets	220	220
Maximum number of bunches	210	210
Beam crossing angle	head–on collision, 0 mrad	
Bunch distance	28.8 m (96 ns)	
Bunch length at max. energy (1σ)	7.8 mm	110–150 mm
Beam width at the int. points	0.3 mm	0.32 mm
Beam height at the int. points	0.04 mm	0.1 mm
Radiation energy loss per revolution	70.38 MeV	1.4×10^{-10} MeV
Polarisation time at 30 GeV	27 min	—
Filling time	15 min	20 min

Table 3.1: HERA *ring design parameters according to [27].*

called **medium energy runs (MER)** the energy of proton beam was reduced to 575 GeV. For the second, called **low energy runs (LER)**, the energy of proton beam was reduced to 460 GeV. The performance of Hera machine before upgrade, after upgrade and during MER/LER periods is shown in Fig. 3.2. The delivered luminosity of machine and the performance of data taking by Zeus experiment is summarised in Tab. 3.2.

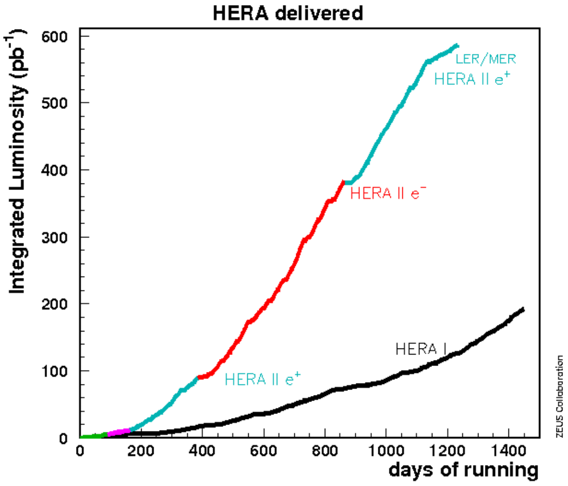

Figure 3.2: Hera-I *and* Hera-II *delivered luminosities vs. operation time [29].*

Period	Hera-I			Hera-II				
Year	94-97	97-98	99-00	03-04	04-06	06-07	07LER	07MER
Collision	e^+p	e^-p	e^+p	e^-p	e^+p	e^+p	e^+p	e^+p
Proton energy, GeV	820	920	920	920	920	920	460	575
Electron energy, GeV	27.5							
CMS energy, GeV	301	314	314	314	314	314	225	296
Hera delivered, pb^{-1}	70.9	25.2	95.0	84.5	290.9	180.5	15.7	9.4
Zeus taken, pb^{-1}	48.3	16.7	65.9	40.6	213.5	145.9	13.2	7.8

Table 3.2: Hera *delivered and* Zeus *taken luminosity for different data taking periods [29].*

3.2 Zeus detector

Zeus was one of two general purpose detectors at the Hera collider. It was developed for a broad range of studies at Hera. It had a size of 12 m × 11 m × 20 m, weight of 3600 ton and was installed in the **Halle Süd**. The major components of Zeus included a system for charged particle tracking for polar angles $7.5^\circ < \theta < 170^\circ$ within a high-field superconducting solenoid, a high resolution depleted-uranium calorimeter and a tracking system for muons. The detector was completed by forward proton detectors and a luminosity monitor.

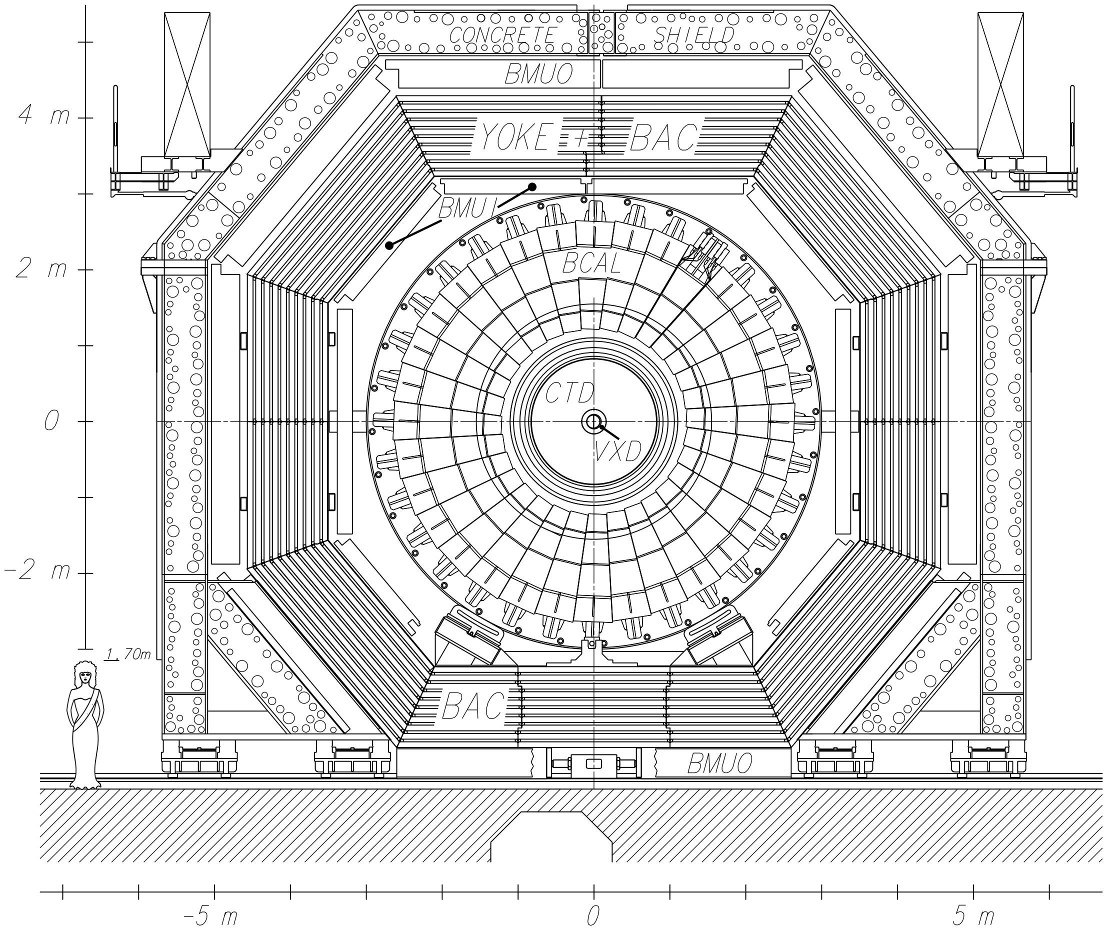

Figure 3.3: *Cross section of the* Zeus *detector in the transverse plane [30].*

The X-Y[13] section of the ZEUS detector is shown in Fig. 3.3. The R-Z section of the ZEUS detector (the central part) is shown in Fig. 3.4.

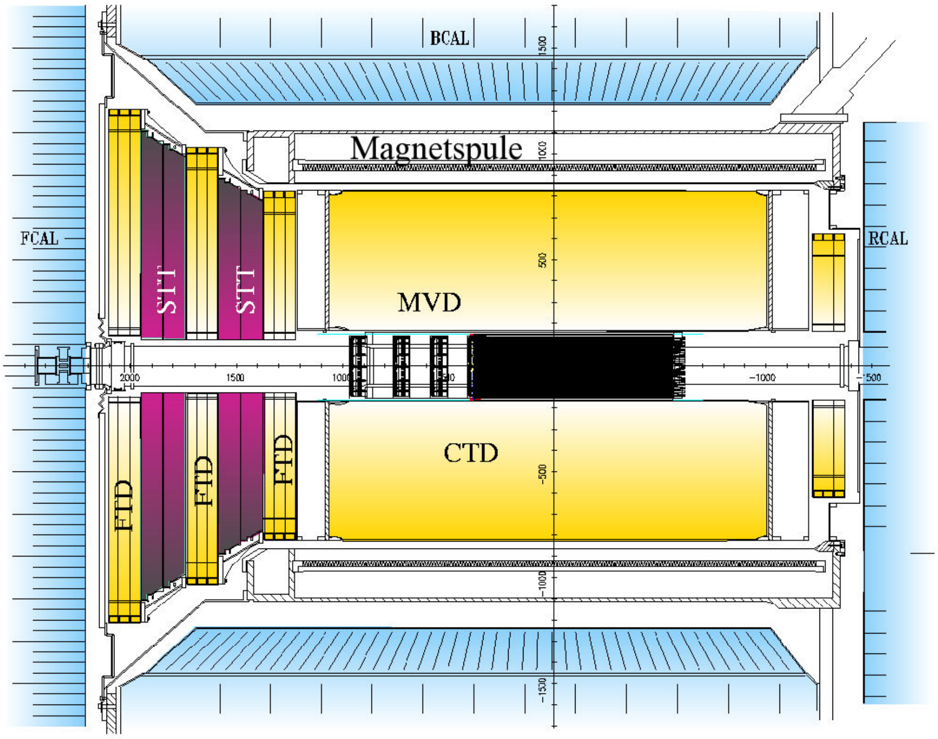

Figure 3.4: *General schematic view of* ZEUS *tracking system [31].*

3.3 The Central Tracking detector (CTD)

This section describes the central tracking detector (CTD), the most important component of the tracking system. The CTD detector was completely located in a strong magnetic field and surrounded by the depleted uranium calorimeter. It serves the following purposes: to reconstruct tracks over the polar angle range $15° < \theta < 164°$, provide dE/dx information for the particle identification, locate

---

[13] The ZEUS coordinate system is a right-handed Cartesian system, with the Z axis pointing in the proton beam direction, referred to as the "forward direction", and the X axis pointing left towards the centre of HERA. The coordinate origin is at the nominal interaction point.

the primary interaction point and to provide information for the ZEUS first and second-level triggers. The detailed design description of the CTD can be found elsewhere [32]. The design criteria of the CTD were:

- measure tracks with p_T a low as 150 MeV;
- have good tracking for dense jets;
- high resolution in p_T;
- high readout rate (less than 96 ns);
- be a part of first level trigger;
- possibility of data based alignment.

The CTD was build as a multi-cell stereo superlayer chamber. To provide precision momentum measurements the CTD was designed to operate in high magnetic field and B = 1.43 T and use $Ar/CO_2/C_2H_6$ gas mixture. It contains nine superlayers with a total of 4608 wires, grouped by cells of 8 sense wires with surrounding field(18), ground(9), guard(2) and shaper(4) wires [32] as shown in Fig. 3.5. Five

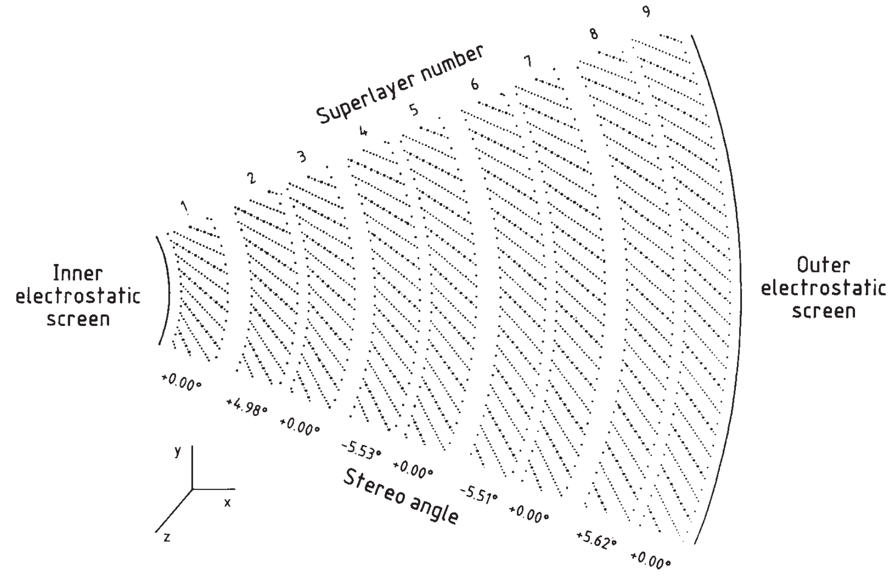

Figure 3.5: *Schematic X-Y-view of CTD superlayers [32].*

Parameter	Value
Inner radius	16.2 cm (18.2 cm active)
Outer radius	85.0 cm (79.4 cm active)
Length	241 cm (203 cm active)
Weight	945 kg (with amplifiers and on-chamber cables)
No. of cells	576
No. of wires total	24192
No. of sense wires	4608
Position resolution	$100 - 120\,\mu$m (θ-dependent)
Z resolution	1.4 mm (stereo)/30 mm (timing)
Two track resolution	< 2.5 mm
dE/dx resolution	$< 6\%$ (e^-)
Magnetic field	1.4-1.8 T
Maximum drift time	500 ns
Lorentz angle	45°
Gas mixture	$Ar/C_2H_6/C_2H_5OH : 50/50/1.49 (B = 1.8\,\mathrm{T})$ $Ar/CO_2/C_2H_6/C_2H_5OH : 85/13/2/0.96 (B = 1.8\,\mathrm{T})$ $Ar/CO_2/C_2H_6/C_2H_5OH : 90/8/2/0.84 (B = 1.43\,\mathrm{T})$
Mom. resolution at 90°:	$\frac{\sigma(p_T)}{p_T}, \% = 0.58 p_T[\,\mathrm{GeV}] \oplus 0.65 \oplus \frac{0.14}{p_T[\,\mathrm{GeV}]}.$

Table 3.3: *Properties of the CTD detector [27].*

of those superlayers are parallel to the beam direction and the other four have a small angle. The angle was chosen to provide a similar resolution for polar and azimuthal angles. In addition to a high-precision measurement of the Z coordinate position of a track using stereo layers (1.4 mm), Z-by-T information was used. The superlayers 1, 3 (partially), 5 (partially) were equipped with Z-by-timing electronics, which measure the Z coordinate of track hits by measuring the difference in arrival times at the two ends of each wire. This, using 704 wires, gives Z position resolution of ∼3 cm. The voltage of each wire was optimised to have the best tracking performance. A short summary of CTD parameters is given in Tab. 3.3.

3.4 The Microvertex Detector (MVD)

During the 2000/2001 HERA shut-down period, the tracking system of ZEUS was upgraded with a silicon Micro Vertex Detector (MVD). The main goal of this detector was to improve resolution for heavy flavour measurements. The MVD essentially is split in two parts – barrel and forward as it is shown in Fig. 3.6. The barrel part is 60 cm long and has silicon sensors arranged around the beam pipe. The forward part consists of four circular shaped disks. The detector had the following design parameters [33]:

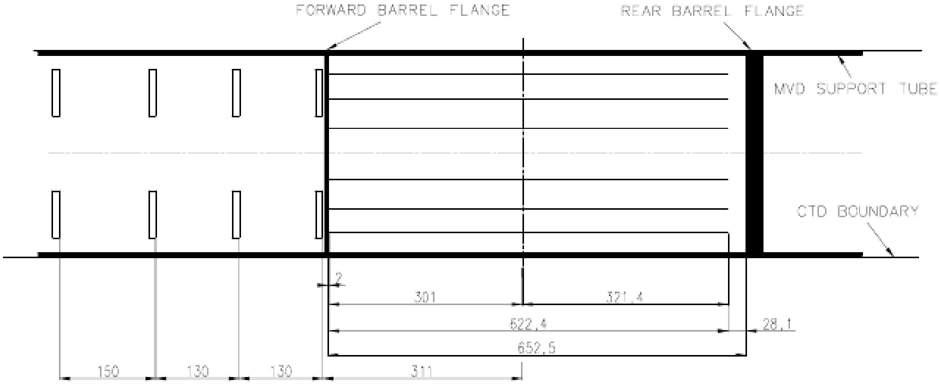

Figure 3.6: *Layout the MVD along the beam (Z) axis. Protons go from the right to left [33].*

- ability to detect tracks in range 7°– 160°;
- three spatial measurements per track, in two projections;
- $> 20\,\mu$m intrinsic hit resolution for normal incident tracks;
- impact parameter resolution of order $100\,\mu$m for polar angle of 90°, increasing gradually to 1 mm at 20°, for tracks with momentum greater than 2 GeV;
- noise occupancy $< 10^{-3}$;
- hit efficiency $> 97\%$;
- alignment accuracy better than $20\,\mu$m;

- two-track separation better than 200 μm.

The obtained single hit resolution in the MVD detector is about 24 μm.

Three layers of silicon strip sensors were arranged in concentric cylindrical planes surrounding the interaction point. A small fraction ~25% of the azimuth angle was covered by two cylinders due to limited space. The polar angular coverage for tracks with three hits ranges from 30° to 150°. The forward section was equipped with four planes of silicon strip sensors arranged around the beam pipe. This gives angular coverage down to 7° from the beam line; the rear section is kept free for cabling and cooling access. More details can be found elsewhere [33].

High resistivity n-type silicon is used to produce the single-sided 320 μm thick strip sensors. Two sensors (half modules) are glued together and one sensor is electrically connected to the other, forming a module with a surface of $123.68 \times 64.24\,\mathrm{mm}^2$. The readout strips of the two sensors within one half module perpendicular to each other as shown in Fig. 3.7(a). The modules have different shape for barrel and forward parts of detector and were placed, on ladders (see Fig. 3.7) and wheels respectively (see Fig. 3.8) The geometrical details of the MVD are summarised in Tab. 3.4. Details on their characteristics and performance under test beam conditions are described elsewhere [33].

Parameter	Value
Outer dimension	64240×64240 μm
Sensitive area	62200×61440 μm
Thickness	320 μm
Intermediate strip pitch	20 μm
Readout pitch	120 μm
Number of readout strips	512

Table 3.4: *Properties of silicon strip sensors [34].*

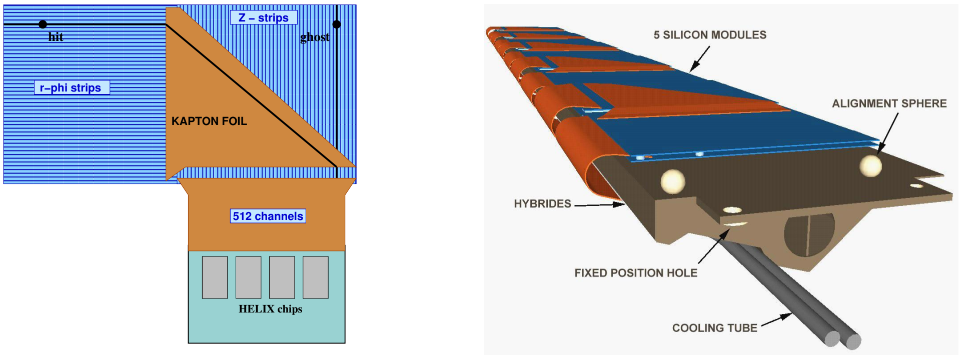

(a) An MVD outer half module. The dimensions of a single sensor are $6.2 \times 6.2\,\mathrm{cm}^2$ [34].

(b) MVD barrel ladder structure which supports 5 modules [34].

Figure 3.7: *Barrel MVD structure and modules [34].*

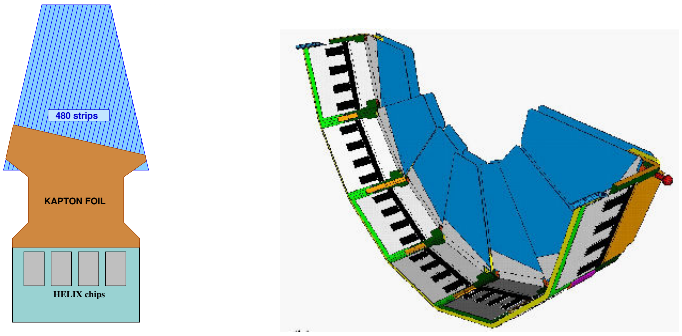

(a) Wedge shaped forward module [34].

(b) Half forward wheel which includes 14 forward modules [34].

Figure 3.8: *Forward MVD structure and modules [34].*

3.5 The Straw Tube tracker (STT)

In the 2000 a new detector, Straw-Tube-Tracker (STT) [35], was build as a replacement for Transition Radiation Detector (TRD) [27]. It was installed in the place in which the TRD had been installed before 2000 (see Fig. 3.4) and used the same read-out system. The STT detector was designed to improve the tracking in the forward region and improve electron identification for events with high Q^2. The coverage region of the detector was 6°– 25°(the maximal pseudorapidity $\eta = 3.0$).

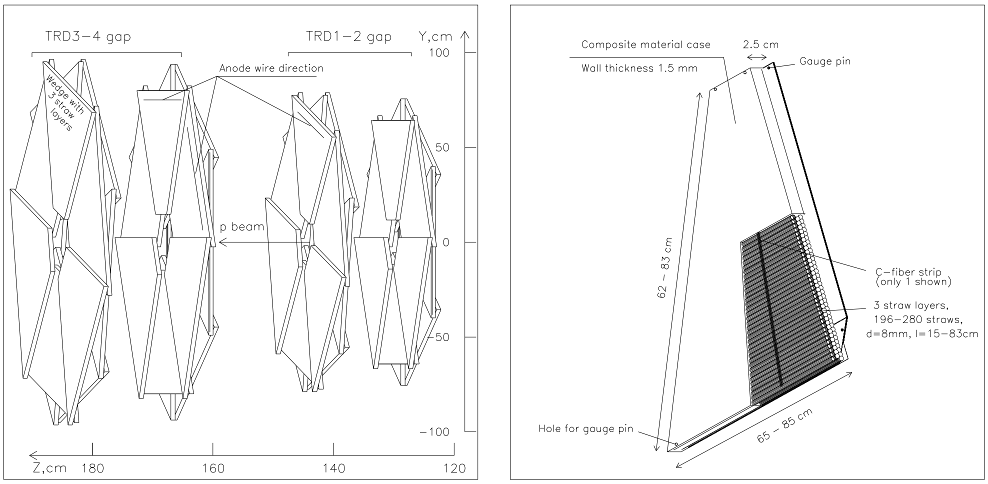

(a) Four layers of STT detector [35]. (b) The structure of STT sector [35].

Figure 3.9: *STT position and layers.*

Straw-chamber technology was used for this detector for several reasons. The limited available space for installation required a high mechanical and electrostatic stability of the detector, which was easy to reach with straw tube technology. Additional advantages were: good radiation hardness, small radiation length (only $0.15X_0$), precision tracking in an inhomogeneous magnetic field and costs. The STT consisted of two types of sectors (see Fig. 3.9): small sectors with 194 straws, large sectors with 266. In each sector the straws are arranged into three layers. Altogether, the STT consisted of six sectors per superlayer, four superlayers per module and of two modules. This makes a total of about 11000 straws in the whole detector. A schematic drawing is shown in Fig. 3.9. Each straw was made of two layers of 50 μm kapton foil. Together with the *Al* coating, this makes

Parameter	Value
Angular acceptance	5°–25°
Number of straw tubes/layers	11616/24
Straw tube outward diameter	8 mm
Straw tube wall thickness	120 μm
Straw tube wall length	15-83 cm
Max drift time	80 ns
Gas mixture	Xe/CO_2: 90/10 or $Ar/CO_2/CF_4$: 70/20/10
Straw occupancy	<1.5% average/ <15% in DIS jet
Single wire spatial resolution	140 μm
Efficiency per straw	98.5%

Table 3.5: *Properties of the STT detector [35].*

a tube wall thickness of ~120 μm. The internal diameter of a straw tube was 7.5 mm. All other parameters of STT detector are given in Tab. 3.5.

3.6 The calorimeter (CAL)

The calorimeter (CAL) was a sampling calorimeter consisting of plates of depleted uranium interleaved with plastic scintillator as an active material. The ratio of absorber and scintillator thickness was chosen to achieve compensation, an equal response for electrons and hadrons, and the best possible resolution for hadrons. The calorimeter provides precise energy measurements for hadrons and jets, an angular resolution for jets better than 10 mrad, the ability to discriminate between hadrons and electrons using their different energy depositions and a time resolution of 1 ns. The energy resolution for hadrons and jets with a relative energy resolution obtained from tests was $35\%/\sqrt{E[\,\text{GeV}]} + 1\%$ for hadrons and $17\%/\sqrt{E[\,\text{GeV}]} + 1\%$ for electrons. The calorimeter energy response was calibrated with an accuracy of about 1%. The ZEUS calorimeter was subdivided in three parts: the Barrel Calorimeter (BCAL), the Forward Calorimeter (FCAL) and the Rear Calorimeter (RCAL) covering the range of polar angles shown in Tab. 3.6. The three sections of the calorimeter were divided in modules (see

Parameter	Value		
Weight, ton	700		
Number of modules	80		
Solid angle/4π	99.8%		
Sub-detector	FCAL	BCAL	RCAL
θ-range	2.2°–39.9 °	36.7°–129.1°	128.1°–176.5°
η-range	-4.0-1.0	-1.1-0.74	0.72-3.49
Radiation length X_0	25.9	24.6	24.3
Absorption length,λ	7	5	4

Table 3.6: *Properties of the CAL calorimeter [27].*

Fig. 3.10), which were oriented perpendicular to the beam axis in the BCAL and longitudinal to the beam axis for FCAL and RCAL. Each module was subdivided into towers of dimensions $20 \times 20\,cm^2$. Each tower had a longitudinal structure of one electromagnetic section (EMC) and two (only one in RCAL) hadronic sections (HAC1 and HAC2). Every EMC section consists of four $5 \times 20\,cm^2$ cells (two $10 \times 20\,cm^2$ in RCAL) to give a fine segmentation for electron reconstruction. Each cell of the calorimeter is read out on two sides by wavelength shifters, coupled to photo-multipliers tubes. The energy corresponds to the sum of both photomultiplier tubes and is therefore independent of the impact point of the particle on the cell. However, a comparison of both photo-multipliers tubes allows the position along the cell to be reconstructed.The most important properties of the ZEUS calorimeter are given in Tab. 3.6.

3.7 Detectors for luminosity measurements (PCAL and SPEC)

Precise knowledge of the luminosity is required for precise determination of a cross section associated with any process; such measurements depend on luminosity integrated over time, $\int Ldt$.

The main reaction used in the measurements of luminosity in ZEUS was This process is well understood, has a high rate and an accurately calculable cross section.

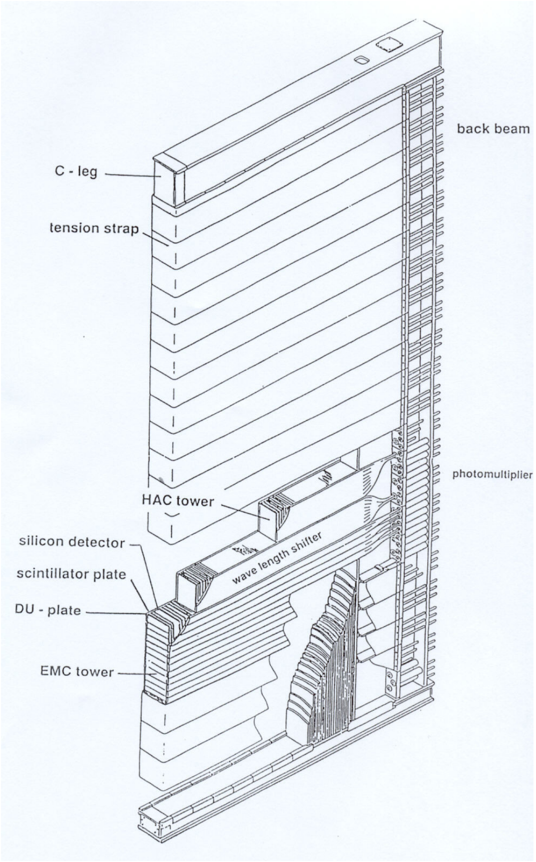

Figure 3.10: *Schematic view of FCAL module [36].*

The produced photons follow the direction of the colliding beam electrons and are observed about 100 m downstream in Photon Calorimeter (PCAL), schematically shown in Fig. 3.11. The PCAL is a lead-scintillator calorimeter preceded by a thick carbon filter [37]. The scattered electrons were registered by 45 m and 35 m taggers, which used technology similar to that of the PCAL (described elsewhere [37]).

Initially the luminosity was measured by counting the number of events with a detected scattered electron and photon. After the measurement of electron and γ energy in the PCAL, there was a well separated class of events with $E_{e'} + E_e = E_{\text{beam}}$, as expected from the bremsstrahlung process. But already in 1992, with improved background conditions it was decided to use only photons for the

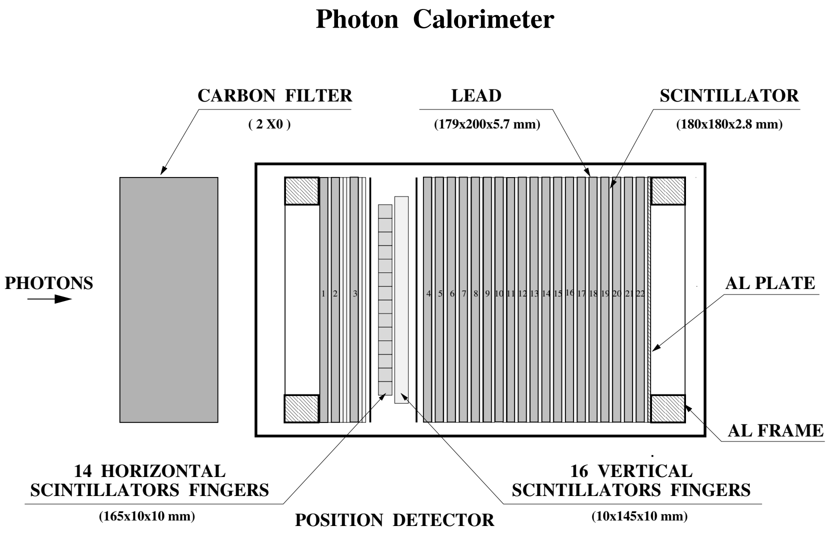

Figure 3.11: *Schematic view of photon detector (PCAL) [37].*

luminosity determination. To estimate the background from beam-gas events $eA \rightarrow eA\gamma$, unpaired bunches of electrons were used. The estimated background (~5%) was subtracted.

The ZEUS HERA-I technique, with a calorimeter to directly measure all bremsstrahlung photons, faced new difficulties at HERA-II. A new detector, the luminosity Spectrometer (SPEC), was therefore installed (see Fig. 3.12). The luminosity spectrometer utilised a method of measuring luminosity at ZEUS which addressed the post-upgrade problems of synchrotron flux, pile-up, and other requirements, while meeting the specifications for luminosity accuracy required by ZEUS physics goals. In the spectrometer system, the bremsstrahlung photons were detected through their well-understood pair conversion, $\gamma \rightarrow e^+e^-$, in the material of the beam-pipe exit window well downstream of the interaction region, where these photons have been spatially separated from the circulating beams. After the converted electron pair has been spatially split by the magnetic field of a dipole magnet, the particles were individually detected by two small electromagnetic calorimeters placed at transverse distances separated from the direct synchrotron radiation and unconverted bremsstrahlung beams. The observed rate of converted photons is proportional to the luminosity.

During the HERA-II period, the two luminosity detectors were operated simultaneously by two independent groups. The results from those detectors agreed

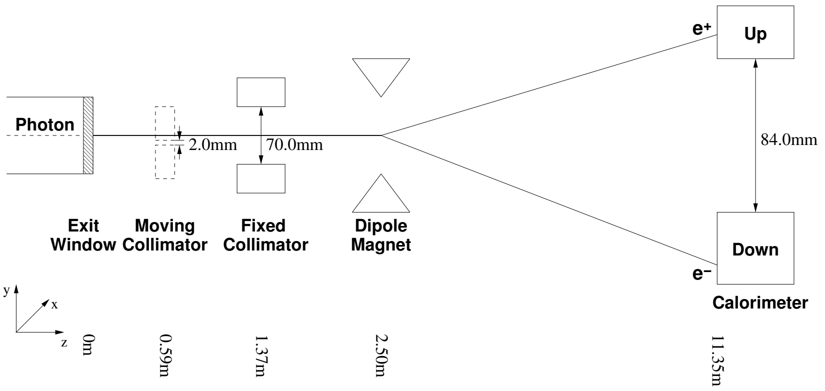

Figure 3.12: *Schematic showing major elements of the luminosity spectrometer (SPEC) [38].*

within 1%. The total accuracy in the luminosity measurement for Hera-II was 1.8%, which is similar to the most accurate luminosity measurement at Hera-I.

3.8 Zeus trigger system

The Zeus trigger chain was designed to select the most interesting events of *ep* collisions from a large background consisting mostly of protons in the accelerated beam scattering from residual gas in the beam-pipe – known as "beam-gas" events.The Zeus trigger chain had three levels. The issuing of a first-level trigger caused component data to be transferred to buffers for processing by the second-level trigger. The second-level trigger processor functioned as an asynchronous pipeline, i.e. a series of parallel processors. The second-level trigger decisions were made in the order of events received. The second-level trigger has access to a large fraction of the full data for the event. For example, in the case of the calorimeter, while the first-level trigger would examine groups of cells with a reduced digitisation accuracy, the second-level trigger performed calculations on the individual cells with the full dynamic range. The second-level trigger was able to perform iterative calculations that were not possible in the pipeline structure of the first-level trigger. The second-level trigger achieved a reduction of the first-level trigger rate from 1 kHz to 100 Hz. The data passing the second-level trigger as then sent to the level-3 computer farm, where trigger decisions were based on the full analysis software algorithms. The third-level trigger runs a (reduced) version of the full offline analysis code and passes an output rate of 3-5 Hz.

3.9 ZEUS detector simulation

The simulation of ZEUS events can be split in two parts: the hadron level, which is simulated inside MC event generators like PYTHIA [39], RAPGAP [40] or ARIADNE [41] and the interaction of the particles with the material of the detector together with detector response. The penetration of the particles through the material of detector is simulated with the GEANT 3.21 [42] package. The set of routines for simulation of each detector component with corresponding tuning is called MOZART[14]. The MOZART package calculates the propagation of particles through the whole detector taking into account particle decays, energy losses, multiple scattering and the effects of the magnetic field. It also simulates the effects of detector resolution and readout electronics. The MOZART executable accepts as an input an event record in ADAMO[15] format, a steering cards with set-up of the detector that depends on period and a GAF[16] file with supplementary information. The output of the MOZART package is used as an input for the ZGANA[17] package, which simulates ZEUS trigger behaviour. As the trigger simulation required a lot of issues specific to each period, many of them were hard-coded in the package routines. For this reason for each trigger period a separate ZGANA executable is used. A major difference between the real trigger and ZGANA is that ZGANA keeps events even if they did not pass the trigger criteria. The output of the ZGANA package has the same format as raw event data from the detector. The further reconstruction of the simulated event is done is the same way as for real events. The package that provides the reconstruction is called ZEPHYR. Its output is stored in ADAMO format in the same way as for real events and might be used in the user analysis. Typically the user analysis is done with EAZE and ORANGE/PHANTOM libraries and includes refined tracking, jet and decay reconstruction. The final set of Ntuples is stored in ROOT [43] or/and PAW [44] format and can be used for physics analysis. The diagram of the simulation process is given in Fig. 3.13.

---

[14] Monte Carlo for Zeus Analysis, Reconstruction and Trigger

[15] ADAMO is an acronym of words Aleph Data Model and stands for a data format developed for the ALEPH experiment and used in ZEUS software.

[16] General Adamo File

[17] Zeus Geant Analysis

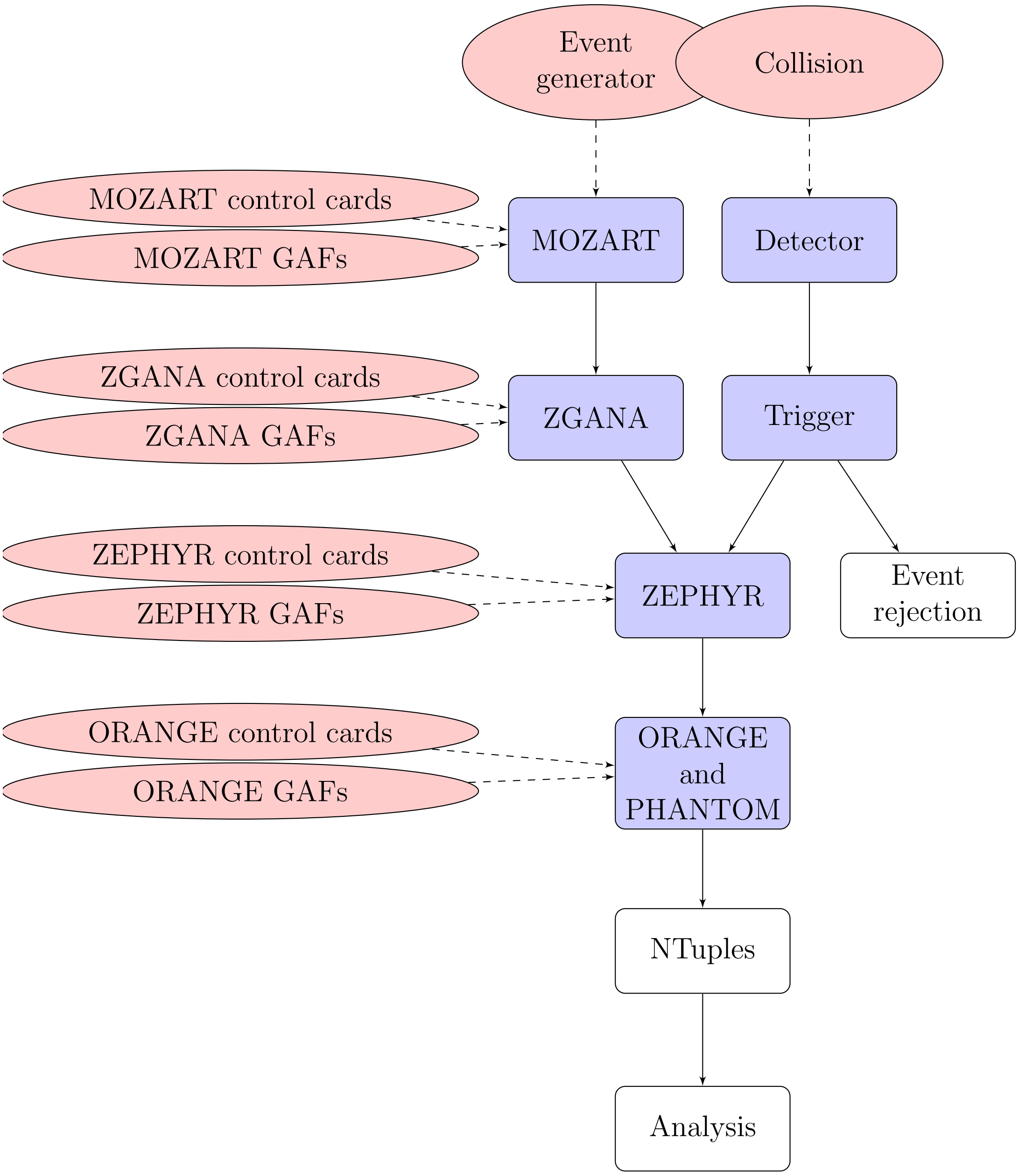

Figure 3.13: *Event reconstruction and simulation in* Zeus.

4 Track and vertex reconstruction

This section introduces and describes several quantities, algorithms and procedures used in the analysis: the general pattern recognition algorithm used for ZEUS tracking (Kalman filter), vertex fitting procedures and their application for the reconstruction of D-meson decays. The description starts from track fitting and pattern recognition procedures. The earlier stages of reconstruction (e.g. hits) are described elsewhere [34, 45, 46]. As the energy losses and multiple scattering strongly influence the track reconstruction procedure, and are used for track identification, a brief description is given below. The section ends with the description of kinematic variable reconstruction in ep scattering.

4.1 Energy losses and multiple scattering

The particles produced in the ep collisions interact with the material of the detector, and for a proper event reconstruction this should be taken into account. The nature of the interaction depends on the flavour of the particle, its charge, energy and the detector material. The main types of interaction are elastic Rutherford scattering on the nuclei of the material, radiation losses, δ electrons production, ionisation losses and nuclear interactions. For the most common charged particles in the ZEUS detector (e, μ, π, K, p) and an energy range between 0.1 GeV and 50 GeV, the dominant process of energy losses is ionisation [1].

The ionisation losses are basically caused by particles scattering on electrons in the material. The electrons in material are not free, so there exists a minimal energy which charged particles can transfer to an electron. This energy is called ionisation potential I and has typical values between 13.6 eV for hydrogen and 810 eV for uranium. The maximal transferred energy is given by energy and momenta conservation rules $E_{max} = 2mv^2$, where m is the mass of the electron and v is the speed of the charged particle. Taking into account those limits, Bethe obtained a formula for the ionisation losses of a charged particle with sufficiently high velocity[18]:

$$-dE/dx = (4\pi e^4 z^2/(mv^2))nZ(ln(2mv^2/I) - \beta^2 - ln(1-\beta^2)) \tag{4.1}$$

---

[18] For low velocity the ionisation potential depends on the velocity.

where $b = v/c$, and nZ is a concentration of electrons in the material. The energy losses of the charged particle given by Eq. (4.1) depend only on the velocity of the particle, so, it is possible to distinguish particles using the information about their momenta p and energy losses dE/dx. In the ZEUS experiment, the energy losses were measured in relative units: MIPs[19]. For each small sub-period of data taking, to define this unit, a set of tracks with minimal dE/dx signal was selected and the average was taken as the unit. The signals of other tracks, normalised to this unit were used in the particle identification procedure. The procedure used in this analysis is similar to one used in Ref. [47]. The main idea is to use well identified protons and pions from the $\Lambda^0 \to p\pi$ and $K^0_S \to \pi^+\pi^-$ decays to measure dE/dx vs. v in the detector. The selection of those decays was tuned to obtain purity close to 100% while keeping the cuts on the decay track momenta as low as possible. Fig. 4.1(a) shows the dE/dx vs. p distribution for those tracks. For both protons and pions from $\Lambda^0 \to p\pi$ decays, an average value of $\ln(dE/dx)$ in the CTD[20] was calculated for every p/m bin (see Fig. 4.1(b)). The obtained distribution was fitted with a function that is close to Bethe-Bloch function (see Eq. (4.1)):

$$\ln(dE/dx)(p,m) = a_0 + a_1/(p/m+a_7) + a_2/(p/m+a_7)^2 + a_3\ln(p/m)/(p/m+a_7) + \tag{4.2}$$
$$\begin{cases} p_4\ln(p/m)/(p/m+a_7)^2 & \text{for } p/m \leq 1, \\ p_6\ln(p/m)^2/(p/m+a_7)^2 & \text{for } p/m \geq 1. \end{cases}$$

The fit yielded $a_0 = 0.25774$, $a_1 = -8.7390$, $a_2 = 26.980$, $a_3 = 4.0824$, $a_4 = -9.6358$, $a_5 = 0.76675$, $a_6 = 5.0188$ and $a_7 = 1.9687$. The resolution of the dE/dx measurements was estimated in the following way:

- The resolution was assumed to be proportional to the inverse square root of the number of the hits n and independent of the track momentum: $\sigma(\ln(dE/dx)) = a/\sqrt{n}$.

- The value of a was estimated from a fit of the $\frac{(\ln(dE/dx)_{\text{measured}} - \ln(dE/dx)_{\text{expected}})^2}{\sigma(\ln(dE/dx))}$ distribution to a Gaussian function (see Fig. 4.1(c)). It was found to be that $\sigma = a = 0.5092$.

---

[19] Minimal Ionisation Potential.

[20] As the CTD detector is the key element of tracking system, the CTD dE/dx information considered as more important than the dE/dx information from the MVD and STT detectors.

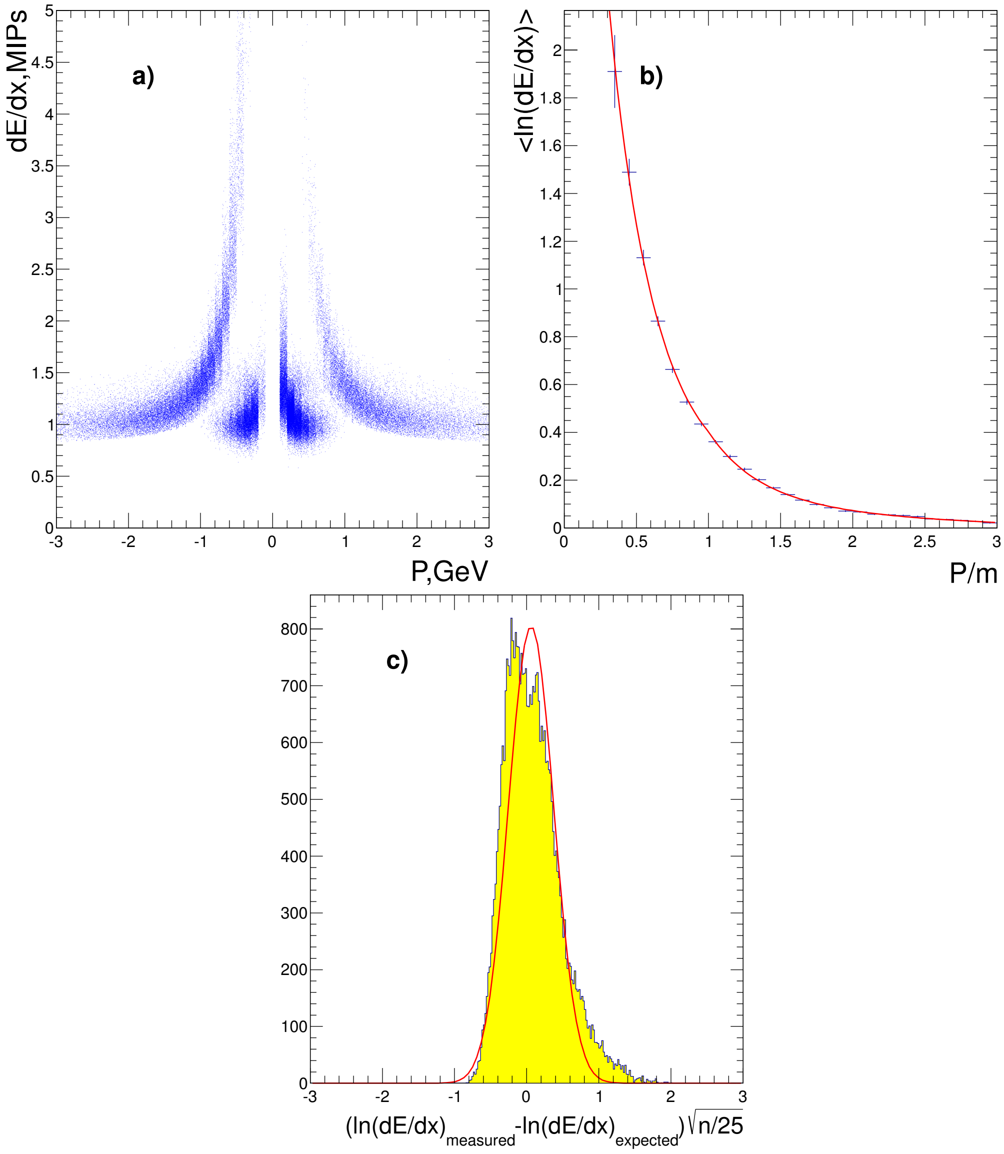

Figure 4.1: *Studies of the* dE/dx *with reconstructed* $\Lambda^0 \to p\pi$ *decays. a) The* dE/dx *vs. momentum* p *scattered plot for proton and pion tracks. b) The distribution of average* $\ln(dE/dx)$ *as function of* p/m *for proton and pion tracks (black dots) and the fit to an empirical function (red line). c) The distribution of* $(\ln(dE/dx)_{\text{measured}} - \ln(dE/dx)_{\text{expected}})^2\sqrt{n/25}$ *for proton and pion tracks (yellow) and the fit to a Gaussian function (red line).*

The χ^2 estimation of a certain mass hypothesis in this approach is:

$$\chi^2(m) = \frac{(\ln(dE/dx) - \ln(dE/dx)_{\text{expected}})^2 n}{a^2},$$

where the $(dE/dx)_{\text{expected}}$ is calculated from Eq. (4.2).

During the penetration process the particles will not only lose energy but also they will scatter in the presence of material in the detector. It can be assumed that the positional component of multiple scattering is small and only the angular component of multiple scattering is taken into account (see Ref. [48] for details). The effect of multiple scattering is a change of the trajectory described by an angle θ with respect to the initial track direction. The distribution of this angle (projected on a plane parallel to the track to the track direction) is approximately Gaussian [1] with mean zero and a width of:

$$\sigma(\theta) = \theta_0 = \frac{0.0136z}{\beta p[\,\text{GeV}]}\sqrt{(x/X_0(1 + 0.038\ln(x/X_0))}, \tag{4.3}$$

with p, β, z the momentum, velocity and the charge, respectively, of the incident particle, and x/X_0 the path in the scattering medium in units of radiation length X_0. From Eq. (4.3) it is seen that for low momentum tracks the effect of multiple scattering becomes bigger. To take into account the multiple scattering in the track reconstruction, the following approach is used:

- For the each volume passed by the particle, the traversed thickness is calculated from a material database and the incoming angle of the track.
- Eq. (4.3) gives the 1σ scattering angle $\sigma(\theta)$ that is taken as the uncertainty of the track direction due to the multiple scattering.
- A scattering matrix is calculated by transforming the uncertainty in two angles to the uncertainty of the track parameters.
- Finally the scattering matrix is added to the track covariance and used in the track fit procedure described below.

4.2 Track fitting with the Kalman filter

The path of the particle in the detector depends on many factors: magnetic field, scattering in the material, energy losses etc. It makes the estimation of the particle trajectory (track) a complicated task. To solve that task the Kalman filter algorithm has been developed.

The Kalman filter algorithm is an iterative procedure for the reconstruction of tracks from measured hits. The algorithm iteratively reconstructs the track from the outermost point of the tracking system to the origin. The reconstruction takes into account the energy losses and multiple scattering as described above.

Let us consider a track trajectory in different regions of the detector system and label them starting from the outermost one. For the time being we avoid the procedure of starting the fit (search of track seeds) and assume that the track parameters in the region 1, α_1, and the corresponding covariance matrix, $\mathbf{V'}_{\alpha\,1}$, are already known. The next iteration of the reconstruction procedure should consider the hits in region 2. The track parameters in region 2 will be obtained using the extrapolated track parameters from region 1, estimated energy losses in the material ($\alpha_1 \rightarrow \alpha'_1$), measurements in the region 2 (see Fig. 4.3(b)) and taking into account magnetic field. This also applies to the covariance matrix of track parameters, which should be corrected to take multiple scattering ($\mathbf{V}_{\alpha\,1} \rightarrow \mathbf{V'}_{\alpha\,1}$) into account. The formulae for corresponding equations could be found elsewhere [48]. In the end, the χ^2 for region 2 consist of two terms: the first one is related to measurements in region 2 and the second is calculated from the track parameter and covariance matrix in the previous regions (region 1). The procedure iterates through all regions of the detector system to the origin of the track or till it fails to find a reasonable continuation. The basic strategy is to update the track parameters on the each step. In the Kalman filter algorithm it is possible to add several measurements to the track simultaneously. However, the case when only one hit is added at a time is the most profitable, as the number of calculations will be smallest. A full review of Kalman filter advantages/properties can be found elsewhere [48]. Here is a brief list of the most important ones:

- The Kalman filter method uses *all* the information and cannot, if used correctly, give poorer track parameters by adding more measurements. Including more hits can only improve the quality of result.
- As the Kalman filter starts the fit from the outermost point, and ends it at the innermost, the precision of track parameters will be highest at the innermost part (in the end of the fit procedure). That is why a global refitting starting from the innermost point of the track is done in the end. The resulting track might have the end point of “swim” that differs from the track seed in the outermost part of detector.

- It is not necessary to have hits in every region of the detector through which the track passed. The track can be extrapolated through a region without hits to the next one that contains hits.

- The track might be fitted in pieces in different parts of detector and then added together.

- As the fit procedure uses estimation of energy losses and multiple scattering, the result of the fit, especially for low momentum tracks, is sensitive to the mass hypothesis of the particle. The best option would be to store fit results for all needed mass hypothesis (e, μ, π, K or p), but that is expensive from point of view of storing the data. Also, the comparison of fit quality for the different hypothesis can help with particle identification.

- The Kalman filter is a widespread and well studied technique that has been implemented in various experiments.

One of the biggest problems in the Kalman filter algorithm is the starting procedure. The fit should start from the outermost part of the detector, but only a few hits are available in that region. More seriously, track parameters are oversensitive to the quality of those hits leading to the possibility that there are no enough good measurements to start the fit properly.

The recipe to start the fit procedure, which is a nontrivial task is described in Ref. [48].

The Kalman filter algorithm is implemented in ZEUS software in packages RTFIT and KTFIT. Those packages refit the trajectory in the CTD, MVD and STT detectors. The obtained relative resolution of transverse momentum, p_T for the full length tracks (i.e. passed through the MVD and 9 CTD superlayers) is [49]

$$\sigma(p_T[\,\mathrm{GeV}])/p_T[\,\mathrm{GeV}] = 0.0029 p_T[\,\mathrm{GeV}] \oplus 0.0081 \oplus 0.0012/p_T[\,\mathrm{GeV}].$$

For the tracks with not less than 2 hits in MVD z and $r\phi$ sensors the corresponding average resolution of **the impact parameter (IP)** [21] is [49]

$$\sigma(IP)[\,\mu\mathrm{m}] = 46 \oplus 122/p_T[\,\mathrm{GeV}].$$

---

[21] The X-Y distance between the track and some point, as usual a primary vertex or the beamspot (see explanation on these quantities below).

The momentum bias/underestimation due to the limited precision of the magnetic field measurements is taken into account in the RTFIT package and estimated to be at level of 0.3%. Although the ZEUS software supports tracking for different types of particles, in the default tracking all the tracks have the pion mass hypothesis, which leads to a small momentum underestimation for low-energy kaons and protons.

4.3 Track parametrisation in ZEUS

The ZEUS coordinate system (see Fig. 4.2) is a right-handed Cartesian system, with the Z axis pointing in the proton beam direction, referred to as the "forward direction", and the X axis pointing left towards the centre of HERA. The coordinate origin is at the nominal interaction point.

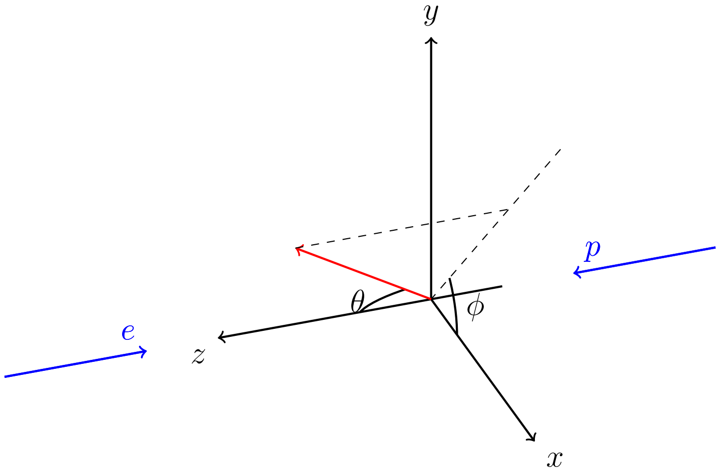

Figure 4.2: *The* ZEUS *coordinate system.*

Inside the coil the magnetic field is approximately parallel to the Z axis. At any point of a track's trajectory, its path is approximately an axial helix. Several different track parametrisation are used in HEP experiments. The parametrisation used in ZEUS is a **perigee parametrisation**. Each trajectory is specified by the 5 helix parameters α_{μ}, a 5×5 covariance matrix V, and an arbitrarily chosen reference point in the X-Y plane. The reference point is chosen to be (X_{ref};

$Y_{\mathrm{ref}}) = (0; 0)$. Fig. 4.3 shows a helix in the X-Y view for a positively charged track. The helix parameters are:

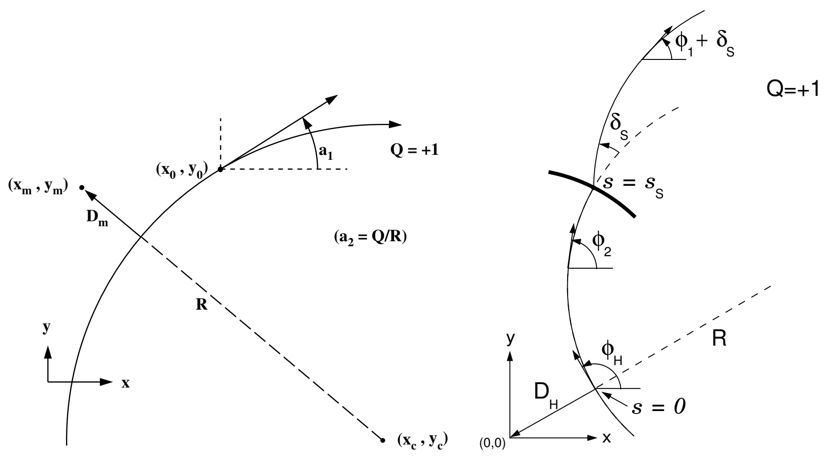

(a) Track parametrisation. (b) Track fitting iteration.

Figure 4.3: *Track parametrisation and fitting in* Zeus *[46].*

- $\alpha_1 = \phi_H$ (angle tangent to the helix in the X-Y plane);
- $\alpha_2 = Q/R$ (Q is the charge, and R the local radius);
- $\alpha_3 = QD_H$ (D_H is the **impact parameter**[22], connects the helix to the reference point in X-Y plane);
- $\alpha_4 = Z_H$;
- $\alpha_5 = \cot\theta$ (θ is the angle of dip with respect to the X-Y plane).

The coordinate of the closest approach to the reference point, is:

$$X_H = X_{\mathrm{ref}} + QD_H \sin\phi_H$$

$$Y_H = Y_{\mathrm{ref}} - QD_H \cos\phi_H$$

$$Z_H = Z_{\mathrm{ref}}$$

---

[22] with respect to reference point

Any point on the helix can be expressed as a function of the trajectory's outbound path length in the X-Y plane,

$$s(\phi) = QR(\phi - \phi_H)$$

where ϕ is the outbound tangent angle in the X-Y plane. In the immediate vicinity of $s = 0$, the coordinate and momentum components are:

$$X = X_H + QR(-\sin\phi_H + \sin\phi)$$

$$Y = Y_H + QR(\cos\phi_H - \cos\phi)$$
$$Z = Z_H + s(\phi)\cot(\theta)$$

The RTFIT and KTFIT packages as well as other ZEUS reconstruction software use this parametrisation for track fitting and reconstruction. One of the most important applications of this parametrisation is a fitting multiple tracks to a single point. The point is called **vertex**, the corresponding procedure is called **vertexing** and is briefly described below.

4.4 The reconstruction of vertices

With the installation of the MVD in the ZEUS detector the space resolution of the tracking system improved dramatically. It became possible to use much more sophisticated reconstruction of the charm hadron decays, estimate the track impact parameters, the distances between tracks and reconstruct the vertices. This section describes algorithms of charm decay reconstruction and introduces corresponding quantities.

The evaluation of vertices serves two purposes. The first is to evaluate the position of the decay or of the **primary vertex**, which is an estimated position of the primary *ep* interaction point, and calculate the appropriate track momenta at that point with improved precision due to the vertex constraint. The second purpose of using vertices is to estimate the probability whether the tracks originate from a certain vertex. This probability might be estimated from the vertex evaluation quality (e.g. the χ^2 of the vertex fit) and used for the decision on the decay chain selection. The essential information that is used in the fit consists of track parameters and their covariance matrices.

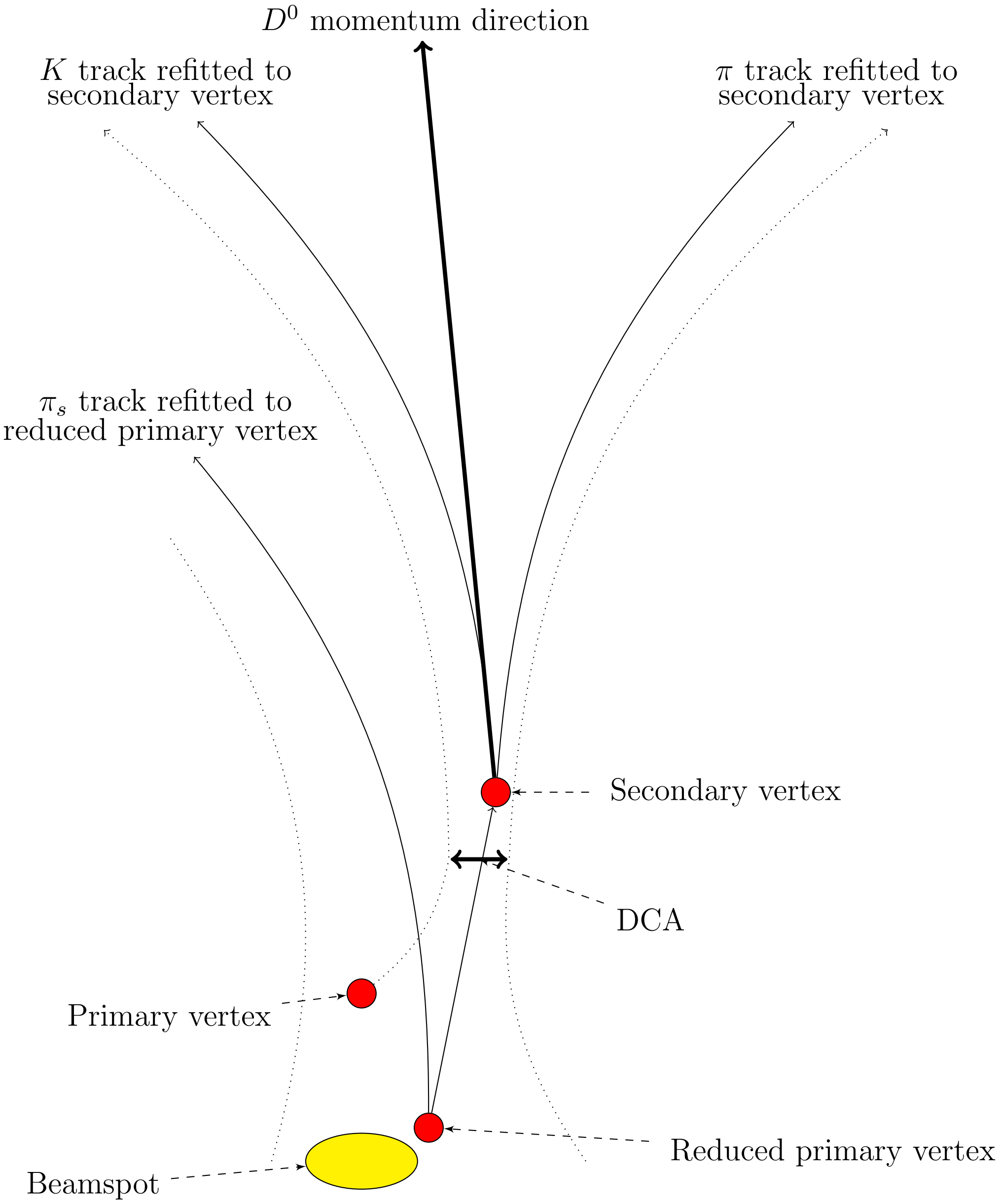

Figure 4.4: *The tracks before the revertexing procedure (dots) and refitted tracks (solid). The K candidate track from the primary vertex was combined together with the non-vertex π candidate track after the* **distance of closest approach** (DCA) *between tracks was found to be small. The K and π candidate tracks were fitted to a common* **secondary vertex**. *The non-vertex π_s candidate track was fitted with all primary tracks but K in the* **reduced primary vertex**, *using* **beamspot** *constraint.*

For the reconstruction of the relatively long-lived resonances, a set of tracks which fulfils some predefined criteria is selected (e.g. the p_T or η requirements) and the closest distance between the helices of two tracks, **distance of closest approach, DCA** (see Fig. 4.4) is evaluated. If the distance is small enough, the tracks can be combined into a single **secondary vertex**, which is a candidate for a resonance decay (e.g. K^0, D^0 or D^+). For each pair of tracks that fulfils the criteria, the midpoint of the tracks[23] at closest approach is evaluated (see Fig. 4.4) and taken as a starting point of the vertex fit. Then, the iterative fitting procedure starts. The vertexing algorithm in ZEUS relies on the global vertex fit [50]; the C++ implementation of this algorithm for ZEUS is called TLITE [51]. The procedure uses an approximation of the track helix with a straight line (with expansion of the helix parameters and covariance matrices around the reference point) and iteratively evaluates the most probable vertex position with a linear least-squares fit. The procedure terminates when the difference between the χ^2 in two sequential iterations is less that 10^{-4}. The new helix parameters, track momenta, the vertex position, the covariance matrix and the χ^2 of the fit are delivered as a final result. To improve the separation of the secondary and primary vertices, the following approach is used. From the set of tracks originally used for the primary vertex fit, the tracks used for the secondary vertex reconstruction are removed and the tracks supposed to be in the primary vertex (e.g. π_s from $D^{*+} \to D^0\pi_s$ decay) are added. The obtained set of tracks is refitted to form the so-called **reduced primary vertex**. With these results of vertexing the analysis of decays can be refined using selection on the following quantities:

- 3-D **decay length** – the distance between the secondary vertex and the (reduced) primary vertex

  $$L_{3\text{-}D} = |\vec{r}_{\text{sec}} - \vec{r}_{\text{prim}}|,$$

  where the $\vec{r}_{\text{sec}}$ and $\vec{r}_{\text{prim}}$ are the coordinates of secondary and primary vertices.

- 2-D **decay length** – the distance between the secondary vertex and the (reduced) primary vertex

  $$L_{2\text{-}D} = |\vec{r}_{\text{sec 2-D}} - \vec{r}_{\text{prim 2-D}}|,$$

---

[23] In case the number of tracks is more than two, an average position of all calculated midpoints is taken.

where the notation 2-D means the X-Y component of the vector.

- 3-D **collinearity angle**, $\alpha_{3\text{-}D}$ – an angle between the line connecting the (reduced) primary vertex and the secondary vertex and the reconstructed decay momentum

  $$\cos(\alpha_{\text{3-D}}) = \frac{(\vec{r}_{\text{sec}} - \vec{r}_{\text{prim}}) \cdot \vec{p}}{\sqrt{(\vec{r}_{\text{sec}} - \vec{r}_{\text{prim}}) \cdot (\vec{r}_{\text{sec}} - \vec{r}_{\text{prim}}) \vec{p} \cdot \vec{p}}},$$

  where $\vec{p}$ is the momentum of decay particle.

- 2-D **collinearity angle**, $\alpha_{2\text{-}D}$ – the same as previous, but in X-Y plane

  $$\cos(\alpha_{\text{2-D}}) = \frac{(\vec{r}_{\text{sec 2-D}} - \vec{r}_{\text{prim 2-D}}) \cdot \vec{p}}{\sqrt{(\vec{r}_{\text{sec 2-D}} - \vec{r}_{\text{prim 2-D}}) \cdot (\vec{r}_{\text{sec 2-D}} - \vec{r}_{\text{prim 2-D}}) \vec{p}_{\text{2-D}} \cdot \vec{p}_{\text{2-D}}}}.$$

- 2-D **projected decay length significance** (or just **significance**) the distance between the secondary and reduced primary vertices, projected onto the momentum of the decay particle and divided by the precision of its measurement in X-Y plane.

  $$S_{\text{2-D proj}} = \frac{(\vec{r}_{\text{sec 2-D}} - \vec{r}_{\text{prim 2-D}}) \cdot \vec{p}_{\text{2-D}}}{\sqrt{\vec{p}_{2\text{-}D} (\hat{\sigma}_{\text{sec 2-D}} + \hat{\sigma}_{\text{prim 2-D}}) \vec{p}^{\,T}_{\text{2-D}}}}, \tag{4.4}$$

  where $\hat{\sigma}_{\text{prim 2-D}} = \begin{pmatrix} \sigma_{\text{prim xx}} & \sigma_{\text{prim yx}} \\ \sigma_{\text{prim xy}} & \sigma_{\text{prim yy}} \end{pmatrix}$ and $\hat{\sigma}_{\text{sec 2-D}} = \begin{pmatrix} \sigma_{\text{sec xx}} & \sigma_{\text{sec yx}} \\ \sigma_{\text{sec xy}} & \sigma_{\text{sec yy}} \end{pmatrix}$ are the "2-D" parts of primary vertex and secondary vertex covariance matrices $\hat{\sigma}_{\text{prim}}$ and $\hat{\sigma}_{\text{sec}}$.

For a good reconstruction of relatively long-lived particles and corresponding vertices it is expected $S_{\text{2-D proj}} > 0$ (see Fig. 4.5(a,b)), $\alpha_{2\text{-}D} \sim 0$ (see Fig. 4.5(c,d)). Cuts on these quantities (e.g. $S_{\text{2-D proj}}(D^+) > 3$ or $\alpha_{2\text{-}D}(K^0_S) < 0.1$) were used to suppress the background. A more sophisticated vertex fitting procedure can constrain the mass, momentum, vertex position, drop or weight individual tracks in the fit. The latter option is used for the reconstruction of the (reduced)primary vertex position with a Deterministic Annealing Filter (**DAF**). The DAF fit algorithm is basically identical to the fitting routine described above, but uses

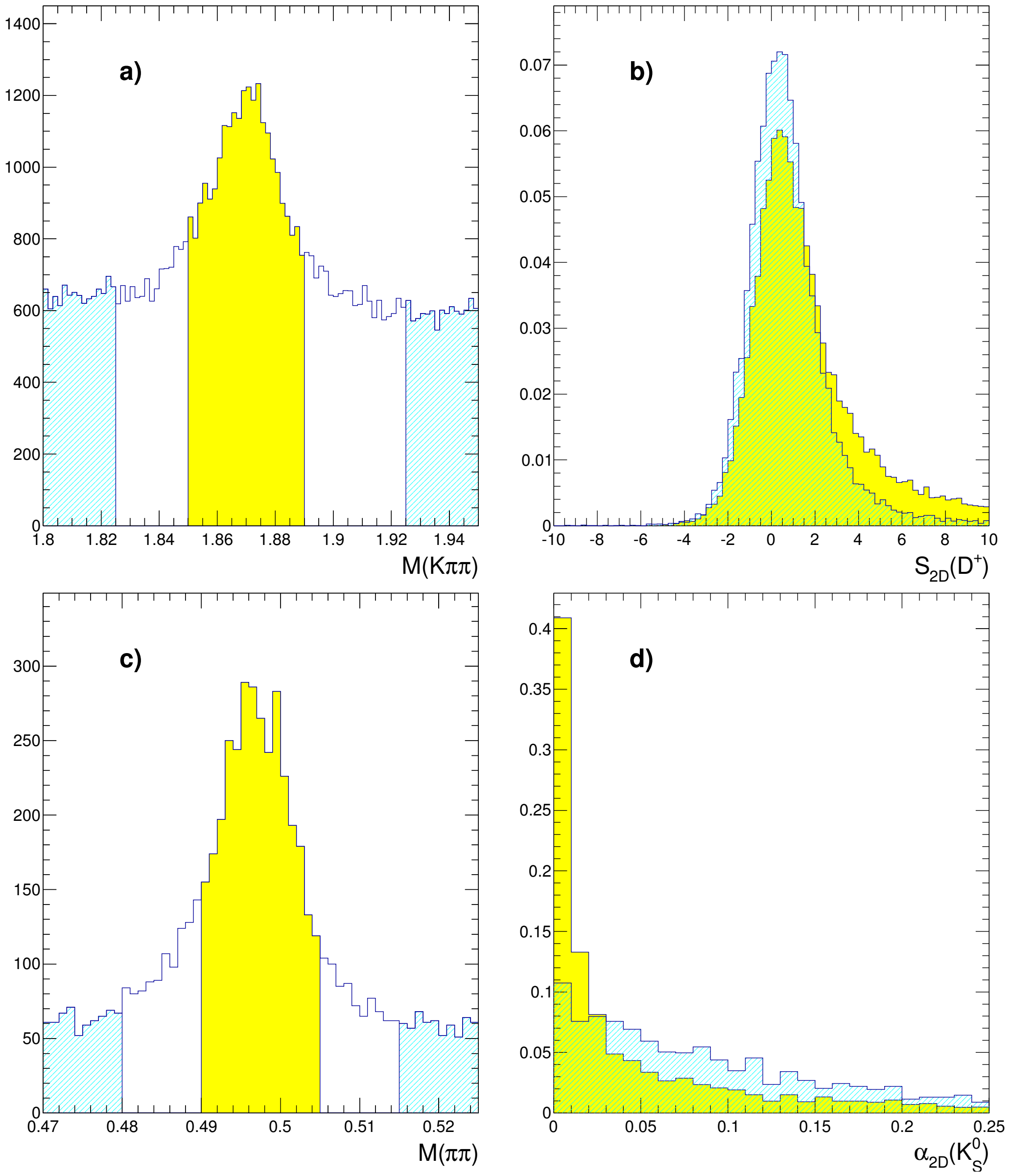

Figure 4.5: *a)* $M(K\pi\pi)$ *spectrum with* D^+ *signal region (yellow) and non-signal region (shaded cyan) b) normalised distributions of* 2-*D decay-length-significance for* D^+ *signal region (yellow) and non-signal region (shaded cyan) c)* $M(\pi\pi)$ *spectrum with* K_S^0 *signal region (yellow) and non-signal region (shaded cyan) d) normalised distributions of* $\alpha_{2\text{-}D}$ *for* K_S^0 *signal region (yellow) and non-signal region (shaded cyan).*

weights for tracks at each iteration:

$$w = \frac{1}{1 + e^{\frac{\chi^2(\mathrm{helix}) - \chi^2_{\mathrm{min}}(\mathrm{helix})}{2T}}},$$

where the χ^2(helix) is a contribution of a particular track to the χ of the vertex fit at the current iteration and χ^2_{min}(helix) is a parameter of the procedure. The default value of χ^2_{min} was set to 20. The parameter T is called "temperature". The fit starts with a "temperature" equal to 100 and then three iterations are performed for $T = 25$, $T = 9$ and $T = 4$. The fit ends when the sum over all track weights is less than one or when the difference between the χ^2 in two sequential iterations is less that 10^{-4}. The DAF algorithm has the following advantages in the primary vertex reconstruction:

- the tracks with the best quality get the largest weight in the fit;
- the tracks that are far from the vertex get the smallest weight in the fit.

Another option to refine the primary-vertex reconstruction is to take into account the **beam spot** position and covariance matrix. The beamspot is a region where most primary interactions occurs. For each short period of data, typically 2000-10000 events, the average position of the interaction point is evaluated together with its errors. This quantity is called the beam-spot position. As the interaction region is not perfectly aligned with the Z axis, tilts in X and Y dimensions, dX/dZ_{bspt} and dY/dZ_{bspt} exist. The most probable primary interaction position $(X_{\mathrm{prob}}, Y_{\mathrm{prob}}, Z_{\mathrm{prob}})$ for of an event is

$$X_{\mathrm{prob}} = X_{\mathrm{bspt}} + dX/dZ_{\mathrm{bspt}}(Z_{\mathrm{bspt\ offset}} - Z_{\mathrm{prim}}),$$

$$Y_{\mathrm{prob}} = Y_{\mathrm{bspt}} + dY/dZ_{\mathrm{bspt}}(Z_{\mathrm{bspt\ offset}} - Z_{\mathrm{prim}}),$$

$$Z_{\mathrm{prob}} = Z_{\mathrm{prim}},$$

where $(X_{\mathrm{prim}}, Y_{\mathrm{prim}}, Z_{\mathrm{prim}})$ is the primary vertex position and $Z_{\mathrm{bspt\ offset}}$ is a parameter called beam-spot offset. The average dispersion of the beam spot position is called **beam-spot width** and was calculated in X and Y directions for each run period separately. The values of the beam-spot width in X-Y, $W_x \times W_y$ are $24\,\mu\mathrm{m} \times 88\,\mu\mathrm{m}$ for positron data and $22\,\mu\mathrm{m} \times 80\,\mu\mathrm{m}$ for electron data [52]. The width in the Z dimension was estimated to be 10 cm. To use this information in the vertex fit, an extra term, related to the beamspot, is added to the χ^2 function minimised in the vertex fit:

$$\chi^2_{bspt} = \vec{r}\hat{\sigma}_{\text{bspt}}\vec{r}^T; \vec{r} = (X_{\text{prob}} - X_{\text{vtx}}, Y_{\text{prob}} - Y_{\text{vtx}}, Z_{\text{prob}} - Z_{\text{vtx}}),$$

where $(X_{\text{vtx}}, Y_{\text{vtx}}, Z_{\text{vtx}})$ is the fitted vertex position and $\hat{\sigma}_{bspt}$ is the beam spot covariance matrix. In the same time the beamspot position can be used in Eq. (4.4) to calculate the 2-D decay-length significance. This option has been used in this analysis with an assumption $\hat{\sigma}_{\text{prim 2-D}} = \begin{pmatrix} W_x^2 & 0 \\ 0 & W_y^2 \end{pmatrix}$. The combination of the DAF technique with a beam-spot constraint has been used as the default in this analysis and brought a significant improvement in the determination of (reduced) primary vertices.

4.5 Track matching

To study the track reconstruction performance (e.g. momentum resolution), it is important to match the particles produced by MC generator to the reconstructed tracks. The matching procedure for the ZEUS tracking was implemented in the VMCU package. The package allows the study of pattern-recognition performance with MC simulated events. The algorithm is based on the matching of hits simulated in MOZART to hits reconstructed by ZEPHYR in CTD, MVD and STT detectors. In this analysis the matching was used to estimate the mass resolution in the reconstructed charm-meson mass spectra. Unfortunately, the efficiency of VMCU matching procedure, $p \approx 0.8$ [53], significantly lower than unity and depends on many factors: the length of the track, the p_T and η etc. An attempt to match all tracks of reconstructed candidate (e.g. $D^+ \to K_{\text{reconstructed}}\pi_{\text{reconstructed}}\pi_{\text{reconstructed}}$) to the tracks of generated decay (**direct matching**) (e.g. $D^+ \to K_{\text{generated}}\pi_{\text{generated}}\pi_{\text{generated}}$) fails with a large probability; the candidates with poorly reconstructed daughter tracks will be dropped. It means the resolution estimated with direct matching might be underestimated.

To avoid the underestimation, a **weak matching** procedure was developed in this analysis. According to this procedure, only the tracks matched with VMCU to background (i.e. do not belong to the $D^+ \to K_{\text{generated}}\pi_{\text{generated}}\pi_{\text{generated}}$ decay chain) are dropped. With this procedure the fraction of remaining background candidates with all VMCU matched tracks ($k = 3$ in case of D^+) is

$$f \approx (1-p)^k \approx 0.008,$$

while the remaining number of signal candidates will stay the same [24]. So, in comparison to the direct matching, weak matching has two big advantages:

- it avoids bias of VMCU matching towards high quality tracks/candidates;
- it does not drop signal candidates.

For events that contain a generator level charm-meson decay the typical signal-to-background ratio is $1-10$; the weak matched mass spectrum will contain $\sim$1% of background candidates and can be used for a proper estimation of resolution and other studies.

4.6 Kinematic variable reconstruction

As mentioned in Sec. 2.5, the general *ep* scattering process can be described with kinematic variables Q^2, x and y. For each event the following variables can be reconstructed from the measured quantities: energy (E'_e), the azimuthal angle (θ_e) of the scattered electron, the total hadronic transverse momentum ($P_{\mathrm{T,had}}$) and the hadronic angle (γ_{had}). The last two quantities are defined as:

$$P_{\mathrm{T,had}} = \sqrt{\sum_i (P^i_{x,\mathrm{had}})^2 + \sum_i (P^i_{y,\mathrm{had}})^2},$$

$$\gamma_{\mathrm{had}} = \frac{\sum_i E^i_{\mathrm{had}} \cos\theta^i}{\sum_i E^i_{\mathrm{had}}},$$

where the sum goes over all hadronic components but the scattered electron. In the ZEUS experiment, different reconstruction methods were used to calculate kinematic variables. In the present analysis, the kinematic variables were used only in the studies of relative tracking efficiency in Sec. 13.1. For this reason the detailed overview of these methods, including their advantages and disadvantages is given elsewhere [54, 55] and only a brief outlook is given below.

The reconstruction with the **electron method** relies only on the electron energy and the scattered angle:

$$Q^2_{el} = 2E_e E'_e(1+\cos\theta_e),$$

---

[24] Note, that in case of direct matching, the fraction of remaining true candidates would be $f \approx p^k \approx 0.5$.

$$y_{el} = 1 - \frac{E'_e}{2E_e}(1 - \cos\theta_e),$$

$$x_{el} = \frac{Q^2_{el}}{sy_{el}}.$$

The **Jaquet-Blondel method** [55] relies on the parameters of the hadronic final state:

$$Q^2_{JB} = \frac{P_{\mathrm{T,had}}}{1 - y_{JB}},$$

$$y_{JB} = \frac{\sum_i (E^i_{\mathrm{had}} - P^i_{z,\mathrm{had}})}{2E_e},$$

$$x_{JB} = \frac{Q^2_{JB}}{sy_{JB}}.$$

4.7 Outlook

The tracking and vertexing algorithms briefly described in this section provide a set of tools that can be used to improve the quality of every tracking-based analysis. The author implemented some of the described methods (e.g. vertexing of charm meson decays) in the official ZEUS software and used in this analysis.

5 Data analysis

The measurements of heavy hadron properties provides unique data for the understanding of low-energy QCD and properties of heavy quarks. The HERA experiments produced a large amount of charm quarks, thus it is possible to analyse excited charm meson states. This section describes the reconstruction and candidates selection of excited charm and excited charm-strange mesons in ZEUS.

5.1 Event simulation

This subsection describes the event simulation for the analysis and the corresponding tuning of the event generators. In this study Monte Carlo (MC) simulations are used for the determination of signal acceptances and resolutions.

The MC samples of charm and beauty events were produced with the PYTHIA 6.221 [39] and RAPGAP 3.000 [40] event generators. The general set-up is very similar to the one used in previous studies [56], the code for the generation set-up was modified by the author to be compatible with PYTHIA 6.221.

The PYTHIA and RAPGAP generators were tuned to describe the PHP and the DIS regimes, respectively. Consequently, the PYTHIA events, generated with $Q^2 < 1.5\,\mathrm{GeV}^2$, were combined with the RAPGAP events, generated with $Q^2 > 1.5\,\mathrm{GeV}^2$, where Q^2 is the exchanged-photon virtuality.

The generation included direct photon processes, in which the photon couples directly to a parton in the proton, and resolved photon processes, where the photon acts as a source of partons, one of which participates in the hard scattering process. The included processes in the PYTHIA and RAPGAP generators (the numbers are given according to the PYTHIA manual [39]):

- 81, 82, 84 – boson-gluon fusion for charm, see Fig. 2.3(a);
- 11, 28 – charm excitation in photon, see Fig. 2.3(d);
- 11, 28, 33 – charm excitation in proton, see Figs. 2.3(e,f);
- 81, 82, 84 – boson-gluon fusion for beauty, similar as for charm;
- 11, 28 – beauty excitation in photon, similar as for charm;
- 11, 28, 33 – beauty excitation in proton, similar as for charm.

The CTEQ5L [57] and GRV LO [58] parametrisations were used for the proton and photon parton density functions, respectively. The charm and beauty quark masses were set to 1.5 GeV and 4.75 GeV, respectively. Monte Carlo events were generated proportionally to the luminosity of each data-taking period (see Tab. 3.2).

An important part of the generation process is the hadronisation tuning. The Lund string model was used for hadronisation in Pythia and Rapgap. The longitudinal fragmentation is specified by the fragmentation function $f(z)$, where z is the fragmentation variable[25]. The Bowler modification [59] of the Lund symmetric fragmentation function [60] was used for the charm and beauty quark fragmentation.

$$f(z) = 1/z^{r_Q b m_Q^2}(1/z)(1-z)^a e^{-b m_T^2/z}$$

Here $m_Q, Q = c, b$ is the quark mass and a, b, r_Q are fragmentation function parameters with the default values $a = 0.3$, $b = 0.8$, $r_c = 1.0$.

To produce realistic hadronisation fractions, the following Pythia's parameters are set to non-default values [39], [61], [5].

- The spin 1 meson production rates were set to
  - $PARJ(13) = 0.6$ for charm;
  - $PARJ(13) = 0.75$ for beauty.
- The specific production rates were set to
  - $PARJ(14) = 0.13$ for D_1 (narrow states);
  - $PARJ(15) = 0.01$ for D_0^* (wide states);
  - $PARJ(16) = 0.03$ for D_1^* (wide states);
  - $PARJ(17) = 0.13$ for D_2^* (narrow states).

The strangeness suppression factor was set to 0.3. The masses and widths of most charm mesons were set to the PDG [1] values. The masses and widths of D_1 and D_2^* mesons were set to the values published by BaBar [62].

The generated events were passed through a full simulation of the detector using Geant 3.13 [42] and processed with the same reconstruction program as used

---

[25] The quantity defined for a jet as $z = \frac{(E+P_{||})_{D^{*+}}}{(E+P)_{\text{jet}}}$, where $P_{||}$ stands for the momenta projected on jet axis, P is the momentum and E is the energy.

for the data. The total number of generated events is 10×10^6 for Rapgap and 52×10^6 for Pythia.

To simulate the events more efficiently, a preselection procedure was added to the generation procedure. Only events that satisfied at least one of the following criteria were kept for further reconstruction:

$$\begin{aligned}
D^{*+} \to (K,\pi),\pi_s^+ \text{with } p_T(D^{*+}) &> 1.25\,\text{GeV}, & -2 < \eta(D^{*+}) < 2 \\
D^{*+} \to (K_s^0,\pi,\pi),\pi_s^+ \text{with } p_T(D^{*+}) &> 1.35\,\text{GeV}, & -2 < \eta(D^{*+}) < 2 \\
D^{*+} \to (K,\pi,\pi,\pi),\pi_s^+ \text{with } p_T(D^{*+}) &> 2.3\,\text{GeV}, & -2 < \eta(D^{*+}) < 2 \\
D^0 \to K,\pi \text{with } p_T(D^0) &> 2.6\,\text{GeV}, & -2 < \eta(D^0) < 2 \\
D_s^+ \to (K,K),\pi^+ \text{with } p_T(D_s^+) &> 1.7\,\text{GeV}, & -2 < \eta(D_s^+) < 2 \\
D^+ \to (K,K),\pi+ \text{with } p_T(D^+) &> 1.7\,\text{GeV}, & -2 < \eta(D^+) < 2 \\
D^+ \to K,\pi,\pi \text{with } p_T(D^+) &> 2.8\,\text{GeV}, & -2 < \eta(D^+) < 2 \\
\Lambda_c^+ \to K,p,\pi \text{with } p_T(\Lambda_c^+) &> 2.8\,\text{GeV}, & -2 < \eta(\Lambda_c^+) < 2
\end{aligned} \qquad (5.1)$$

The specific decay-modes selection makes the branching ratios of ground charm-mesons in the produced sample significantly different from the PDG [1]. The selection influences the amount of background in the ground charm-meson mass spectra, however, the background in the excited-charm-meson mass spectra mostly originates from the events selected according to Eqs. (5.1) and is reasonably simulated in the MC sample.

5.2 Event selection

To ensure the high quality of the data, only events with non-corrupted online information from CTD, CAL, trigger, luminosity detectors and nominal current in solenoid were used in the analysis. Those events were selected with requirement for the online reconstruction flag $EVTAKE = 1, 2$. To exclude beam-gas events, it was required that the reconstructed primary vertex had Z-position between -30 cm and 30 cm. No explicit trigger selection was applied, but as expected, most events come from third-level triggers, which require the presence of any of the lowest-mass charm mesons $D^+ \to K^-\pi^+\pi^+$, $D^0 \to K^-\pi^+$ and $D^{*+} \to D^0\pi^+ \to (K^-\pi^+)\pi^+$ or $(K^-\pi^+\pi^-\pi^+)\pi^+$ (see detailed description of Zeus trigger system in Sec. 3.8).

However, as even untriggered events are present in the MC, a special check of trigger selection influence was done. For events with a D^{*+} candidate, the firing of at least one of the following third -level triggers was required (see detailed description elsewhere [63]): HFM01–HFM32, HFL1–HFL32, HPP01–HPP32.

The largest contribution came from the dedicated HFM triggers with the following logic:

- HFM1: $1.65\,\text{GeV} < M(D^0) < 2.10\,\text{GeV}$ and $M(D^{*+}) - M(D^0) < 0.17\,\text{GeV}$ or $1.40\,\text{GeV} < M(D^0) < 2.20\,\text{GeV}$ and $M(D^{*+}) - M(D^0) < 0.151\,\text{GeV}$ with $p_T(D^{*+}) > 1.35\,\text{GeV}$, $p_T(K,\pi) > 0.35\,\text{GeV}$, $p_T(\pi_s) > 0.1\,\text{GeV}$ for DIS and $p_T(D^{*+}) > 1.8\,\text{GeV}$, $p_T(K,\pi) > 0.35\,\text{GeV}$, $p_T(\pi_s) > 0.1\,\text{GeV}$ for PHP;
- HFL18: $p_T(D^{*+}) > 1.4\,\text{GeV}$, $p_T(K,\pi) > 0.45\,\text{GeV}$, $p_T(\pi_s) > 0.11\,\text{GeV}$, $1.78\,\text{GeV} < M(D^0) < 1.95\,\text{GeV}$, $M(D^{*+}) - M(D^0) < 0.162\,\text{GeV}$,
- HFM07: $1.70\,\text{GeV} < M(D^+) < 2.10\,\text{GeV}$, $p_T(D^+)/E > 0.12$, $p_T(D^+) > 1.35\,\text{GeV}$, $p_T(K,\pi) > 0.18\,\text{GeV}$ for DIS, $p_T(D^+) > 3.6\,\text{GeV}$, $p_T(K,\pi) > 0.45\,\text{GeV}$ for PHP;
- HFM04: $1.60\,\text{GeV} < M(D^0) < 2.20\,\text{GeV}$, $p_T(D^0) > 2.8\,\text{GeV}$, $p_T(K,\pi) > 0.7\,\text{GeV}$ for DIS, $p_T(D^0) > 3.6\,\text{GeV}$, $p_T(K,\pi) > 0.7\,\text{GeV}$ for PHP,

where E is the energy deposit in calorimeter outside of $\theta = 10^\circ$ cone, M stands for the reconstructed mass of the charm meson candidate and p_T for the corresponding transverse momentum. The efficiency of the on-line charm-meson reconstruction, determined relative to the efficiency of the offline reconstruction, was above 95%. Events missed by the nominal charm-meson triggers but selected with many other trigger branches, dominantly from an inclusive DIS trigger and a photoproduction dijet trigger, were also used in this analysis.

5.3 Track selection

The selection of tracks for each particular mode was driven by several different aims. For the modes that relied on the reconstruction of a displaced secondary vertex the essential issue was the quality of the decay tracks close to the primary interaction point so, the tracks were required to have: at least two BMVD measurements in the X–Y plane and two in the Z direction for D^+ reconstruction mode; at least one BMVD measurement in the X–Y plane and one in the Z direction for D^0 (not from D^{*+}). All tracks were required to start not further out than the first CTD superlayer and to reach at least the third superlayer. The pseudorapidity region for the tracks was in range from -2 to 2, unless other range not stated explicitly. The cuts on transverse momenta were essential to obtain a good signal-over-background ratio and were tuned from MC separately for each mode, taking into account that the generic ZEUS tracking is limited to the region $p_T > 0.1\,\text{GeV}$. Each track was required for each track to have good dE/dx information and at least 8 CTD hits used for its extraction. Based on the dE/dx information, a cut on the likelihood of the mass hypothesis $l_{K,\pi,p,e,\mu}$ (see Sec. 4.1) was applied: $l_K > 0.03$ (for kaons), $l_\pi > 0.01$ (for pions). This selection does not have a strong impact on the signal and is mainly used as a veto to reject protons and kaons in case of pion selection and vice-verse (see Fig. 5.1). To reduce combinatorial background and exclude tracks with poor fits or originally from hadronic interaction in the detector material, only tracks that have a Z position of the point of closest approach in the range $-50\,\text{cm}$ and $50\,\text{cm}$ were used for reconstruction. For the same reason, only tracks with impact parameter less than 1 cm were used for the charm-meson reconstruction.

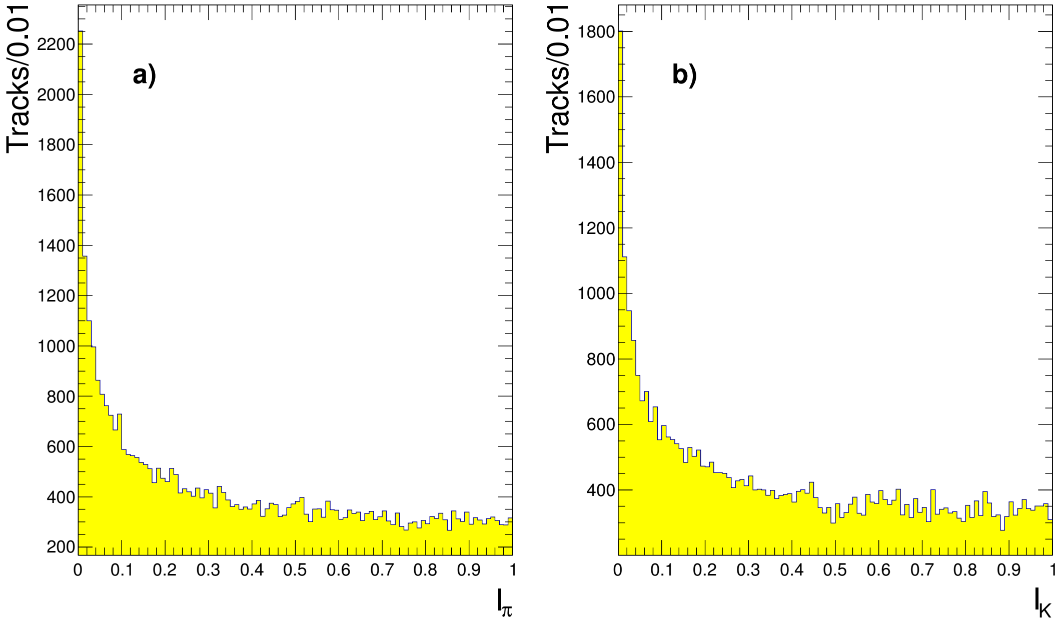

Figure 5.1: *The likelihood of mass hypotheses for tracks from* $D^{**} \to D^{*+}\pi^-, D^{*+} \to D^0\pi^+, D^0 \to K\pi$ *candidates in data events. The likelihood is calculated from* dE/dx *for a) pion mass hypothesis, b) kaon mass hypothesis.*

5.4 Reconstruction and selection of the charm meson candidates

The reconstruction of the candidates was performed by combining of selected tracks to form vertices as described in Sec. 4. The selection of candidates for each particular mode was mainly driven by the requirement of a clear signal for the excited charm states. To suppress combinatorial background, a cut on the ratio $p_T(D)/E_T^{\theta>10^\circ}$, motivated by the hard character of charm fragmentation, was applied. The transverse energy outside a cone, $E_T^{\theta>10^\circ}$, was calculated as $\Sigma_{i,\theta_i>10^\circ}(E_i \sin\theta_i)$, where the sum runs over all energy deposits in the CAL the cone of $\theta = 10^\circ$ around the forward direction. Cuts on the distance of closest approach between tracks (DCA), the quality of the vertex fit (χ^2) and 2-D decay-length significance with respect to the beam-spot position (S) were applied for the weakly decaying charm mesons (D^0 and D^+) candidates to improve the signal-to-background ratio.

5.5 D^{*+} reconstruction

D^{*+} mesons were identified via the decay modes $D^{*+} \to D^0\pi_s^+ \to (K^-\pi^+)\pi_s^+$ and $D^{*+} \to D^0\pi_s^+ \to (K^-\pi^+\pi^-\pi^+)\pi_s^+$, where π_s is a low-momentum ("soft") pion, due to the small mass difference between D^{*+} and D^0. The tracks with a DCA < 0.1 cm for the 2-prong mode and DCA < 0.3 cm for the 4-prong mode were combined to form a D^0 candidate vertex with total charge zero. The χ^2 of the decay vertex was required to be less than 20 for the 2-prong mode and less than 30 for the 4-prong mode. The invariant mass of the candidate was calculated assuming pion and kaon mass hypothesis for the track. The wrong charge D^{*+} candidates were formed by adding a soft pion, π_s, with the same charge as the kaon. Combinatorial background was reduced by applying cuts as detailed in Tab. 5.1. The mass differences $\Delta M = M(K\pi\pi_s) - M(K\pi)$ and $\Delta M = M(K\pi\pi\pi\pi_s) - M(K\pi\pi\pi)$ were calculated for the D^{*+} candidates that passed the cuts of Tab. 5.1. Fig. 5.2 shows the ΔM distributions for these D^{*+} candidates. Clean peaks are seen at the nominal value of $M(D^{*+}) - M(D^0)$ [1]. The ΔM distributions were fitted to a sum of a background function and a modified Gaussian function [56]. The fit yielded[26] D^{*+} signals of 64988 ± 430 candidates for $D^0 \to K\pi$ and 24441 ± 310 candidates for $D^0 \to K\pi\pi\pi$. The fitted mass differences were 145.400 ± 0.003 MeV and 145.420 ± 0.003 MeV respectively, in agreement with the PDG average value [1].

---

[26] The number of signal candidates was obtained as an integral of the fitted modified Gaussian function over the fit range.

Variable	$D^0 \to K^-\pi^+$	$D^0 \to K^-\pi^+\pi^+\pi^-$
$p_T(K)$ (GeV)	> 0.45	> 0.3
$p_T(\pi)$ (GeV)	> 0.45	> 0.3
$p_T(\pi_s)$ (GeV)	> 0.1	> 0.1
$p_T(D^{*+})$ (GeV)	> 1.5	> 3
$\|\eta(D^{*+})\|$	< 1.6	< 1.6
$p_T(D^{*+})/E_\perp^{\theta>10°}$	> 0.12	> 0.18
$M(D^0)$ (GeV) for $p_T(D^{*+}) < 3.25$ GeV	$1.83 - 1.90$	$1.84 - 1.89$
$M(D^0)$ (GeV) for $3.25 < p_T(D^{*+}) < 5$ GeV	$1.82 - 1.91$	$1.84 - 1.89$
$M(D^0)$ (GeV) for $5 < p_T(D^{*+}) < 8$ GeV	$1.81 - 1.92$	$1.84 - 1.89$
$M(D^0)$ (GeV) for $p_T(D^{*+}) > 8$ GeV	$1.80 - 1.93$	$1.84 - 1.89$
$\chi^2_{D^0 \text{ vtx.}}$	< 20	< 30

Table 5.1: *Cuts on $D^{*+} \to D^0\pi_s^+$ candidates for the decay channels $D^0 \to K^-\pi^+$ and $D^0 \to K^-\pi^+\pi^+\pi^-$.*

Only D^{*+} candidates with $0.144 < \Delta M < 0.147$ GeV were used for the excited-charm-meson analysis.

5.6 $\boldsymbol{D^+}$ reconstruction

D^+ mesons were reconstructed from the decay $D^+ \to K^-\pi^+\pi^+$ with looser kinematic cuts than in the previous analysis [56], made possible by the cleaner identification with the MVD. For each event, track pairs with equal charge and pion mass assignment were combined with a track with opposite charge and a kaon mass assignment to form a D^+ candidate. These tracks were refitted to a common decay vertex, and the invariant mass, $M(K\pi\pi)$, was calculated. The K

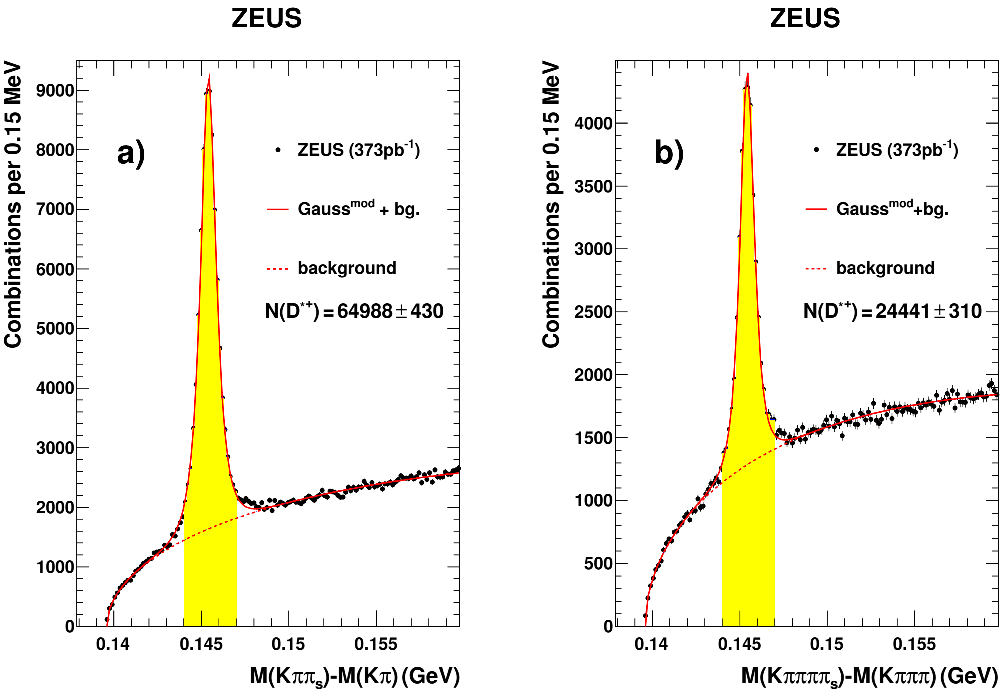

Figure 5.2: *The distribution of the mass difference (dots), (a)* $\Delta M = M(K\pi\pi_s) - M(K\pi)$ *and (b)* $\Delta M = M(K\pi\pi\pi\pi_s) - M(K\pi\pi\pi)$*. The solid curves are fits to the sum of a modified Gaussian function and a background function (dashed lines). Events from the shaded area,* $0.144 - 0.147\,\text{GeV}$*, are used for the excited-charm-mesons analysis.*

and π tracks were required to have transverse momentum $p_T^K > 0.5$ GeV and $p_T^\pi > 0.35$ GeV. To suppress combinatorial background, the following cuts were applied:

- $\cos\theta^*(K) > -0.75$, where $\theta^*(K)$ is the angle between the kaon in the $K\pi\pi$ rest frame and the $K\pi\pi$ line of flight in the laboratory frame;
- the χ^2 of the fit of the decay vertex (see Sec. 4) was less than 10;
- the DCA between tracks (see Sec. 4) was less than 0.3 cm;
- the decay-length significance, $S(D^+)$(see Sec. 4), was greater than 3.

Background from D^{*+} decays was removed by requiring $M(K\pi\pi) - M(K\pi) > 0.15$ GeV. Background from $D_s^+ \to \phi\pi$, $\phi \to K^+K^-$ was suppressed by requiring that the invariant mass of any two D^+ decay candidate tracks with opposite charge should be outside ± 8 MeV around the nominal ϕ mass when the kaon mass was assigned to both tracks. The background and reflections from other decays are described in Sec. 11. D^+ candidates in the kinematic range $p_T(D^+) > 2.8$ GeV and $|\eta(D^+)| < 1.6$ were kept for further analysis.

Fig. 5.3 (a) shows the $M(K^-\pi^+\pi^+)$ distribution for D^+ candidates after the cuts. A clear signal is seen at the nominal value of the D^+ mass [1]. The mass distribution was fitted to a sum of a modified Gaussian function and a polynomial background. The integral over the gaussian function was considered as the signal. The fit yielded a D^+ signal of 39283 ± 452 events and a D^+ mass of 1869.1 ± 0.1 MeV, in agreement with the PDG average value [1]. Only D^+ candidates with $1.85 < M(K\pi\pi) < 1.89$ GeV were used for the excited-charm-mesons analysis.

5.7 $\boldsymbol{D^0}$ reconstruction

D^0 mesons were reconstructed from the decay $D^0 \to K^-\pi^+$. For each event, two tracks with opposite charge and with K and π mass assignments, respectively, were combined to form a D^0 candidate. These tracks were refitted to a common decay vertex, and the invariant mass, $M(K\pi)$, was calculated. Both tracks were required to have transverse momentum $p_T^K > 0.5$ GeV and $p_T^\pi > 0.7$ GeV and the distance of closest approach between these tracks was required to be less than 0.1 cm. To suppress combinatorial background, the following cuts were applied:

- $|\cos\theta^*(K)| < 0.85$, where $\theta^*(K)$ is the angle between the kaon in the $K\pi$ rest frame and the $K\pi$ line of flight in the laboratory frame;
- the χ^2 of the decay vertex is less than 20;
- the decay-length significance, $S(D^0)$, is bigger than 0.

D^0 candidates which are consistent with a $D^{*+} \to D^0\pi_s^+$ decay, when combined with a third “soft” pion π_s with charge opposite to that of the kaon, were removed by requiring $M(K\pi\pi_s) - M(K\pi) > 0.15$ GeV. D^0 candidates in the kinematic range $p_T(D^0) > 2.6$ GeV and $|\eta(D^0)| < 1.6$ were kept for further analysis.

Fig. 5.3 (b) shows the $M(K^-\pi^+)$ distribution for D^0 candidates after the cuts. A clear signal is seen at the nominal value of the D^0 mass [1]. The mass distribution

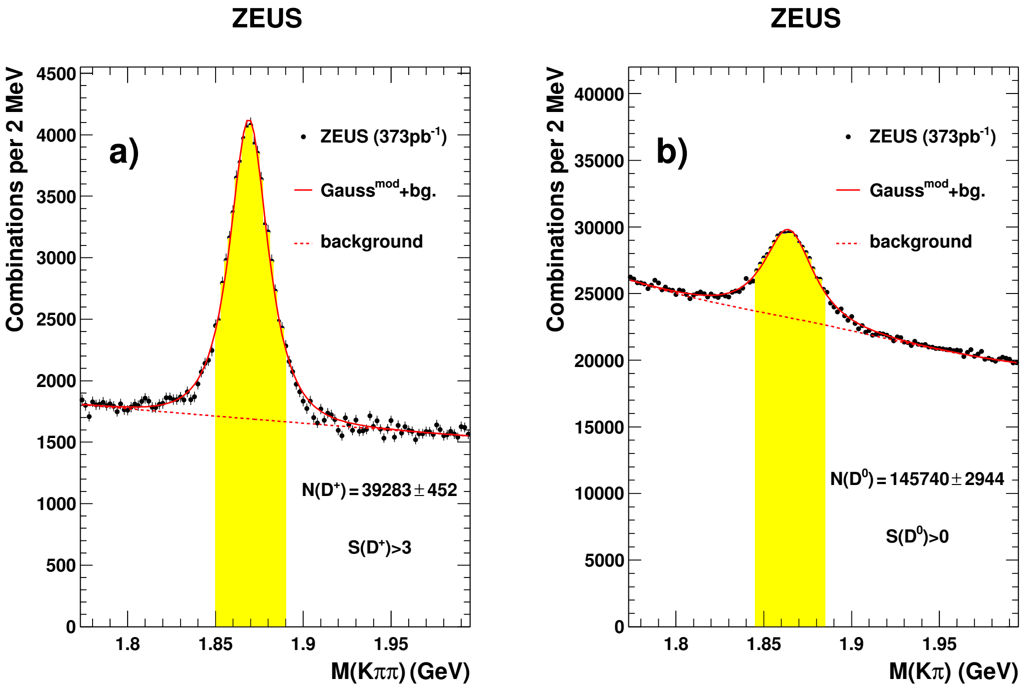

Figure 5.3: *The mass distributions (dots), (a)* $M(K^-\pi^+\pi^+)$ *for events with significance* $S > 3$ *and (b)* $M(K^-\pi^+)$ *for events with significance* $S > 0$*. The solid curves are fits to the sum of a modified Gaussian function and a background function (dashed lines). Events from the shaded areas, (a)* $1.85 - 1.89\,\mathrm{GeV}$ *and (b)* $1.845 - 1.885\,\mathrm{GeV}$*, are used for the excited charm mesons analysis.*

was fitted to a sum of a modified Gaussian function, a broad modified Gaussian representing the reflection produced by D^0 mesons with the wrong (opposite) kaon and pion mass assignment and a polynomial background. For the reflection, the shape parameters of the broad Gaussian were obtained from a study of the MC signal sample and the normalisation (integral) was set equal to that of the modified Gaussian. The fit yielded[26] a D^0 signal of 145740 ± 2944 events and a D^0 mass of $1864.1 \pm 0.1\,\mathrm{MeV}$ which is $0.8\,\mathrm{MeV}$ lower[27] than the PDG average value [1]. Only D^0 candidates with $1.845 < M(K\pi\pi) < 1.885$ GeV were used for the excited-charm-mesons analysis.

---

[27] Despite the discrepancy is not negligible, the excited charm-meson mass spectra were reconstructed with the "extended" mass difference explained below and, therefore should not be biased.

5.8 K_S^0 reconstruction

The K_S^0 were used only for the reconstruction of the $D_1^{*+} \to D^{*+}K_S^0$ decays, so the K_S^0 mesons were reconstructed for those events containing a D^{*+} candidate. The K_S^0 were reconstructed in their charged-decay mode, $K_S^0 \to \pi^+\pi^-$. To identify K_S^0 candidates, secondary vertices were reconstructed from pairs of oppositely charged tracks with DCA < 0.5 cm. To reduce the combinatorial background, in addition to the general cuts on considered tracks, it was required that $p_T > 0.15$ GeV for each track from the K_S^0 candidate. The identification efficiency degraded for secondary vertices close to the primary vertex. To reduce the combinatorial background originating from tracks from the primary vertex, the cuts on the two-dimensional and three-dimensional collinearity angles (see Sec. 4 for details) $\alpha_{2\text{-}D} < 0.25$ and $\alpha_{3\text{-}D} < 0.35$ were applied. Fig. 5.4 shows the

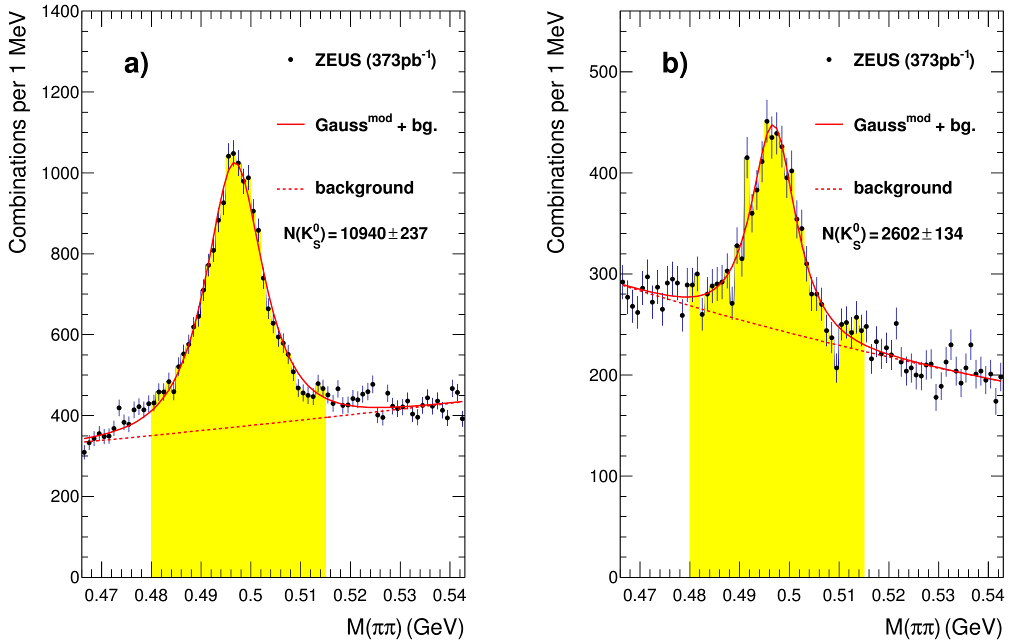

Figure 5.4: *The distribution of the mass $M(\pi^+\pi^-)$ (dots) in events with D^{*+} candidates, (a) $D^{*+} \to D^0\pi^+, D^0 \to K\pi$ and (b) $D^{*+} \to D^0\pi^+, D^0 \to K3\pi$ candidates. The solid curves are fits to the sum of a modified Gaussian function and a background function (dashed lines). Events from the shaded area,* $0.480 - 0.515$ GeV, *are used for the excited-charm-mesons analysis.*

invariant-mass distribution,$M(\pi^+\pi^-)$, for all remaining K^0_S candidates. Only K^0_S candidates with $0.490 < M(\pi^+\pi^-) < 0.515\,\mathrm{GeV}$ were kept for the reconstruction of excited charm-strange mesons. The mass distribution was fitted to a sum of a modified Gaussian function describing the signal and a linear function describing the non-resonant background. The fit yielded the K^0_S mass values $496.7 \pm 0.1\,\mathrm{MeV}$ and $496.8 \pm 0.2\,\mathrm{MeV}$, respectively, $0.9\,\mathrm{MeV}$ and $0.8\,\mathrm{MeV}$ lower[27] than the PDG value [1]. The widths of the signals, $5.4 \pm 0.1\,\mathrm{MeV}$ and $4.2 \pm 0.3\,\mathrm{MeV}$, reflected the detector resolution. The number of reconstructed K^0_S mesons yielded by the fit was $N(K^0_S)$ =10940 ± 237 for the events with $D^{*+} \to D^0\pi^+_s, D^0 \to K\pi$ candidates and $N(K^0_S)$ =2602 ± 134 for the events with $D^{*+} \to D^0\pi^+_s, D^0 \to K3\pi$ candidates.

5.9 $D_1(2420)^0$ and $D^*_2(2460)^0$ reconstruction

The $D_1(2420)^0$ and $D^*_2(2460)^0$ mesons were reconstructed in the decay mode $D^{*+}\pi^-$ by combining each D^{*+} candidate with an additional track, assumed to be a pion (π_a), with a charge opposite to that of the D^*. Combinatorial background was reduced by applying the following cuts:

- $p_T(\pi_a) > 0.15$ GeV;
- $\eta(\pi_a) < 1.1$;
- $p_T(D^{*+}\pi_a)/E_\perp^{\theta>10^\circ} > 0.25$ (0.30) for the $D^0 \to K\pi$ ($D^0 \to K\pi\pi\pi$) channel;
- $\cos\theta^*(D^{*+}) < 0.9$, where $\theta^*(D^{*+})$ is the angle between the D^{*+} in the $D^{*+}\pi_a$ rest frame and the $D^{*+}\pi_a$ line of flight in the laboratory frame;
- the cut $l_\pi > 0.01$ was applied for π_a.

For each excited-charm-meson candidate, the "extended" mass difference, $\Delta M^{\mathrm{ext}} = M(K\pi\pi_s\pi_a) - M(K\pi\pi_s)$ or $\Delta M^{\mathrm{ext}} = M(K\pi\pi\pi\pi_s\pi_a) - M(K\pi\pi\pi\pi_s)$, were calculated. Fig. 5.5 (a) shows the invariant mass $M(D^{*+}\pi_a) = \Delta M^{\mathrm{ext}} + M(D^{*+}_{\mathrm{PDG}})$, where $M(D^{*+}_{\mathrm{PDG}})$ is the nominal D^{*+} mass [1]. A clear signal in the D^0_1/D^{*0}_2 mass region is seen. To distinguish between $D^0_1, D^{*0}_2 \to D^{*+}\pi^-$, their helicity angular distributions were used (see Eq. (2.2)). Fig. 5.6 shows the $M(D^{*+}\pi_a)$ distribution in four helicity bins. From the HQET predictions $h(D^0_1) = 3$ and $h(D^{*0}_2) = -1$ it is expected that the D^0_1 contribution increases and the D^{*0}_2 contribution decreases with $|\cos\alpha|$. The distributions in Fig. 5.6 qualitatively confirms those expectations.

The $D_2^*(2460)^0$ was also reconstructed in the decay mode $D_2^*(2460)^0 \to D^+\pi^-$ by combining each D^+ candidate with an additional track, assumed to be a pion π_a, with a charge opposite to that of the D^+. Combinatorial background was reduced by applying the following cuts:

- $p_T(\pi_a) > 0.3$ GeV;
- $\eta(\pi_a) < 1.5$;
- $p_T(D^+\pi_a)/E_\perp^{\theta>10^\circ} > 0.35$;
- $\cos\theta^*(D^+) < 0.8$, where $\theta^*(D^+)$ is the angle between the D^+ in the $D^+\pi_a$ rest frame and the $D^+\pi_a$ line of flight in the laboratory frame;
- the cut $l_\pi > 0.01$ was applied for π_a.

The $D_2^*(2460)^0 \to D^+\pi^-$ decay mode was reconstructed by calculating the "extended" mass difference $\Delta M^{\mathrm{ext}} = M(K\pi\pi\pi_a) - M(K\pi\pi)$. Fig. 5.5 (b) shows the invariant mass $M(D^+\pi_a) = \Delta M^{\mathrm{ext}} + M(D^+_{\mathrm{PDG}})$, where $M(D^+_{\mathrm{PDG}})$ is the nominal D^+ mass [1]. A clear D_2^{*0} signal is seen. No indication of the $D_1^0 \to D^+\pi^-$ decay is seen, as expected from angular momentum and parity conservation for a $J^P = 1^+$ state.

A small excess of events over background is seen around 2.3 GeV in the $D^+\pi^-$ mass distribution (Fig. 5.5(b)). This excess originates from the decay chains $D_1^0, D_2^{*0} \to D^{*+}\pi^-$ with $D^{*+} \to D^+\pi^0$ or $D^{*+} \to D^+\gamma$. The π^0/γ are not seen in the tracking detectors; thus, the reconstruction is incomplete. However, since the available phase space in the $D^{*+} \to D^+\pi^0$ decay is small and D^+ is much heavier than π^0, the energy and momentum of D^+ are close to those of D^{*+}. Consequently, the enhancements seen in the $M(D^+\pi_a)$ (Fig. 5.5(b)) distribution are called a **feed-down** of the excited charm mesons D_1^0, D_2^{*0}, shifted down approximately by the value of the π^0 mass, as verified by MC simulations. The feed-down fitting procedure is described in Sec. 11. Further details on various contributions to the mass spectrum will be discussed below.

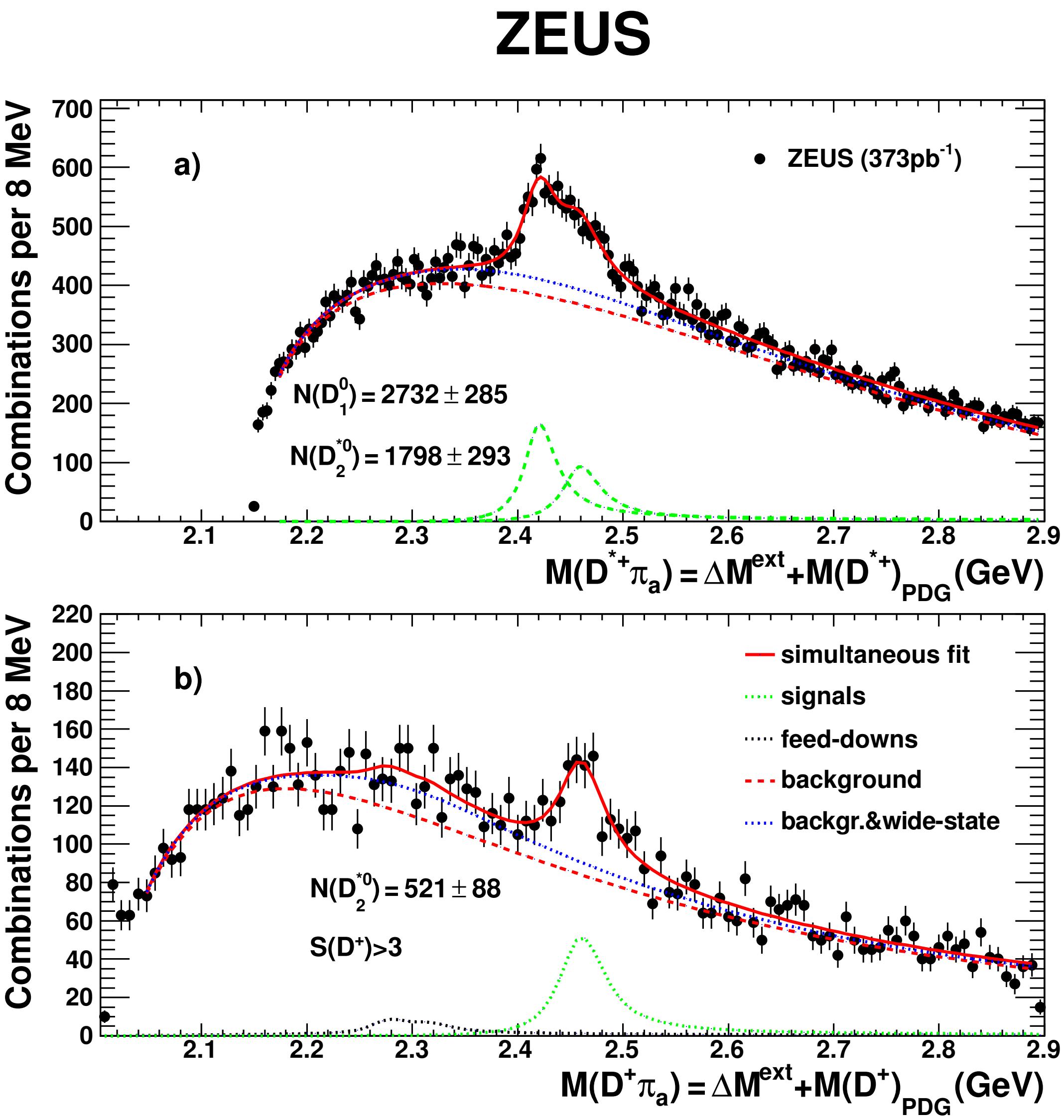

Figure 5.5: *The mass distributions (dots) a) $M(D^{*+}\pi_a)$ and b) $M(D^{+}\pi_a)$. The solid curves are the result of a simultaneous fit to a) D_1^0 and D_2^{*0} and to b) D_2^{*0} and feed-downs plus background function (dashed curves). The contributions of the wide states $D_1(2430)^0$ and $D_0^*(2400)^0$ are given between the dashed and dotted curves. The lowest curves are the contributions of the D_1^0 and D_2^{*0} to the fit.*

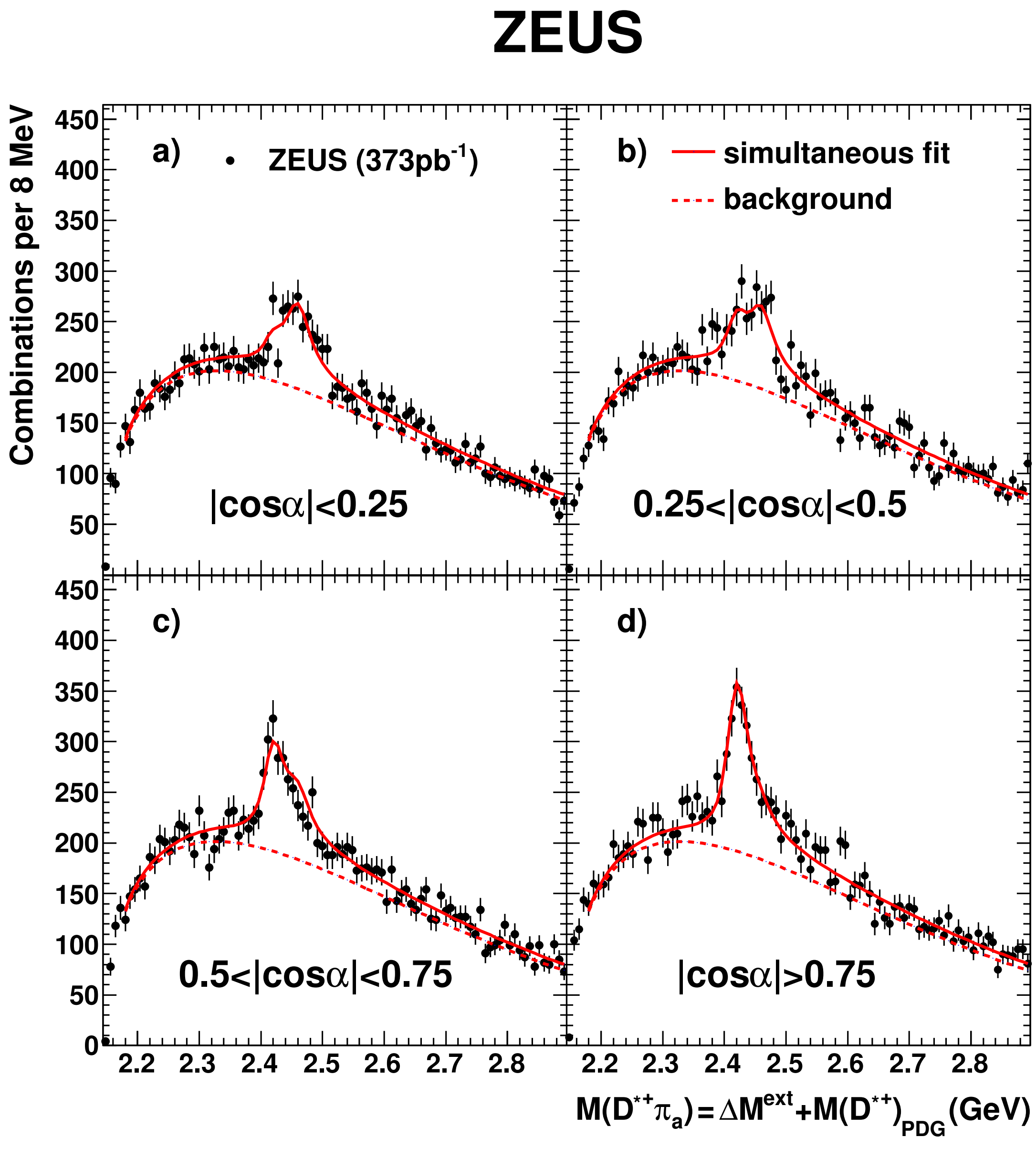

Figure 5.6: *The mass distributions (dots) $M(D^{*+}\pi_a)$ in four helicity intervals: (a) $|\cos\alpha| < 0.25$; (b) $0.25 < |\cos\alpha| < 0.50$; (c) $0.50 < |\cos\alpha| < 0.75$; (d) $|\cos\alpha| > 0.75$. The solid curves are the result of the simultaneous fit to D_1^0 and D_2^{*0} plus background function (dashed curves).*

5.10 $D_1(2420)^+$ and $D_2^*(2460)^+$ reconstruction

The charged excited meson $D_1(2420)^+$ has been seen [1] in the decay modes $D^{*0}\pi^+$ and $D^+\pi^+\pi^-$ and the charged excited meson $D_2^*(2460)^+$ has been seen [1] in the decay modes $D^{*0}\pi^+$ and $D^0\pi^+$. A search for D_1^+ and D_2^{*+} signals was performed in the mass distribution $M(D^0\pi^+)$. For the D_1^+ a possible $D^0\pi^+$ signal can arise only via a feed-down contribution (see Sec. 11). Each D^0 candidate was combined with an additional track, assumed to be a pion (π_a), with either positive or negative charge. Combinatorial background was reduced by applying the following cuts:

- $p_T(\pi_a) > 0.35$ GeV;
- $\eta(\pi_a) < 1.6$;
- $p_T(D^0\pi_a)/E_\perp^{\theta>10^\circ} > 0.3$;
- $\cos\theta^*(D^0) < 0.85$, where $\theta^*(D^0)$ is the angle between the D^0 in the $D^0\pi_a$ rest frame and the $D^0\pi_a$ line of flight in the laboratory frame;
- the cut $l_\pi > 0.01$ was applied for π_a.

For each excited-charm-meson candidate, the "extended" mass difference $\Delta M^{\text{ext}} = M(K\pi\pi_a) - M(K\pi)$ was calculated. Fig. 5.7 shows the invariant mass $M(D^0\pi_a) = \Delta M^{\text{ext}} + M(D^0_{\text{PDG}})$, where $M(D^0_{\text{PDG}})$ is the nominal D^0 mass [1]. A clear signal of $D_2^{*+} \to D^0\pi^+$ is seen. An enhancement above background is also seen at the mass region around 2.3 GeV. It is a sum of feed-downs of D_1^+ and D_2^{*+} states, which originates from the decay chains $D_1^+, D_2^{*+} \to D^{*0}\pi^+$ with $D^{*0} \to D^0\pi^0$ or $D^{*0} \to D^0\gamma$. Further details on contributions to the mass spectrum will be discussed below.

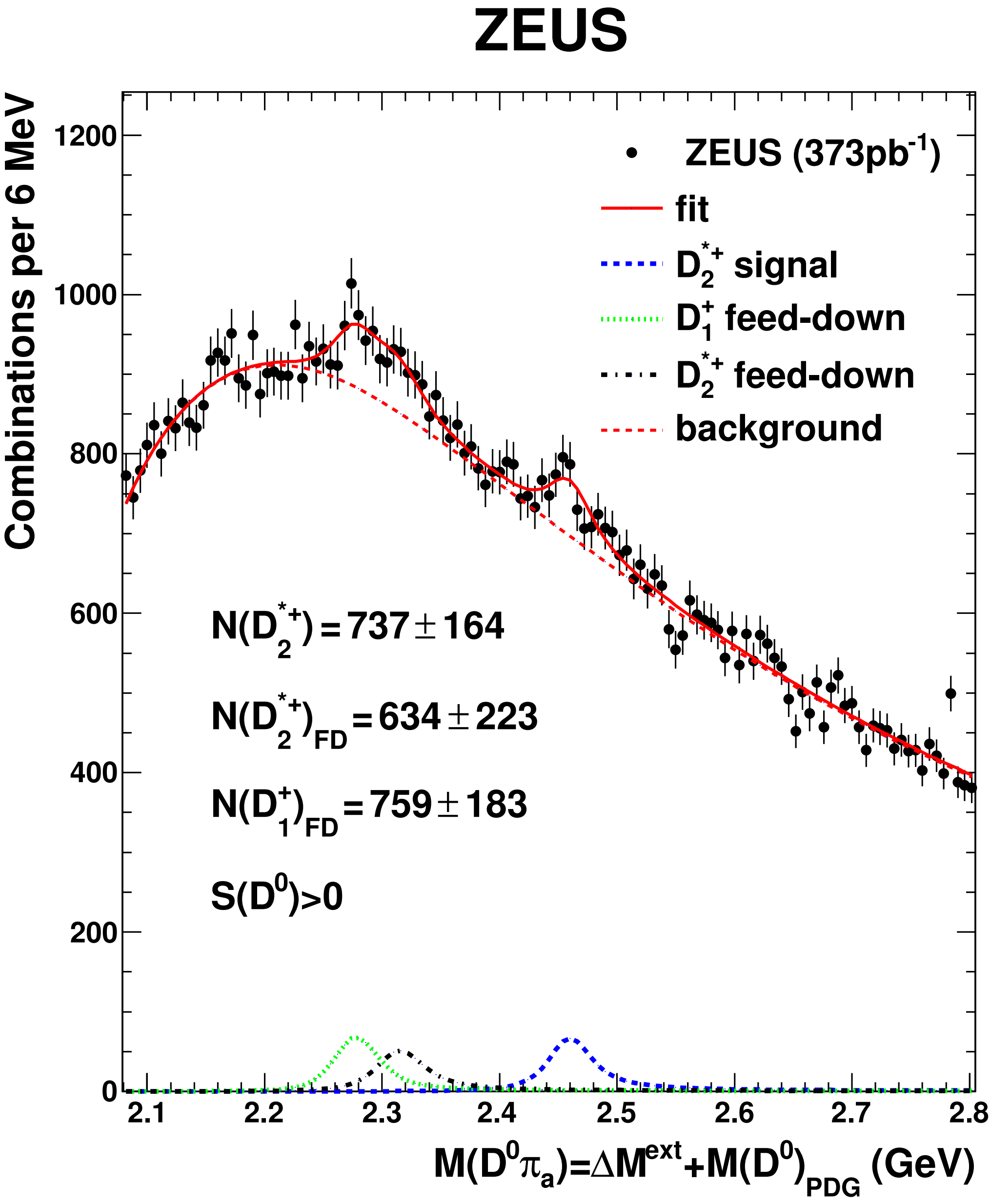

Figure 5.7: *The mass distribution (dots) $M(D^0\pi_a)$. The solid curve is the result of a simultaneous fit to the feed-down (FD) D_1^+ and D_2^{*+} contributions and to the D_2^{*+} signal plus background function (dashed curves). The lowest curves are the contributions of the D_1^+ and D_2^{*+} to the fit.*

5.11 $D_{s1}^{+}(2535)$ reconstruction

To reconstruct the $D_{s1}^{+} \to D^{*+}K_S^0$ decays, a D_{s1}^{+}-meson candidate was formed by combining each selected D^{*+} candidate with the K_S^0 candidates reconstructed in the same event. For each excited charm-strange-meson candidate, the "extended" mass difference, $\Delta M^{\mathrm{ext}} = M(K\pi\pi_s\pi^+\pi^-) - M(K\pi\pi_s) - M(\pi^+\pi^-)$ or $\Delta M^{\mathrm{ext}} = M(K\pi\pi\pi\pi_s\pi^+\pi^-) - M(K\pi\pi\pi\pi_s) - M(\pi^+\pi^-)$, was calculated. The invariant mass of the $D^{*+}K_S^0$ system was calculated as $M(D^{*+}K_S^0) = \Delta M^{\mathrm{ext}} + M(D^{*+})_{\mathrm{PDG}} + M(K_S^0)_{\mathrm{PDG}}$, where $M(K_S^0)_{\mathrm{PDG}}$ is the nominal K_S^0 mass [1]. Fig. 5.8(a) shows the $M(D^{*+}K_S^0)$ distribution for D^{*+} meson candidates reconstructed in both decay channels. A clear signal is seen at the nominal value of $M(D_{s1}^{+})$. To reconstruct the $D_{s1}^{+} \to D^{*0}K^{+}$ decays, an excited charm-strange-meson candidate was formed by combining each selected D^0 candidate with an additional track, assumed to be a kaon (K_a), with a charge opposite to that of the particle taken as a kaon to form the D^0 candidate. To reduce the combinatorial background, the following requirements were applied:

- $\eta(K_a) < 1.6$;
- $p_T(K_a) > 0.35\,\mathrm{GeV}$;
- $p_T(D^0K_a)/E_T^{\theta>10} > 0.30$;
- $\cos\theta^*(D^0) < 0.85$, where $\theta^*(D^0)$ is the angle between the D^0 in the D^0K_a rest frame and the D^0K_a line of flight in the laboratory frame.

For each excited charm-strange-meson candidate, the "extended" mass difference, $\Delta M^{\mathrm{ext}} = M(K\pi K_a) - M(K\pi)$ was calculated. The invariant mass of the D^0K_a system was calculated as $M(D^0K_a) = \Delta M^{\mathrm{ext}} + M(D^0)_{\mathrm{PDG}}$, where $M(D^0)_{\mathrm{PDG}}$ is the nominal D^0 mass [1]. Fig. 5.8(b) shows the $M(D^0K_a)$ distribution for the selected excited charm-strange-meson candidates. A feed-down of $D_{s1}^{+} \to D^{*0}K^{+}$ decay is seen at the expected position in D^0K^+ mass spectrum. A tiny indication of the known decay $D_{s2}(2573)^+ \to D^0K^+$ [1] is seen in the D^0K^+ mass spectrum around 2.6 GeV.

The helicity distribution of the D_{s1}^{+} state was studied (see Eq.(2.2)) with distributions of the $M(D^{*+}K_S^0)$ mass spectrum in four helicity bins (see Fig. 5.9). Further details on contributions to the mass spectrum will be discussed below.

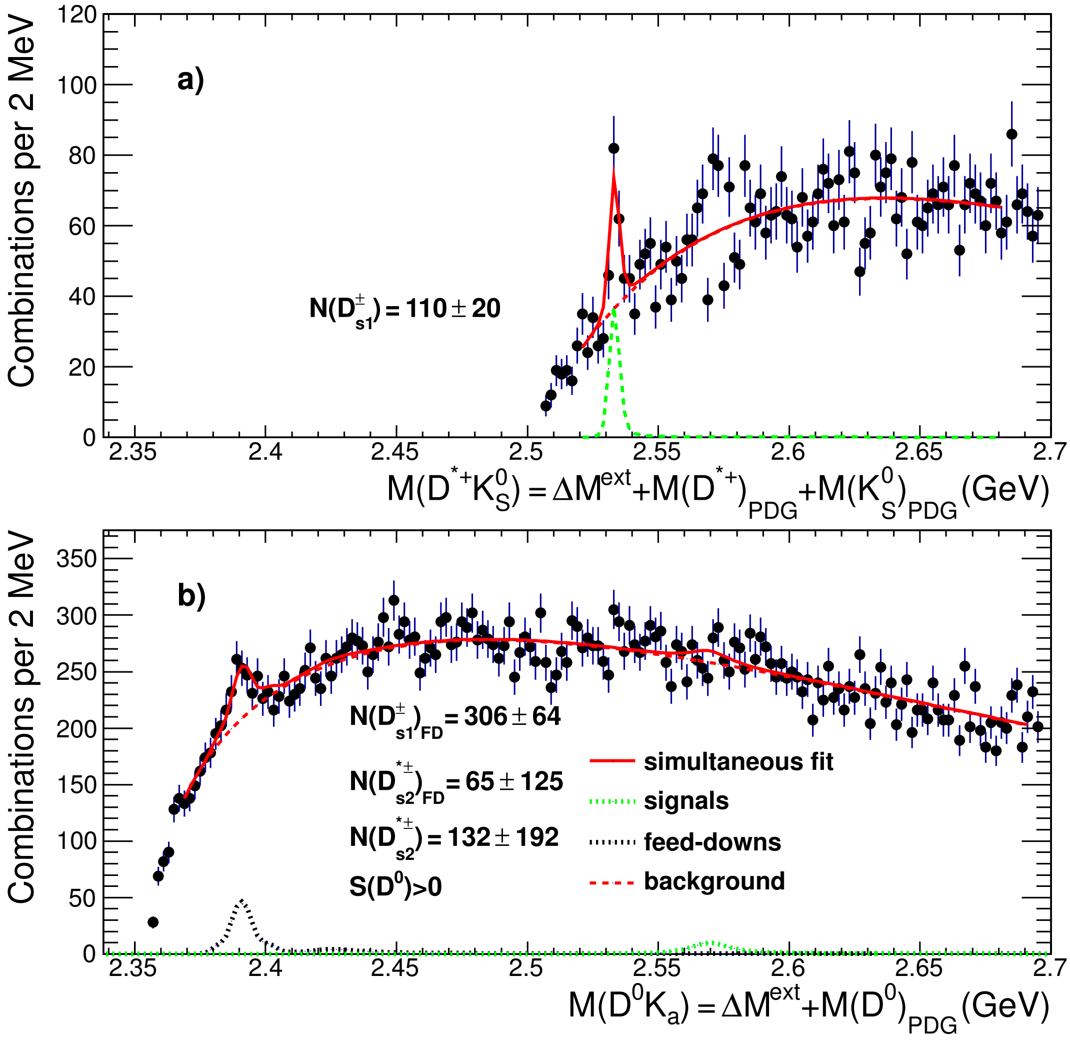

Figure 5.8: *The mass distributions (dots), a)* $M(D^{*+}K_S^0)$ *and b)* $M(D^0K^+)$*. The solid curves are the result of a simultaneous fit to a)* D_{s1}^+ *and to b)* D_{s2}^{*+} *and feed-downs plus background function (dashed curves).*

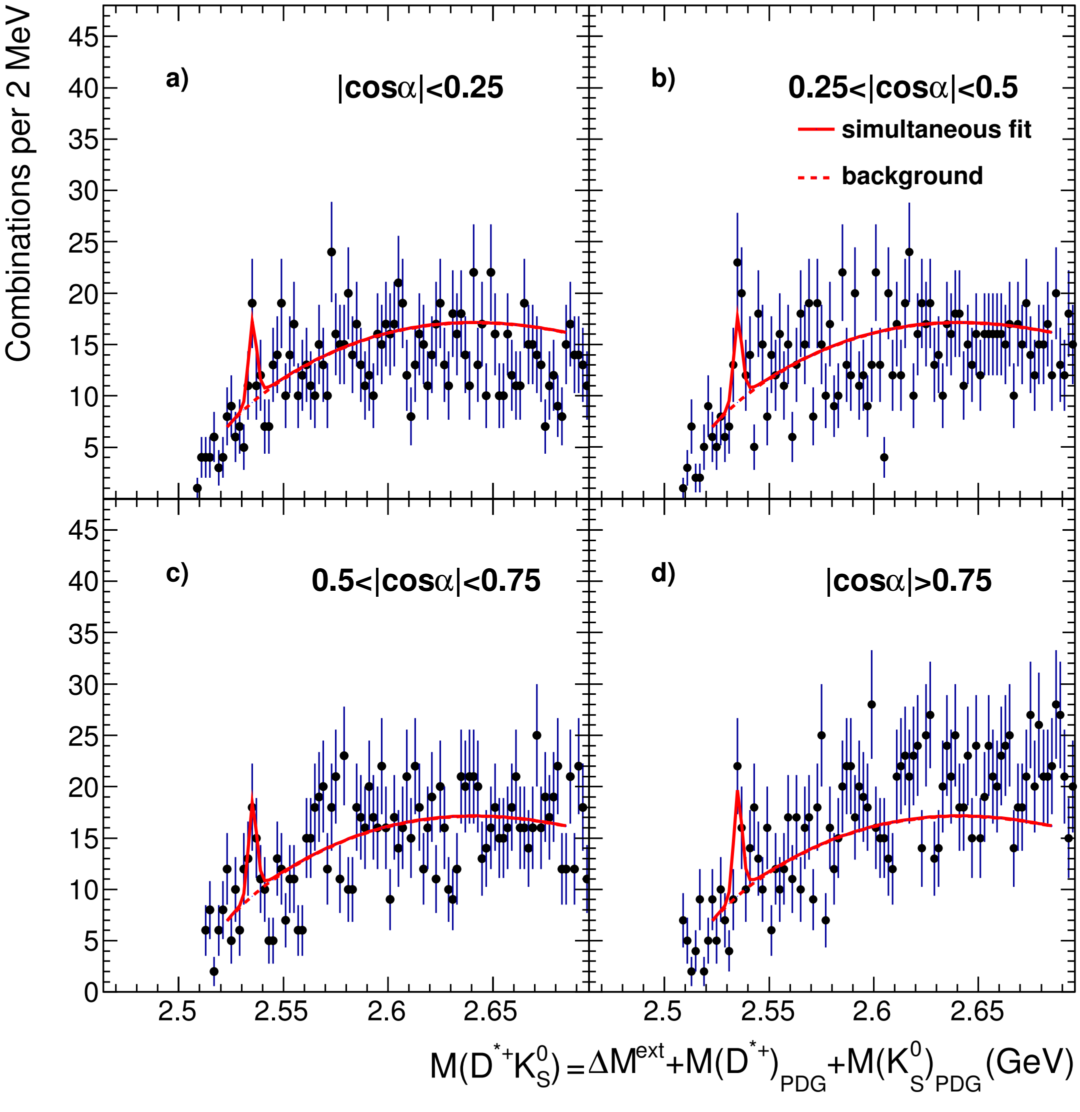

Figure 5.9: *The mass distributions (dots), $M(D^{*+}K^0_S)$ in four helicity intervals: (a) $|\cos\alpha| < 0.25$; (b) $0.25 < |\cos\alpha| < 0.50$; (c) $0.50 < |\cos\alpha| < 0.75$; (d) $|\cos\alpha| > 0.75$. The solid curves are the result of the simultaneous fit to D^+_{s1} plus background function (dashed curves).*

6 Discussion on spectroscopy results

This subsection describes the considered excited-charm-meson contributions to the reconstructed mass spectra. The obtained fit results on the excited charm states are discussed and compared to the previous measurements, PDG averages and the theoretical expectations.

6.1 Neutral excited charm mesons in the $D^{*+}\pi^-$ and $D^+\pi^-$ spectra

To extract the signals of the excited neutral charm mesons, a χ^2 fit was performed using simultaneously the $M(D^+\pi_a)$ distribution shown in Fig. 5.5(b) and the $M(D^{*+}\pi_a)$ distributions in four helicity bins shown in Fig. 5.6.

For the $D^{*+}\pi_a$ spectrum the fit included:

- the background contribution;
- the signals of $D_1^0(2420)$, $D_2^{*0}(2460)$ and $D^0(2430)$ states.

For the $D^+\pi_a$ spectrum the fit included:

- the background contribution;
- the signals of $D_2^{*0}(2460)$ and $D^{*0}(2400)$ states;
- the feed-downs from the $D_1^0(2420)$, $D_2^{*0}(2460)$ and $D^0(2430)$ states.

The background for the $D^{*+}\pi$ mode was parametrised with **four** parameters a_1, b_1, c_1, d_1 as $B(x) = a_1 x^{b_1} \exp(-cx_1 - dx_1^2)$, where $x = \Delta M^{\text{ext}} - M_{\pi^+}$. The same background function has been used in all helicity bins. The background for the $D^+\pi$ mode has been parametrised with **four** other parameters a_2, b_2, c_2, d_2 as $B(x) = a_2 x^{b_2} \exp(-c_2 x - d_2 x^2)$, where $x = \Delta M^{\text{ext}} - M_{\pi^+}$.

Each signal was fitted to a relativistic D-wave Breit-Wigner (BW) function (see Sec. 11) convoluted with a Gaussian resolution function with a width fixed to the corresponding MC prediction (see Sec. 11). In the most general case this implies the following list of fit parameters:

- $N(D_1^0(2430) \to D^{*+}\pi^-)$, $M(D_1^0(2430))$, $\Gamma(D_1^0(2430))$, $h(D_1^0(2430))$;
- $N(D_1^0(2420) \to D^{*+}\pi^-)$, $M(D_1^0(2420))$, $\Gamma(D_1^0(2420))$, $h(D_1^0(2420))$;
- $N(D_2^{*0}(2460) \to D^{*+}\pi^-)$, $M(D_2^{*0}(2460))$, $\Gamma(D_2^{*0}(2460))$, $h(D_2^{*0}(2460))$;

- $N(D_2^{*0}(2460) \to D^+\pi^-)$;
- $N(D^{*0}(2400) \to D^+\pi^-)$, $M(D^{*0}(2400))$, $\Gamma(D^{*0}(2400))$[28].

However, because of the large background, it was impossible to find from the fit the parameters of the known wide states $D^{*0}(2400)$ and $D^0(2430)$. Thus, the masses and widths of $D^{*0}(2400)$ and $D^0(2430)$ were set to the PDG [1] values and the helicity parameters of $D^{*0}(2400)$ and $D^0(2430)$ to the HQET predictions $h(D^{*0}(2400)) = 0$ and $h(D^0(2430)) = 0$ (see Sec. 2). As both $D^0(2430)$ and $D_1^0(2420)$ mesons are $J^P = 1^+$ states, the yield of $D^0(2430)$ was required to be the same as that of $D^0(2420)$. The $h(D_2^{*0})$ parameter in the fit has been fixed to the HQET prediction (see Sec. 2) $h(D_2^{*0}) = -1$. (A test fit with free $h(D_2^{*0})$ parameter yielded the value $h(D_2^{*0}) = -1.16 \pm 0.35$.) These assumptions reduced the number of free signal parameters to **nine**:

- $N(D_1^0(2420) \to D^{*+}\pi^-)$, $M(D_1^0(2420))$, $\Gamma(D_1^0(2420))$, $h(D_1^0(2420))$;
- $N(D_2^{*0}(2460) \to D^{*+}\pi^-)$, $M(D_2^{*0}(2460))$, $\Gamma(D_2^{*0}(2460))$;
- $N(D_2^{*0}(2460) \to D^+\pi^-)$;
- $N(D^{*0}(2400) \to D^+\pi^-)$.

The feed-down shape was modelled as described in Sec. 11 and convoluted with a Gaussian resolution function with a width fixed to the corresponding MC prediction (see Sec. 11). The masses, widths and helicity parameters of feed-downs were the same as for the signal. The total normalisation of the sum of the feed-down processes was fitted relative to the signal peak yield from $N(D_2^{*0}(2460) \to D^+\pi^-)$ decay, i.e. with **one** parameter. The relative yields of the $D_1^0(2420)$, $D_1^0(2430)$, $D_2^{*0}(2460)$ feed-down contributions were taken to be equal to those for the direct signals in the $D^{*+}\pi^-$ decay channel.

The fit results are shown in Tab. 6.1 together with the parameters used in the fits. The results are compared to the previous ZEUS publication [56] (HERA-I) and PDG [1]. The given systematical uncertainties are discussed in Sec. 9. All results from this analysis [64] (HERA-II) are shown in Tab. 6.2 and are consistent with those from the previous ZEUS publication [56] (HERA-I). The masses of both D_1^0 and D_2^{*0} are consistent with the latest PDG values [1] and with a recent BABAR measurement [62]. The theoretical predictions for the D_1^0 and D_2^{*0} masses in general agree (within $3-4\,\text{MeV}$) with the measurements and PDG values,

---

[28] the $h(D^{*0}(2400))$ is not needed for the fit

	HERA-II [64](this)	HERA-I [56]	PDG [1]
$N(D_1^0 \to D^{*+}\pi)$	2732 ± 285	3110 ± 340	
$N(D_2^{*0} \to D^{*+}\pi)$	1798 ± 293	870 ± 170	
$N(D_2^{*0} \to D^{+}\pi)$	521 ± 88 ($S(D^+) > 3$)	690 ± 160	
$M(D_1^0)$, MeV	$2423.1 \pm 1.5^{+0.4}_{-1.0}$	$2420.5 \pm 2.1 \pm 0.9$	2421.3 ± 0.6
$\Gamma(D_1^0)$, MeV	$38.8 \pm 5.0^{+1.9}_{-5.4}$	$53.2 \pm 7.2^{+3.3}_{-4.9}$	27.1 ± 2.7
$h(D_1^0)$	$7.8^{+6.7+4.6}_{-2.7-1.8}$	$5.9^{+3.0+2.4}_{-1.7-1.0}$	
$M(D_2^{*0})$, MeV	$2462.5 \pm 2.4^{+1.3}_{-1.1}$	$2469.1 \pm 3.7^{+1.2}_{-1.3}$	2462.6 ± 0.7
$\Gamma(D_2^{*0})$, MeV	$46.6 \pm 8.1^{+5.9}_{-3.8}$	43 fixed	49.0 ± 1.4
$h(D_2^{*0})$	-1 fixed	-1 fixed	
$D_1(2430)^0/D_1^0$	1.0 fixed	1.0 fixed	
$D_0^*(2400)^0/D_2^{*0}$	1.1 ± 1.1	1.7 fixed	
Feed-downs/D_2^{*0}	0.3 ± 0.4		

Table 6.1: *Results of the simultaneous fit for the yields (N), masses (M), widths (Γ) and helicity parameters (h) of the D_1^0 and D_2^{*0} mesons, for the ratios of the $D_1(2430)^0$ and $D_0^*(2400)^0$ to the D_1^0 and D_2^{*0} states, and for the ratio of the feed-downs (see text) to the $D_2^{*0} \to D^+\pi^-$. The $D_1(2430)^0$ and $D_0^*(2400)^0$ mass and width parameters used in the fit were fixed to the PDG [1] values. The results are compared to those of PDG [1].*

	$M(D_1^0)$, MeV	$\Gamma(D_1^0)$, MeV	$h(D_1^0)$	$M(D_2^{*0})$, MeV	$\Gamma(D_2^{*0})$, MeV	$h(D_2^{*0})$
This, [64]	$2423.1\pm1.5^{+0.4}_{-1.0}$	$38.8\pm5.0^{+1.9}_{-5.4}$	$7.8^{+6.7+4.6}_{-2.7-1.8}$	$2462.5\pm2.4^{+1.3}_{-1.1}$	$46.6\pm8.1^{+5.9}_{-3.8}$	-1.16 ± 0.35
PDG [1]	2421.3 ± 0.6	27.1 ± 2.7	5.72 ± 0.25	2462.6 ± 0.7	49.0 ± 1.4	
BaBar [62]	$2420.1\pm0.1\pm0.8$	$31.4\pm0.5\pm1.3$	5.72 ± 0.25	$2462.2\pm0.1\pm0.8$	$50.5\pm0.6\pm0.7$	-1^*
Belle [65]	$2426\pm3\pm1$	$24\pm7\pm8$				
Belle [15]	$2421.4\pm1.5\pm0.9$	$23.7\pm2.7\pm4.0$		$2461.6\pm2.1\pm3.3$	$45.6\pm4.4\pm6.7$	
Cleo-II [66]	$2421^{+1}_{-2}\pm2$	$20^{+6}_{-5}\pm3$	$2.74^{+1.40*}_{-0.93}$	$2465\pm3\pm3$	$28^{+8}_{-7}\pm6$	$-0.74^{+0.49*}_{-0.38}$
E687 [67]	$2422\pm2\pm2$	$15\pm8\pm4$		$2453\pm3\pm2$	$25\pm10\pm5$	
Cleo [68]	$2428\pm3\pm2$	23^{+8+10}_{-6-3}		$2461\pm3\pm1$	$20^{+9}_{-12}{}^{+9}_{-10}$	
Argus [69]	$2414\pm2\pm5$	$13\pm6^{+10}_{-5}$				
TPS [70]	$2428\pm8\pm5$	$58\pm14\pm10^*$		$2459\pm3\pm2$	$20\pm10\pm5$	
Zeus [56]	$2420.5\pm2.1\pm0.9^*$	$53.2\pm7.2^{+3.3*}_{-4.9}$	$5.9^{+3.0+2.4}_{-1.7-1.0}$	$2469.1\pm3.7^{+1.2*}_{-1.3}$		
CDF [71]	$2421.7\pm0.7\pm0.6^*$	$20.0\pm1.7\pm1.3$		$2463.3\pm0.6\pm0.8^*$	$49.2\pm2.3\pm1.3$	
Delphi [72]	$2425\pm3^*$			$2461\pm6^*$		
Focus [73]				$2464.5\pm1.1\pm1.9$	$38.7\pm5.3\pm2.9$	
BaBar [74]			$3.8\pm0.6\pm0.8^*$			
Model [10]	2417			2460		
Model [11]	2426			2460		
Model [12]	2425			2468		
No mixing			3			-1

Table 6.2: *Comparison of D_1^0 and D_2^{*0} mass, width and helicity parameter results of this analysis to other measurements, PDG averages and theoretical predictions. The most precise measurements are shaded in yellow. Measurements not used for PDG averages are marked with *.*

however, using only two masses it is impossible to discriminate between models (i.e. a certain model can give good predictions for D_1^0 and D_2^{*0} masses, but completely unsatisfactory predictions for higher states).

The D_1^0 width, $\Gamma(D_1^0) = 38.8 \pm 5.0(stat.)^{+1.9}_{-5.4}(syst.)$ MeV, is consistent with the PDG value [1] of 27.1 ± 2.7 MeV, and is in good agreement with the BaBar measurement [62] of $31.4 \pm 0.5 \pm 1.3$ MeV. However, the measured width of D_1^0 is much bigger than most of other measurements. and the origin of this discrepancy is unclear. The measurements of E687, Cleo-II, Cleo yield $\Gamma(D_1^0) = 15{-}23$ MeV and $\Gamma(D_2^{*0}) = 20 - 28$ MeV (i.e. both widths are significantly smaller than the PDG [1] averages), which can be an indication of underestimation of $\Gamma(D_1^0)$ and $\Gamma(D_2^{*0})$ due to systematic effects. On the other hand, the small values of $\Gamma(D_1^0)$ obtained by Belle [75] $\Gamma(D_1^0) = 23.7 \pm 2.7 \pm 4.0$ MeV and CDF [71] $\Gamma(D_1^0) = 20.0 \pm 1.7 \pm 1.3$ MeV are coupled with the values of $\Gamma(D_2^{*0}) = 46 - 50$ MeV and cannot be easily explained. One of the possible explanations for those results might be the difference in the functions used for the mass spectra fits: the analysis of Belle included the contributions from the virtual states of D^0 and B^{*0} (see details in Ref. [75]) and in the analysis of CDF [71] the signals were parametrised with non-relativistic Breit-Wigner functions.

The D_2^{*0} width, $\Gamma(D_2^{*0}) = 46.6 \pm 8.1(stat.)^{+5.9}_{-3.8}(syst.)$ MeV, is consistent with the PDG value [1] of 49.0 ± 1.4 MeV, and with the BaBar measurement of $50.5 \pm 0.6 \pm 0.7$ MeV.

The D_1^0 helicity parameter, $h(D_1^0) = 7.8^{+6.7}_{-2.7}(stat.)^{+4.6}_{-1.8}(syst.)$, is consistent with the BaBar value of $h(D_1^0) = 5.72 \pm 0.25$ and somewhat above the theoretical prediction of $h = 3$ and measurements by Cleo [76] with $h(D_1^0) = 2.74^{+1.40}_{-0.93}$. The simultaneous fit with $h(D_1^0)$ fixed to the theoretical prediction, $h(D_1^0) = 3$, yielded masses and widths of D_2^{*0} and D_1^0 that are somewhat away from the PDG values [1]. The simultaneous fit with $h(D_2^{*0})$ as a free parameter yielded similar results for all other free parameters with somewhat larger errors and with $h(D_2^{*0}) = -1.16 \pm 0.35$, in good agreement with the theoretical prediction of $h = -1$. As was discussed in Sec. 2, the helicity angular distribution for a $J^P = 1^+$ state with a mixture of D- and S-wave is

$$\frac{d\Gamma_{D_1}}{d\cos\alpha} \propto 1 + h\cos^2\alpha,$$

$$h = 3\frac{1 - r - 2\sqrt{2r(1-r)}\cos\phi}{1 + r + 2\sqrt{2r(1-r)}\cos\phi},$$

where $r = \Gamma_S/(\Gamma_S + \Gamma_D)$, $\Gamma_S(\Gamma_D)$ is the $S(D)$-wave partial width and ϕ is relative phase between the two amplitudes. The range of the measured $h(D_1^0)$ restricted to one standard deviation is shown in Fig. 6.1 in a plot of $\cos\phi$ versus r. A similar measurement by the BELLE collaboration [65] is consistent with a pure D-wave, i.e. $\Gamma_S/(\Gamma_S + \Gamma_D) = 0$.

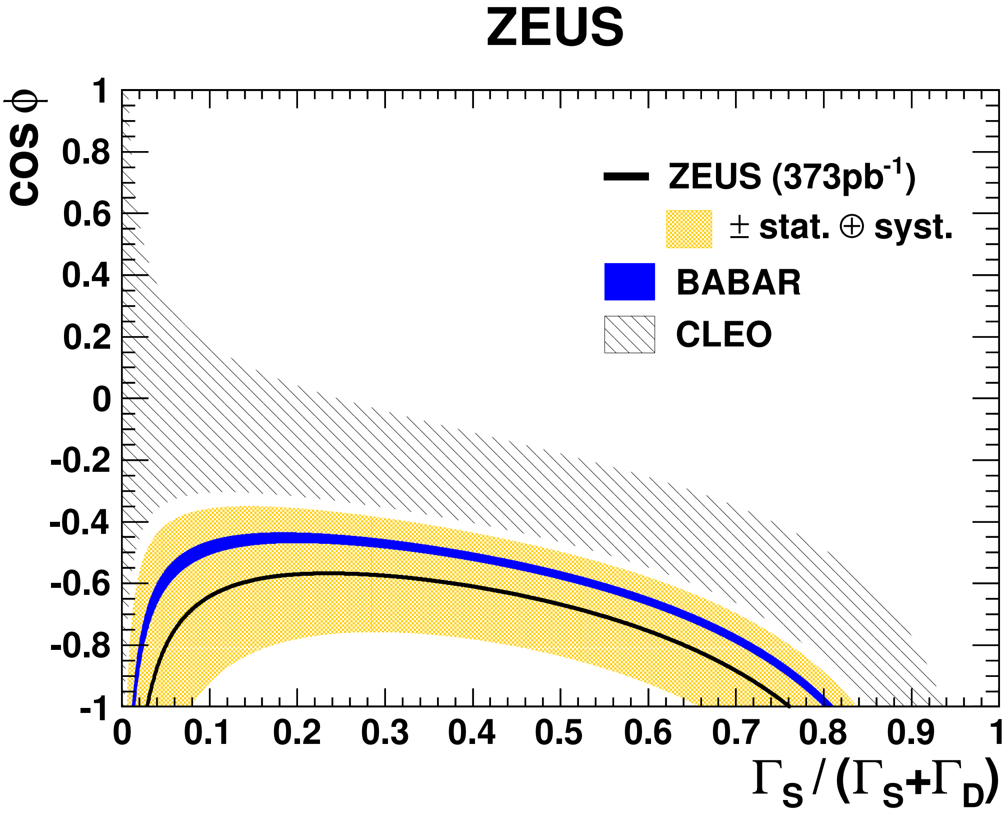

Figure 6.1: *The allowed region of $\cos\phi$, where ϕ is the relative phase of S- and D-wave amplitudes, versus the fraction of S-wave in the $D_1^0 \to D^*\pi$ decay for* ZEUS, BABAR *and* CLEO *measurements.*

A particular interest has a comparison of obtained results to those of HERA-I analysis. In addition to some discrepancy of $M(D_2^{*0})$ and $\Gamma(D_1^0)$ values, there is a discrepancy of the relative yields of D_1^0 and D_2^{*0} states in the $D^{*+}\pi$ spectrum. The ratio of the two yields and approximate uncertainty (the correlation coefficient obtained from the fit is $\rho = -0.39$) is

$$R_{\mathrm{HERA-II}} = \frac{N(D_1^0 \to D^{*+}\pi)}{N(D_2^{*0} \to D^{*+}\pi)} = 1.52 \pm 0.34$$

for the HERA-II analysis and

$$R_{\mathrm{HERA-I}} = \frac{N(D_1^0 \to D^{*+}\pi)}{N(D_2^{*0} \to D^{*+}\pi)} = 3.57 \pm 0.92$$

for the HERA-I analysis (assuming $\rho = -0.39$ as for HERA-II). However, it was suggested that the discrepancies HERA-I vs. HERA-II for $M(D_2^{*0})$, $\Gamma(D_1^0)$ and R might be correlated. To check this assumption, a fit of HERA-II spectrum was performed with D_1^0 and D_2^{*0} masses and widths fixed to the HERA-I values. The fit yielded $N(D_1^0 \to D^{*+}\pi) = 1650 \pm 155$, $N(D_1^0 \to D^{*+}\pi) = 3314 \pm 168$ and $R = 2.01 \pm 0.25$. The obtained value $R = 2.01 \pm 0.25$ indicates that the difference between $R_{\mathrm{HERA-I}}$ and $R_{\mathrm{HERA-II}}$ is correlated with smaller value of $\Gamma(D_1^0)$ in the HERA-II analysis and related to the better description of the D_2^{*0} resonance, which became possible with refined reconstruction of this state in the $D^+\pi$ channel.

6.2 Charged excited charm mesons in the $D^0\pi^+$ spectrum

To extract the signals of the charged excited charm mesons, a χ^2 fit was performed using the $M(D^0\pi_a)$ distribution shown in Fig. 5.7. The fit included:

- the background contribution;
- the signal of $D_2^{*+}(2460)$;
- the feed-downs of the $D_1^+(2420)$ and $D_2^{*+}(2460)$ states.

The background for the $D^0\pi^+$ mode has been parametrised with **four** parameters a, b, c, d as $B(x) = ax^b \exp(-cx - dx^2)$, where $x = \Delta M^{\mathrm{ext}} - M_{\pi^+}$).

The $D_2^{*+}(2460)$ signal was fitted to relativistic Breit-Wigner distributions convoluted with the appropriate resolution function. Because of low statistics, only **two** signal parameters were free in the fit: the mass $M(D_2^{*+}(2460))$ and the yield $N(D_2^{*+}(2460) \to D^0\pi^+)$. The width $\Gamma(D_2^{*+}(2460))$ was set to the PDG value and the helicity parameter $h(D_2^{*+}(2460))$ to the HQET prediction, $h(D_2^{*+}(2460)) = -1$ (see Sec. 2).

	HERA-II [64](this)	PDG [1]
$N(D_1^+ \to D^{*0}\pi^+)$	759 ± 183	
$N(D_2^{*+} \to D^{*0}\pi^+)$	634 ± 223	
$N(D_2^{*+} \to D^0\pi^+)$	737 ± 164	
$M(D_1^+)$, MeV	$2421.9 \pm 4.7^{+3.4}_{-1.2}$	2423.4 ± 3.1
$\Gamma(D_1^+)$, MeV	25 fixed	25 ± 6
$h(D_1^+)$	3 fixed	
$M(D_2^{*+})$, MeV	$2460.6 \pm 4.4^{+3.6}_{-0.8}$	2464.4 ± 1.9
$\Gamma(D_2^{*+})$, MeV	37 fixed	37 ± 6
$h(D_2^{*+})$	-1 fixed	

Table 6.3: *Results for the yields (N) and masses (M) of the D_1^+ and D_2^{*+} mesons; widths (Γ) and helicity parameters (h) used in the fit. The results are compared to those of PDG [1].*

The feed-down shapes were modelled as described in Sec. 11 and convoluted with the appropriate resolution function. The detailed description of the convolution procedure for signals and feed-downs can be found in Sec. 11. The masses, widths and helicity parameters of feed-downs were the same as for the signal, implying **three** free parameters for the description of the feed-downs $N(D_2^{*+}(2460) \to D^{*0}\pi^+)$, $N(D_1^+(2420) \to D^{*0}\pi^+)$ and $M(D_1^+(2420))$. The width $\Gamma(D_1^+(2420))$ was set to the PDG value and the helicity parameter $h(D_2^+(2420))$ to the HQET predictions $h(D_1^+(2420)) = 3$ (see Sec. 2).

The fit results are shown in Tab. 6.3 together with the parameters used in the fits. The given systematic uncertainties are discussed in Sec. 9.

The measured masses $M(D_1^+) = 2421.9 \pm 4.7(stat.)^{+3.4}_{-1.2}(syst.)$ MeV and $M(D_2^{*+}) = 2460.6 \pm 4.4(stat.)^{+3.6}_{-0.8}(syst.)$ MeV agree to the average values from PDG [1] $M(D_1^+) = 2423.4 \pm 3.1$ MeV and $M(D_2^{*+}) = 2464.4 \pm 2.9$ MeV and to many other measurements (see Tab. 6.4). The measurements of $M(D_1^+)$ and $M(D_2^{*+})$ have a precision comparable to the measurements from other experiments. The theoretical predictions for the D_1^+ and D_2^{*+} masses in general agree (within $3-4$ MeV) to the measurements and PDG values, as is in the case for neutral states.

	$M(D_2^{*+})$, MeV	$\Gamma(D_2^{*+})$, MeV	$h(D_2^{*+})$	$M(D_1^+)$, MeV	$\Gamma(D_1^+)$, MeV	$h(D_1^+)$
This, [64]	$2460.6\pm4.4^{+3.6}_{-0.8}$			$2421.9\pm4.7^{+3.4}_{-1.2}$		
PDG [1]	2464.4 ± 1.9	37 ± 6		2423.4 ± 3.1	25 ± 6	
BaBar [62]	$2465.4\pm0.2\pm1.1$					
Belle [65]				$2421\pm2\pm1$	$21\pm5\pm8$	
E687 [67]	$2463\pm3\pm3$	$27^{+11}_{-8}\pm5$		$2425\pm2\pm2$	$26^{+8}_{-7}\pm4$	
TPS [70]				$2443\pm7\pm5$	$41\pm19\pm8$	
BaBar [77]	$2460.4\pm1.2\pm2.2$	$41.8\pm2.5\pm2.9$				
Focus [73]	$2467.6\pm1.5\pm0.8^{*}$	$34.1\pm6.5\pm4.2$				
Argus [78]	$2455\pm3\pm5$	15^{+13+5}_{-10-10}				
BBCNC [79]	2466 ± 7					
Belle [75]	$2465.7\pm1.8^{+1.4}_{-4.8}$	$49.7\pm3.8\pm6.4$				
Argus [80]	$2469\pm4\pm6$					
Model [10]	2460			2417		
Model [11]	2460			2426		
Model [12]	2468			2425		
No mixing			-1			3

Table 6.4: *Comparison of D_1^+ and D_2^{*+} mass results of this analysis to other measurements, PDG averages and theoretical predictions. The most precise measurements are shaded in yellow. The measurements not used for PDG averages are marked with *.*

6.3 Strange excited charm mesons in the $D^{*+}K^0_S$ and D^0K^+ spectra

To extract the signals of the excited strange charm mesons, a χ^2 fit was performed using simultaneously the $M(D^0K_a)$ distribution shown in Fig. 5.8(b)) and the $M(D^{*+}K^0_S)$ distributions in four helicity bins shown in Fig. 5.9.

For the $D^{*+}K^0_S$ spectrum the fit included:

- the background contribution;
- the signal of $D^+_{s1}(2535)$ state.

For the D^0K^+ spectrum the fit included:

- the background contribution;
- the $D^{*+}_{s2}(2573)$ signal;
- the feed-downs from the $D^+_{s1}(2535)$ and $D^{*+}_{s2}(2573)$ states.

The background for $D^{*+}K^0_S$ mode was parametrised with **four** parameters a_1, b_1, c_1, d_1 as $B(x) = a_1x^{b_1}\exp(-c_1x - d_1x^2)$, where $x = \Delta M^{\text{ext}} - M_{K^0_S}$. The same background function was used in all helicity bins. The background for D^0K^+ mode was parametrised with **four** parameters a_2,b_2,c_2,d_2 as $B(x) = a_2x^{b_2}\exp(-c_2x - d_2x^2)$, where $x = \Delta M^{\text{ext}} - M_{K^+}$.

The signals were fitted to the relativistic Breit-Wigner distributions convoluted with the appropriate resolution function. The mass resolution in both spectra was not sufficient for the measurement of the small D^+_{s1} width. In the fit this width was fixed to the PDG [1] value. The observed signals of D^{*+}_{s2} were not significant enough for any measurement, so the width and the mass of D^{*+}_{s2} state were set to the PDG [1] values and the helicity parameter to the HQET predictions $h(D^{*+}_{s2}) = -1$ (see Sec. 2). The following **four** signal parameters were free in the fit: $N(D^+_{s1}) \to D^{*+}K^0_S$, $M(D^+_{s1})$, $h(D^+_{s1})$ and $N(D^{*+}_{s2} \to D^0K^+)$.

The feed-down shapes were modelled as described in Sec. 11 and convoluted with the appropriate resolution function. The detailed description of the convolution for both modes can be found in Sec. 11. The masses, widths and helicity parameters of feed-downs were the same as for the signals. Only **two** feed-down yields were free in the fit: $N(D^+_{s1}) \to D^{*0}K^+$ and $N(D^{*+}_{s2}) \to D^{*0}K^+$. The fit results are shown in Tab. 6.5 together with the parameters used in the fits. The results are compared to the previous Zeus publication [56] (Hera-I) and the PDG [1]. The given systematical uncertainties are discussed in Sec. 9.

	Hera-II (this)	Hera-I [56]	PDG [1]
$N(D^+_{s1} \to D^{*+}K^0_S)$	110 ± 20	100 ± 13	
$N(D^+_{s1} \to D^{*0}K^+$	306 ± 64	136 ± 27	
$N(D^{*+}_{s2} \to D^0K)$	132 ± 194		
$N(D^{*+}_{s2} \to D^{*0}K^+)$	65 ± 125		
$M(D^+_{s1}),$ MeV	$2535.37 \pm 0.45^{+0.18}_{-0.22}$	$2535.57^{+0.44}_{-0.41} \pm 0.10$	2535.12 ± 0.13
$\Gamma(D^+_{s1}),$ MeV	0.9 fixed		0.92 ± 0.05
$h(D^+_{s1})$	$0.09 \pm 0.58^{+0.52}_{-0.43}$	$-0.74^{+0.23+0.06}_{-0.17-0.05}$	
$M(D^{*+}_{s2}),$ MeV	2571.9 fixed		2571.9 ± 0.8
$\Gamma(D^{*+}_{s2}),$ MeV	17 fixed		17 ± 4
$h(D^{*+}_{s2})$	-1 fixed		

Table 6.5: *Results of the simultaneous fit for the D^+_{s1}, D^{*+}_{s2} yields (N), mass (M), and helicity parameter (h) of the D^+_{s1} meson. The values of D^+_{s1}, D^{*+}_{s2} widths, D^{*+}_{s2} mass and helicity parameter used in the fit were fixed to the PDG [1] values. The results are compared to the PDG [1].*

The measured mass $M(D^+_{s1}) = 2535.37 \pm 0.45(stat.)^{+0.18}_{-0.49}(syst.)$ MeV agrees with the average values from PDG [1] $M(D^+_{s1}) = 2535.12 \pm 0.13$ MeV and to other measurements listed in Tab. 6.6, including the previous Zeus measurement [56] $M(D^+_{s1}) = 2535.57^{+0.44}_{-0.41} \pm 0.10$ MeV. The theoretical predictions of D^+_{s1} agree with the measurements very well (see Tab. 6.6).

The measured D^+_{s1} helicity parameter $h(D^+_{s1}) = 0.09 \pm 0.58^{+0.52}_{-0.43}$ allows for some S- and D-wave mixing in its decay to $D^{*+}K^0_S$ (see Fig. 6.2). The result agrees very well with the Cleo measurement $h(D^+_{s1}) = -0.23^{+0.40}_{-0.32}$, consistent with the previous Zeus result $h(D^+_{s1}) = -0.74^{+0.23+0.06}_{-0.17-0.05}$ and contradicts the pure D-wave hypothesis $h(D^+_{s1}) = 3$.

	$M(D_{s1}^{+})$, MeV	$\Gamma(D_{s1}^{+})$, MeV	$h(D_{s1}^{+})$
This, [64]	$2535.37{\pm}0.45^{+0.18}_{-0.49}$		$0.09 \pm 0.58^{+0.52}_{-0.43}$
PDG [1]	2535.12 ± 0.13	0.92 ± 0.05	
E687 [67]	$2535{\pm}0.6{\pm}1$	< 3.2	
Cleo [68]	$2536.6{\pm}0.7{\pm}0.4$	< 5.44	
Zeus [56]	$2535.57^{+0.44}_{-0.41}{\pm}0.10^{*}$		$-0.74^{+0.23+0.06}_{-0.17-0.05}$
D0 [81]	$2535.7{\pm}0.6{\pm}0.5$		
BaBar	$2534.78{\pm}0.31{\pm}0.40$		
BaBar [82]	$2534.6{\pm}0.3{\pm}0.7$	< 2.5	
Aleph [83]	$2535.3{\pm}0.7$		
BBCNC [84]	$2534.2{\pm}1.2$		
Cleo [85]	$2535.3{\pm}0.2{\pm}0.5$	< 2.3	
Cleo [85]	$2534.8{\pm}0.6{\pm}0.6$		$-0.23^{+0.40}_{-0.32}$
Argus [86]	$2535.2{\pm}0.5{\pm}1.5$	< 3.9	
Argus [87]	$2535.9{\pm}0.6{\pm}2.0$	< 4.6	
Belle [88]	$2534.1{\pm}0.6^{*}$	$0.75{\pm}0.23$	
BaBar [89]	$2535.08{\pm}0.01{\pm}0.15^{*}$	$0.92{\pm}0.03{\pm}0.04$	
HLBC [90]	$2535{\pm}28^{*}$		
Model [10]	2535		
Model [11]	2536		
No mixing			3.0

Table 6.6: *Comparison of D_{s1}^{+} mass and helicity parameter results of this analysis to other measurements, PDG averages and theoretical predictions. The most precise measurements are shaded in yellow. The measurements not used for PDG averages are marked with *.*

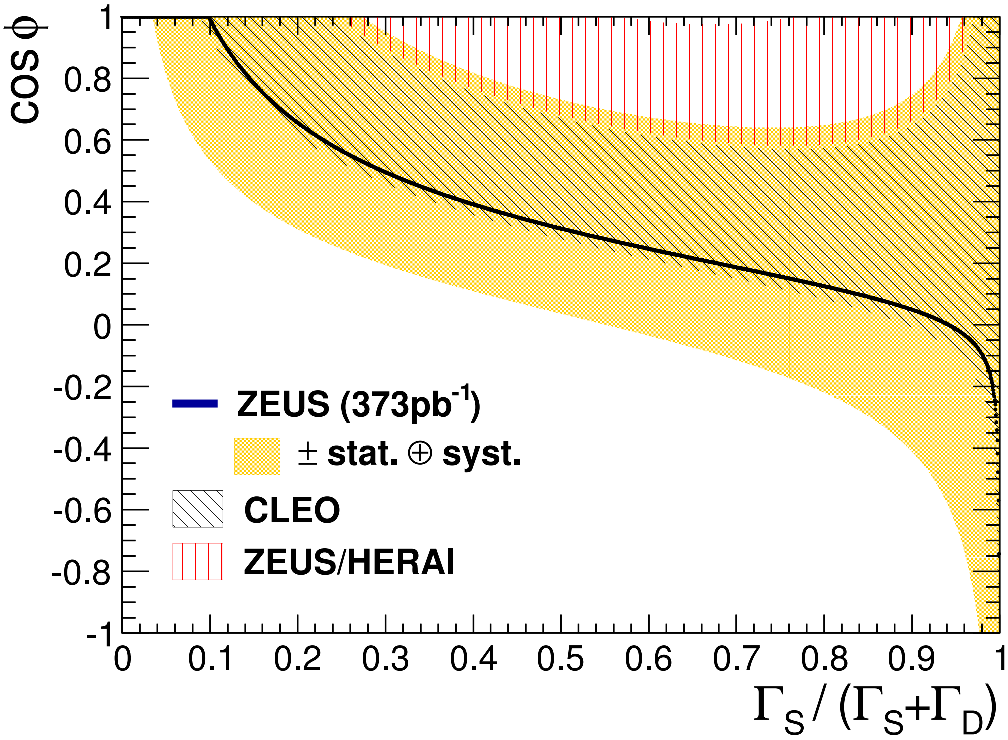

Figure 6.2: *The allowed region of* $\cos\phi$*, where* ϕ *is the relative phase of* S*- and* D*-wave amplitudes, versus the fraction of* S*-wave in the* $D_{s1}^+ \to D^{*+}K_S^0$ *decay for* ZEUS*,* ZEUS/HERA-I *and* CLEO *measurements.*

6.4 Searches for other excited charm mesons

In a recent paper [62] the BABAR Collaboration searched for excited D meson states in $e^+e^- \to c\bar{c} \to D^{(*)}\pi + X$ with very large statistics. In addition to the D_1^0 and D_2^{*0} resonances, BABAR observed two new structures near 2.6 GeV in the $D^+\pi^-$ and $D^{*+}\pi^-$ mass distributions, $D(2550)^0$ and $D^*(2600)^0$, and interpreted them as being radial excitations of the well-known D^0 and D^{*0}, respectively (see Fig. 6.3). In this analysis, a small enhancement of events above the background is seen in the region near 2.6 GeV in the $M(D^{*+}\pi^-)$ distribution (Figs. 5.5(a), 5.6). However, the fit with $D(2550)^0$ and $D^*(2600)^0$ states yielded insignificant signals (see Fig. 6.4, Tab. 6.7) and did not significantly change the results of the other fit parameters. The χ^2 change for the two extra degrees of freedom was 3.5, not large enough to be evidence for $D(2550)^0$ and/or $D^*(2600)^0$ production in ZEUS.

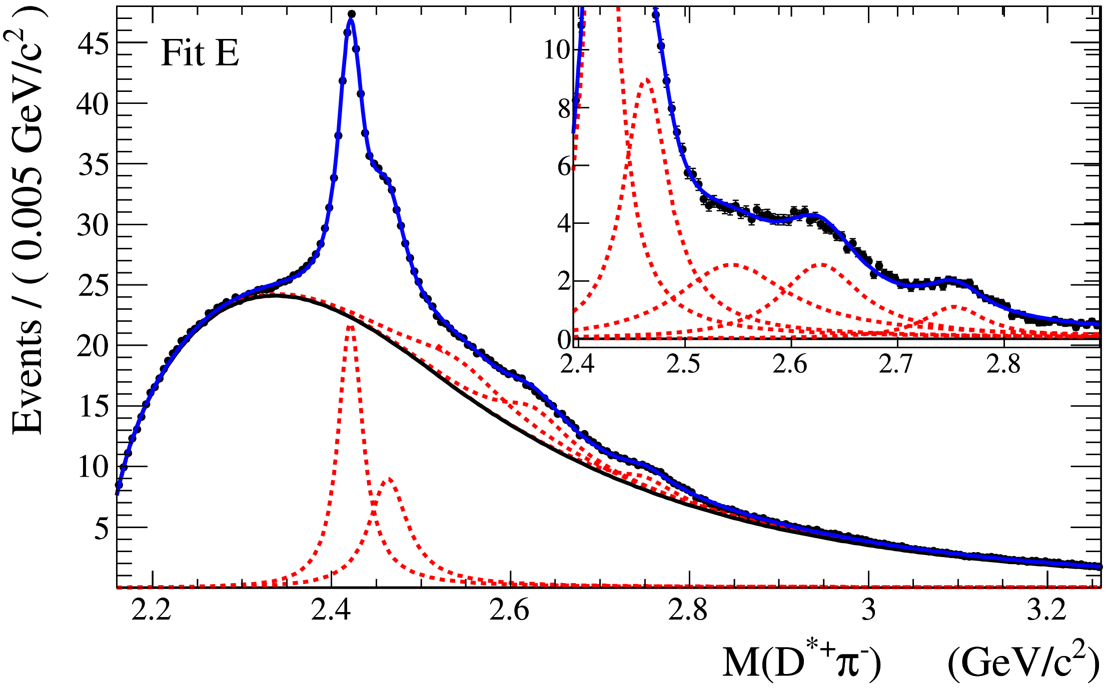

Figure 6.3: *$M(D^{*+}\pi)$ mass spectrum from BaBar [62]. Fit (top solid curve) of the data (points) to the sum of signals (dots) and background (bottom solid curve). The inset plots show the distributions after the background subtraction.*

	Hera-II (this)	PDG [1]
$N(D(2550)^0 \to D^{*+}\pi)$	378 ± 199	
$N(D(2600)^0 \to D^{*+}\pi)$	113 ± 224	
$M(D(2550)^0)$, MeV	2539(fixed)	2539 ± 8
$\Gamma(D(2550)^0)$, MeV	130(fixed)	130 ± 18
$h(D(2550)^0)$, MeV	-1(fixed)	
$M(D(2600)^0)$, MeV	2612(fixed)	2612 ± 6
$\Gamma(D(2600)^0)$, MeV	93(fixed)	93 ± 14
$h(D(2600)^0)$, MeV	∞(fixed)	

Table 6.7: *Results of the simultaneous fit for the yields (N), masses (M), widths (Γ) and helicity parameters (h) of the $D(2550)^0$, $D(2600)^0$, mesons.*

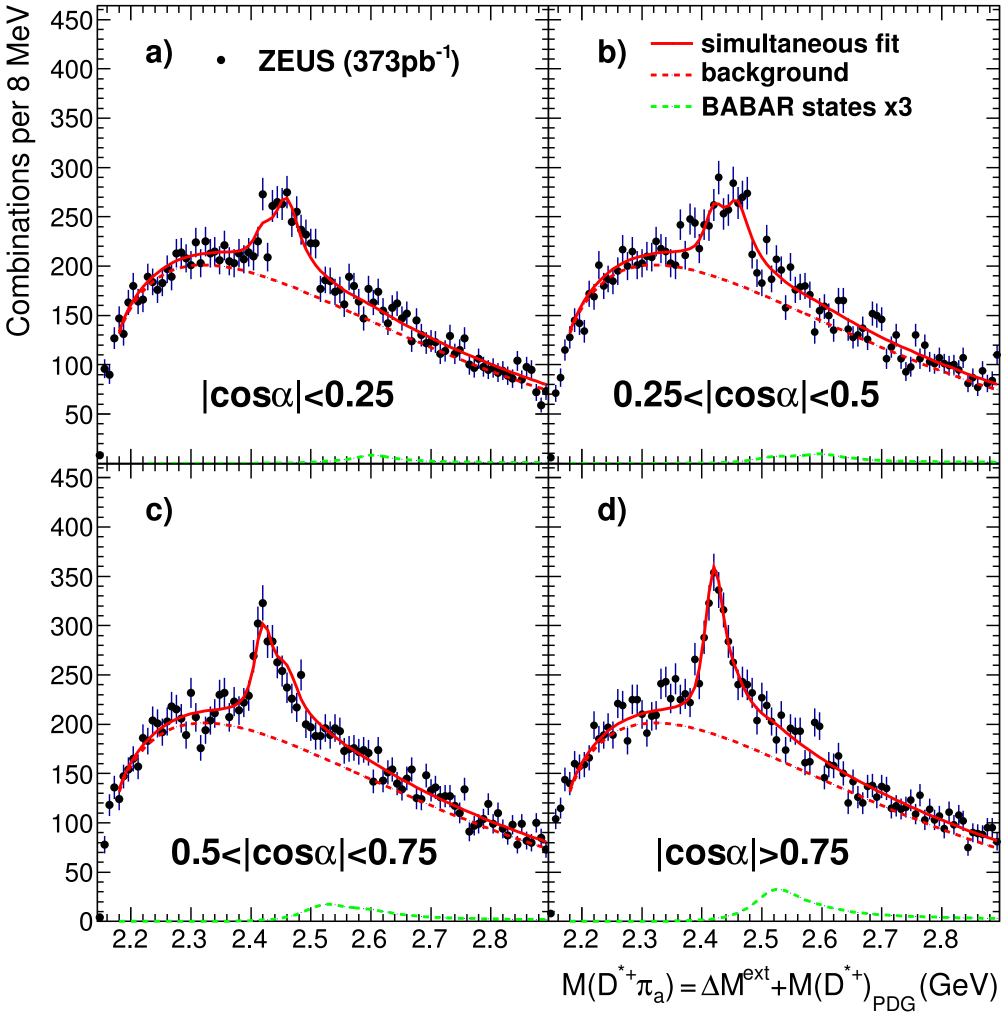

Figure 6.4: *The mass distributions (dots) $M(D^{*+}\pi_a)$ in four helicity intervals: (a) $|\cos\alpha| < 0.25$; (b) $0.25 < |\cos\alpha| < 0.50$; (c) $0.50 < |\cos\alpha| < 0.75$; (d) $|\cos\alpha| > 0.75$. The solid curves are the result of the simultaneous fit to D_1^0, D_2^{*0}, $D(2550)^0$ and $D(2600)^0$ plus background function (dashed curves). The $D(2550)^0$ and $D(2600)^0$ signal distributions (dotted curves) scaled by factor 3.*

7 Excited charm meson fragmentation fractions

The calculation of charm fragmentation fractions requires the number of produced charm quarks and corresponding charm mesons. While the measurement of the number of produced charm mesons is a straightforward procedure as described in Sec. 5, it is not so easy to estimate the number of produced charm quarks. Various techniques can be used for this, but a technique based on charm meson tagging has important advantages, which help to make the measurement more precise. Firstly it does not require luminosity and the secondly – it exploits the well measured charm fragmentation fractions of the D^0, D^* and D^+ mesons. This chapter describes the calculation procedure for charm quark fragmentation fractions to excited-mesons using D^0, D^* and D^+ charm-meson tagging.

7.1 Calculations of fragmentation fractions

The fragmentation fractions of charmed mesons are defined as:

$$\begin{aligned} f(c \to D_1^0) &= \frac{N(D_1^0)}{N(c)},\ f(c \to D_2^{*0}) = \frac{N(D_2^{*0})}{N(c)}, \\ f(c \to D_1^+) &= \frac{N(D_1^+)}{N(c)},\ f(c \to D_2^{*+}) = \frac{N(D_2^{*+})}{N(c)}, \\ f(c \to D^+) &= \frac{N(D^+)}{N(c)},\ f(c \to D^{*+}) = \frac{N(D^{*+})}{N(c)}, \\ f(c \to D^0) &= \frac{N(D^0)}{N(c)},\ f(c \to D^{*0}) = \frac{N(D^{*0})}{N(c)}, \end{aligned} \tag{7.1}$$

where $N(c)$ is the true number of charm quarks in the data and $N(D_1^+)$, $N(D_2^{*+})$, $N(D^0)$, $N(D^{*0})$ etc. stand for the true number of corresponding charm mesons. The number of c quarks in the same sample can be tagged with different mesons:

$$N(c) = \frac{N(D^0)}{f(c \to D^0)} = \frac{N(D^{*0})}{f(c \to D^{*0})} = \dots \tag{7.2}$$

The number of D mesons can be measured if the branching ratio for a corresponding decay is known, e.g.:

$$N(D) = \frac{N(D \to X)}{\mathcal{B}_{D\to X}} = \frac{N(D \to Y)}{\mathcal{B}_{D\to Y}} = \frac{N(D \to Z)}{\mathcal{B}_{D\to Z}} = \dots$$

The use of the two (or more) decay modes can improve the precision of the measurement or make it simpler. In this case

$$N(D) = \frac{N(D \to X) + N(D \to Y)}{\mathcal{B}_{D\to X} + \mathcal{B}_{D\to Y}}.$$

Consider decays of excited mesons. For the decays $D_2^{*+} \to D^{*0}\pi^+$, $D_1^+ \to D^{*0}\pi^+$ and $D_2^{*+} \to D^0\pi^+$

$$N(D_1^+) = \frac{N(D_1^+ \to D^{*0}\pi^+)}{\mathcal{B}_{D_1^+\to D^{*0}\pi^+}},$$

$$N(D_2^{*+}) = \frac{N(D_2^{*+} \to D^{*0}\pi^+) + N(D_2^{*+} \to D^0\pi^+)}{\mathcal{B}_{D_2^{*+}\to D^{*0}\pi^+} + \mathcal{B}_{D_2^{*+}\to D^0\pi^+}}.$$

As the D^{*0} decays to D^0 with probability 100% [1]

$$N(D_1^+ \to D^{*0}\pi^+) = N(D_1^+ \to D^{*0}\pi^+, D^{*0} \to D^0\pi^0/\gamma),$$

$$N(D_2^{*+} \to D^{*0}\pi^+) = N(D_2^{*+} \to D^{*0}\pi^+, D^{*0} \to D^0\pi^0/\gamma),$$

and

$$N(D_2^{*+}) = \frac{N(D_2^{*+} \to D^{*0}\pi^+, D^{*0} \to D^0\pi^0/\gamma) + N(D_2^{*+} \to D^0\pi^+)}{\mathcal{B}_{D_2^{*+}\to D^{*0}\pi^+} + \mathcal{B}_{D_2^{*+}\to D^0\pi^+}}, \tag{7.3}$$

$$N(D_1^+) = \frac{N(D_1^+ \to D^{*0}\pi^+, D^{*0} \to D^0\pi^0/\gamma)}{\mathcal{B}_{D_1^+\to D^{*0}\pi^+}}. \tag{7.4}$$

The combination of Eqs. (7.3), (7.4) and Eq. (7.1) gives

$$f(c \to D_1^+) = \frac{f(c \to D^0)}{N(D^0)} \frac{N(D_1^+ \to D^{*0}\pi^+, D^{*0} \to D^0\pi^0/\gamma)}{\mathcal{B}_{D_1^+\to D^{*0}\pi^+}}, \tag{7.5}$$

$$f(c \to D_2^{*+}) = \frac{f(c \to D^0)}{N(D^0)} \frac{N(D_2^{*+} \to D^{*0}\pi^+, D^{*0} \to D^0\pi^0/\gamma) + N(D_2^{*+} \to D^0\pi^+)}{\mathcal{B}_{D_2^{*+} \to D^{*0}\pi^+} + \mathcal{B}_{D_2^{*+} \to D^0\pi^+}}. \tag{7.6}$$

For neutral excited mesons, the expression for $f(c \to D_1^0)$ is obtained from Eq. (7.1). using D^{*+} meson tagging:

$$N(c) = \frac{N(D^{*+})}{f(c \to D^{*+})},$$

$$f(c \to D_1^0) = \frac{f(c \to D^{*+})}{N(D^*)} \frac{N(D_1^0 \to D^{*+}\pi^-)}{\mathcal{B}_{D_1^0 \to D^{*+}\pi^-}}. \tag{7.7}$$

The samples for reconstruction of $D_1^0, D_2^{*0} \to D^{*+}\pi^-$ and $D_2^{*0} \to D^+\pi^-$ decays are different; they contain a fully reconstructed D^{*+} or D^+ respectively. Thus they contain different numbers of charm quarks. Consider two samples of events used for reconstruction of $D_2^{*0} \to D^{*+}\pi^-/D_1^0 \to D^{*+}\pi^-$(I) and $D_2^{*0} \to D^+\pi^-$(II) decay chains. From the definition in Eqs. (7.1), (7.2) for samples (I) and (II):

$$f(c \to D_2^{*0}) = \frac{N(D_2^{*0} \to D^{*+}\pi^-)}{N_I(c)\mathcal{B}_{D_2^{*0} \to D^{*+}\pi^-}}$$

$$f(c \to D_2^{*0}) = \frac{N(D_2^{*0} \to D^+\pi^-)}{N_{II}(c)\mathcal{B}_{D_2^{*0} \to D^+\pi^-}}$$

Moving branching ratios to the left and adding the equations gives:

$$f(c \to D_2^{*0})(\mathcal{B}_{D_2^{*0} \to D^+\pi^-} + \mathcal{B}_{D_2^{*0} \to D^{*+}\pi^-}) = \frac{N(D_2^{*0} \to D^{*+}\pi^-)}{N_I(c)} + \frac{N(D_2^{*0} \to D^+\pi^-)}{N_{II}(c)}$$

Expressing $N_I(c)$ and $N_{II}(c)$ with $N(D^{*+})$ and $N(D^+)$:

$$f(c \to D_2^{*0}) = \frac{\frac{N(D_2^{*0} \to D^{*+}\pi^-)}{N(D^{*+})} f(c \to D^{*+}) + \frac{N(D_2^{*0} \to D^+\pi^-)}{N(D^+)} f(c \to D^+)}{\mathcal{B}_{D_2^{*0} \to D^+\pi^-} + \mathcal{B}_{D_2^{*0} \to D^{*+}\pi^-}} \tag{7.8}$$

For the case of charm-strange excited mesons, the expression for $f(c \to D_{s1}^+)$ is obtained in a similar way, using samples with $D_{s1}^+ \to D^{*0}K^+$(I) and $D_{s1}^+ \to D^{*+}K_S^0$(II) decays.

From the definition in Eqs. (7.1), (7.2) for samples (I) and (II):

$$f(c \to D_{s1}^+) = \frac{N(D_{s1}^+ \to D^{*0}K^+)}{N_I(c)\mathcal{B}_{D_{s1}^+ \to D^{*0}K^+}}$$
$$f(c \to D_{s1}^+) = \frac{N(D_{s1}^+ \to D^{*+}K_S^0)}{N_{II}(c)\mathcal{B}_{D_{s1}^+ \to D^{*+}K_S^0}}$$

Moving branching ratios to the left and adding the equations we have:

$$f(c \to D_{s1}^+)(\mathcal{B}_{D_{s1}^+ \to D^{*0}K^+} + \mathcal{B}_{D_{s1}^+ \to D^{*+}K_S^0}) = \frac{N(D_{s1}^+ \to D^{*0}K^+)}{N_I(c)} + \frac{N(D_{s1}^+ \to D^{*+}K_S^0)}{N_{II}(c)}$$

Expressing $N_I(c)$ and $N_{II}(c)$ with $N(D^{*+})$ and $N(D^0)$:

$$f(c \to D_{s1}^+) = \frac{\frac{N(D_{s1}^+ \to D^{*+}K_S^0)}{N(D^{*+})} f(c \to D^{*+}) + \frac{N(D_{s1}^+ \to D^{*0}K^+)}{N(D^0)} f(c \to D^0)}{\mathcal{B}_{D_{s1}^+ \to D^{*0}K^+} + \mathcal{B}_{D_{s1}^+ \to D^{*+}K_S^0}} \tag{7.9}$$

The branching ratios in Eqs. (7.7), (7.8), (7.5), (7.6) are not known, but can be estimated assuming isospin conservation in excited charm strong decays. The isospin parts of the wave function with decomposition with Clebsch-Gordan coefficients [1] of π and D mesons are given in Tab. 7.1: The isospin part of the wave functions $|I, I_z\rangle$ of the excited charm states are given in Tab. 7.2:

For each transition between initial and final state, the branching ratio in this approximation can be calculated as:

$$\sum \mathcal{B}_{I,I_z \to I',I'_z} = |\langle I, I_z | 1 | I', I'_z \rangle|^2,$$

where the sum is taken for all final states with certain I' and I'_z.

Neglecting the non-dominant decays $D_1^0 \to D^0\pi\pi$ and $D_1^+ \to D^+\pi\pi$, the branching ratios of D_1^0 and D_1^+ decays are:

$$\mathcal{B}_{D_1^0 \to D^{*+}\pi^-} = |\langle 1/2, -1/2 | 1 | 1/2, 1/2 \rangle \otimes |1, -1\rangle|^2 = 2/3$$
$$\mathcal{B}_{D_1^+ \to D^{*0}\pi^+} = |\langle 1/2, 1/2 | 1 | 1/2, -1/2 \rangle \otimes |1, 1\rangle|^2 = 2/3$$

State	$\|I, I_z\rangle$
$\|\pi^+\rangle$	$\|1,1\rangle$
$\|\pi^-\rangle$	$\|1,-1\rangle$
$\|D^0\rangle$	$\|1/2,-1/2\rangle$
$\|D^{*0}\rangle$	$\|1/2,-1/2\rangle$
$\|D_1^0\rangle$	$\|1/2,-1/2\rangle$
$\|D_2^{*0}\rangle$	$\|1/2,-1/2\rangle$
$\|D^+\rangle$	$\|1/2,1/2\rangle$
$\|D^{*+}\rangle$	$\|1/2,1/2\rangle$
$\|D_1^+\rangle$	$\|1/2,1/2\rangle$
$\|D_2^{*+}\rangle$	$\|1/2,1/2\rangle$

Table 7.1: *Isospin states of π and D mesons.*

State	$\|I', I'_z\rangle$
$\|D^0\rangle \otimes \|\pi^+\rangle$	$\|1/2,-1/2\rangle \otimes \|1,1\rangle = \sqrt{\frac{2}{3}}\|1/2,1/2\rangle + \sqrt{\frac{1}{3}}\|3/2,1/2\rangle$
$\|D^{*0}\rangle \otimes \|\pi^+\rangle$	$\|1/2,-1/2\rangle \otimes \|1,1\rangle = \sqrt{\frac{2}{3}}\|1/2,1/2\rangle + \sqrt{\frac{1}{3}}\|3/2,1/2\rangle$
$\|D^+\rangle \otimes \|\pi^-\rangle$	$\|1/2,1/2\rangle \otimes \|1,-1\rangle = -\sqrt{\frac{2}{3}}\|1/2,-1/2\rangle + \sqrt{\frac{1}{3}}\|3/2,-1/2\rangle$
$\|D^{*+}\rangle \otimes \|\pi^-\rangle$	$\|1/2,1/2\rangle \otimes \|1,-1\rangle = -\sqrt{\frac{2}{3}}\|1/2,-1/2\rangle + \sqrt{\frac{1}{3}}\|3/2,-1/2\rangle$

Table 7.2: *Isospin decomposition of excited charm states.*

Similarly,

$$\mathcal{B}_{D_2^{*0}\to D^+\pi^-} + \mathcal{B}_{D_2^{*0}\to D^{*+}\pi^-} = |\langle 1/2,-1/2|1|1/2,1/2\rangle \otimes |1,-1\rangle|^2 = 2/3$$
$$\mathcal{B}_{D_2^{*+}\to D^0\pi^+} + \mathcal{B}_{D_2^{*0}\to D^{*0}\pi^+} = |\langle 1/2,1/2|1|1/2,-1/2\rangle \otimes |1,1\rangle|^2 = 2/3$$

The formulae above are correct in case of no kinematic restrictions on decay products. In case of restricted kinematic space, some corrections should be applied. The corrections can be estimated from fragmentation functions of charm-quark mesons e.g. using theoretical calculations or phenomenological models of fragmentation. The second choice is much more robust, and therefore the correction factors were calculated using the Lund string fragmentation model with a Peterson fragmentation function as implemented in PYTHIA [39].

As the number of true mesons enters the Eqs. (7.7), (7.8), (7.5), (7.6), (7.9) only as a ratio e.g. $\frac{N(D_2^{*0})}{N(D^+)}$, the most robust way is to calculate corrections that will be applied to this ratio. The procedure of calculating the corrections is the following:

1. calculate the number of excited charm mesons in the full kinematic space in the MC sample;
2. calculate the number of relevant ground charm mesons in the full kinematic space in the MC sample;
3. get the ratio of the two numbers above;
4. calculate the number of excited charm mesons in restricted kinematic space in the MC sample;
5. calculate the number of relevant ground charm mesons in restricted kinematic space in the MC sample;
6. get the ratio of the two numbers above;
7. the ratio of the numbers from 3) and 6) is an extrapolation factor of order of unity that is denoted as $\mathcal{G}$, e.g. $\mathcal{G}_{D_2^{*0}\to D^+/D^+}$.

Taking into account the extrapolation factors, Eqs. (7.7), (7.8), (7.5), (7.6), (7.9) can be rewritten as:

$$f(c\to D_1^0)=\frac{\frac{N(D_1^0\to D^{*+}\pi^-)}{N(D^*)}\mathcal{G}_{D_1^0\to D^{*+}/D^{*+}}}{\mathcal{B}_{D_1^0\to D^{*+}\pi^-}}f(c\to D^{*+})$$

$$f(c\to D_2^{*0})=$$
$$\frac{\mathcal{G}_{D_2^{*0}\to D^{*+}/D^{*+}}\frac{N(D_2^{*0}\to D^{*+}\pi^-)}{N(D^{*+})}f(c\to D^{*+})+\mathcal{G}_{D_2^{*0}\to D^{+}/D^{+}}\frac{N(D_2^{*0}\to D^{*+}\pi^-)}{N(D^{+})}f(c\to D^{+})}{\mathcal{B}_{D_2^{*0}\to D^+\pi^-}+\mathcal{B}_{D_2^{*0}\to D^{*+}\pi^-}} \tag{7.10}$$

$$
\begin{aligned}
f(c \to D_1^+) &= \frac{\frac{N(D_1^+ \to D^{*0}\pi^+, D^{*0} \to D^0\pi^0/\gamma)}{N(D^0)} \mathcal{G}_{D_1^+ \to D^{*0}/D^0}}{\mathcal{B}_{D_1^+ \to D^{*0}\pi^+}} f(c \to D^0) \\
f(c \to D_2^{*+}) &= f(c \to D^0) \times \\
&\times \frac{\frac{N(D_2^{*+} \to D^{*0}\pi^+, D^{*0} \to D^0\pi^0/\gamma)}{N(D^0)} \mathcal{G}_{D_2^{*+} \to D^{*0}/D^0} + \frac{N(D_2^{*+} \to D^0\pi^+)}{N(D^0)} \mathcal{G}_{D_2^{*+} \to D^0/D^0}}{\mathcal{B}_{D_2^{*+} \to D^{*0}\pi^+} + \mathcal{B}_{D_2^{*+} \to D^0\pi^+}}
\end{aligned}
\tag{7.11}
$$

$$
\begin{aligned}
&f(c \to D_{s1}^+) = \\
&\frac{\mathcal{G}_{D_{s1}^+ \to D^{*+}/D^{*+}} \frac{N(D_{s1}^+ \to D^{*+}K_S^0)}{N(D^{*+})} f(c \to D^{*+}) + \mathcal{G}_{D_{s1}^+ \to D^0/D^0} \frac{N(D_{s1}^+ \to D^{*0}K^+)}{N(D^0)} f(c \to D^0)}{\mathcal{B}_{D_{s1}^+ \to D^{*0}K^+} + \mathcal{B}_{D_{s1}^+ \to D^{*+}K_S^0}}
\end{aligned}
\tag{7.12}
$$

As is clear from the equations above, the fragmentation-fraction formulae have only combinations like

$$
\mathcal{F}^{\text{extr}}_{D_2^{*0} \to D^{*+}/D^{*+}} = \mathcal{G}_{D_2^{*0} \to D^{*+}/D^{*+}} \frac{N(D_2^{*0} \to D^{*+}\pi^-)}{N(D^{*+})}, \tag{7.13}
$$

which is basically the fraction of D^{*+} that originated from D_2^{*0} decays. In this analysis these quantities are considered a part of the final results and are given together with fragmentation fractions.

The formulae in this section assume that all D mesons originate from the charm quark fragmentation process; the small fraction that originate from the decays of the beauty mesons has been neglected. The effect of taking beauty into account can be seen by taking the $\frac{N(D_1^0)}{N(D^{*+})}$ ratio as an example:

$$
\frac{N(D_1^0)}{N(D^{*+})} = \frac{\sigma_c f(c \to D_1^0) + \sigma_b f(b \to D_1^0)}{\sigma_c f(c \to D^{*+}) + \sigma_b f(b \to D^{*+})},
$$

where σ_c and σ_b are inclusive charm and beauty cross sections and $f(b \to D)$ are the fragmentation fractions of the beauty quark to D mesons. To a good approximation:

$$
\frac{N(D_1^0)}{N(D^{*+})} \approx \frac{f(c \to D_1^0)}{f(c \to D^{*+})} \left(1 + \frac{\sigma_b}{\sigma_c} \left(\frac{f(b \to D_1^0)}{f(c \to D_1^0)} - \frac{f(b \to D^{*+})}{f(c \to D^{*+})} \right) \right).
$$

Taking into account the values obtained by OPAL [91] $f(b \to D_1^0) = 5.0 \pm 0.14 \pm 0.06\%$, the estimate of $f(b \to D^{*+}) \sim 40\%$ [1] and much higher charm cross-section at HERA $\frac{\sigma_b}{\sigma_c} \sim 1 \times 10^{-2}$ we have:

$$\frac{N(D_1^0)}{N(D^{*+})} \approx \frac{f(c \to D_1^0)}{f(c \to D^{*+})}(1 + \epsilon_b)$$

The small value of $\epsilon_b \sim 1 \times (2.5 - 2.0) \times 10^{-2}$ indicates a negligible impact of beauty on these results. In the previous ZEUS analysis [56] a subtraction of the b-quark relative contribution (see details in Ref. [56]) changed the relative acceptances (excited states with respect to ground states) by less than 1.5% of their values (i.e. close to the estimation of ϵ_b). Consequently, no such subtraction was performed in this analysis and the MC simulation included the beauty production processes. A variation of this contribution was considered for the systematics (Sec. 9).

7.2 The neutral excited charm mesons

The branching ratio for D_2^{*0} and the fragmentation fractions for D_1^0 and D_2^{*0} were measured using the channels $D_2^{*0} \to D^+\pi^-$ and $D_1^0, D_2^{*0} \to D^{*+}\pi^-$ with $D^{*+} \to D^0\pi_s^+ \to (K^-\pi^+)\pi_s^+$. The numbers of reconstructed $D_1^0, D_2^{*0} \to D^{*+}\pi^-$ and $D_2^{*0} \to D^+\pi^-$ decays were divided by the numbers of reconstructed D^{*+} and D^+ mesons, yielding the fractions of D^{*+} and D^+ mesons originating from the D_1^0 and D_2^{*0} decays. To correct the measured fractions for detector effects, ratios of acceptances were calculated using the MC simulation for the $D_1^0, D_2^{*0} \to D^{*+}\pi^-$ and $D_2^{*0} \to D^+\pi^-$ states to the inclusive D^{*+} and D^+ acceptances, respectively.

The fractions, $\mathcal{F}$, of D^{*+} mesons originating from D_1^0 and D_2^{*0} decays were calculated in the kinematic range $|\eta(D^{*+})| < 1.6$ and $p_T(D^{*+}) > 1.5\,\text{GeV}$ for the D^{*+} decay and the fraction of D^+ mesons originating from D_2^{*0} decays was calculated in the kinematic range $p_T(D^+) > 2.8\,\text{GeV}$ and $|\eta(D^+)| < 1.6$.

The fractions measured in the restricted $p_T(D^{*+}, D^+)$ and $\eta(D^{*+}, D^+)$ kinematic ranges were extrapolated to the fractions in the full kinematic phase space using the Bowler modification [59] of the Lund symmetric fragmentation function [60] as implemented in PYTHIA [92]. Applying the estimated extrapolation factors, $\mathcal{G}_{D_1^0 \to D^{*+}\pi^-/D^{*+}} \sim 1.13$ $\mathcal{G}_{D_2^{*0} \to D^{*+}\pi^-/D^{*+}} \sim 1.15$ and $\mathcal{G}_{D_2^{*0} \to D^+\pi^-/D^+} \sim 1.34$ yields

$$\mathcal{F}^{\text{extr}}_{D_1^0 \to D^{*+}\pi^-/D^{*+}} = 8.5 \pm 1.4(stat.)^{+1.2}_{-1.6}(syst.)\,\%,$$

$$\mathcal{F}^{\text{extr}}_{D_2^{*0}\to D^{*+}\pi^-/D^{*+}} = 4.7 \pm 1.3(stat.)^{+1.2}_{-0.8}(syst.)\,\%, \tag{7.14}$$

$$\mathcal{F}^{\text{extr}}_{D_2^{*0}\to D^{+}\pi^-/D^{+}} = 6.7 \pm 2.4(stat.)^{+1.5}_{-1.1}(syst.)\,\%. \tag{7.15}$$

From the Eqs. (7.10) and definition of $\mathcal{F}^{\text{extr}}$, the fragmentation fractions $f(c \to D_1^0)$, $f(c \to D_2^{*0})$ and the ratio of the two branching fractions for the D_2^{*0} meson is:

$$f(c \to D_1^0) = \frac{\mathcal{F}^{\text{extr}}_{D_1^0\to D^{*+}\pi^-/D^{*+}}}{\mathcal{B}_{D_1^0\to D^{*+}\pi^-}} f(c \to D^{*+}), \tag{7.16}$$

$$\begin{gathered} f(c \to D_2^{*0}) = \frac{\mathcal{F}^{\text{extr}}_{D_2^{*0}\to D^{*+}\pi^-/D^{*+}} f(c \to D^{*+}) + \mathcal{F}^{\text{extr}}_{D_2^{*0}\to D^{+}\pi^-/D^{+}} f(c \to D^{+})}{\mathcal{B}_{D_2^{*0}\to D^{*+}\pi^-} + \mathcal{B}_{D_2^{*0}\to D^{+}\pi^-}}, \\ \frac{\mathcal{B}_{D_2^{*0}\to D^{+}\pi^-}}{\mathcal{B}_{D_2^{*0}\to D^{*+}\pi^-}} = \frac{\mathcal{F}^{\text{extr}}_{D_2^{*0}\to D^{+}\pi^-/D^{+}} f(c \to D^{+})}{\mathcal{F}^{\text{extr}}_{D_2^{*0}\to D^{*+}\pi^-/D^{*+}} f(c \to D^{*+})}. \end{gathered} \tag{7.17}$$

The $f(c \to D^{*+})$ and $f(c \to D^{+})$ values used were obtained as a combination of data from HERA and e^+e^- colliders [93]:

$$f(c \to D^{*+}) = 22.87 \pm 0.56(\text{stat.} \oplus \text{syst.})^{+0.45}_{-0.56}(\text{br.})\,\%,$$

$$f(c \to D^{+}) = 22.56 \pm 0.77(\text{stat.} \oplus \text{syst.}) \pm 1.00(\text{br.})\,\%,$$

where the third uncertainties are due to the branching-ratio uncertainties.

As stated above, to a good approximation

$$\mathcal{B}_{D_1^0\to D^{*+}\pi^-} = 2/3, \quad \mathcal{B}_{D_2^{*0}\to D^{*+}\pi^-} + \mathcal{B}_{D_2^{*0}\to D^{+}\pi^-} = 2/3,$$

so that Eqs. (7.16) and (7.17) yields

$$f(c \to D_1^0) = 2.9 \pm 0.5(stat.)^{+0.5}_{-0.5}(syst.)\,\%,$$

$$f(c \to D_2^{*0}) = 3.9 \pm 0.9(stat.)^{+0.8}_{-0.6}(syst.)\,\%,$$

$$f(c \to D_1^0) + f(c \to D_2^{*0}) = 6.8 \pm 1.0(stat.)^{+0.9}_{-0.8}(syst.)\,\%.$$

Assuming uncorrelated errors the ratio of two fragmentation fractions is

$$f(c \to D_1^0)/f(c \to D_2^{*0}) = 0.8 \pm 0.2(stat.) \pm 0.2(syst.).$$

Taking into account the correlations in the simultaneous fit performed to obtain the values in Eqs. (7.14) and (7.15) yields

$$\frac{\mathcal{B}_{D_2^{*0}\to D^+\pi^-}}{\mathcal{B}_{D_2^{*0}\to D^{*+}\pi^-}} = 1.4 \pm 0.3(stat.)\pm 0.3(syst.).$$

7.3 The charged excited charm mesons

The branching ratio for D_2^{*+} and the fragmentation fractions for D_1^+ and D_2^{*+} were measured using the channels $D_2^{*+} \to D^0\pi^+$ and $D_1^+, D_2^{*+} \to D^{*0}\pi^+$ with $D^{*0} \to D^0\pi^0/\gamma$, where the π^0/γ are not measured directly. Since D^{*0} always decays to D^0 [1], the number of D^{*0} and D^0 originating from D_1^+/D_2^{*+} are identical. The number of reconstructed $D_1^+/D_2^{*+} \to D^{*0}\pi^+; D^{*0} \to D^0\pi^0/\gamma$ and $D_2^{*+} \to D^0\pi^+$ decays were thus divided by the total number of reconstructed D^0 mesons, yielding the fractions of D^0 mesons originating from D_1^+/D_2^{*+} decays. Detector effects were corrected as described in Sec. 7.2. The above fractions were calculated in the kinematic range $p_T(D^0) > 2.6$ GeV and $|\eta(D^0)| < 1.6$ and extrapolated to the fractions in the full kinematic phase space as for the D_1^0 and D_2^{*0} (Sec. 7.2). Applying the extrapolation factors, $\mathcal{G}_{D_1^0\to D^{*+}\pi^-/D^{*+}} \sim 1.28$ $\mathcal{G}_{D_1^0\to D^{*+}\pi^-/D^{*+}} \sim 1.18$, and $\mathcal{G}_{D_1^0\to D^{*+}\pi^-/D^{*+}} \sim 1.35$ gives

$$\mathcal{F}^{\text{extr}}_{D_1^+\to D^{*0}\pi^+/D^0} = 5.4 \pm 2.1(stat.)^{+2.3}_{-0.3}(syst.)\,\%,$$

$$\mathcal{F}^{\text{extr}}_{D_2^{*+}\to D^{*0}\pi^+/D^0} = 1.8 \pm 0.9(stat.)^{+0.5}_{-0.3}(syst.)\,\%,$$

$$\mathcal{F}^{\text{extr}}_{D_2^{*+}\to D^0\pi^+/D^0} = 2.0 \pm 0.5(stat.)^{+0.4}_{-0.2}(syst.)\,\%.$$

From the Eqs. (7.11) and definition of $\mathcal{F}^{\text{extr}}$, the fragmentation fractions $f(c \to D_1^+)$, $f(c \to D_2^{*+})$ and the ratio of the two branching fractions for the D_2^{*+} meson is:

$$f(c \to D_1^+) = \frac{\mathcal{F}^{\text{extr}}_{D_1^+\to D^{*0}\pi^-/D^{*0}}}{\mathcal{B}_{D_1^+\to D^{*0}\pi^+}} f(c \to D^{*+}), \tag{7.18}$$

$$f(c \to D_2^{*+}) = \frac{\mathcal{F}^{\text{extr}}_{D_2^{*+}\to D^{*0}\pi^+/D^0} f(c \to D^0) + \mathcal{F}^{\text{extr}}_{D_2^{*+}\to D^0\pi^+/D^0} f(c \to D^0)}{\mathcal{B}_{D_2^{*+}\to D^{*0}\pi^+} + \mathcal{B}_{D_2^{*+}\to D^0\pi^+}}, \tag{7.19}$$

$$\frac{\mathcal{B}_{D_2^{*+}\to D^+\pi^-}}{\mathcal{B}_{D_2^{*+}\to D^{*0}\pi^+}} = \frac{\mathcal{F}^{\rm extr}_{D_2^{*+}\to D^0\pi^+/D^0} f(c\to D^0)}{\mathcal{F}^{\rm extr}_{D_2^{*+}\to D^{*0}\pi^+/D^0} f(c\to D^0)} .$$

Using Eqs. (7.18), (7.19) and the fragmentation fraction [93]

$$f(c\to D^0) = 56.43\pm 1.51({\rm stat.}\oplus{\rm syst.})^{+1.35}_{-1.64}({\rm br.})\,\%,$$

gives

$$f(c\to D_1^+) = 4.6\pm 1.8(stat.)^{+2.0}_{-0.3}(syst.)\,\%,$$
$$f(c\to D_2^{*+}) = 3.2\pm 0.8(stat.)^{+0.5}_{-0.2}(syst.)\,\%,$$
$$f(c\to D_1^+) + f(c\to D_2^{*+}) = 7.8\pm 2.0(stat.)^{+2.0}_{-0.4}(syst.)\,\%.$$

Assuming uncorrelated errors

$$f(c\to D_1^+)/f(c\to D_2^{*+}) = 1.4\pm 0.7(stat.)^{+0.7}_{-0.1}(syst.).$$

The ratio of the branching fractions of the two dominant decay modes of the D_2^{*+},

$$\frac{\mathcal{B}_{D_2^{*+}\to D^0\pi^+}}{\mathcal{B}_{D_2^{*+}\to D^{*0}\pi^+}} = 1.1\pm 0.4(stat.)^{+0.3}_{-0.2}(syst.), \tag{7.20}$$

The ratio $\frac{\mathcal{B}_{D_2^{*+}\to D^0\pi^+}}{\mathcal{B}_{D_2^{*+}\to D^0\pi^+}+\mathcal{B}_{D_2^{*+}\to D^{*0}\pi^+}} = 0.52^{+0.08}_{-0.13}(stat.)\pm 0.05(syst.)$ has been calculated from Eq. (7.20) and found to be in agreement with BaBar result

$$\frac{\mathcal{B}_{D_2^{*+}\to D^0\pi^+}}{\mathcal{B}_{D_2^{*+}\to D^0\pi^+}+\mathcal{B}_{D_2^{*+}\to D^{*0}\pi^+}} = 0.62\pm 0.03\pm 0.02.$$

7.4 The strange excited charm mesons

The numbers of reconstructed $D_{s1}^+\to D^{*+}K_S^0$ and $D_{s1}^+\to D^{*0}K^+$ decays were divided by the numbers of reconstructed D^{*+} and D^0 mesons, respectively, yielding rates of D^{*+} and D^0 mesons originating from D_{s1}^+ decays. To correct the measured rates for detector effects, the relative acceptances were calculated using the MC simulation as ratios of acceptances for the $D_{s1}^+\to D^{*+}K_S^0$ and $D_{s1}^+\to D^{*0}K^-$ states to the inclusive D^{*+} and D^0 acceptances, respectively.

The fractions measured in the restricted $p_T(D^{*+}, D^0)$ and $\eta(D^{*+}, D^0)$ kinematic ranges were extrapolated to the fractions in the full kinematic phase space. Applying the estimated extrapolation factors, $\mathcal{G}_{D_{s1}^+ \to D^{*0}K^+/D^0} \sim 1.61$ for $\mathcal{F}_{D_{s1}^+ \to D^{*0}K^+/D^0}$, and $\mathcal{G}_{D_{s1}^+ \to D^{*+}K^0/D^{*+}} \sim 1.30$ for $\mathcal{F}_{D_{s1}^+ \to D^{*+}K^0/D^{*+}}$ gives

$$\mathcal{F}^{\text{extr}}_{D_{s1}^+ \to D^{*+}K^0/D^{*+}} = 1.31 \pm 0.24(stat.)^{+0.18}_{-0.17}(syst.)\,\%,$$

$$\mathcal{F}^{\text{extr}}_{D_{s1}^+ \to D^{*0}K^+/D^0} = 0.82 \pm 0.19(stat.)^{+0.12}_{-0.04}(syst.)\,\%.$$

From the Eq. (7.12) and definition of $\mathcal{F}^{\text{extr}}$, the fragmentation fraction $f(c \to D_{s1}^+)$ and the ratio of the two branching fractions for the D_{s1}^+ meson is:

$$f(c \to D_{s1}^+) = \frac{\mathcal{F}^{\text{extr}}_{D_{s1}^+ \to D^{*+}K^0/D^{*+}} f(c \to D^{*+}) + \mathcal{F}^{\text{extr}}_{D_{s1}^+ \to D^{*0}K^+/D^0} f(c \to D^0)}{\mathcal{B}_{D_{s1}^+ \to D^{*+}K^0} + \mathcal{B}_{D_{s1}^+ \to D^{*0}K^+}},$$

$$\frac{\mathcal{B}_{D_{s1}^+ \to D^{*0}K^+}}{\mathcal{B}_{D_{s1}^+ \to D^{*+}K^0}} = \frac{\mathcal{F}^{\text{extr}}_{D_{s1}^+ \to D^{*0}K^+/D^0} f(c \to D^0)}{\mathcal{F}^{\text{extr}}_{D_{s1}^+ \to D^{*+}K^0/D^{*+}} f(c \to D^{*+})}.$$

Assuming the decay width of the D_{s1}^+ is saturated by the D^*K final states, i.e.

$$\mathcal{B}_{D_{s1}^+ \to D^{*+}K^0} + \mathcal{B}_{D_{s1}^+ \to D^{*0}K^+} = 1,$$

yields

$$f(c \to D_{s1}^+) = 0.76 \pm 0.12(stat.)^{+0.08}_{-0.04}(syst.)\,\%.$$

The ratio for the two 1^+ states

$$f(c \to D_{s1}^+)/f(c \to D_1^0) = 0.26 \pm 0.06(stat.)^{+0.06}_{-0.05}(syst.)$$

represents the strangeness-suppression factor for P-wave charm mesons.

Using $f(c \to D^{*+})$ and $f(c \to D^0)$ [93], yields

$$\frac{\mathcal{B}_{D_{s1}^+ \to D^{*0}K^+}}{\mathcal{B}_{D_{s1}^+ \to D^{*+}K^0}} = 1.5 \pm 0.5(stat.)^{+0.3}_{-0.2}(syst.).$$

8 Discussion on charm quark fragmentation fractions results

8.1 Fragmentation fractions

The measured charm-quark fragmentation fractions, the available measurements from other sources and theoretical predictions are summarised in the Tab. 8.1. The results are given with statistical uncertainties obtained from the fits, followed by systematic uncertainties (see Sec. 9 for details).

The measured fragmentation fractions $f(c \to D_1^0)$, $f(c \to D_2^{*0})$ were found to be consistent with those obtained in e^+e^- annihilations [83, 91], see Tab. 8.1. The sum of the two fragmentation fractions, $f(c \to D_1^0)+f(c \to D_2^{*0}) = 6.8 \pm 1.0^{+0.9}_{-0.8}\,\%$ agrees with the prediction of the tunnelling model of 8.5% [22].
The ratio $f(c \to D_1^0)/f(c \to D_2^{*0}) = 0.8 \pm 0.2(stat.) \pm 0.2(syst.)$ is in good agreement with the simple spin-counting prediction of 3/5.

This analysis presents one of the first measurements of $f(c \to D_1^+)$ and $f(c \to D_2^{*+})$, so it is possible to compare the obtained results only to the theoretical predictions and $f(c \to D_1^0)$, $f(c \to D_2^{*0})$ values. The measured values of $f(c \to D_1^+)$ and $f(c \to D_2^{*+})$ and the sum of the two fragmentation fractions, $f(c \to D_1^+) + f(c \to D_2^{*+})$, are in good agreement with those of the neutral excited charm mesons. The sum of the two fragmentation fractions, $f(c \to D_1^+) + f(c \to D_2^{*+}) = 7.8 \pm 2.0^{+2.0}_{-0.4}\,\%$ agrees with the prediction of the tunnelling model of 8.5% [22]. The ratio $f(c \to D_1^+)/f(c \to D_2^{*+}) = 1.4 \pm 0.7(stat.)^{+0.7}_{-0.1}(syst.)$ is in agreement with the simple spin-counting prediction of 3/5.

The measured $f(c \to D_{s1}^+) = 0.76 \pm 0.12(stat.)^{+0.08}_{-0.04}(syst.)\,\%$ is lower than the previous ZEUS measurement [56] $f(c \to D_{s1}^+) = 1.11 \pm 0.16^{+0.08}_{-0.10}\,\%$ and OPAL results [91]. However, it agrees with the measurements of ALEPH [83].

The strange suppression factor for $L = 1$ mesons $\gamma_s = 0.26 \pm 0.06^{+0.06}_{-0.05}$ is in agreement with the previous HERA-I measurement $0.31 \pm 0.06^{+0.05}_{-0.04}$ and with the results for $L = 0$ mesons from a recent fragmentation fractions studies [94] $0.217 \pm 0.013^{+0.006}_{-0.0} \pm 0.013$[29]. The obtained value of γ_s is close to the value used as default in the PYTHIA generator $\gamma_s = 0.3$ [39].

---

[29] The uncertainty ±0.013 is related to PDG branching ratios.

	$f(c\to D_1^0)$	$f(c\to D_2^{*0})$	$f(c\to D_1^0)+f(c\to D_2^{*0})$	$\frac{f(c\to D_2^{*0})}{f(c\to D_1^0)}$	$f(c\to D_1^+)$	$f(c\to D_2^{*+})$	$f(c\to D_1^+)+f(c\to D_2^{*+})$	$\frac{f(c\to D_2^{*+})}{f(c\to D_1^+)}$	$f(c\to D_{s1}^+)$	$\frac{f(c\to D_{s1}^+)}{f(c\to D_1^0)}$
This, [64]	$2.9\pm0.5^{+0.5}_{-0.5}$	$3.9\pm0.9^{+0.8}_{-0.6}$	$6.8\pm1.0^{+0.9}_{-0.8}$	$0.8\pm0.2\pm0.2$	$4.6\pm1.8^{+2.0}_{-0.3}$	$3.2\pm0.8^{+0.5}_{-0.2}$	$7.8\pm2.0^{+2.0}_{-0.4}$	$1.4\pm0.7^{+0.7}_{-0.1}$	$0.76\pm0.12^{+0.08}_{-0.04}$	$0.26\pm0.06^{+0.06}_{-0.05}$
Zeus [56]	$3.5\pm0.4^{+0.4}_{-0.6}$	$3.8\pm0.7^{+0.5}_{-0.6}$	$7.3\pm0.8^{+0.7}_{-0.8}$	$0.93\pm0.2\pm0.16$					$1.11\pm0.16^{+0.08}_{-0.10}$	$0.31\pm0.06^{+0.05}_{-0.04}$
Opal [91]	$2.1\pm0.7\pm0.3$	$5.2\pm2.2\pm1.3$	$7.3\pm2.3\pm1.3$	$0.4\pm0.2\pm0.1$					$1.6\pm0.4\pm0.3$	$0.8\pm0.3\pm0.2$
Aleph [83]									$0.94\pm0.22\pm0.07$	
Model [24]	3.5	4.7	8.2	0.7					0.54	
Model [22]			8.5				8.5			
S.C.				0.6				0.6		

Table 8.1: *Comparison of fragmentation-fraction-results of this analysis to other measurements and theoretical predictions. The most precise measurements are shaded in yellow. S.C. corresponds to an estimate based on simple spin counting.*

8.2 Branching ratios

The measured branching ratios, the available measurements from other sources and the theoretical predictions are summarised in Tab. 8.2.

The measured value $\frac{\mathcal{B}_{D_2^{*0}\to D^+\pi^-}}{\mathcal{B}_{D_2^{*0}\to D^{*+}\pi^-}}$ $=1.4 \pm 0.3^{+0.3}_{-0.3}$ is lower than most other measurements, including the previous ZEUS measurement [56] $\frac{\mathcal{B}_{D_2^{*0}\to D^+\pi^-}}{\mathcal{B}_{D_2^{*0}\to D^{*+}\pi^-}} = 2.8 \pm 0.8^{+0.5}_{-0.6}$. However, the measured value is in agreement with the precise measurements of BABAR [62] $\frac{\mathcal{B}_{D_2^{*0}\to D^+\pi^-}}{\mathcal{B}_{D_2^{*0}\to D^{*+}\pi^-}} = 1.47 \pm 0.03 \pm 0.16$, which constrains the PDG average [1] $\frac{\mathcal{B}_{D_2^{*0}\to D^+\pi^-}}{\mathcal{B}_{D_2^{*0}\to D^{*+}\pi^-}} = 1.56 \pm 0.16$.

The PDG [1] cites only two measurements of $\frac{\mathcal{B}_{D_2^{*+}\to D^0\pi^+}}{\mathcal{B}_{D_2^{*+}\to D^{*0}\pi^+}}$. The measured value in this work, $\frac{\mathcal{B}_{D_2^{*+}\to D^0\pi^+}}{\mathcal{B}_{D_2^{*+}\to D^{*0}\pi^+}}$ $=1.1 \pm 0.4^{+0.3}_{-0.2}$ is slightly lower, but still consistent with the precise measurement of BABAR [74] $\frac{\mathcal{B}_{D_2^{*+}\to D^0\pi^+}}{\mathcal{B}_{D_2^{*+}\to D^{*0}\pi^+}} = 1.63^{+0.14+0.22}_{-0.12-0.19}$. However, the measurement of BABAR is not taken into account[30] in the PDG average, which relies only on the imprecise CLEO [95] result $\frac{\mathcal{B}_{D_2^{*+}\to D^0\pi^+}}{\mathcal{B}_{D_2^{*+}\to D^{*0}\pi^+}} = 1.9 \pm 1.1 \pm 0.3$. For this reason the measurement presented in this thesis, if taken into account, can significantly improve the accuracy of the $\frac{\mathcal{B}_{D_2^{*+}\to D^0\pi^+}}{\mathcal{B}_{D_2^{*+}\to D^{*0}\pi^+}}$ PDG average.

Theoretical models [5, 20, 21, 96] predict the ratios $\frac{\mathcal{B}_{D_2^{*0}\to D^+\pi^-}}{\mathcal{B}_{D_2^{*0}\to D^{*+}\pi^-}}$ and $\frac{\mathcal{B}_{D_2^{*+}\to D^0\pi^+}}{\mathcal{B}_{D_2^{*+}\to D^{*0}\pi^+}}$ to be in the range from 2.3 to 3, well above the values measured in this analysis. Those discrepancies can be explained with the limited precision of the experimental data used for those predictions (i.e. masses and widths).

The measured value $\frac{\mathcal{B}_{D_{s1}^+\to D^{*+}K_S^0}}{\mathcal{B}_{D_{s1}^+\to D^{*0}K^+}}$ $=1.5 \pm 0.5^{+0.3}_{-0.2}$ is consistent with most other

---

[30] The note on this measurement in PDG is "Assuming $\Gamma(\Upsilon(4S) \to B^+B^-)/\Gamma(\Upsilon(4S) \to B^0B^0) = 1.065 \pm 0.026$ and equal partial widths for charged and neutral D_2^* mesons".

	$\frac{\mathcal{B}_{D_2^{*0}\to D^+\pi^-}}{\mathcal{B}_{D_2^{*0}\to D^{*+}\pi^-}}$	$\frac{\mathcal{B}_{D_2^{*+}\to D^0\pi^+}}{\mathcal{B}_{D_2^{*+}\to D^{*0}\pi^+}}$	$\frac{\mathcal{B}_{D_{s1}^+\to D^{*+}K_S^0}}{\mathcal{B}_{D_{s1}^+\to D^{*0}K^+}}$
This, [64]	$1.4\pm0.3^{+0.3}_{-0.3}$	$1.1\pm0.4^{+0.3}_{-0.2}$	$1.5\pm0.5^{+0.3}_{-0.2}$
PDG [1]	1.56 ± 0.16	$1.9 \pm 1.1 \pm 0.3$	1.18 ± 0.16
ZEUS [56]	$2.8 \pm 0.8^{+0.5}_{-0.6}$		$2.3 \pm 0.6 \pm 0.3$
BABAR [62]	$1.47 \pm 0.03 \pm 0.16$		
CLEO-II [66]	$2.2 \pm 0.7 \pm 0.6$		
CLEO [68]	2.3 ± 0.8		
ARGUS [69]	$3.0 \pm 1.1 \pm 1.5$		
BELLE [15]	1.9 ± 0.5		
BABAR [74],recalculated		$1.63^{+0.14+0.22}_{-0.12-0.19}$	
CLEO [95]		$1.9 \pm 1.1 \pm 0.3$	
BELLE [88]			$0.88 \pm 0.24 \pm 0.08$
ALEPH [83]			$1.32 \pm 0.47 \pm 0.23$
OPAL [91]			$1.9^{+1.1}_{-0.9} \pm 0.4$
CLEO [85]			1.1 ± 0.3
ARGUS [86],recalculated by PDG			$1.4 \pm 0.3 \pm 0.2$
Prediction [5]	3.0		
Prediction [20]	2.7		
Prediction [21]	2.280 ± 0.007	2.266 ± 0.015	
Prediction [18]			1.2-1.7
Prediction [96]	2.3		

Table 8.2: *Comparison of branching ratio results of this analysis to other measurements and theoretical predictions. The most precise measurements are shaded in yellow.*

measurements cited in the PDG [1], with an exception of previous ZEUS measurement [56] $\frac{\mathcal{B}_{D_{s1}^{+}\to D^{*+}K_{S}^{0}}}{\mathcal{B}_{D_{s1}^{+}\to D^{*0}K^{+}}} = 2.3 \pm 0.6 \pm 0.3$, which is slightly higher.

A theoretical model [18] predicts the ratio $\frac{\mathcal{B}_{D_{s1}^{+}\to D^{*+}K_{S}^{0}}}{\mathcal{B}_{D_{s1}^{+}\to D^{*0}K^{+}}}$ to be in the range from 1.2 to 1.7, which is in good agreement with the measured value of $\frac{\mathcal{B}_{D_{s1}^{+}\to D^{*+}K_{S}^{0}}}{\mathcal{B}_{D_{s1}^{+}\to D^{*0}K^{+}}}$.

All the measured values, $\frac{\mathcal{B}_{D_{2}^{*0}\to D^{+}\pi^{-}}}{\mathcal{B}_{D_{2}^{*0}\to D^{*+}\pi^{-}}}$, $\frac{\mathcal{B}_{D_{2}^{*+}\to D^{0}\pi^{+}}}{\mathcal{B}_{D_{2}^{*+}\to D^{*0}\pi^{+}}}$ and $\frac{\mathcal{B}_{D_{s1}^{+}\to D^{*+}K_{S}^{0}}}{\mathcal{B}_{D_{s1}^{+}\to D^{*0}K^{+}}}$, if taken into account, can significantly improve the accuracy of the PDG [1] averages.

9 Systematic uncertainties and checks

It is assumed that systematic uncertainties might have three origins: the reconstruction procedure, the signal extraction procedure and model uncertainties.

As there is no a straightforward way to estimate the uncertainty of the reconstruction procedure, a reconstruction cut variation way used, with a concentration on cuts that might have the largest impact on the reconstruction. In each particular case the sizes of considered variations were deduced from the detector resolution (e.g. the D^+ mass window) or were chosen large enough to test the stability of the selection procedure without dramatic changes of the reconstructed spectra. A detailed study of tracking was not carried out since the expected uncertainties are much smaller than the statistic and systematic uncertainties of other kinds. The estimation of the signal-extraction procedure uncertainty was based on the modifications of the fit procedure and its parameters (e.g. resolution). The model uncertainties were relevant only for the part of the analysis that relies on MC simulations.

9.1 Systematic uncertainties

On the basis described above, the systematic uncertainty sources were grouped as follows:

- $\{\delta_1\}$ The stability of the results was checked by a variation of the selection cuts which have the largest effect on the ratio of signal and background in the data:
  - the cut on the minimal transverse momentum of the D^{*+}, D^+ and D^0 candidates was varied by $\pm 100\,\mathrm{MeV}$;
  - the cut on the minimal transverse momentum of the extra pion in the excited D meson analysis was varied by $\pm 10\,\mathrm{MeV}$;
  - the selection cut on the cosine of angle between extra pions and charged (neutral) excited D meson candidates was changed by ± 0.1 (± 0.05);
    The examples of spectra fitted with those variations are shown in Fig. 9.1 (neutral states), in Fig. 9.2 (charged states) and in Fig. 9.3 (strange states).

  - the widths of the mass windows used for the selection of D^{*+} and D^0 candidates in the excited charm meson analyses were varied by ±5% for each p_T dependent window (see Tab. 5.1), while for the D^+ candidates it was varied by ±12.5%. The examples of spectra fitted with those variations are shown in Fig. 9.4 (neutral states), in Fig. 9.5 (charged states) and in Fig. 9.6 (strange states).

- $\{\delta_2\}$ The CAL energy scale is known with ±2% uncertainty and was varied accordingly.

- $\{\delta_3\}$ The uncertainties related to the signal-extraction procedure were obtained as follows:

  - the ranges for the signal fits were reduced on either sides by 16 MeV for the $D^{*+}\pi$ and $D^+\pi$ mass spectra, by 24 MeV for the $D^0\pi$ mass spectrum and by 8 MeV for the $D^{*+}K^0_S$ and D^0K mass spectra;

  - the background shape was changed to the one used in [62] ;

  - the widths of the Gaussians used to parametrise the mass resolutions were changed by ±20%;

  - all the masses and widths of wide states were set free in the fit. Since with the present data alone one cannot determine these parameters well (the fit is not stable when the parameters are free), the world average values from the PDG [1] were used as additional constraints. This was implemented by adding for each parameter P (width or mass) a term $\frac{(P-P_{\mathrm{PDG}})^2}{\sigma(P_{\mathrm{PDG}})^2}$ to the χ^2-function. Here P_{PDG} and $\sigma(P_{\mathrm{PDG}})$ denote the parameter value and its uncertainty from the PDG [1];

  - the background functions in the four helicity intervals were allowed to have separate sets of parameters (for $D^{*+}\pi$ and $D^{*+}K^0_S$);

  - the helicity parameter of the D_2^{*0} meson in the fit was set free (Sec. 5.9).

  The effects of fit range and mass resolution parameters variations on the fit results were small for all reconstructed spectra. The background-shape modifications, wide-states variations caused large changes of wide states and feed-down yields. For example, the $D(2400)$ yield was found to be equal to zero, for the cases when the background function was not flexible enough. At the same time, the background-shape modification changed the spectroscopy results only by a small amount.

However, the fit with separate background functions in four helicity bins yields $\Gamma(D_1^0)$ value lower than the nominal. The examples of spectra fitted with those variations are shown in Fig. 9.7 (neutral states), in Fig. 9.8 (charged states) and in Fig. 9.9 (strange states).

- $\{\delta_4\}$ The uncertainties of $M(D^{*+})_{\text{PDG}}$, $M(D^0)_{\text{PDG}}$, $M(D^+)_{\text{PDG}}$ were taken into account. The variation of of $M(D^{*+})_{\text{PDG}}$, $M(D^0)_{\text{PDG}}$, $M(D^+)_{\text{PDG}}$ were performed separately with a shift of corresponding mass spectra by the PDG uncertainty.

- $\{\delta_5\}$ The width of D_1^+ and D_2^{*+} were varied within their uncertainties taken from the PDG [1].

- $\{\delta_6\}$ The uncertainty of the beauty contamination was determined by varying the beauty fraction in the MC sample between 0 and 200% of the reference amount. As it was explained in Sec. 7, any bias in the result related to the beauty contamination depends on the beauty-quark fragmentation fractions and the branching ratios of the beauty hadrons decaying into the excited charm mesons. Those quantities are not known well and are not simulated well in MC samples. For this reason a huge variation of the beauty contribution is reasonable.

- $\{\delta_7\}$ The extrapolation uncertainties were determined by varying relevant parameters of the PYTHIA simulation using the Bowler modification [59] of the Lund symmetric fragmentation function [60]. The following variations were performed:
  - the mass of the c quark was varied from its nominal value of 1.5 GeV by ± 0.2 GeV;
  - the strangeness suppression factor was varied from its nominal value of 0.3 by ± 0.1;
  - the fraction of the lowest-mass charm mesons produced in a vector state was varied from its nominal value of 0.6 by ± 0.1;
  - the Bowler fragmentation function parameter r_c was varied from the predicted value 1 to 0.5; the a and b parameters of the Lund symmetric function were varied by $\pm 20\%$ around their default values [92].

The variations were calculated from samples with a number of generated decays high enough to neglect the statistical uncertainties. The obtained values are listed in Tab. 9.1.

Parameter	Value
$\mathcal{G}_{D_1^0 \to D^{*+}/D^{*+}}$	$1.130^{+0.017}_{-0.013}$
$\mathcal{G}_{D_2^{*0} \to D^{*+}/D^{*+}}$	$1.147^{+0.040}_{-0.022}$
$\mathcal{G}_{D_2^{*0} \to D^{+}/D^{+}}$	$1.336^{+0.083}_{-0.086}$
$\mathcal{G}_{D_1^+ \to D^{0}/D^{0}}$	$1.283^{+0.076}_{-0.025}$
$\mathcal{G}_{D_1^+ \to D^{*0}/D^{*0}}$	$1.179^{+0.124}_{-0.025}$
$\mathcal{G}_{D_2^{*+} \to D^{0}/D^{0}}$	$1.351^{+0.164}_{-0.052}$
$\mathcal{G}_{D_{s1}^+ \to D^{*+}/D^{*+}}$	$1.298^{+0.025}_{-0.118}$
$\mathcal{G}_{D_{s1}^+ \to D^{*0}/D^{0}}$	$1.614^{+0.121}_{-0.145}$

Table 9.1: *Extrapolation factors with their systematic uncertainties.*

The statistical, systematical and branching ratio uncertainties of the fragmentation fractions $f(c \to D^{*+})$, $f(c \to D^{+})$ and $f(c \to D^{0})$ were added in quadrature and the resulting uncertainty was included in δ_7.

The contributions from all systematic uncertainties were calculated separately for positive and negative variations and added in quadrature. The obtained values are listed in Tabs. 9.2, 9.3, 9.4, 9.5, 9.7, 9.6. The individual contributions from the systematic variations are shown in Figs. 9.10, 9.11, 9.12 (neutral states), in Figs. 9.13, 9.14 (charged states) and in Figs. 9.15, 9.16 (strange states).

In addition to the variations described above, to check the stability of the systematic uncertainties estimation, intermediate variations have been performed. The size of each positive (negative) intermediate variation amounts half of the corresponding main positive (negative) systematic variation. For example, for the CAL energy scale variations the positive intermediate variation was +1% and the negative -1%. There was no intermediate variations for the change of background parametrisation and for other obvious cases. The individual contributions from the intermediate systematic variations are shown together with main systematic variations in Figs. 9.10, 9.11, 9.12 (neutral states), in Figs. 9.13, 9.14 (charged states) and in Figs. 9.15, 9.16 (strange states).

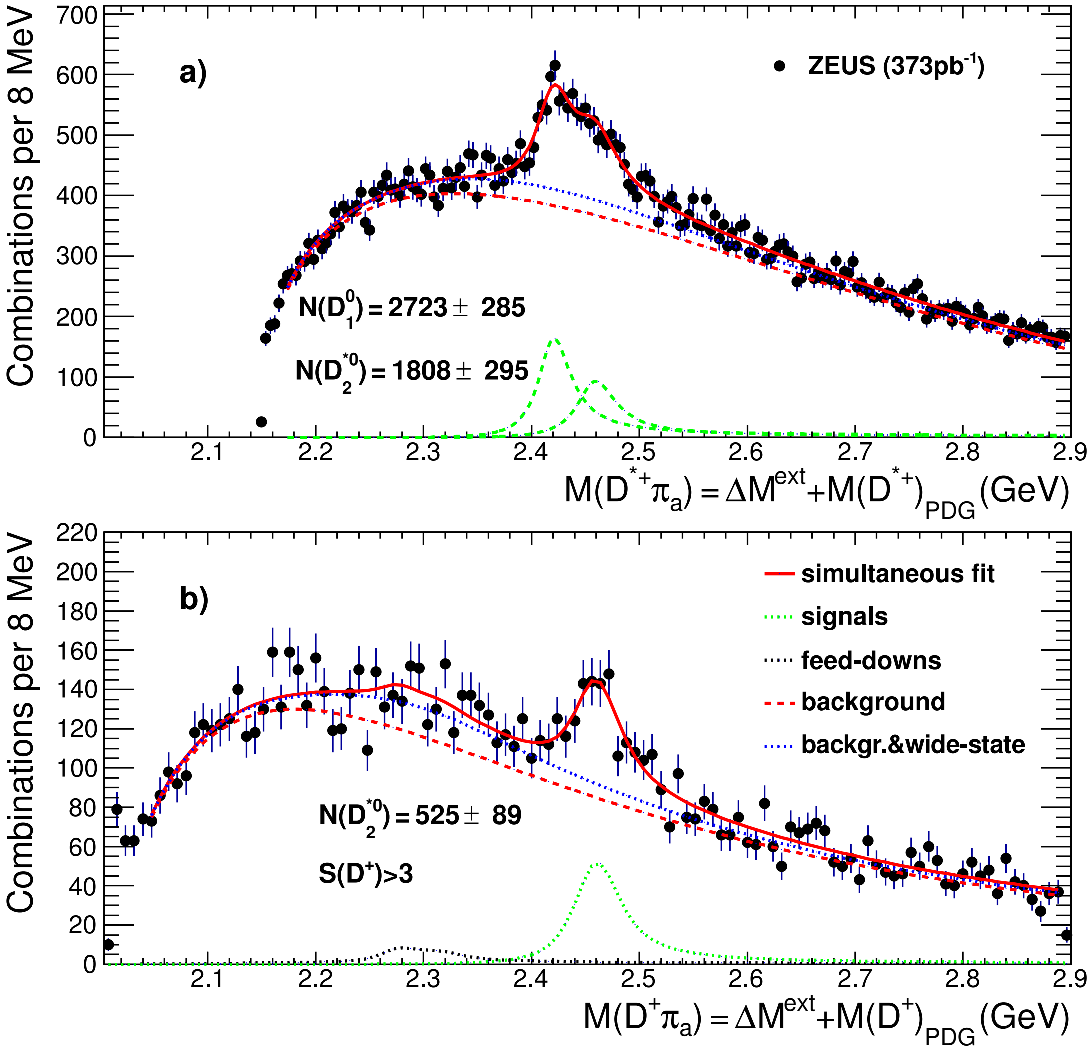

Figure 9.1: *Example of cut variation, δ_1. The $\cos\theta^*(D^{*+})$ cut has been increased by 0.1. The mass distributions (dots) a) $M(D^{*+}\pi_a)$ and b) $M(D^+\pi_a)$ are shown. Compare to the spectra in Fig. 5.6 with the nominal selection and fit. The solid curves are the result of a simultaneous fit to a) D_1^0 and D_2^{*0} and to b) D_2^{*0} and feed-downs plus background function (dashed curves). The contributions of the wide states $D_1(2430)^0$ and $D_0^*(2400)^0$ are given between the dashed and dotted curves. The lowest curves are the contributions of the D_1^0 and D_2^{*0} to the fit.*

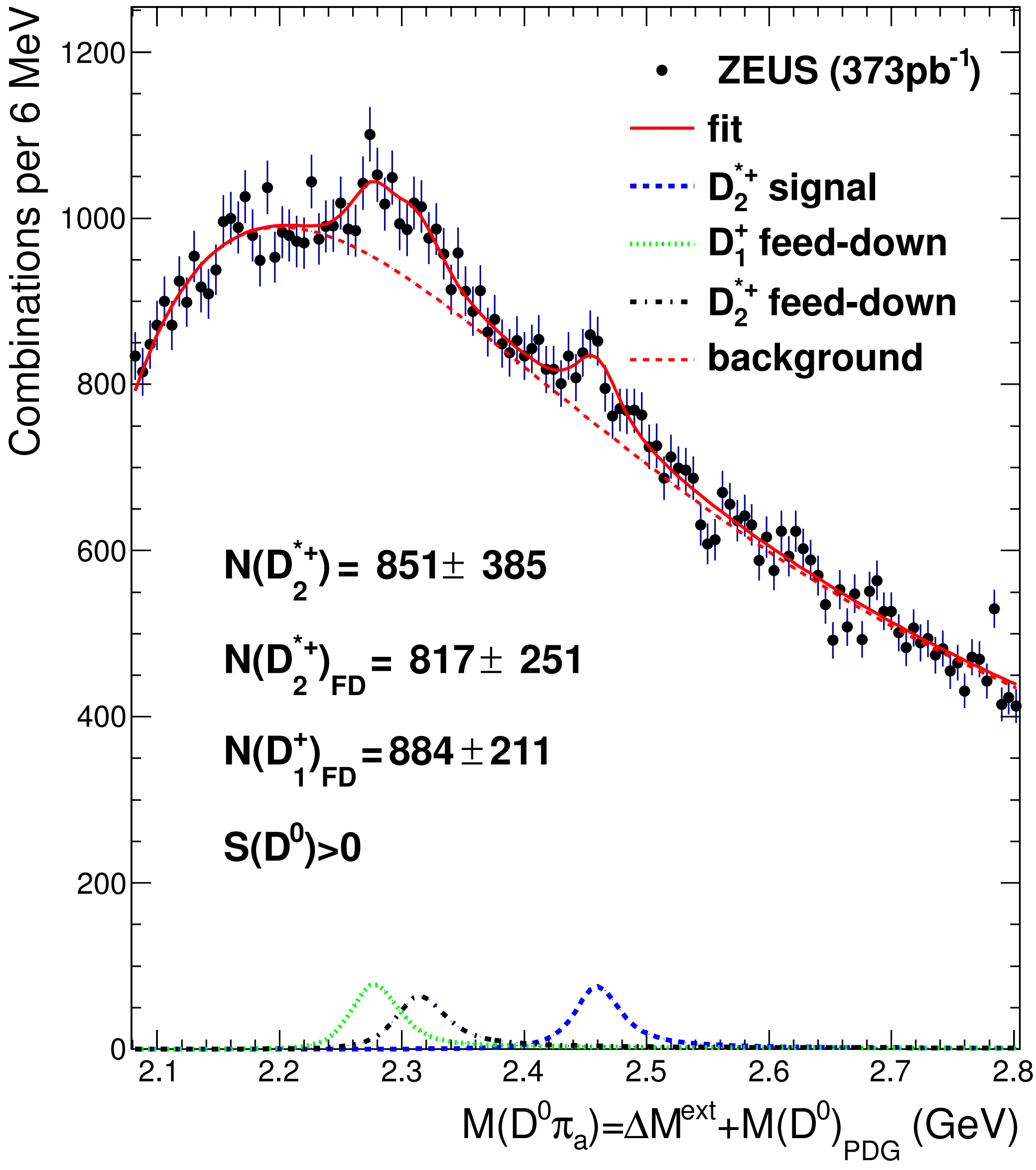

Figure 9.2: *Example of cut variation, δ_1. The $\cos\theta^*(D^0)$ cut has been increased by 0.1. The mass distribution (dots) $M(D^0\pi_a)$ is shown. Compare to the spectrum in Fig. 5.7 with the nominal selection and fit. The solid curve is the result of a simultaneous fit to the feed-down (FD) D_1^+ and D_2^{*+} contributions and to the D_2^{*+} signal plus background function (dashed curves). The lowest curves are the contributions of the D_1^+ and D_2^{*+} to the fit.*

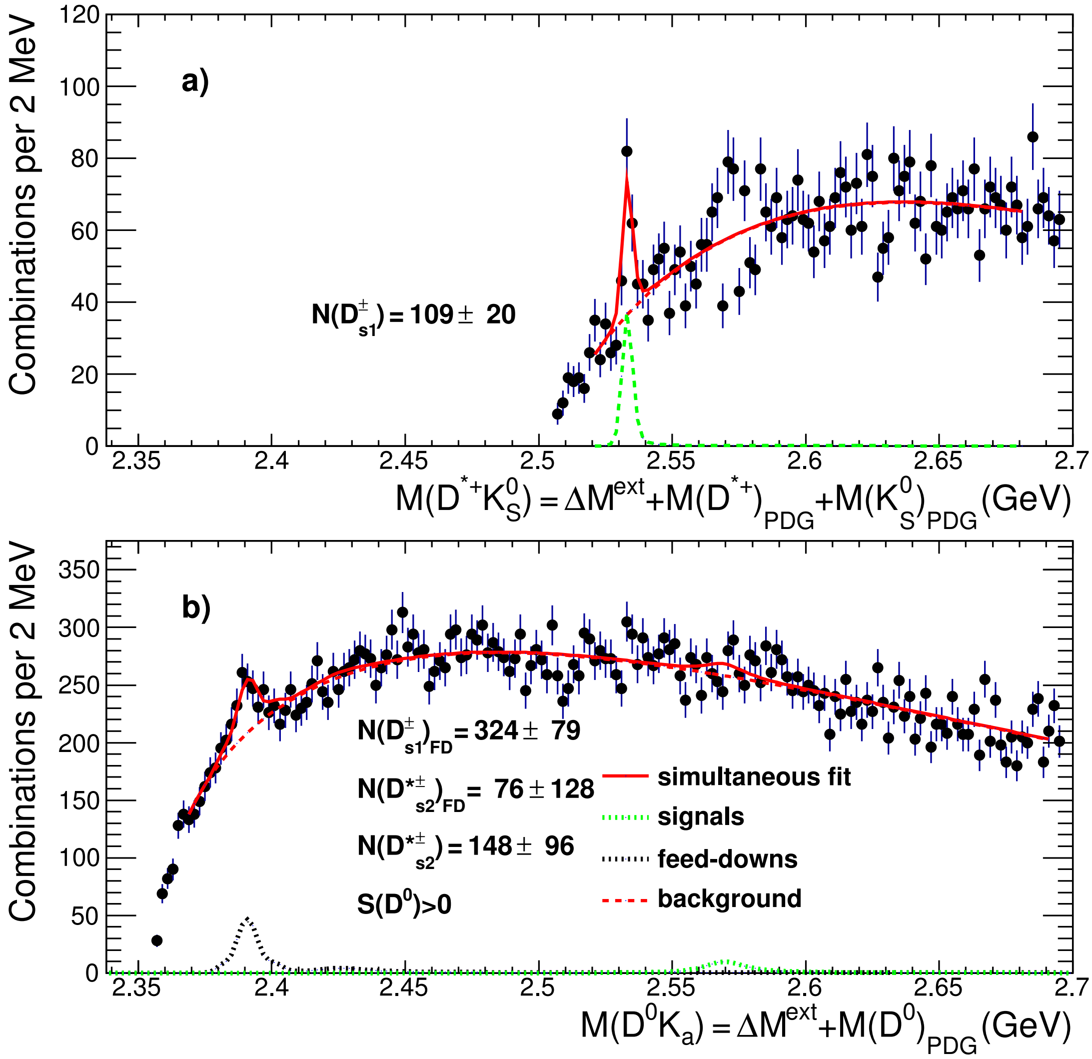

Figure 9.3: *Example of cut variation, δ_1. The $p_T(D^{*+})$ cut has been increased by 0.1. The mass distributions (dots), a) $M(D^{*+}K^0_S)$ and b) $M(D^0K_a)$ are shown. Compare to the spectra in Fig. 5.8 with the nominal selection and fit. The solid curves are the result of a simultaneous fit to a) D^+_{s1} and to b) D^{*+}_{s2} and feed-downs plus background function (dashed curves).*

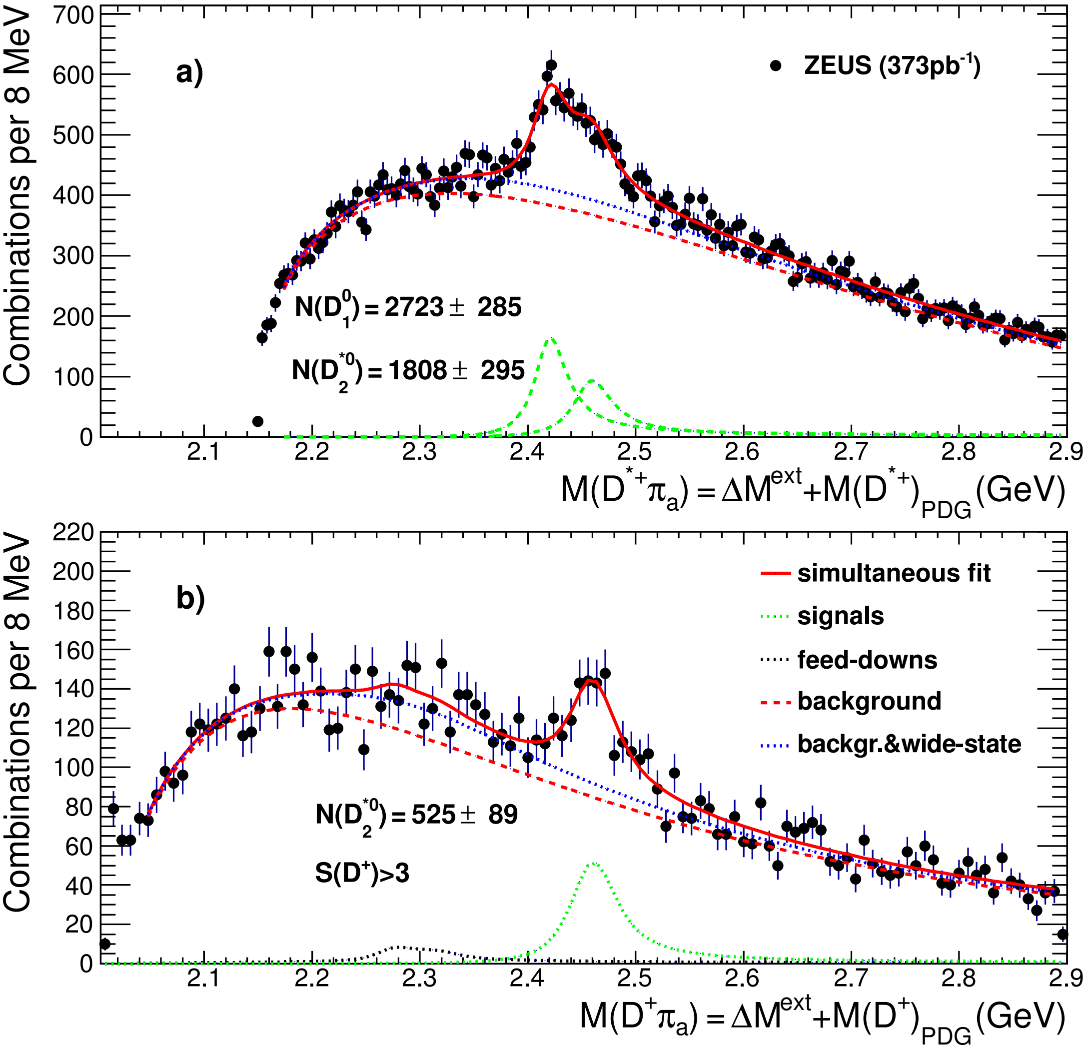

Figure 9.4: *Example of cut variation, δ_1. The $\cos\theta^*(D^{*+})$ cut has been increased by 0.1. The mass distributions (dots) a) $M(D^{*+}\pi_a)$ and b) $M(D^+\pi_a)$ are shown. Compare to the spectra in Fig. 5.6 with the nominal selection and fit. The solid curves are the result of a simultaneous fit to a) D_1^0 and D_2^{*0} and to b) D_2^{*0} and feed-downs plus background function (dashed curves). The contributions of the wide states $D_1(2430)^0$ and $D_0^*(2400)^0$ are given between the dashed and dotted curves. The lowest curves are the contributions of the D_1^0 and D_2^{*0} to the fit.*

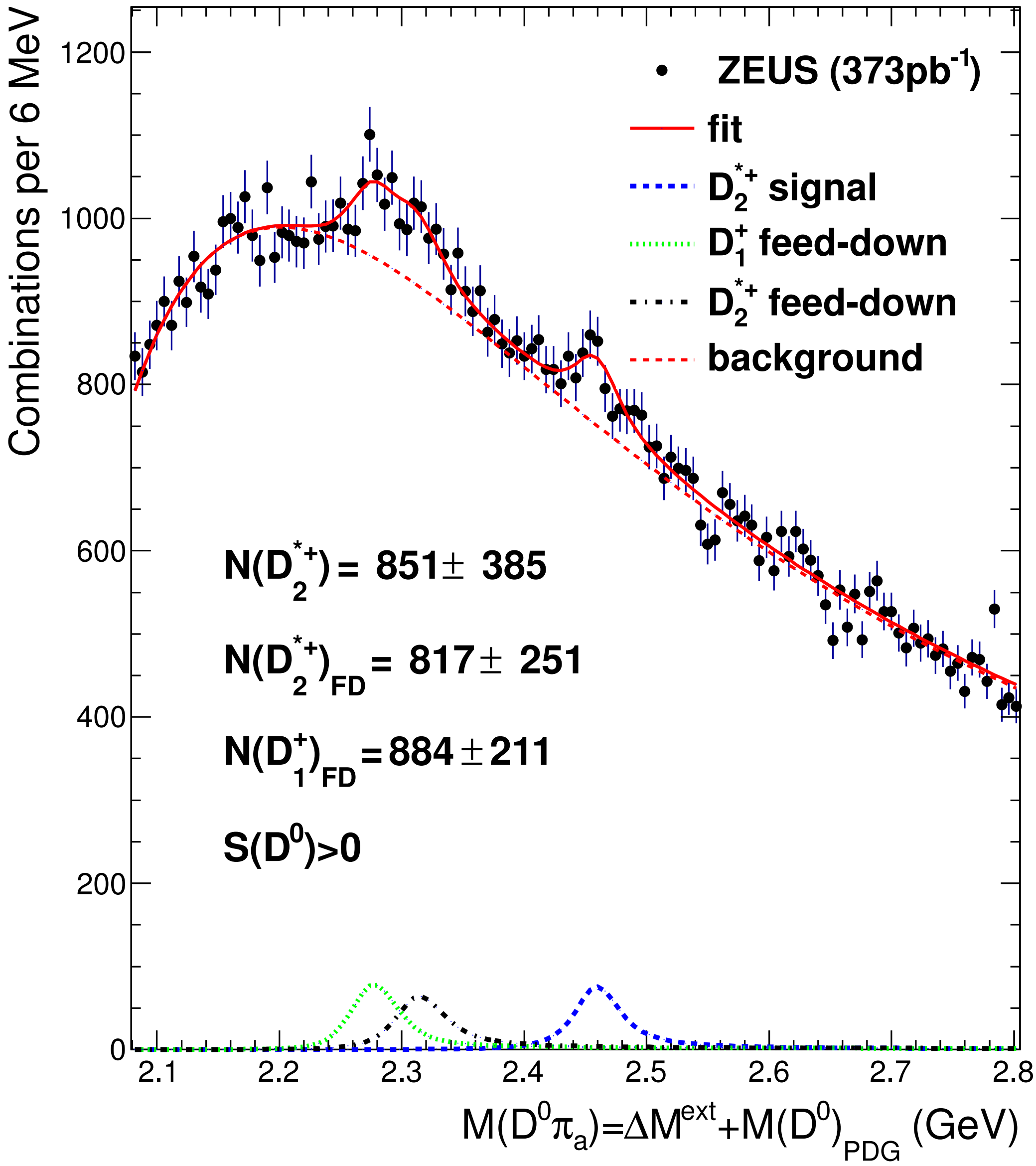

Figure 9.5: *Example of cut variation, δ_1. The $\cos\theta^*(D^0)$ cut has been increased by 0.1 GeV. The mass distribution (dots) $M(D^0\pi_a)$ is shown. Compare to the spectrum in Fig. 5.7 with the nominal selection and fit. The solid curve is the result of a simultaneous fit to the feed-down (FD) D_1^+ and D_2^{*+} contributions and to the D_2^{*+} signal plus background function (dashed curves). The lowest curves are the contributions of the D_1^+ and D_2^{*+} to the fit.*

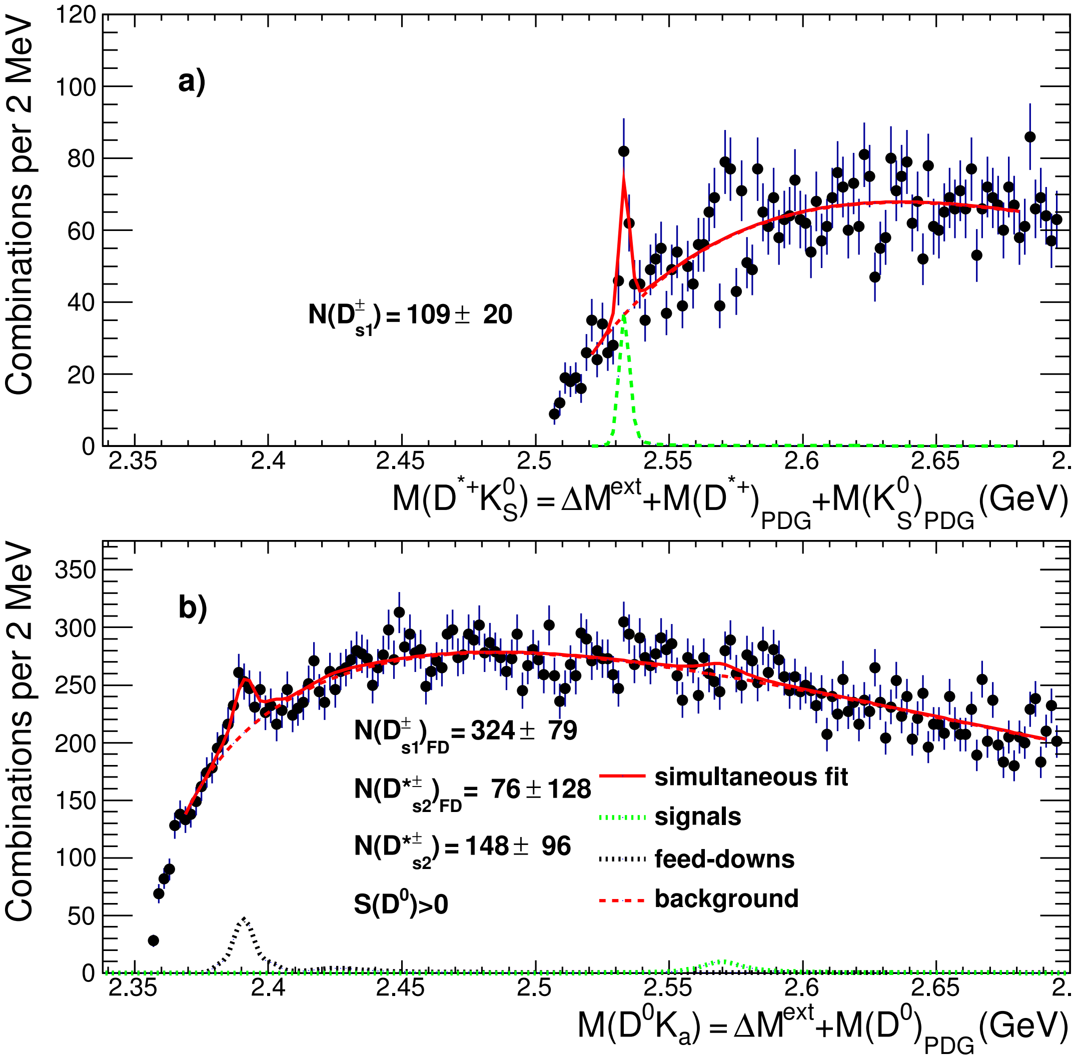

Figure 9.6: *Example of cut variation, δ_1. The $p_T(D^{*+})$ cut has been increased by 0.1 GeV. The mass distributions (dots), a) $M(D^{*+}K_S^0)$ and b) $M(D^0K_a)$ are shown. Compare to the spectra in Fig. 5.8 with the nominal selection and fit. The solid curves are the result of a simultaneous fit to a) D_{s1}^+ and to b) D_{s2}^{*+} and feed-downs plus background function (dashed curves).*

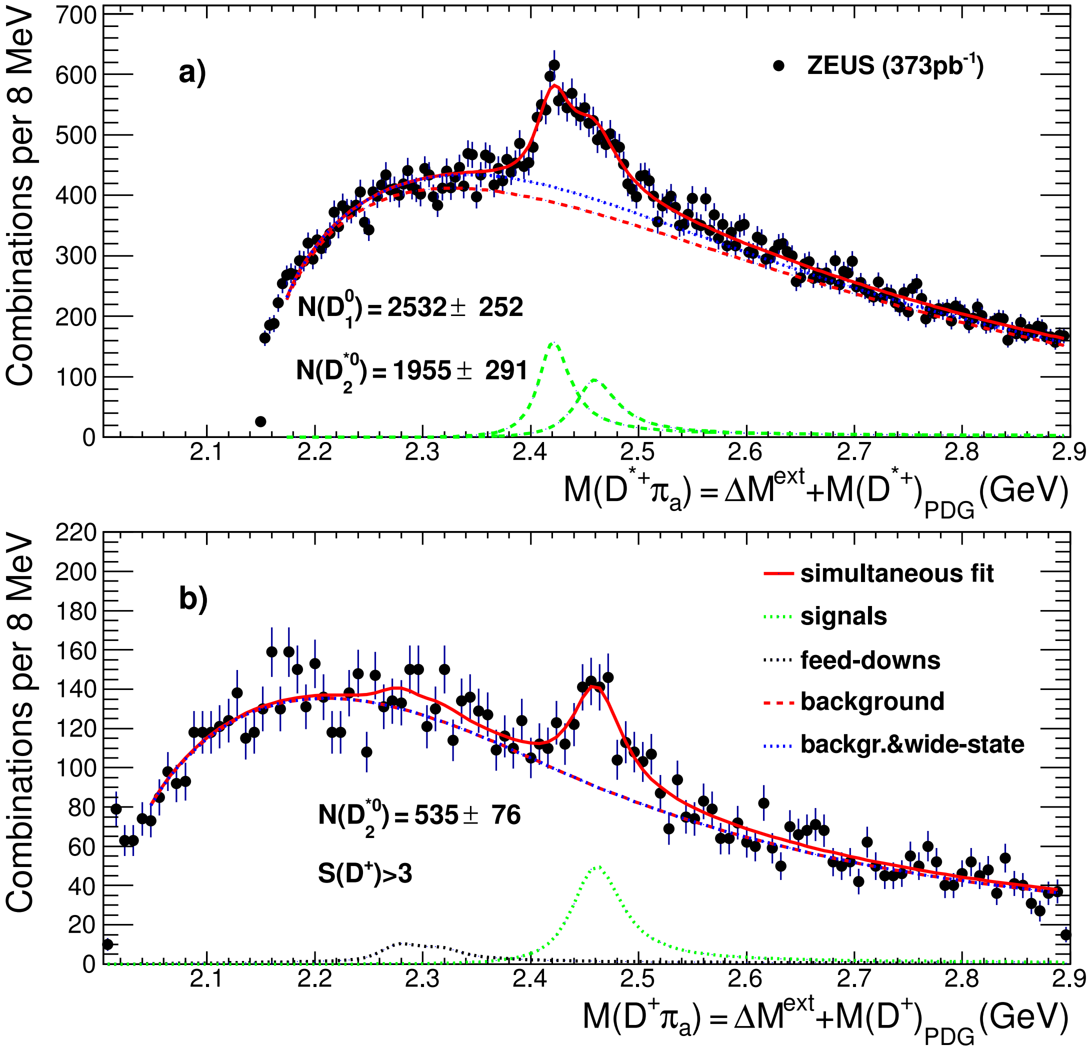

Figure 9.7: *Example of signal extraction procedure variation. The background shape was changed to the one used in [62] ; The mass distributions (dots) a)* $M(D^{*+}\pi_a)$ *and b)* $M(D^{+}\pi_a)$ *are shown. Compare to the spectra in Fig. 5.6 with the nominal selection and fit. The solid curves are the result of a simultaneous fit to a)* D_1^0 *and* D_2^{*0} *and to b)* D_2^{*0} *and feed-downs plus background function (dashed curves). The contributions of the wide states* $D_1(2430)^0$ *and* $D_0^*(2400)^0$ *are given between the dashed and dotted curves. The lowest curves are the contributions of the* D_1^0 *and* D_2^{*0} *to the fit.*

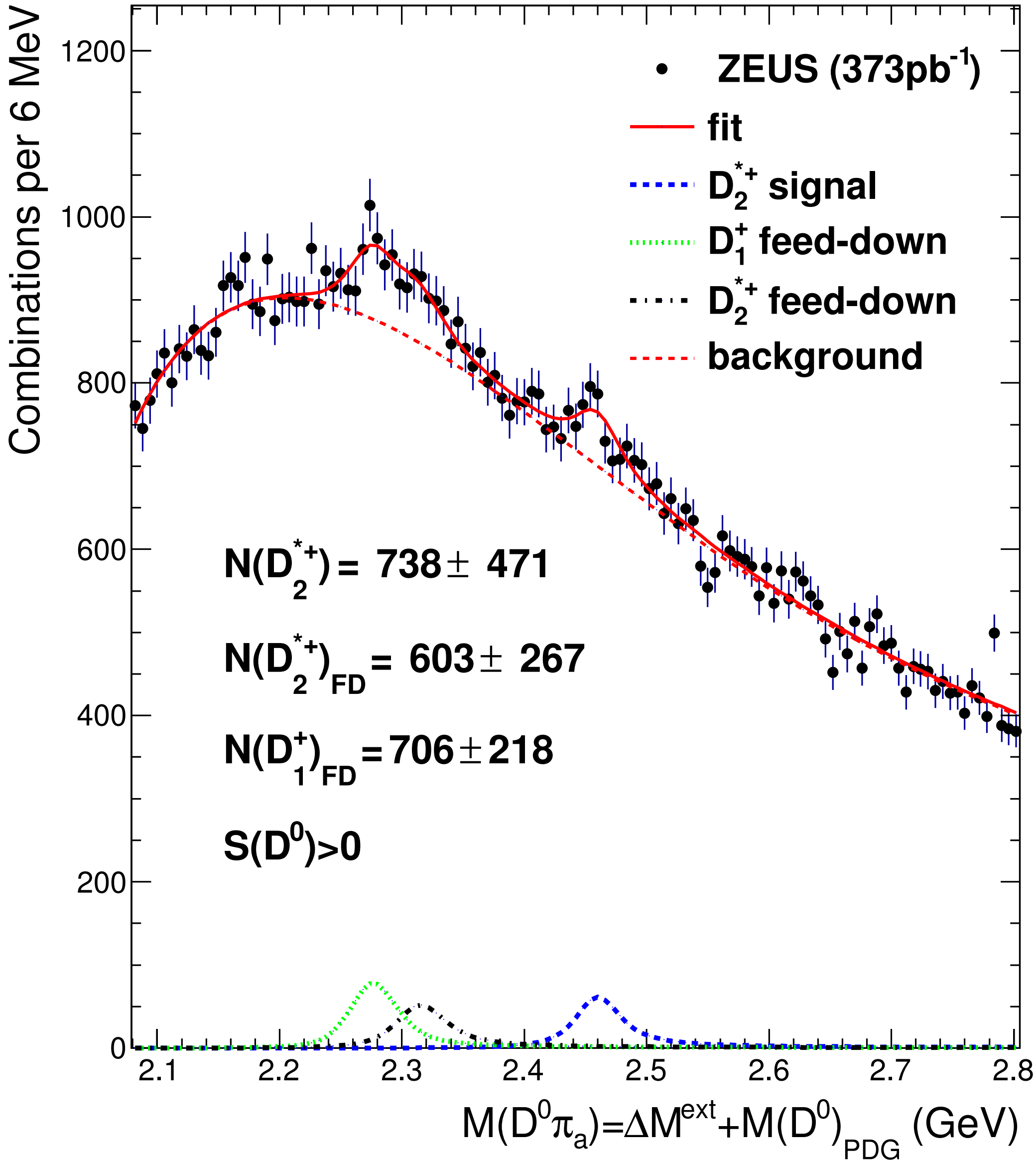

Figure 9.8: *Example signal extraction procedure variation. The background shape was changed to the one used in [62] ; The mass distribution (dots)* $M(D^0\pi_a)$ *is shown. Compare to the spectrum in Fig. 5.7 with the nominal selection and fit. The solid curve is the result of a simultaneous fit to the feed-down (FD)* D_1^+ *and* D_2^{*+} *contributions and to the* D_2^{*+} *signal plus background function (dashed curves). The lowest curves are the contributions of the* D_1^+ *and* D_2^{*+} *to the fit.*

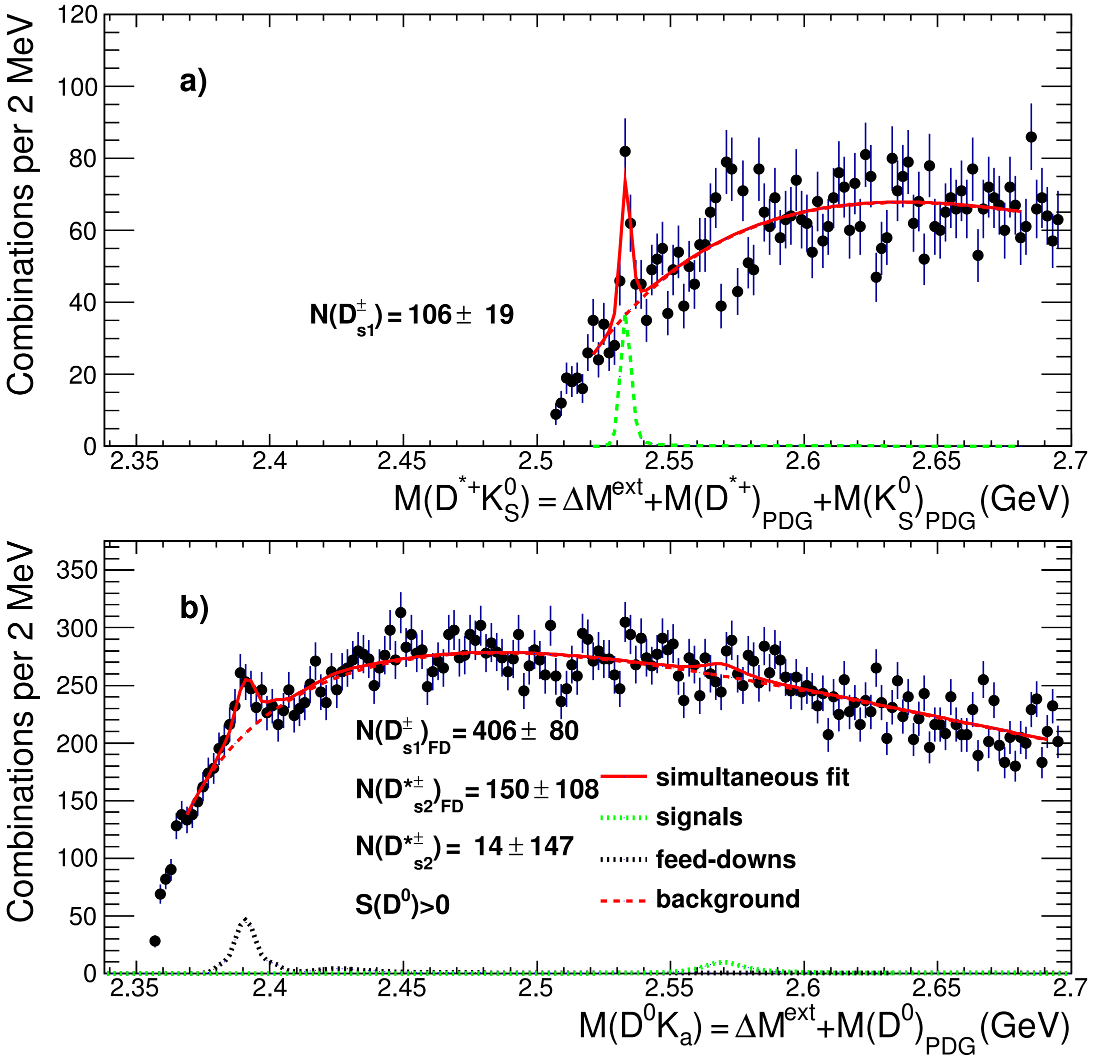

Figure 9.9: *Example of signal extraction procedure variation. The background shape was changed to the one used in [62] ; The mass distributions (dots), a) $M(D^{*+}K_S^0)$ and b) $M(D^0K_a)$ are shown. Compare to the spectra in Fig. 5.8 with the nominal selection and fit. The solid curves are the result of a simultaneous fit to a) D_{s1}^+ and to b) D_{s2}^{*+} and feed-downs plus background function (dashed curves).*

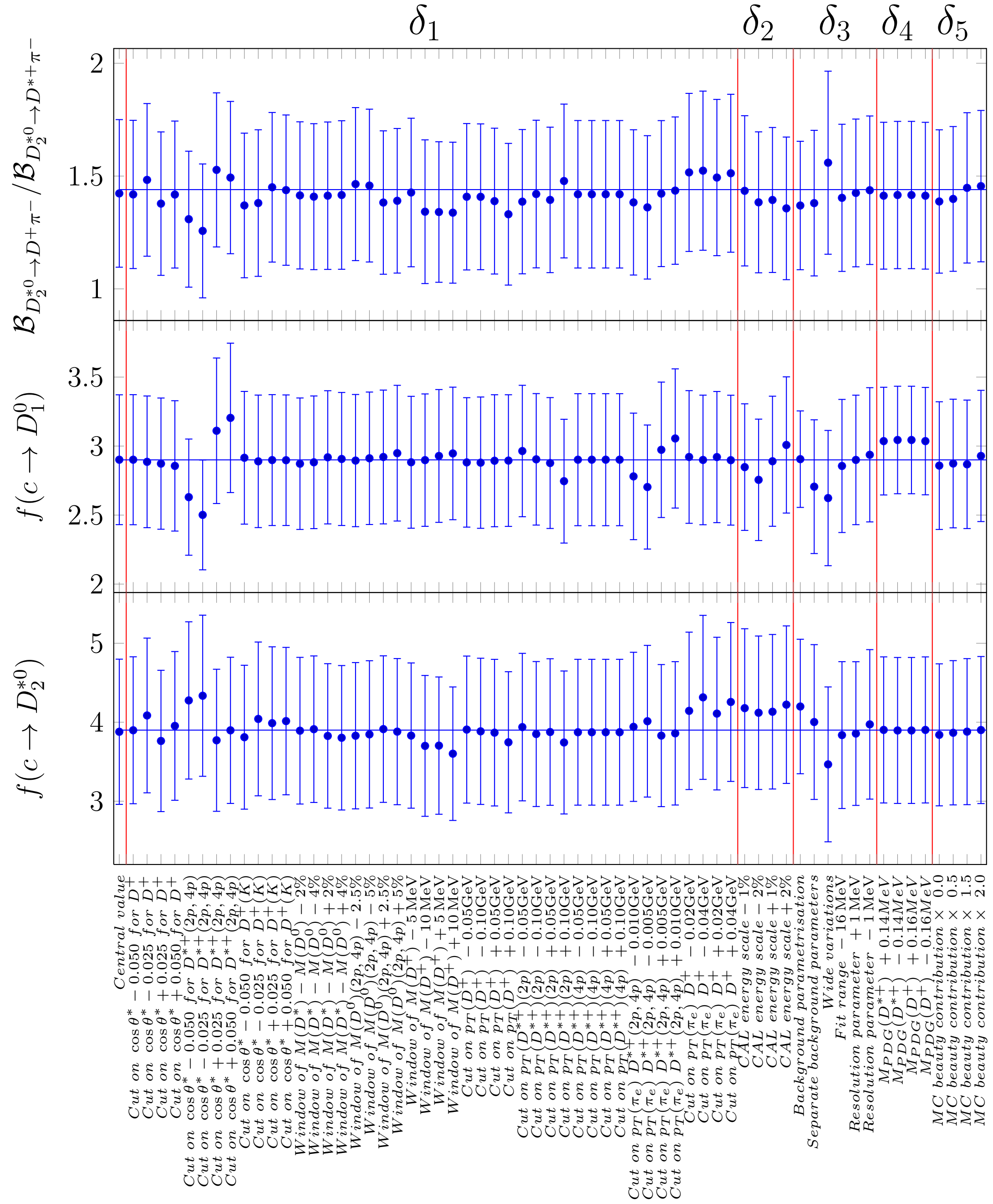

Figure 9.10: *The results of neutral excited charm meson fragmentation fractions and branching ratio with systematic variations. The individual systematic variations are put into groups* δ_1-δ_5 *(see text).*

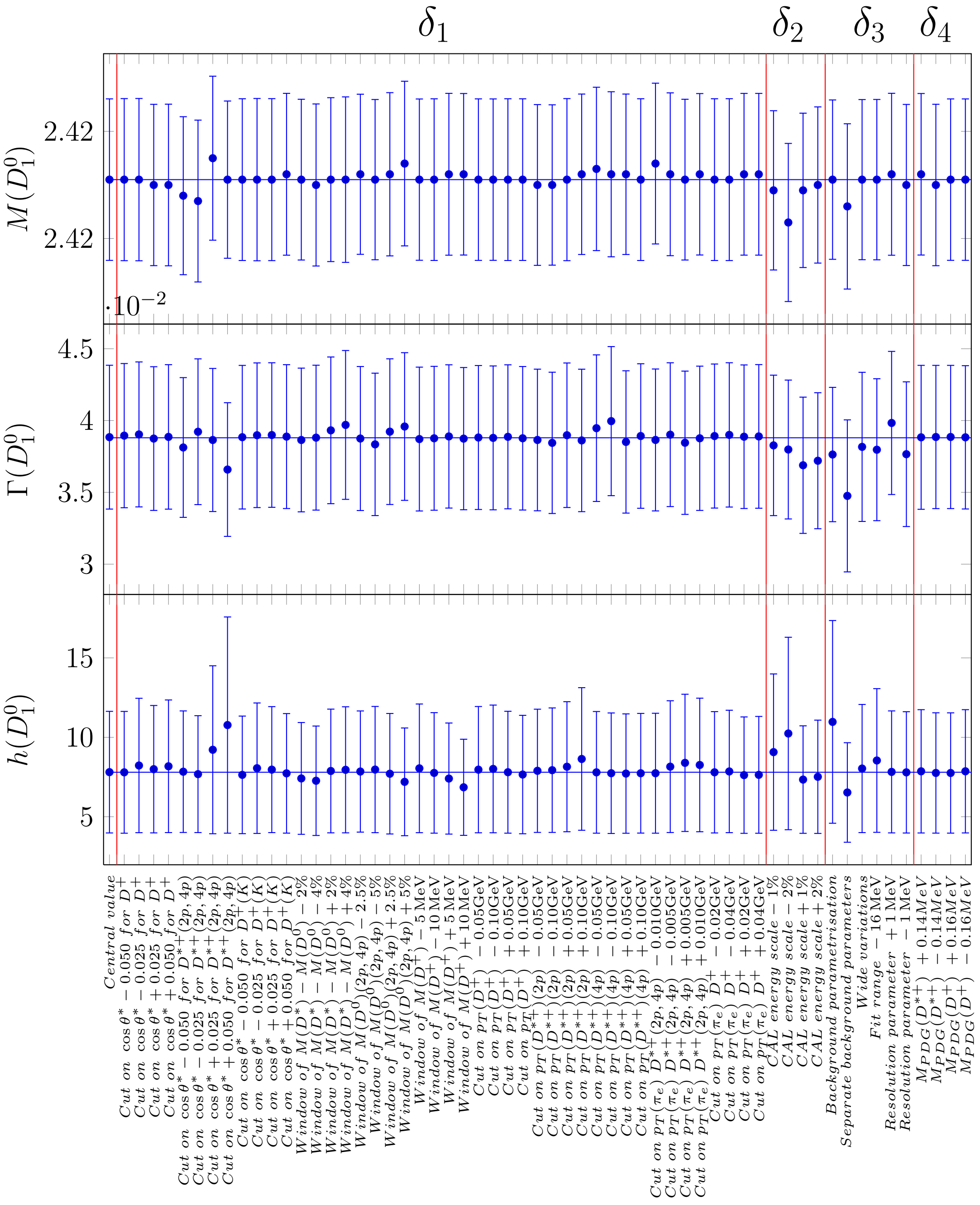

Figure 9.11: *The results of neutral excited charm meson fragmentation fractions and branching ratio with systematic variations. The individual systematic variations are put into groups* δ_1-δ_5 *(see text).*

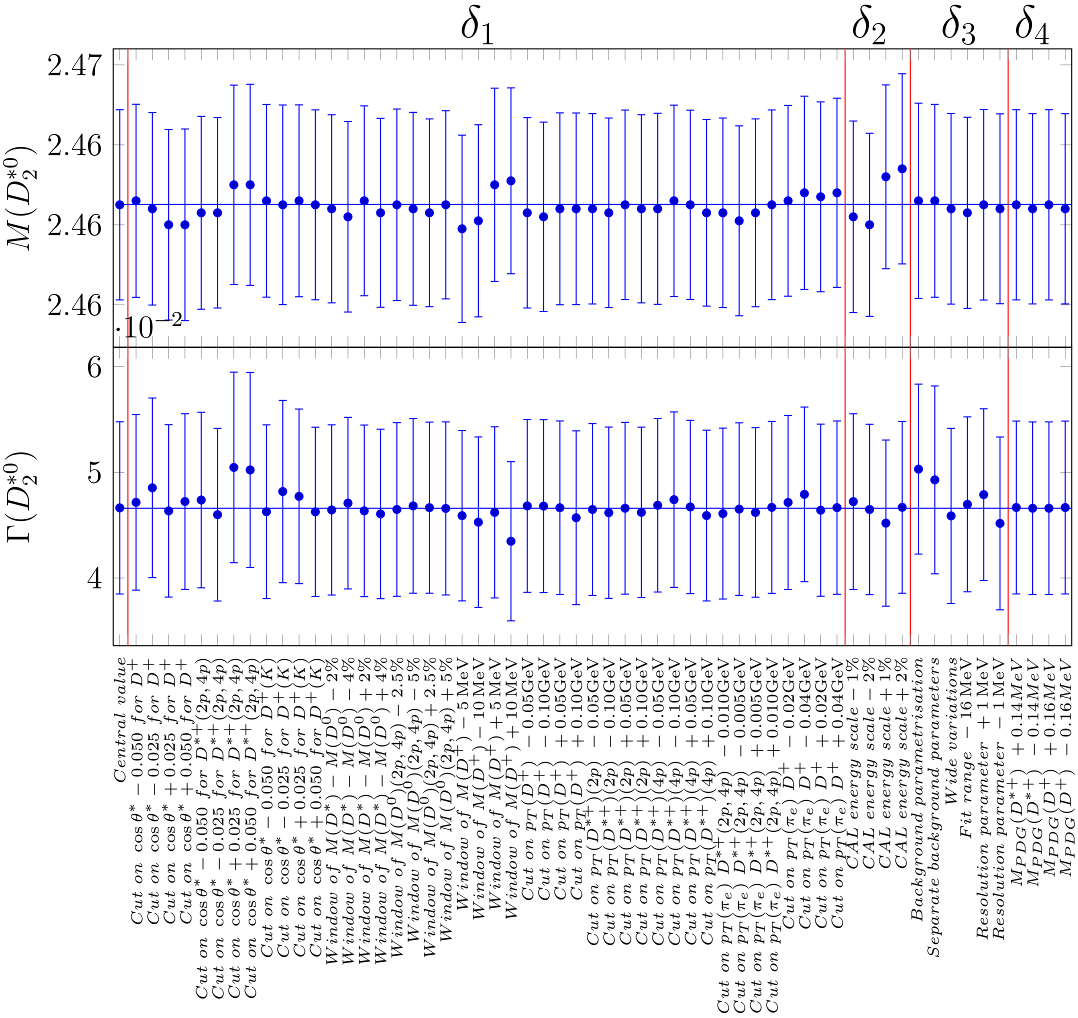

Figure 9.12: *The results of neutral excited charm meson fragmentation fractions and branching ratio with systematic variations. The individual systematic variations are put into groups δ_1-δ_5 (see text).*

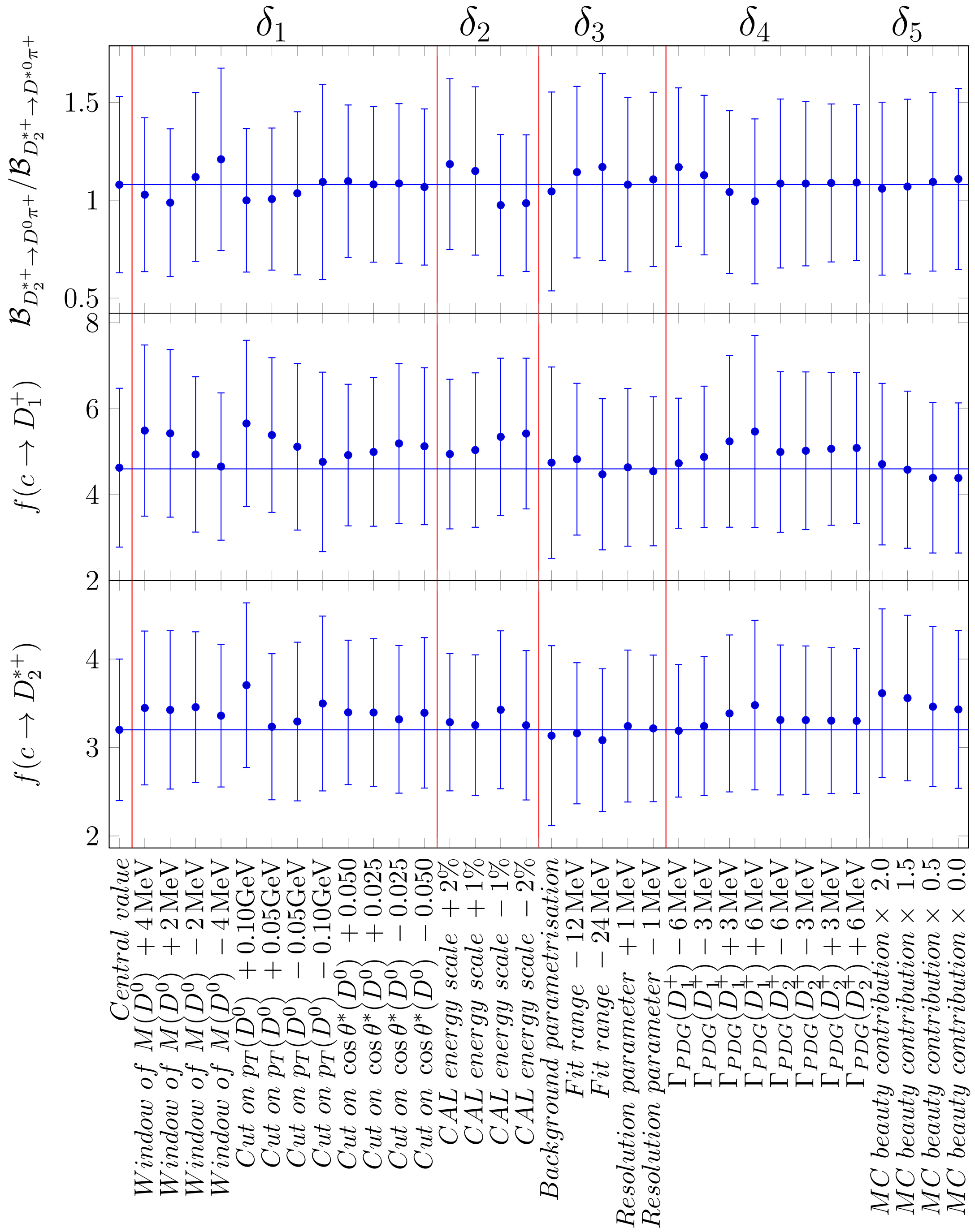

Figure 9.13: *The results of charged excited charm meson fragmentation fractions and branching ratio with systematic variations. The individual systematic variations are put into groups δ_1-δ_5 (see text).*

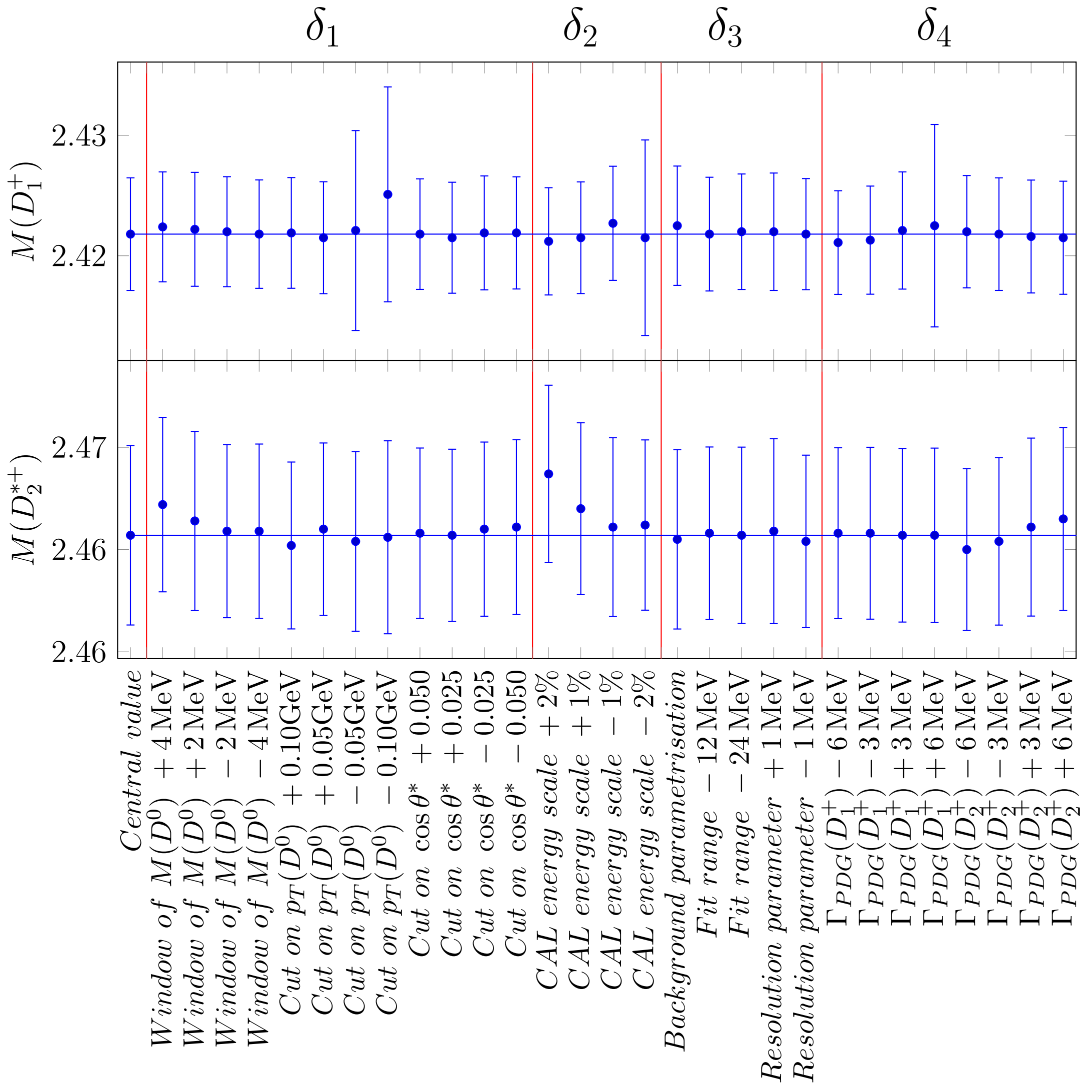

Figure 9.14: *The results of charged excited charm meson masses with systematic variations. The individual systematic variations are put into groups* δ_1-δ_4 *(see text).*

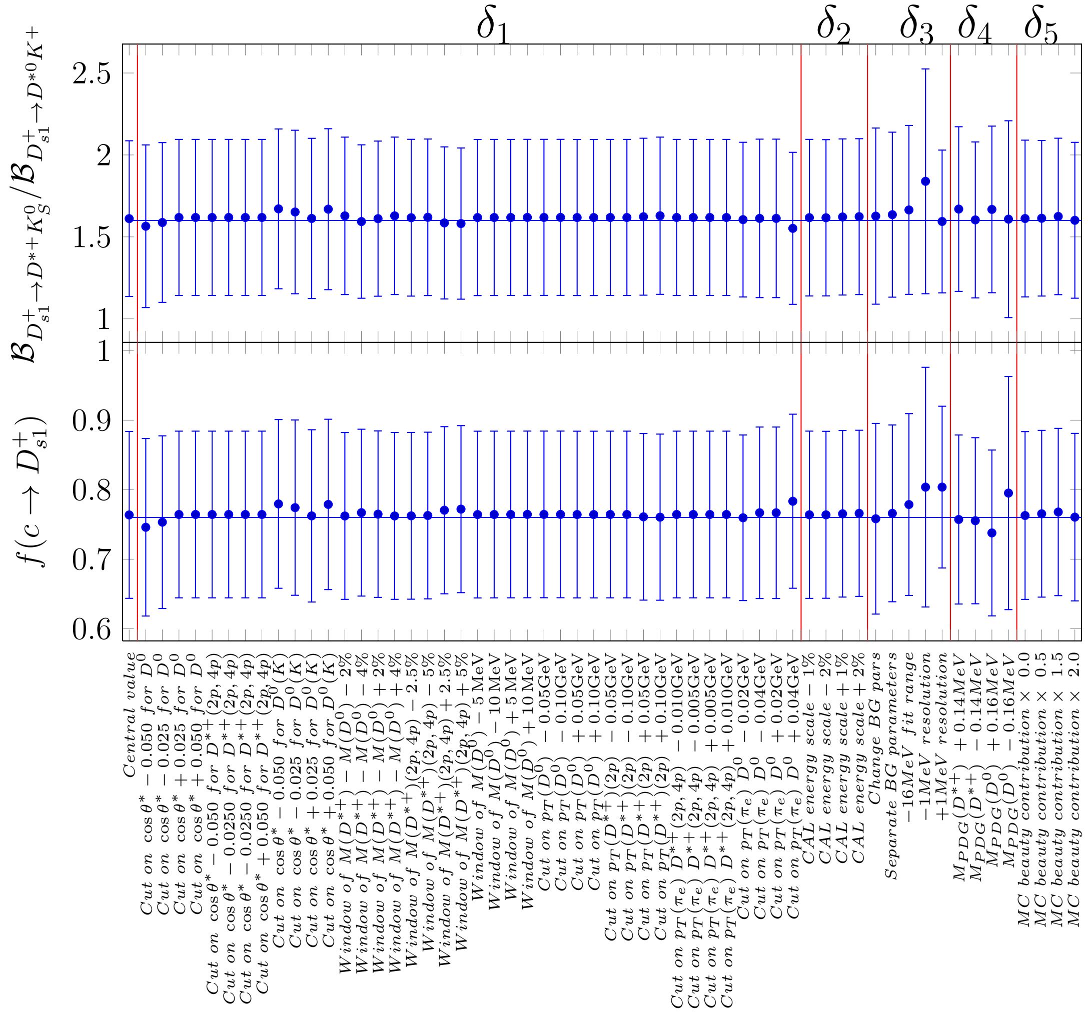

Figure 9.15: *The results of strange excited charm meson fragmentation fraction and branching ratio with systematic variations. The individual systematic variations are put into groups δ_1-δ_5 (see text).*

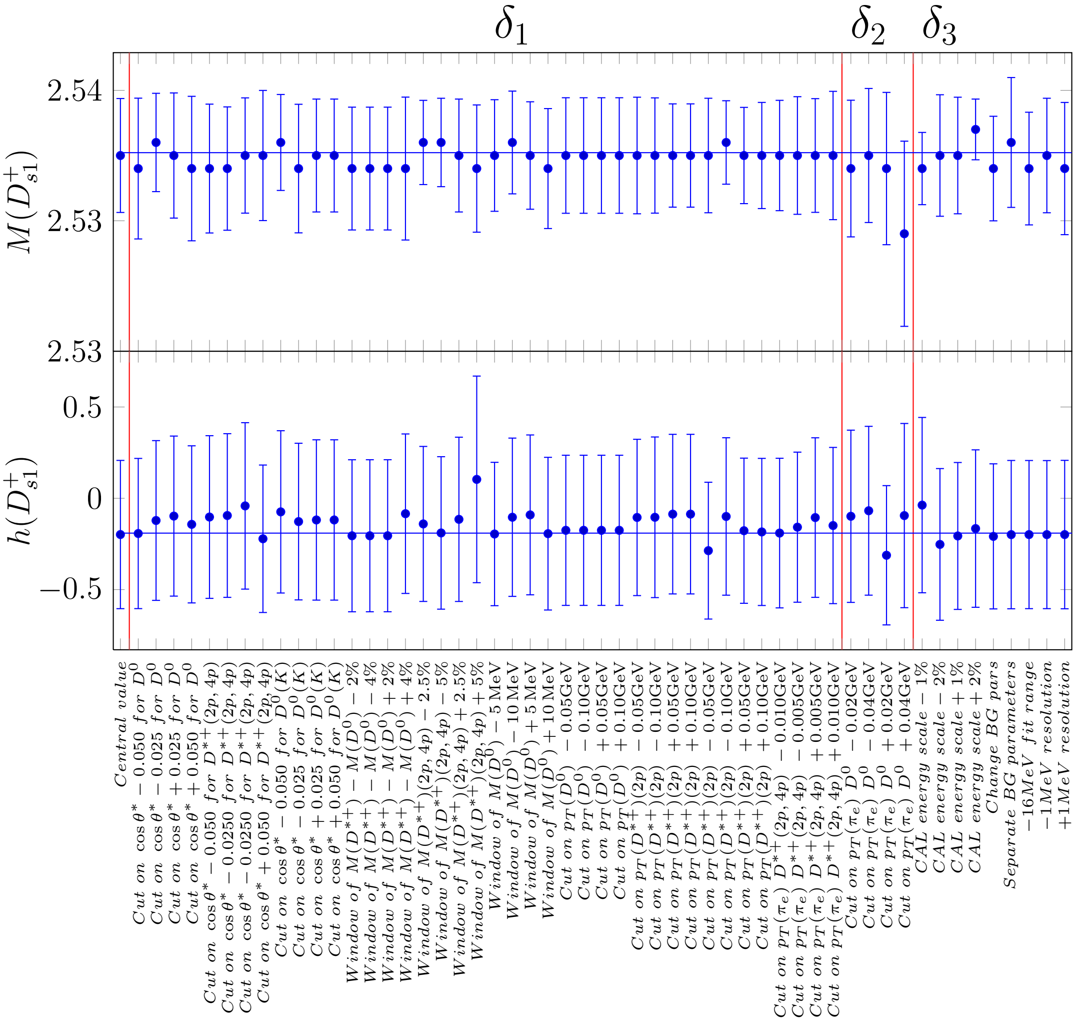

Figure 9.16: *The results of strange excited charm meson mass and helicity parameter with systematic variations. The individual systematic variations are put into groups δ_1-δ_4 (see text).*

	total	δ_1	δ_2	δ_3	δ_4
$M(D_1^0)$, MeV	$^{+0.4}_{-1.0}$	$^{+0.4}_{-0.3}$	$^{+0.0}_{-0.8}$	$^{+0.1}_{-0.5}$	$^{+0.1}_{-0.1}$
$M(D_2^{*0})$, MeV	$^{+1.3}_{-1.1}$	$^{+0.9}_{-0.9}$	$^{+0.9}_{-0.5}$	$^{+0.2}_{-0.2}$	$^{+0.0}_{-0.1}$
$\Gamma(D_1^0)$, MeV	$^{+1.9}_{-5.4}$	$^{+1.6}_{-2.3}$	$^{+0.0}_{-1.6}$	$^{+1.0}_{-4.5}$	$^{+0.0}_{-0.0}$
$\Gamma(D_2^{*0})$, MeV	$^{+5.9}_{-3.8}$	$^{+4.0}_{-3.5}$	$^{+0.1}_{-0.2}$	$^{+4.3}_{-1.7}$	$^{+0.0}_{-0.0}$
$h(D_1^0)$	$^{+4.6}_{-1.8}$	$^{+3.1}_{-1.3}$	$^{+2.4}_{-0.3}$	$^{+2.3}_{-1.3}$	$^{+0.1}_{-0.1}$

Table 9.2: *Total and δ_1-δ_4 (see text) systematic uncertainties for the mass, width and helicity parameters of the neutral excited charm mesons.*

	total	δ_1	δ_2	δ_3	δ_4	δ_5
$M(D_1^+)$, MeV	$^{+3.4}_{-1.2}$	$^{+3.2}_{-0.1}$	$^{+0.0}_{-0.7}$	$^{+0.6}_{-0.1}$	$^{+0.1}_{-0.1}$	$^{+0.6}_{-0.9}$
$M(D_2^{*+})$, MeV	$^{+3.7}_{-0.8}$	$^{+1.7}_{-0.5}$	$^{+3.1}_{-0.0}$	$^{+0.4}_{-0.2}$	$^{+0.1}_{-0.1}$	$^{+0.9}_{-0.6}$

Table 9.3: *Total and δ_1-δ_5 (see text) systematic uncertainties for the mass, width and helicity parameters of the charged excited charm mesons.*

	total	δ_1	δ_2	δ_3	δ_4
$M(D_{s1}^+)$, MeV	$^{+0.41}_{-0.22}$	$^{+0.35}_{-0.17}$	$^{+0.00}_{-0.10}$	$^{+0.20}_{-0.00}$	$^{+0.10}_{-0.10}$
$h(D_{s1}^+)$	$^{+0.43}_{-0.12}$	$^{+0.40}_{-0.02}$	$^{+0.13}_{-0.10}$	$^{+0.08}_{-0.06}$	$^{+0.00}_{-0.00}$

Table 9.4: *Total and δ_1-δ_4 (see text) systematic uncertainties for the mass, width and helicity parameters of the strange excited charm mesons.*

	total,%	$\delta_1, \%$	$\delta_2, \%$	$\delta_3, \%$	$\delta_4, \%$	$\delta_6, \%$	$\delta_7, \%$
$\mathcal{F}^{\rm extr}_{D_1^{*0}\to D^{*+}\pi^-/D^{*+}}$	$^{+19.2}_{-14.5}$	$^{+16.4}_{-12.2}$	$^{+6.7}_{-0.0}$	$^{+3.4}_{-7.5}$	$^{+0.3}_{-0.0}$	$^{+1.5}_{-2.0}$	$^{+6.5}_{-0.0}$
$\mathcal{F}^{\rm extr}_{D_2^{*0}\to D^{*+}\pi^-/D^{*+}}$	$^{+13.5}_{-18.2}$	$^{+11.9}_{-12.9}$	$^{+3.7}_{-5.0}$	$^{+1.2}_{-11.8}$	$^{+4.9}_{-0.0}$	$^{+0.9}_{-1.5}$	$^{+0.1}_{-0.0}$
$\mathcal{F}^{\rm extr}_{D_2^{*0}\to D^{+}\pi^-/D^{+}}$	$^{+25.2}_{-17.3}$	$^{+18.6}_{-7.8}$	$^{+11.9}_{-0.0}$	$^{+5.4}_{-15.4}$	$^{+1.0}_{-0.0}$	$^{+0.5}_{-0.8}$	$^{+10.7}_{-0.0}$
$\frac{\mathcal{B}_{D_2^{*0}\to D^{+}\pi^-}}{\mathcal{B}_{D_2^{*0}\to D^{*+}\pi^-}}$	$^{+20.1}_{-19.5}$	$^{+9.9}_{-13.5}$	$^{+0.0}_{-4.7}$	$^{+9.6}_{-3.3}$	$^{+0.0}_{-0.7}$	$^{+2.3}_{-2.5}$	$^{+14.4}_{-12.7}$
$f(c \to D_1^0)$	$^{+15.8}_{-18.6}$	$^{+11.9}_{-12.9}$	$^{+3.7}_{-5.0}$	$^{+1.2}_{-11.8}$	$^{+4.9}_{-0.0}$	$^{+0.9}_{-1.5}$	$^{+8.1}_{-3.6}$
$f(c \to D_2^{*0})$	$^{+22.4}_{-15.1}$	$^{+16.1}_{-9.1}$	$^{+8.9}_{-0.0}$	$^{+4.0}_{-10.7}$	$^{+0.6}_{-0.0}$	$^{+0.6}_{-1.0}$	$^{+12.2}_{-5.3}$

Table 9.5: *Total and δ_1-δ_7 (see text) relative systematic uncertainties for extrapolated fractions, for ratios of the dominant branching fractions and for fragmentation fractions of the D_1^0 and D_2^{*0} mesons.*

	total,%	$\delta_1, \%$	$\delta_2, \%$	$\delta_3, \%$	$\delta_4, \%$	$\delta_5, \%$	$\delta_6, \%$	$\delta_7, \%$
$\mathcal{F}^{\rm extr}_{D_1^{*+}\to D^{*0}\pi^+/D^{0}}$	$^{+42.6}_{-6.1}$	$^{+30.5}_{-0.0}$	$^{+18.3}_{-0.0}$	$^{+3.7}_{-2.6}$	$^{+0.0}_{-0.0}$	$^{+22.2}_{-0.0}$	$^{+1.8}_{-5.2}$	$^{+6.0}_{-1.9}$
$\mathcal{F}^{\rm extr}_{D_2^{*+}\to D^{*0}\pi^+/D^{0}}$	$^{+24.6}_{-14.8}$	$^{+14.7}_{-1.3}$	$^{+6.3}_{-2.4}$	$^{+1.2}_{-7.9}$	$^{+0.0}_{-0.0}$	$^{+13.5}_{-4.6}$	$^{+3.5}_{-4.0}$	$^{+12.5}_{-10.5}$
$\mathcal{F}^{\rm extr}_{D_2^{*+}\to D^{0}\pi^+/D^{0}}$	$^{+18.0}_{-8.0}$	$^{+13.4}_{-0.8}$	$^{+5.6}_{-4.3}$	$^{+0.2}_{-5.2}$	$^{+0.0}_{-0.0}$	$^{+3.6}_{-0.0}$	$^{+1.6}_{-1.4}$	$^{+9.8}_{-3.9}$
$\frac{\mathcal{B}_{D_2^{*+}\to D^{0}\pi^+}}{\mathcal{B}_{D_2^{*+}\to D^{*0}\pi^+}}$	$^{+23.8}_{-19.1}$	$^{+10.5}_{-8.5}$	$^{+8.3}_{-10.0}$	$^{+7.0}_{-4.7}$	$^{+0.0}_{-0.0}$	$^{+6.9}_{-9.1}$	$^{+2.7}_{-1.9}$	$^{+16.9}_{-9.3}$
$f(c \to D_1^+)$	$^{+42.7}_{-7.3}$	$^{+30.5}_{-0.0}$	$^{+18.3}_{-0.0}$	$^{+3.7}_{-2.6}$	$^{+0.0}_{-0.0}$	$^{+22.2}_{-0.0}$	$^{+1.8}_{-5.2}$	$^{+7.1}_{-4.4}$
$f(c \to D_2^{*+})$	$^{+16.7}_{-7.1}$	$^{+12.0}_{-0.0}$	$^{+1.8}_{-0.0}$	$^{+0.5}_{-5.4}$	$^{+0.0}_{-0.0}$	$^{+8.2}_{-1.2}$	$^{+2.5}_{-2.7}$	$^{+7.7}_{-3.6}$

Table 9.6: *Total and δ_1-δ_7 (see text) relative systematic uncertainties for extrapolated fractions, for ratios of the dominant branching fractions and for fragmentation fractions of the D_1^+ and D_2^{*+} mesons.*

	total,%	$\delta_1, \%$	$\delta_2, \%$	$\delta_3, \%$	$\delta_4, \%$	$\delta_5, \%$	$\delta_6, \%$	$\delta_7, \%$
$\mathcal{F}^{\rm extr}_{D^+_{s1}\to D^{*0}K^+/D^0}$	$^{+11.2}_{-5.5}$	$^{+3.8}_{-3.4}$	$^{+3.2}_{-0.0}$	$^{+4.1}_{-2.5}$	$^{+0.9}_{-0.7}$	$^{+0.0}_{-0.0}$	$^{+0.0}_{-0.0}$	$^{+9.1}_{-3.5}$
$\mathcal{F}^{\rm extr}_{D^+_{s1}\to D^{*+}K^0_S/D^{*+}}$	$^{+14.5}_{-12.2}$	$^{+5.6}_{-1.6}$	$^{+0.0}_{-0.6}$	$^{+4.2}_{-6.3}$	$^{+0.1}_{-0.1}$	$^{+0.0}_{-0.0}$	$^{+0.0}_{-0.0}$	$^{+12.7}_{-10.3}$
$\frac{\mathcal{B}_{D^+_{s1}\to D^{*+}K^0_S}}{\mathcal{B}_{D^+_{s1}\to D^{*0}K^+}}$	$^{+14.8}_{-11.3}$	$^{+4.2}_{-5.1}$	$^{+3.3}_{-0.0}$	$^{+5.0}_{-0.5}$	$^{+0.8}_{-0.6}$	$^{+0.0}_{-0.0}$	$^{+0.0}_{-0.0}$	$^{+12.8}_{-10.1}$
$f(c \to D^+_{s1})$	$^{+10.4}_{-5.7}$	$^{+3.5}_{-2.4}$	$^{+2.0}_{-0.0}$	$^{+4.1}_{-3.7}$	$^{+0.5}_{-0.4}$	$^{+0.0}_{-0.0}$	$^{+0.0}_{-0.0}$	$^{+8.6}_{-3.6}$

Table 9.7: *Total and δ_1-δ_7 (see text) relative systematic uncertainties for extrapolated fractions, for ratios of the dominant branching fractions and for fragmentation fraction of the D^+_{s1} meson.*

9.2 Additional checks

To increase confidence in the results, in addition to the systematic variations listed above, extra checks were performed:

- the effect of the reweighting of the $p_T(D)$ and $\eta(D)$ distributions of the MC sample was found to be negligible (see Sec. 3.9);
- the effect of the momentum bias (see Sec. 4.2) was checked by scaling the decay-particle momentum by $1 + \epsilon$, where $\epsilon = -0.003$, -0.0015, 0.0015, 0.003;
- the dE/dx selection quality was checked with a variation of l_π and l_K cuts by ±100%, the effect was found to be negligible;
- the possible dependence of the acceptance on $|\cos\alpha|$ was studied. At the generator level in the MC simulated sample, the distributions of $|\cos\alpha|(D^0_1)$ and $|\cos\alpha|(D^+_{s1})$ are flat. It has been found that the reconstructed and reconstructed-matched (see Sec. 4.5 on matching) signal distributions in the MC simulated sample (see Fig. 9.17) are also flat i.e. the acceptances of D^0_1 and D^+_{s1} do not depend on $|\cos\alpha|$.

The obtained results were not included to the total systematic uncertainties.

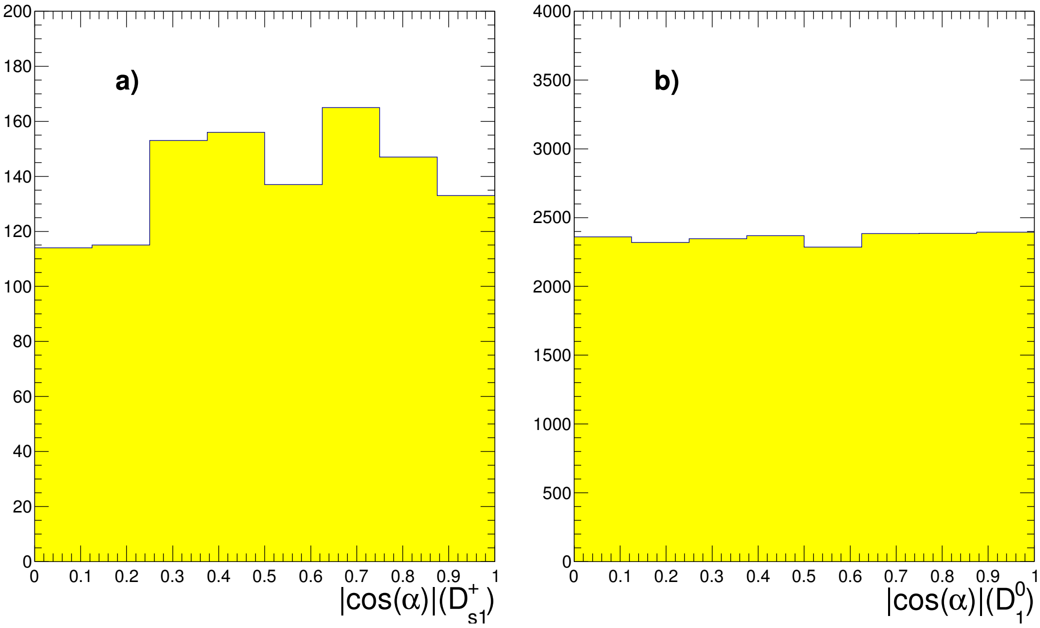

Figure 9.17: *Matched distributions of MC simulated decays a)* $|cos(\alpha)|(D^{+}_{s1})$ *b)* $|cos(\alpha)|(D^{0}_{1})$*. The distributions are consistent with the assumption of helicity independent (flat) acceptance.*

9.3 Conclusions on systematic uncertainties and checks

It is expected that the performed procedures for the estimation of systematic uncertainties cover a possible bias of the analysis results. The estimated systematic uncertainties have approximately the same size as the statistical uncertainties. It was found that there is no single uncertainty source ($\delta_1 - \delta_7$) that is dominant for all the measured quantities. However, the uncertainties related to the selection (δ_1) and signal extraction (δ_2) procedures are the largest. In general, individual variations affect the measurements in expected way, for example:

- the helicity parameter $h(D^0_1)$ is sensitive to background variations;
- the D^+_1 and D^{*+}_2 yields are sensitive to the variations of $\Gamma(D^+_1)$ and $\Gamma(D^{*+}_2)$;
- the D^+_{s1} yields are sensitive to the variation of resolution parameters.

10 Conclusions

In this thesis, the production of excited charm mesons at HERA and their properties were studied. The full available data taken by the ZEUS experiment from 2003 to 2007 has been used. Signals of $D_1(2420)^0$ and $D_2^*(2460)^0$ were seen in the $D^{*+}\pi^-$ decay mode and a clear $D_2^*(2460)^0$ signal was seen in the $D^+\pi^-$ decay mode. The study of excited charm meson properties was concentrated on spectroscopy including mass, width and helicity measurements and the measurement of fragmentation fractions and branching ratios.

The measured D_1^0 and D_2^{*0} masses and widths are in good agreement with the latest PDG values. The measured D_1^0 helicity parameter allows for some S-wave mixing in its decay to $D^{*+}\pi^-$. The result is also consistent with a pure D-wave hypothesis. The helicity of D_2^{*0}, when set free in the fit, is consistent with the HQET prediction, $h = -1$.

A clear $D_2^*(2460)^+$ signal is seen for the first time at HERA in the $D^{*0}\pi^+$ decay mode. Feed-downs of both resonances $D_1(2420)^+$ and $D_2^*(2460)^+$ in the decay mode $D^{*0}\pi^+$ are seen in the expected mass region of $M(D^0\pi^+) \approx 2.3$ GeV. To measure the mass parameters from the latter a special procedure has been developed.

The measured D_1^+ and D_2^{*+} masses are in good agreement with the PDG values and the D_2^{*+} mass is consistent with the precise measurements of BABAR.

The $D_{s1}(2535)^+$ signal is clearly seen in $D^{*+}K_S^0$ and $D^{*0}K$ decay modes. The measured mass is consistent with latest PDG. The measured D_{s1}^+ helicity parameter allows for some S- and D-wave mixing in its decay to $D^{*+}K_S^0$. The result contradicts the pure D-wave hypothesis.

The fractions of c-quarks hadronising into D_1^0, D_2^{*0} and D_{s1}^+ are consistent with those from the previous ZEUS publication and, in comparison with e^+e^- annihilation results, in agreement with charm fragmentation universality. The fractions of c-quarks hadronising into D_1^+ and D_2^{*+} were measured for the first time and are consistent, respectively, with the fractions of the neutral charm excited states D_1^0 and D_2^{*0}.

The ratios of the D_2^{*+}, D_2^{*0}, D_{s1}^+ dominant branching ratios are consistent with the PDG values.

11 Appendix:Fit procedure

The fit procedure is one of the most important parts of the analysis. The current section describes the fit procedure as well as related studies.

11.1 Fit parametrisation

The reconstructed mass spectra of the excited charm meson candidates contain several components. The most important one is the **signal** of excited charm mesons itself, which is present at the true and reconstructed levels. According to the theory, the mass distribution, M, of a resonance with a non-negligible natural width decaying into two particles is described by a relativistic Breit-Wigner function with a mass-dependent width [97]:

$$\frac{dN}{dM} \propto \frac{M M_0 \Gamma(M)}{(M^2 - M_0^2)^2 + M_0^2 \Gamma^2(M)}, \tag{11.1}$$

$$\Gamma(M) = \Gamma_0 \frac{M_0}{M} \left(\frac{p^*}{p_0^*} \right)^{2l+1} F^l(p^*, p_0^*),$$

where Γ_0 is the nominal resonance width, p^* is the momentum of the decay products in the resonance rest frame and p_0^* is the value of p^* at the resonance nominal mass M_0. The hadron transition form-factor, $F^l(p^*, p_0^*)$, in the Blatt-Weisskopf parametrisation [98] equals 1 for S-wave ($l = 0$) decays,

$$F^1(p^*, p_0^*) = \frac{1 + (p_0^* r)^2}{1 + (p^* r)^2}$$

for P-wave decays and

$$F^2(p^*, p_0^*) = \frac{9 + 3(p_0^* r)^2 + (p_0^* r)^4}{9 + 3(p^* r)^2 + (p^* r)^4}$$

for D-wave ($l = 2$) decays, where $r = 1.6\,\mathrm{GeV}^{-1}$ is a hadron scale. An example of a mass distribution according to the Breit-Wigner function is shown in Fig. 11.1. The described parametrisation Eq. (11.1) was used in the fit procedure for the data. In the used MC simulated samples, the shapes of D meson resonances are

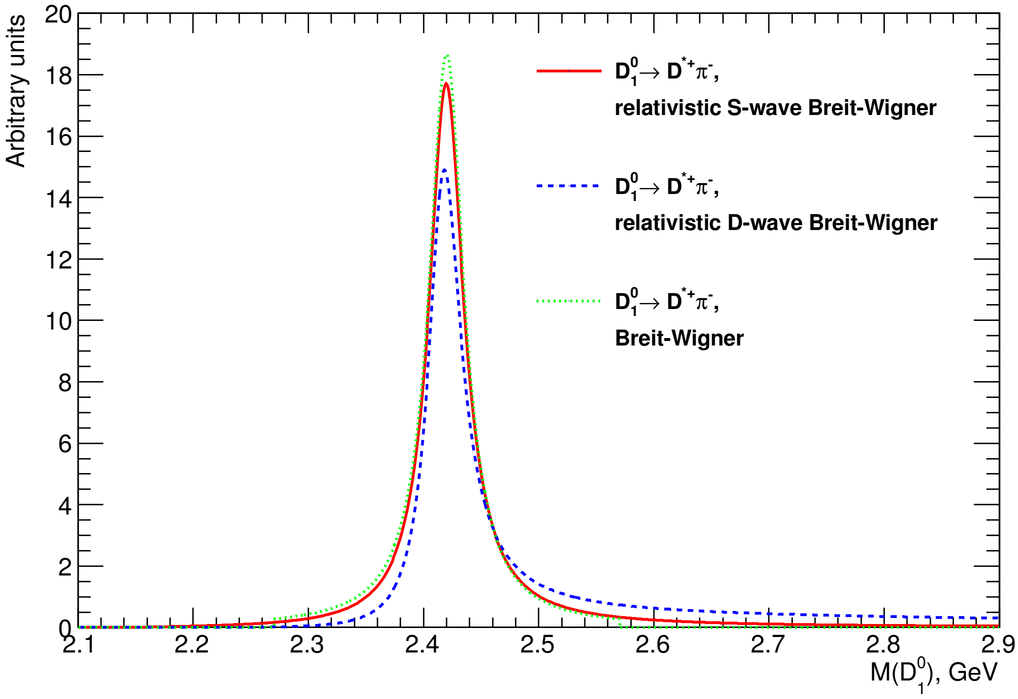

Figure 11.1: *The comparison of shape of the S- and D-wave Breit-Wigner distributions. The plots have the same normalisation. The parameters of signal are* $M(D_1^0) = 2.420\,GeV$, $\Gamma(D_1^0) = 37\,MeV$

simulated with a Breit-Wigner function [39]

$$\frac{dN}{dM} \propto \frac{1}{(M - M_0)^2 + \Gamma^2(M)/4}, \tag{11.2}$$

where $\Gamma = \Gamma_0$ is the nominal resonance width. Consequently, the parametrisation from Eq. (11.2) was used in the fit procedure for the MC simulated events. Near the nominal mass of the resonance, the shape of the Breit-Wigner function is very similar to the one of the relativistic Breit-Wigner, however the behaviour of the tails differs (e.g. the tails go below the physical threshold). For this reason the allowed values of M were limited in the MC simulations with range $[M_0 - 5\Gamma, M_0 + 5\Gamma]$. The same limits were used in the fit function.

Signals are not only peaking structures in the reconstructed mass spectra. Under certain conditions a decay chain with an incomplete reconstruction (i.e. one or more particles is not reconstructed) can produce distinct peaks. We call those peaks **feed-downs**. The main condition for the feed-down appearance is an extremely restricted kinematic space for the missing particle. In this case the reconstructed invariant-mass signal will be shifted from the nominal value and slightly distorted. The shift value will be close to the mass of the missing particle and the distortion strength will be proportional to the available kinematic space of the missing particle. A special procedure has been developed to measure the mass parameters from the feed-down signals. For a more detailed explanation let us consider the decay chain $D_{1,2} \to D^*\pi; D^* \to D\pi^0$ in the D^* centre of mass system. Let us for example assume the D_2^{*+} decay to a neutral D^{*0} meson and π^+ with a subsequent decay of D^{*0} to D^0 and neutral pion π^0 or photon γ. In the centre of mass system of D^{*0}, the D^0 and π^0 are produced with back-to-back momenta. The momenta of particles in this system are:

$$P_{\pi^+}^2 = \left(\frac{M^2 - M_{D^{*0}}^2 - M_{\pi^+}^2}{2M_{D^{*0}}}\right)^2 - M_{\pi}^2,$$

$$P_{D^0}^2 = P_{\pi^0}^2 = \left(\frac{M_{D^{*0}}^2 - M_{D^0}^2 + M_{\pi^0}^2}{2M_{D^{*0}}}\right)^2 - M_{\pi^0}^2,$$

where M is the D_2^{*+} mass. The measured $M^2(D^0\pi^+)$ is given by

$$M_m^2 = M^2(D^0\pi^+) = M_{D^0}^2 + M_{\pi^+}^2 + 2\sqrt{P_{D^0}^2 + M_{D^0}^2}\sqrt{P_{\pi^+}^2 + M_{\pi^+}^2} - 2P_{D^0}P_{\pi^+}\cos\alpha,$$

where α is the helicity angle between π^0 and π. Using the equations above one can parametrise M_m as:

$$M_m^2 = M^2(1-a) + b + g\sqrt{(M^2\text{-}d_1)(M^2\text{-}d_2)}\cos\alpha, \tag{11.3}$$

where

$$a = ({M_{D^{*0}}}^2 + {M_{\pi^0}}^2 - {M_{D^0}}^2)/(2{M_{D^{*0}}}^2),$$

$$b = {M_{\pi^0}}^2 - ({M_{D^{*0}}}^2 - {M_{\pi}}^2)({M_{D^{*0}}}^2 + {M_{\pi^0}}^2 - {M_{D^0}}^2)/(2{M_{D^{*0}}}^2),$$

$$g = \sqrt{({M_{D^{*0}}}^2 + {M_{\pi^0}}^2 - {M_{D^0}}^2)^2 - 4{M_{D^{*0}}}^2{M_{\pi^0}}^2}/(2{M_{D^{*0}}}^2),$$

$$d_1 = (M_{D^{*0}} + M_{\pi^+})^2,$$

$$d_2 = (M_{D^{*0}} - M_{\pi^+})^2.$$

From Eq. (11.3) one obtains M as a function of M_m and α

$$M = M(M_m, \alpha).$$

If the spectrum shape of M is

$$\frac{dN}{dM} = f(M),$$

where N is the number of events, then the M_m spectrum shape is

$$\frac{dN}{dM_m} = f(M(M_m))\frac{dM}{dM_m}.$$

Combining Eq. (11.3) with the normalised helicity angular distribution

$$\frac{dN}{d(\cos\alpha)} = \frac{1 + h\cos^2\alpha}{2(1 + h/3)}$$

yields

$$\frac{d^2N}{dM_m d(\cos\alpha)} = f(M(M_m, \alpha))\frac{dM}{dM_m}\frac{1 + h\cos^2\alpha}{2(1 + h/3)}. \tag{11.4}$$

The integral of the Eq. (11.4) over $\cos\alpha$ gives the shape of the feed-down:

$$\frac{dN}{dM_m} = \int_{-1}^{1} f(M(M_m, \alpha))\frac{dM}{dM_m}\frac{1 + h\cos^2\alpha}{2(1 + h/3)}d(\cos\alpha).$$

Using the explicit form of $M^2(M, \alpha) = \frac{-B\pm\sqrt{D}}{2A}$, where

$$A = (1 - a)^2 - g^2\cos^2\alpha,$$

$$B = 2(b - M_m^2)(1 - a) + g^2\cos^2\alpha(d_1 + d_2),$$

$$C = (b - M_m^2)^2 - g^2\cos^2\alpha d_1 d_2$$

and $D = B^2 - 4AC$ we can calculate $\frac{dM}{dM_m}$. The $f(M)$ is parametrised in the same way as for the prompt signals, with a (relativistic) Breit-Wigner function.

For the description of the $D^0\pi$ spectra, both decays $D^{*0} \to D^0\pi^0$ and $D^{*0} \to D^0\gamma$

are taken into account, while for the $D^+\pi$ spectra the decay $D^{*+} \to D^+\gamma$ was neglected (see Fig. 11.2).

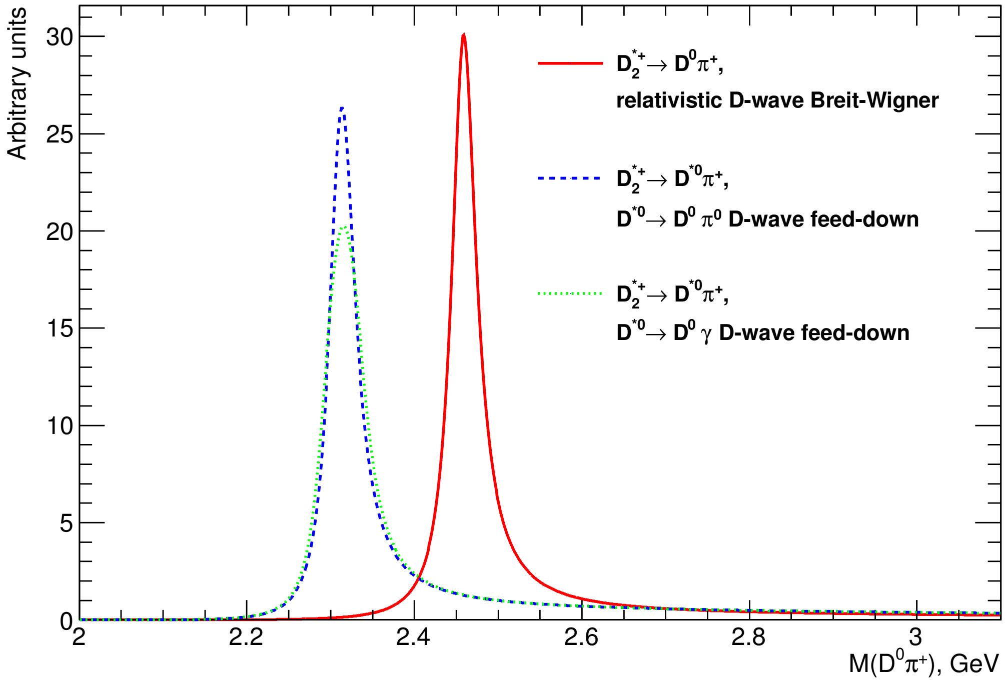

Figure 11.2: *The comparison of shape of the prompt $D_2^{*+} \to D^0\pi^+$ and feed-downs $D_2^{*+} \to D^{*0}\pi^+$, $D^{*0} \to D^0\gamma$, $D^{*0} \to D^0\pi^0$ in $D^0\pi^+$ mass spectrum. The plots have the same normalisation. The parameters of signal are $M(D_2^{*+}) = 2.460\,GeV$, $\Gamma(D_2^{*+}) = 37\,MeV$, $h(D_2^{*+}) = -1$.*

The other significant contribution to the reconstructed mass spectra is combinatorial **background**. As the background does not show any irregular features, it was assumed to be smooth and has been modelled in the following way.

- For the central values, a pure empirical parametrisation has been used.

  $$B(x) = A(x - M_D - M_\pi)^B e^{-C(x-M_D-M_\pi)-D(x-M_D-M_\pi)^2},$$

  where $x = M(D\pi)$.

- For systematical tests a background function from BaBar analysis [62] has been used.
  $$B(x) = P(x) \times \begin{cases} e^{c_1 x + c_2 x^2} & \text{for } x \leq x_0, \\ e^{d_0 + d_1 x + d_2 x^2} & \text{for } x > x_0, \end{cases}$$
  where $x = M(D\pi)$ and $P(x) = \frac{1}{2x}\sqrt{[x^2 - (m_D + m_\pi)^2][x^2 - (m_D - m_\pi)^2]}$ is a two-body phase-space factor. Only four parameters are free in the piecewise exponential: c_1, c_2, d_2, and x_0. The parameters d_0 and d_1 are fixed by requiring that $B(x)$ be continuous and differentiable at the transition point x_0.

The last considered contribution to the reconstructed mass spectra are **reflections and peaking background**. The reconstructed decay chains involve up to 6 different tracks. In the case of wrong combination of these tracks or wrong mass hypothesis assignment, the total mass of the reconstructed decay should fall into background and produce a smooth distribution. However, in many cases those tracks have a correlated origin e.g. belong to the same decay chain. In that case the background will have a complicated structure with possible bumps and dips. This makes the fit procedure more complicated. The following procedures were suggested to avoid non-smooth background in the reconstruction of $D^+ \to K^-\pi^+\pi^+$ decay:

- the signal from $D_s \to \phi(K^-K^+)\pi^+$ decay was removed with a cut on the mass combination $M(KK)$: $1.0115\,\text{GeV} < M(KK) < 1.0275\,\text{GeV}$;
- the signal from $D^{*+} \to K^-\pi^+\pi_s^+$ decay was removed from $M(K\pi\pi)$ mass spectrum with a cut on the mass difference $M(K\pi\pi) - M(K\pi) < 0.15\,\text{GeV}$.

Concerning the D^{*+} reconstruction, it is known that $D^{*+} \to D^0(K^-\pi^+)\pi^+$ and $D^{*+} \to D^0(K^-\pi^-\pi^+\pi^+)\pi^+$ decay modes have a lot of reflections, but all of them are related to the reconstruction of D^0: ($D^0 \to K^-l^+\nu_l$, $D^0 \to K^-\pi^+\pi^0$ etc.) and can be neglected for the D^{*+} reconstruction. The contamination caused by semileptonic decay modes is estimated from the MC simulations to be at a level of few percents.

The following procedure was suggested to avoid non-smooth background in the reconstruction of $D_{s1}^+ \to D^0(\pi^0)K^+$ and $D_{s2}^{*+} \to D^0(\pi^0)K, D^0K^+$ decays:

- The signal of $D^{*+} \to K^-\pi^+\pi_s^+$ decay was removed from the $M(K\pi K)$ mass spectrum with a cut on the mass difference $M(K\pi\pi) - M(K\pi) < 0.15\,\text{GeV}$.

The following reflections were seen in the excited charm meson mass spectra:

- The reflection in the $M(D^{*+}\pi_a)$ spectrum(see Fig. 11.3(a)) appears if K, π and π_a tracks originated from the $D^{*+}_{\text{true}} \to K_{\text{true}}\pi_{\text{true}}\pi_{s\ \text{true}}$ decay. In this decay K_{true} and π_{true} are swapped, but the formed D^0 candidate still has a proper mass. Latter, the D^0 candidate with an incidental track forms a valid D^{*+} candidate that is used for the further combination with π_a, which is in reality $\pi_{s\ \text{true}}$.

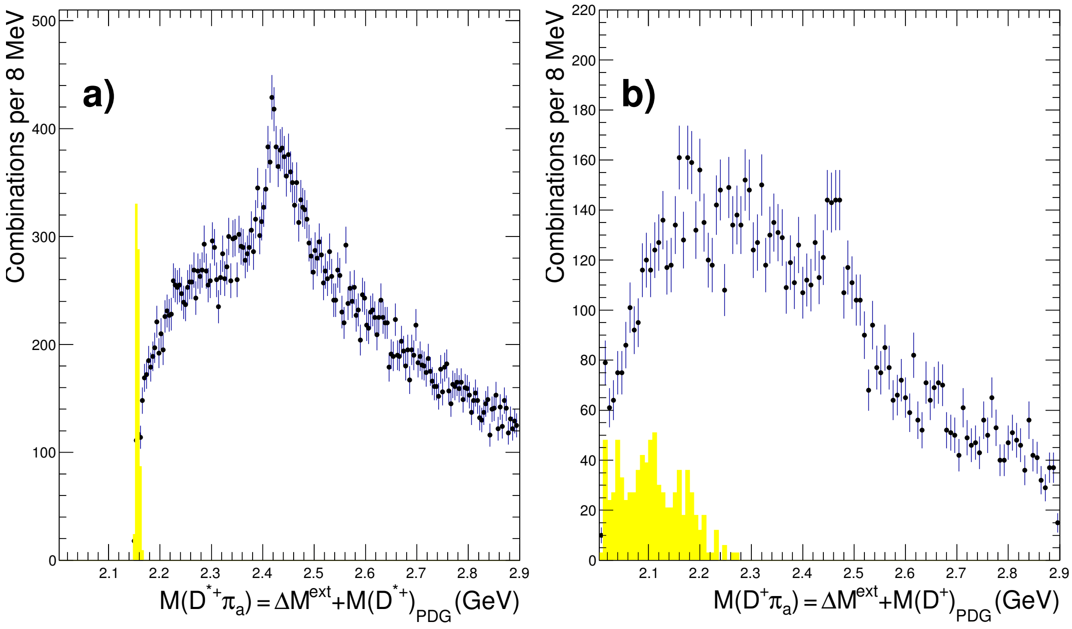

Figure 11.3: *Reflections in reconstructed spectra (dots): a) in* $D^{*+}\pi$ *spectrum, candidates with* $0.1405\,GeV < M(D^0\pi_a) - M(D^0) < 0.1505\,GeV$ *(yellow) and b) in* $D^+\pi$ *spectrum: candidates with* $|M(K\pi\pi\pi_a) - M(D^0)_{\text{PDG}}| < 15\,MeV$ *(yellow). The reflections are scaled by factor 3.*

- The reflection from $D^0 \to K3\pi$ decays in the $M(D^+\pi_a)$ spectrum appears around $M(D^+) + M(\pi)$, when the D^+ candidate is combined from three D^0 decay tracks, with wrong mass assignment (see Fig. 11.3(b)).

Even though it is very easy to reduce significantly the amount of reflections, it is more convenient to exclude the reflection region from the fit.

11.2 Acceptance and resolution

Detector reconstruction distorts the mass spectrum of a resonance. The size of this bias is different in different parts of the spectrum. However, in a very simple approach it can be described with two quantities, acceptance and resolution, with the following definition.

The acceptance in the mass spectrum $E(x)$ is the probability to reconstruct the decay with a true mass x. In the current context only the relative acceptance $E(x)/E(M_0)$ is used.

The resolution in the mass spectrum $R(x, x_0)$ is a probability for the reconstructed decay with true mass x to have the reconstructed mass x_0.

In the case of a binned spectrum, the functions should be replaced with acceptance $\hat{E}$ and resolution $\hat{R}$ "matrices". The "acceptance matrix" is diagonal

$$\hat{E} = diag\{E_1, E_2, \cdots\},$$

and the the elements E_i are the probabilities to reconstruct the resonance with the mass in bin i. Each element R_{ij} of the "resolution matrix" $\hat{R}$ represents the probability for a decay with true mass in bin j to be reconstructed in the bin i. By definition,

$$\sum_{i=1}^{\infty} R_{ij} = 1.$$

In this approach, the binned reconstructed spectrum x' is related to the true spectrum x as

$$x' = \hat{R}\hat{E}x. \tag{11.5}$$

The Eq. (11.5) has been used in the fit procedure to take into account the reconstruction level bias. The acceptance and resolution matrices were estimated using matching of the reconstructed decays to the decays on true level in the MC simulated samples. The obtained matrices were approximated with the following functions separately for signals and feed-downs:

$$R(M, M') = \frac{1}{\sqrt{2\pi}\sigma} e^{-\frac{(M-M')^2}{2\sigma^2}}, \tag{11.6}$$

$$E(M) = 1 + A \times (M - M_0), \tag{11.7}$$

where $\sigma = \sigma_0 + B \times (M - M_0)$ and M_0 is an arbitrary constant, chosen to be close to to the nominal masses of the resonances. It was found that the acceptance is flat in the studied mass range i.e. the coefficients A from Eq. (11.7) are consistent with 0. The result of the resolution fits are listed in Tab. 11.1.

Decay chain	Resolution, MeV
Parametrisation	$\sigma = \sigma_0 + B \times (M[\,\mathrm{GeV}] - M_0[\,\mathrm{GeV}])$
$D_1^0, D_2^{*0} \to D^{*+}\pi^-, D^{*+} \to D^0(K\pi)$ $M(D_1^0, D_2^{*0})_{\mathrm{rec.}} - M(D_1^0, D_2^{*0})_{\mathrm{MC\ true}}$	4.70±0.70+(7.32±5.50)(M-2.44115)
$D_1^0, D_2^{*0} \to D^{*+}\pi^-, D^{*+} \to D^0(K3\pi)$ $M(D_1^0, D_2^{*0})_{\mathrm{rec.}} - M(D_1^0, D_2^{*0})_{\mathrm{MC\ true}}$	5.35±0.88+(10.60±7.14)(M-2.44115)
$D_2^{*0} \to D^+\pi^-$ $M(D_2^{*0})_{\mathrm{rec.}} - M(D_2^{*0})_{\mathrm{MC\ true}}$	6.95±1.06+(9.16±7.00)(M-2.4622)
$D_1^0, D_2^{*0} \to D^{*+}\pi^-, D^{*+} \to D^+$ $M(D^+\pi)_{\mathrm{rec.}} - M(D^+\pi)_{\mathrm{MC\ true}}$	4.56±0.20+(11.14±4.73)(M-2.30617)
$D_2^{*+} \to D^0\pi^+$ $M(D_2^{*+})_{\mathrm{rec.}} - M(D_2^{*+})_{\mathrm{MC\ true}}$	7.57±1.18+(8.17±8.10)(M-2.4654)
$D_1^+, D_2^{*+} \to D^{*0}\pi^+, D^{*0} \to D^0(K\pi)$ $M(D^0\pi)_{\mathrm{rec.}} - M(D^0\pi)_{\mathrm{MC\ true}}$	6.58±1.04+(9.35±7.68)(M-2.30942)
Parametrisation	$\sigma = \sigma_0$
$D_{s1} \to D^{*+}K_S^0$ $M(D_{s1})_{\mathrm{rec.}} - M(D_{s1})_{\mathrm{MC\ true}}$	1.5
$D_{s1} \to D^{*0}K^+, D^{*0} \to D^0(K\pi)$ $M(D^0K)_{\mathrm{rec.}} - M(D^0K)_{\mathrm{MC\ true}}$	1.5

Table 11.1: *Resolution in reconstructed the mass spectra. The values obtained from MC samples using the weak matching procedure.*

As the resolutions for the decay chains $D^{**} \to D^{*+}\pi_a; D^{*+} \to D^0\pi; D^0 \to K\pi$ and $D^{**} \to D^{*+}\pi_a; D^{*+} \to D^0\pi; D^0 \to K3\pi$ is the same within uncertainties, the spectra were added (see Sec. 5) and fitted with a single resolution, the one for the $D^{**} \to D^{*+}\pi_a; D^{*+} \to D^0\pi; D^0 \to K\pi$ decay chain.

11.3 Fit implementation

All fits were performed with a maximal likelihood criteria. The theory expectation in each bin was evaluated as an average (an integral divided by the bin width) of the fit function. The integral was estimated as a Legendre-Gauss Quadrature with 32 points [99]. The integral over the helicity took into account that the helicity dependence of the fit function is quadratic, so that the Newton-Cottes quadrature with 2 points [100] gives the exact result.

The normalisation of the signal function to the signal yield was performed using precalculated (one calculation per call of the minimised function) integrals on the 2-D width-mass grid and quadratic approximation for the values between the grid knots. The normalisation of the wide states was performed with precalculated integrals. All the integrals for normalisation used the ranges of the fit as bounds.

The minimisation has been performed with patched[31] MINUIT package [101]. The main fit algorithm for minimisation was MIGRAD. The symmetric uncertainties on the fit parameters were estimated with HESSE and asymmetric with MINOS algorithms from the MINUIT package. All calculations were performed with double precision (types *double* in C or *double precision* in FORTRAN). To speed up the fitting procedure the code was parallelised with the PTHREADS library [102].

---

[31] The MINUIT code was patched to increase the maximal number of parameters from 30 to 60.

12 Appendix:Using the Grid for the ZEUS experiment

12.1 Introduction

This section describes the general ideas of a computing grid, particularly the EGI Grid [103] and its utilisation for computing in the ZEUS experiment.

A grid is a system for a distributed computing. The basic idea behind the computing grids has an analogy with the electrical "power grid". It implies the accessing of large computer resources from any computer in the Internet should be as simple as accessing electrical power from an electrical grid. Many large projects successfully implemented and utilised these ideas for different purposes. The key of their success is to provide global resource sharing, secure access and efficient resource utilisation based on open standards.

One of the first grid projects established for purposes of HEP was the EDG (European Data Grid) project [104] and its successors, EGEE (Enabling Grids for E-sciencE) [105] and EGI (European Grid Initiative) projects [103]. The EGI project is now in the active phase and coordinates grid efforts of almost 30 NGI (National Grid Initiatives) and two European intergovernmental research organisations – CERN and EMBL (European Molecular Biology Laboratory). Since 2004 DESY operates a Grid Centre in the context of the National Grid Initiative NGI-DE of the EGI. The ZEUS experiment together with the H1 and HERMES is officially supported by EGI. Thus, more than two dozen sites worldwide grant computing resources to the dedicated Grid Virtual Organisation (ZEUS VO)[32].

12.2 EGI infrastructure

Every particular Grid implementation is based on a low-level software, which is called middleware. The most common middleware within EGI is gLite [107]

---

[32] A Virtual Organisation (VO) is basically a group of people that are authorised to run Grid jobs on a set of Grid resources. For example, a research project members can join in a VO, so that they can negotiate access to Grid resources, policies etc. Typically, a VO has a manager which maintains the list of members and contacts resource owners whenever a negotiation is needed, for example, if a new user has a certificate issued by a new CA, or CA public keys have changed. VO managers are normally in charge of negotiating resources available for the VO members. Each site on the Grid can subscribe to different VO's allowing all their members to run grid jobs on the corresponding site [106].

and its successor, EMI [108]. This middleware is currently deployed on hundreds of sites and enables global science in a number of disciplines, notably serving the LCG (LHC Computing Grid) and many other projects. The simplified Grid system, according to Ref. [109] includes:

- A **User Interface (UI)** is an access point to the EGI Grid. This can be any machine where users have a personal account and where their user certificate is installed. From a UI, a user can be authenticated and authorised to use the EGI resources, and can access the functionality offered by the Information, Workload and Data management systems described below. It provides tools to perform some basic Grid operations:
    - list all the resources suitable to execute a given job;
    - submit jobs for execution;
    - cancel jobs;
    - query the status of jobs and retrieve their output;
    - copy, replicate and delete files from the Grid;
    - submit and manage file transfer jobs;
    - retrieve the status of different resources from the Information System.

  In addition, the EGI APIs[33] are also available on the UI to allow development of Grid-enabled applications.

- A **Workload Management System (WMS)** serves to accept user jobs, to assign them to the most appropriate **Computing Element (CE)**, to record their status and retrieve their output. Jobs to be submitted are described using the **Job Description Language (JDL)**, which specifies, for example, which executable to run and its parameters, files to be moved to and from the **Worker Node (WN)**, machine, on which the job is run, input Grid files needed, and any requirements on the CE and the Worker Node. The choice of the CE to which the job is sent is made in a process called match-making, which first selects, among all available CEs, those which fulfil the requirements expressed by the user and which are close[34] to specified input Grid files. It then chooses the CE with the highest rank, a quantity

---

[33] Application Programming Interface

[34] i.e. have the best I/O speed

derived from the CE status information which expresses the "goodness" of a CE (typically a function of the numbers of running and queued jobs). The gLite WMS allows not only the submission of single jobs, but also collections of jobs (possibly with dependencies between them). Finally, the **Logging and Bookkeeping service (LB)** (see Ref. [109]) tracks jobs managed by the WMS. It collects events from many WMS components and records the status and history of the job.

- A **Computing Elements (CE)**, in Grid terminology, is some set of computing resources localised at a site (i.e. a cluster, a computing farm). A CE includes a Grid Gate (GG), which acts as a generic interface to the cluster; a batch system, and the cluster itself, a collection of Worker Nodes (WNs) to run the jobs. The GG is responsible for accepting jobs and dispatching them for execution on the WNs. The WNs have an arbitrary set of installed software applications. VO-specific software may be installed at sites in a dedicated area, typically on a shared file system accessible from all WNs. It is worth stressing that, strictly speaking, a CE corresponds to a single queue in the batch. According to this definition, different queues defined in the same cluster are considered different CEs. This is currently used to define different queues for jobs of different lengths or other properties (e.g. RAM size), or for different VOs.

In addition to that very important components of Grid infrastructure are:

- A **Storage Element (SE)** provides uniform access to data storage resources (dcache, disk arrays) via different data access protocols (GSIFTP) and interfaces (dcap, xroot, NFS). Most sites provide at least one SE. Most storage resources are managed by a Storage Resource Manager (SRM), a service providing capabilities like transparent file migration from disk to tape, space reservation, etc. The storage element might be build with a disk-based storage only or with front-end disks and back-end tape storage.

- A **File Catalogue** provides mappings between different file names: Grid Unique IDentifier (GUID), Logical File Name (LFN), Storage URL (SURL) and Transport URL (TURL). While the GUIDs and LFNs identify a file irrespective of its location, the SURLs and TURLs contain information about where a physical replica is located, and how it can be accessed. In the same time the files are stored in Storage Elements. Currently, the only file catalogue officially supported in WLCG/EGI is the LCG File Catalogue (LFC).

- An **Information Service (BDII)** provides information on the existence of EGI Grid resources and further information about their structure and state. This information is essential for the use and operation of the Grid, as it is via the Information System that resources are discovered. The published information is also used for monitoring and accounting purposes.

A simplified diagram of Grid infrastructure is shown in Fig. 12.1.

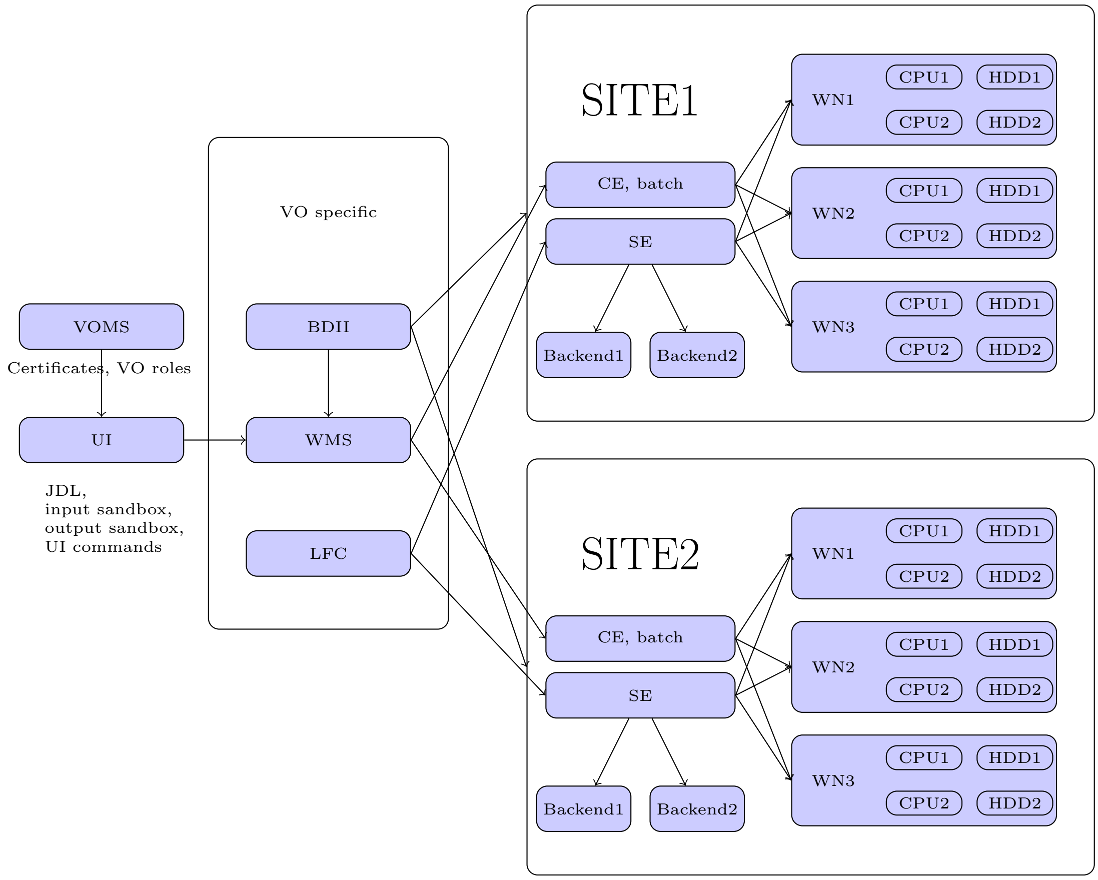

Figure 12.1: *A simplified infrastructure of the EGI Grid.*

Despite the whole Grid infrastructure being quite complicated, the user deals mainly with UI, I/O operations (copy and write to/from SE), and the VO-specific software. The support of the latest one for the ZEUS experiment, as well as ZEUS VO management was on the tasks of the author. The other important task, the support of ZEUS MC event simulation on the Grid is described in the next section.

12.3 Grid usage for ZEUS MC event simulation

The procedure for the event reconstruction on Grid CEs is very similar to the reconstruction performed on a classical FUNNEL, described elsewhere [110]. The most important difference is that on the MOZART, ZGANA and ZEPHYR executables run one after other on the whole output. On the other hand, the life-cycle of a simulation job in ZEUS Grid site system is very similar to any generic Grid job. A brief description of the life-cycle, starting from registration is given below. A scheme for the described work-flow is shown in Fig. 12.2.

- **The registration** of new jobs is implemented in script “gridregister.sh” that is executed via crontab every 5 minutes (in case it is not already running). The script checks the content of a directory where the links to the input files reside and registers all the files on SE. For each file a set of sub-jobs is created in MySQL database with number of events that does not exceed some limit, which is set in “Funnel.properties” file (after the upgrade in 2011 the limit is between 3000 and 5000 and depending on the MC sample). At the same time, a unique ID is assigned for each sub-job. The job gets status “REGISTERED” after this procedure.

- **The Submission** of new jobs is implemented in scripts “gridsubmit1.sh”, “gridsubmit2.sh”, “gridsubmit3.sh” that are executed via crontab every 5 minutes (in case they are not already running). Each of those scripts deals only with sub-jobs with ID in a certain range (e.g. $0 < ID < 51$). Each script loops over all jobs with status “READY” or “FAILED”, prepares a JDL file from template. The content of the template depends on configuration files “Queues.properties”, with the list of used CE sites and a JDL file, where the list of logical conditions is set. The script uses a **delegated**[35] proxy for submission to the WMS. In case of successful submission the job gets status “SUBMITTED”. If the submission fails (e.g. the proxy has expired, there is no CE element that satisfy logical conditions, etc.) the job remains in status “READY”.

---

[35] The same proxy is used for multiple jobs.

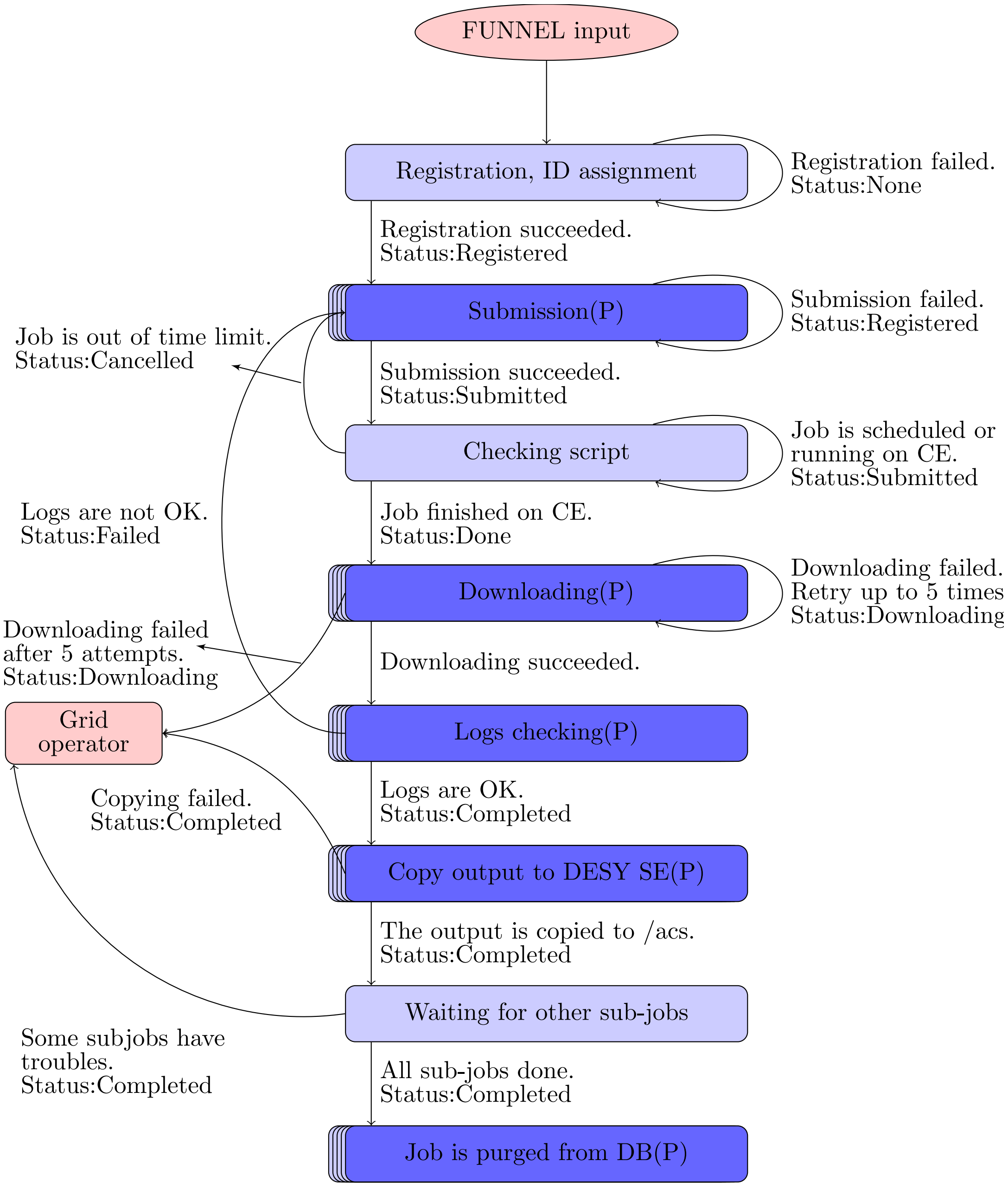

Figure 12.2: *Workflow of the ZEUS MC jobs on the Grid after upgrade. The processes with (P) and dark blue nodes after the upgrade are executed in parallel. Exceptional situations are handled by the Grid operator manually.*

- **The checking** of job status is implemented in script "gridproc.sh", that is executed via crontab every 5 minutes (in case it is not already running). This script checks the status of all "SUBMITTED" jobs. Normally, the jobs with status "SUBMITTED" are submitted on CE, scheduled and then executed. During the execution, jobs run scripts to copy the input from SE, split it, copy the GAF tarball from SE, unpack it, select the proper executables, run Mozart, Zgana and Zephyr sequentially, copy the output to SE and pack logs. The packed logs are put into the output sandbox. At this stage the execution finishes. Jobs that have finished its execution on the Grid enter status "DONE". In case the job is in the "SUBMITTED" status for more than 30 hours and the execution has not started yet, the job is cancelled and returns to "READY" status. In some rare cases the job fails on CE (no libraries/executables or there is no access to SE with input files or GAFs) and the script cancels the job.

- **The downloading of jobs** is implemented in scripts "gridcomplete1.sh" and "gridcomplete2.sh". that are executed via crontab every 5 minutes (in case they are not already running). The scripts download the output sandbox of "DONE" jobs. The sandbox includes log files of Mozart, Zgana and Zephyr. The scripts check content of every log for a certain patterns with error/success messages. If at least one error message is found or at least one success message is not found, the script sets to the job status "FAILED". In the opposite case, the script sets to the job status "DOWNLOADING" and starts copying the output from SE to /acs filesystem ("tape"). In the case of successful downloading of the job to tape the script sets to the job status "COMPLETED". There is no an automatic procedure for the case if the job sticks in "DOWNLOADING" status. In such a case the Grid operator should resubmit or cancel the job manually.

- **Waiting for sub-jobs:** when all sub-jobs have "COMPLETED" status, the job is purged from the MySQL database by "gridproc.sh" script that is executed via crontab every 5 minutes (in case it is not already running).

Working as a Grid operator the author solved problems in the work-flow and supported the production of MC simulated events. One of the key issues of this work was to provide a high performance of the Grid simulations. The Grid produces almost 95% percent of all Zeus MC events. In the beginning of 2011 the Grid site delivered up to $7-11\times10^6$ events per day (up to 75×10^6 events per week, see Fig. 12.3). At that time the machine that was supporting the work-flow and bookkeeping of the MC simulations on the Grid was at the end of its life-cycle. For this reason it was decided to make a simultaneous upgrade of hardware and software. The update included:

- switching on a compressing mechanism for the intermediate MOZART and ZGANA files as suggested in Ref. [111];
- change to a new host: machine with 4 Intel Xeon 5160 CPU cores/4Gb RAM;
- change to a new OS: Scientific Linux 3 → Scientific Linux 5;
- change to modern architecture: 32-bit/i386 → 64-bit/x86_64;
- optimisation of the file system;
- implementation of parallel submission;
- using proxy delegation to avoid limits on number of submissions.

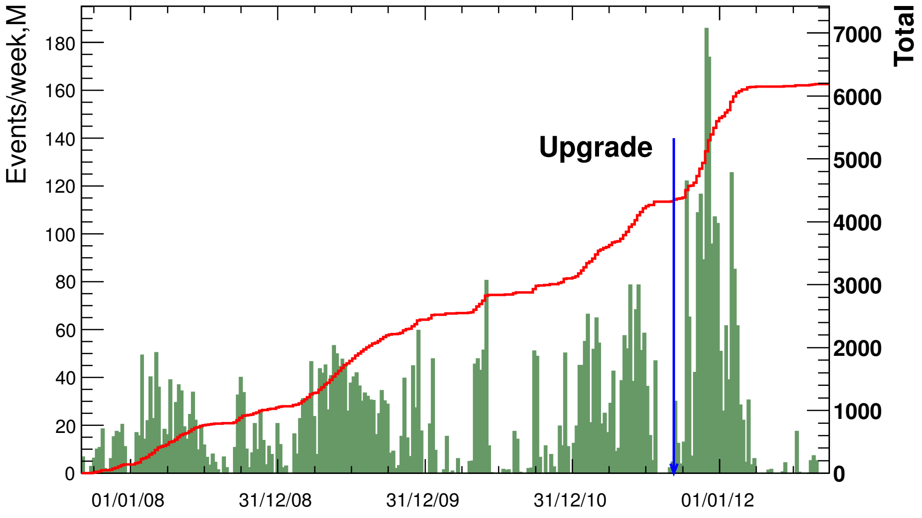

Figure 12.3: *The weekly performance of the production on Grid for the period from September 2009 to September 2012 (green bars) and the total number of events simulated on Grid (red line). Most periods with low entries correspond to periods without submission.*

At first, with the help of M. Lisovyi, the first item was implemented and the production rose to $12 - 15 \times 10^6$ events per day. Later the other upgrade actions have been performed by the author. This increased the efficiency of CPU power utilisation and dramatically boosted performance. The production increased to $27 - 33 \times 10^6$ events per day with some jumps to $35 - 45 \times 10^6$ events per day (up to 180×10^6 events per week, see Fig. 12.3). While the productivity of the system before the upgrade was limited by software [111], the productivity of the updated system is limited only by the I/O rate and the ability of the FUNNEL system to provide the input files. The update system is scalable and efficient enough to have a high output rate even with limited number of sites (see Fig. 12.4) and in case of improved I/O rate the performance might be even increased.

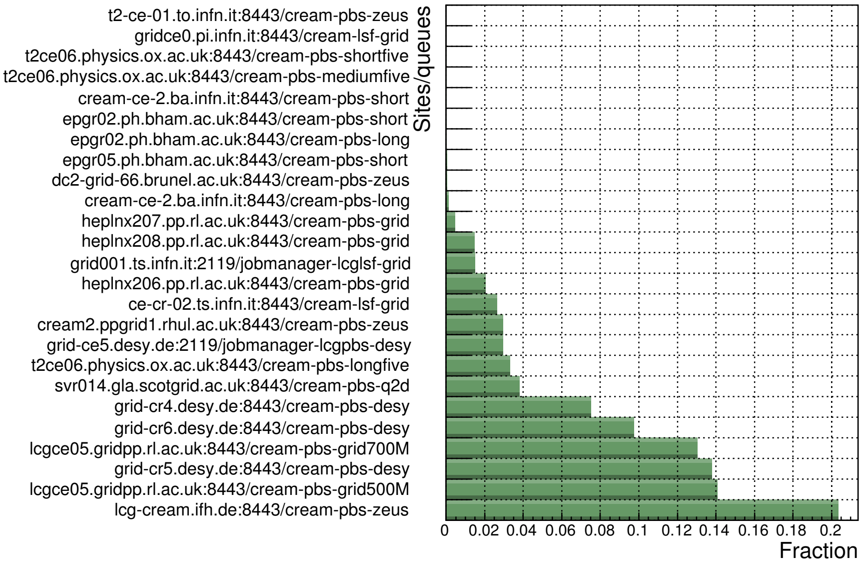

Figure 12.4: *The relative contributions of different CE to the* ZEUS *MC production on Grid for the period from September 2011 to September 2012.*

12.4 Future of ZEUS MC simulations on the Grid

The official support of the current ZEUS MC production system terminates at the end of 2012/beginning of 2013, together with the bulk of other ZEUS computing services. A major effort was put to make a physics analysis possible after the end of 2012. This initiative is an official part of the HEP Data Preservation Project [112], which collects and maintains the data and documentation from the most HEP experiments of the last decades.

One of the most important topics in this context is an ability to produce the MC simulated events after the end of 2012. For this purposes a virtual machine (ZEUS-DPHEP) that emulates an ordinary ZEUS work-group server has been created by the DESY IT division. On this machine the full ZEUS software chain for the MC simulations, reconstruction and analysis has been installed. It was called **ZMCSP**[36]. The software chain is based on the scripting codes used for the MC simulations on the Grid and has been prepared by J. Malka and the author, who wrote the initial proof-of-concept version.

Despite the fact that the software chain has been designed for a specific environment, it has been created to be as much as possible independent from the host system. It makes possible to use ZMCSP outside the ZEUS-DPHEP environment and benefit from the large amount of available computing resources. The possible options include computer farms of DESY and other institutes and Grid sites. The latest option is the most attractive as the Grid technology has been successfully exploited for many years for exactly the same tasks in ZEUS and other HEP experiments. A set of scripts for MC simulations with ZMCSP on the Grid has been implemented and tested by the author.The estimated production rate is $3 - 15 \times 10^6$ events per day [37] using the DESY Grid site and can be significantly increased by exploiting other sites. This rate is much higher than the estimated rate of production on the ZEUS-DPHEP machine and hereby the developed set of scripts can be beneficial for physics analysis.

As any software maintenance for the ZMCSP is not foreseen in the future, an important property of the system is the estimated lifespan. For the ZMCSP on Grid this depends on the lifespan of the host operating system (Scientific Linux 6), which is around 8 years [113] and to a smaller extent on the lifespan of the middleware (EMI), which is 3 years [114]. It means no major software problems are foreseen for the running of ZMCSP on the Grid at least till 2015.

---

[36] ZEUS MC Standalone Package

[37] The estimation is based on the speed of the MC simulation and Common Ntuples production on DESY Grid site. A more precise estimation is impossible without using the package for the massive production.

12.5 Conclusions

The Grid is the technology of the future. The utilisation of the Grid is vital for ZEUS and many other HEP experiments. During recent years more than 95% of ZEUS MC simulated events were produced on the Grid. The upgrade of the production system done by author increased the performance of ZEUS MC simulations by 4-5 times. The upgrade has allowed the completion of the simulations of large MC samples ahead of schedule.

13 Appendix:Estimation of relative tracking efficiency for data and MC

13.1 Introduction

The determination of the absolute and relative efficiency of data and MC tracking is an important task for any tracking-based analysis. As was stated in Sec. 4.2, the reconstruction of tracks depends on the type of particles. It means the absolute and relative tracking efficiencies for different particles might be different. However, as the overwhelming majority of registered particles are pions, the primary goal of tracking efficiency studies is to determinate the relative (data to MC) tracking efficiency for pions.

One of the possible ways to estimate the relative tracking efficiency is to measure the reconstruction rates of $D^0 \to K3\pi$ decay with respect to the two-body decays $D^0 \to K\pi$ in data and Monte Carlo simulated samples. Let us discuss this approach in details.

The numbers of reconstructed decays in selected kinematic region for both modes in data and MC are denoted as:

$$N^{\text{Data reconstructed}}_{D^0\to K\pi} = N^{\text{Data true}}_{D^0\to K\pi} e^{\text{Data}}_{D^0\to K\pi}; \tag{13.1}$$

$$N^{\text{Data reconstructed}}_{D^0\to K3\pi} = N^{\text{Data true}}_{D^0\to K3\pi} e^{\text{Data}}_{D^0\to K3\pi}; \tag{13.2}$$

$$N^{\text{MC reconstructed}}_{D^0\to K\pi} = N^{\text{MC true}}_{D^0\to K\pi} e^{\text{MC}}_{D^0\to K\pi}; \tag{13.3}$$

$$N^{\text{MC reconstructed}}_{D^0\to K3\pi} = N^{\text{MC true}}_{D^0\to K3\pi} e^{\text{MC}}_{D^0\to K3\pi}, \tag{13.4}$$

where the e stands for the reconstruction efficiency and N for the number of reconstructed or true mesons in the corresponding modes/samples. We assume the reconstruction efficiency can be factorised as

$$e = e_{\text{Trigger}} e_{\text{Kinematic}} e_{\text{Tracking efficiency}}. \tag{13.5}$$

For proper simulation of the decay kinematics the kinematic efficiency[38], $e_{\text{Kinematic}}$, should be the same in data and MC.

$$e^{\text{MC}}_{\text{Kinematic}} = e^{\text{Data}}_{\text{Kinematic}}$$

---

[38] The probability that p_T and η of decay particles are in selected kinematic region.

The trigger efficiency, e_{Trigger}, should be, to good approximation, the same for both decay modes.

$$e_{\text{Trigger D}^0\to\text{K}3\pi} = e_{\text{Trigger}D^0\to K\pi}. \tag{13.6}$$

Taking into account Eqs. (13.1), (13.2), (13.3), (13.4), (13.5), we have:

$$\frac{N^{\text{MC reconstructed}}_{D^0\to K\pi}}{N^{\text{MC reconstructed}}_{D^0\to K3\pi}} = \frac{N^{\text{MC true}}_{D^0\to K\pi}}{N^{\text{MC true}}_{D^0\to K3\pi}} \frac{e^{\text{MC}}_{\text{Tracking,D}^0\to\text{K}\pi}}{e^{\text{MC}}_{\text{Tracking,D}^0\to\text{K}3\pi}}$$

and

$$\frac{N^{\text{Data reconstructed}}_{D^0\to K\pi}}{N^{\text{Data reconstructed}}_{D^0\to K3\pi}} = \frac{N^{\text{Data true}}_{D^0\to K\pi}}{N^{\text{Data true}}_{D^0\to K3\pi}} \frac{e^{\text{Data}}_{\text{Tracking,D}^0\to\text{K}\pi}}{e_{\text{Tracking,D}^0\to\text{K}3\pi^{\text{Data}}}}.$$

The ratio of true-level decays is known from the PDG [1]

$$\frac{N^{\text{Data true}}_{D^0\to K\pi}}{N^{\text{Data true}}_{D^0\to K3\pi}} = R_{\text{PDG}}.$$

The equivalent for the MC simulated sample is

$$\frac{N^{\text{MC true}}_{D^0\to K\pi}}{N^{\text{MC true}}_{D^0\to K3\pi}} = R_{\text{MC}}.$$

So, from the previous expressions

$$\frac{N^{\text{MC reconstructed}}_{D^0\to K\pi}}{N^{\text{MC reconstructed}}_{D^0\to K3\pi}} = R_{\text{MC}} \frac{e^{\text{MC}}_{\text{Tracking,D}^0\to\text{K}\pi}}{e^{\text{MC}}_{\text{Tracking,D}^0\to\text{K}3\pi}} \tag{13.7}$$

and

$$\frac{N^{\text{Data reconstructed}}_{D^0\to K\pi}}{N^{\text{Data reconstructed}}_{D^0\to K3\pi}} = R_{\text{PDG}} \frac{e^{\text{Data}}_{\text{Tracking,D}^0\to\text{K}\pi}}{e^{\text{Data}}_{\text{Tracking,D}^0\to\text{K}3\pi}}. \tag{13.8}$$

If assume that the reconstruction efficiency for both modes can be factorised as

$$e_{\text{Tracking,D}^0\to\text{K}3\pi} = e_{K_1}(p_T,\eta)e_{\pi_1}(p_T,\eta)e_{\pi_2}(p_T,\eta)e_{\pi_3}(p_T,\eta),$$

$$e_{\text{Tracking,D}^0\to\text{K}\pi} = e_{K_2}(p_T,\eta)e_{\pi}(p_T,\eta),$$

and select the kinematic region where the efficiency of track reconstruction is constant with p_T and η i.e.

$$e_K = e_{K_2}(p_T,\eta) = e_{K_1}(p_T,\eta) = const, e_\pi == e_\pi(p_T,\eta) = e_{\pi_1}(p_T,\eta) = const,$$

the ratio of Eq. (13.7) and Eq. (13.8) gives

$$\frac{N^{\text{MC reconstructed}}_{D^0\to K\pi}}{N^{\text{MC reconstructed}}_{D^0\to K3\pi}} \Big/ \frac{N^{\text{Data reconstructed}}_{D^0\to K\pi}}{N^{\text{Data reconstructed}}_{D^0\to K3\pi}} = \frac{R_{\text{MC}}}{R_{\text{PDG}}} \left(\frac{e^{\text{Data}}_\pi}{e^{\text{MC}}_\pi}\right)^2$$

or,

$$\frac{e^{\text{Data}}_\pi}{e^{MC}_\pi} = \sqrt{\frac{N^{\text{MC reconstructed}}_{D^0\to K\pi}}{N^{\text{MC reconstructed}}_{D^0\to K3\pi}} \Big/ \frac{N^{\text{Data reconstructed}}_{D^0\to K\pi}}{N^{\text{Data reconstructed}}_{D^0\to K3\pi}} \frac{R_{\text{MC}}}{R_{\text{PDG}}}}. \tag{13.9}$$

Eq. (13.9) provides a recipe to calculate the relative track reconstruction efficiency. To reduce the combinatorial background, the D^0 candidates were tagged with D^{*+} decay $D^{*+} \to D^0\pi_s$ with the assumption that the slow pion registration efficiency is the same for both modes.

13.2 Samples, events and candidates selection

To maximise the statistics, the full HERA-II data sample was used. The MC sample was the same as for excited charm-meson analysis (see Sec.5). To reduce the background, a basic DIS-like selection was used:

- at least one electron candidate with energy $E_e > 10\,\text{GeV}$, and probability of electron identification[39]> 0.9;
- the Q^2, y kinematic cuts $0.7 < y_{\text{el}}$ and $5.0\,\text{GeV}^2 < Q^2_{\text{JB}} < 1000\,\text{GeV}^2$ (see Sec. 4.6 for details and definitions);
- SPP02 trigger (see Ref. [63] for definition) for the 2003, 2004, 2005 data taking periods;
- SPP09 and HPP31 triggers (see Ref. [63] for definition) for the 2006 and 2007 data taking periods.

To ensure high quality of the tracking, the Z position of the primary vertex had to be within $|Z_{\text{vtx}}| < 30$ cm. All selected tracks were required to pass at least three CTD superlayers, starting from the most inner superlayer. The tracks from

---

[39] The probability was estimated in the Sinistra package [115].

D^0 decays were restricted to the region $|\eta| < 1.6$ and $p_T > 0.45\,\mathrm{GeV}$. The cuts on the transverse momenta of reconstructed D^0/D^{*+} mesons were the following: $p_T > 3.0/3.5$ and $|\eta| < 1.8/1.6$. The cuts applied on the slow pion were: $p_T > 0.15\,\mathrm{GeV}$ and $|\eta| < 1.6$. The selected mass region for the D^0 candidates was $1.80\,\mathrm{GeV} < M(D^0) < 1.92\,\mathrm{GeV}$. To minimise the effect of finite spatial resolution, only very loose cuts were to the distance of closest approach between tracks $\mathrm{DCA} < 0.3\,\mathrm{cm}$ and the χ^2 of the D^0 vertex fit $\chi^2(D^0) < 30$.

The obtained mass difference spectra for data and MC simulated samples are shown in Fig. 13.1 and Fig. 13.2.

13.3 Signal extraction

To determine the yield of reconstructed D^{*+}, a fit of the $\Delta M = M(K\pi\pi) - M(K\pi)$ and $\Delta M = M(K3\pi\pi) - M(K3\pi)$ spectra was performed. For the description of signal a relativistic Breit-Wigner function convoluted with Gaussian resolution was used. The width of the Gaussian resolution function was a free parameter in the fit. As the natural width of the D^{*+} state is ∼0.1 MeV [1], well below the resolution of the ZEUS detector, it was not expected to get a reasonable width from the fit. However, it was convenient to use the relativistic Breit-Wigner function in the fit as it has a correct behaviour near the threshold, for the tails and it was possible to reuse the fit set-up for excited charm meson spectra (see Sec. 11). For the background description a phenomenological parametrisation (a,b,c) was used:

$$F(\Delta M) = a(\Delta M)^b e^{-c\Delta M}.$$

For both data and MC simulated samples the right and wrong charge spectra from both modes were fitted simultaneously in order to reduce the uncertainty of the final result; the peak position parameters were the same for both modes. For both data and MC simulated samples it was assumed that right and wrong charge backgrounds for each decay mode have the same shape, but different normalisation. The fits for data and MC simulated samples are shown in Fig. 13.1 and Fig. 13.2.

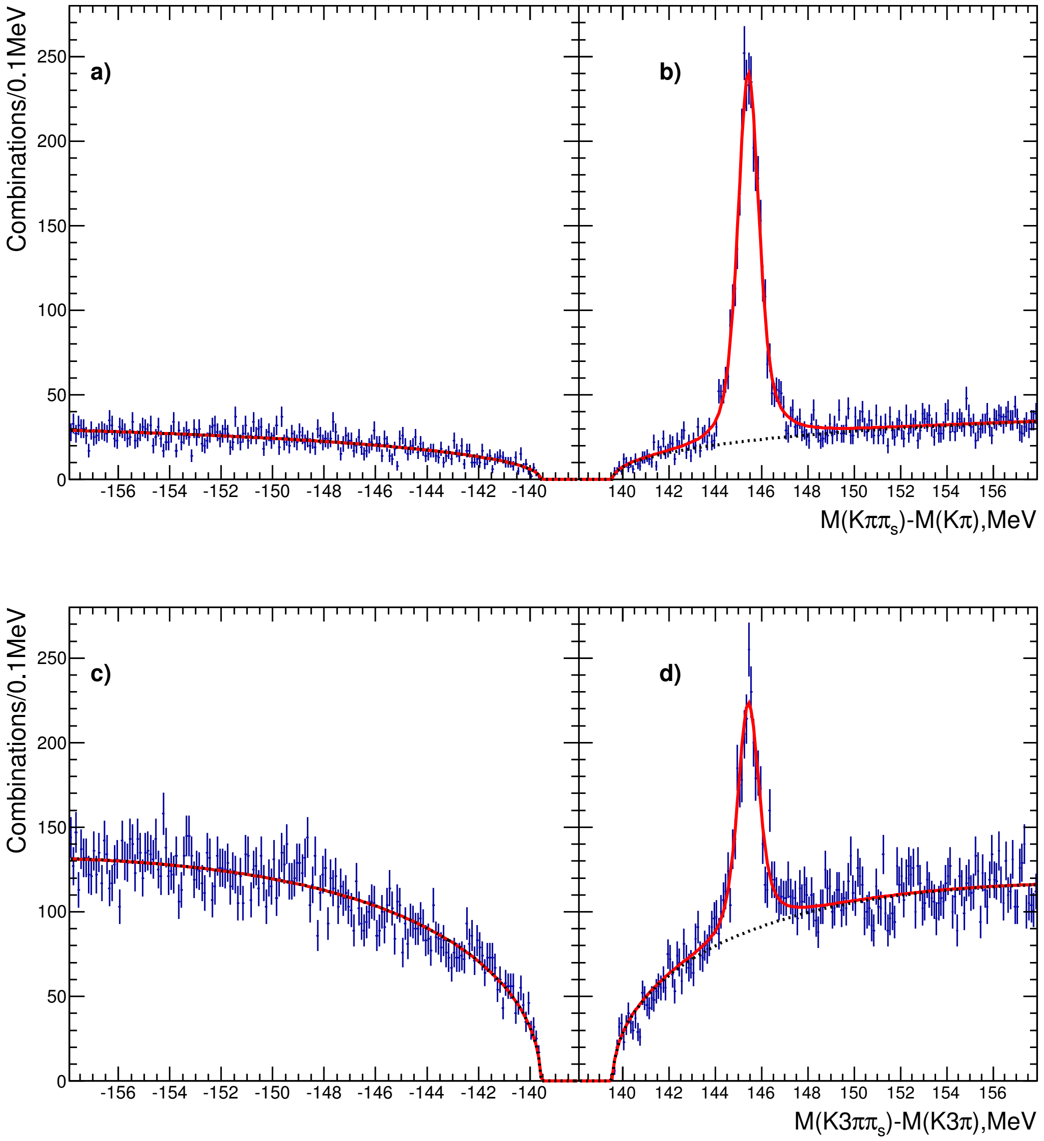

Figure 13.1: *The distribution of the mass difference in the data: a),b)* $\Delta M = M(K\pi\pi_s) - M(K\pi)$*; c),d)* $\Delta M = M(K\pi\pi\pi_s) - M(K\pi\pi)$*. The negative values a),c) correspond to the wrong charge combinations. The curves are fits to the sum (solid line) of a relativistic Breit-Wigner function, convoluted with Gaussian resolution and a background function (dots).*

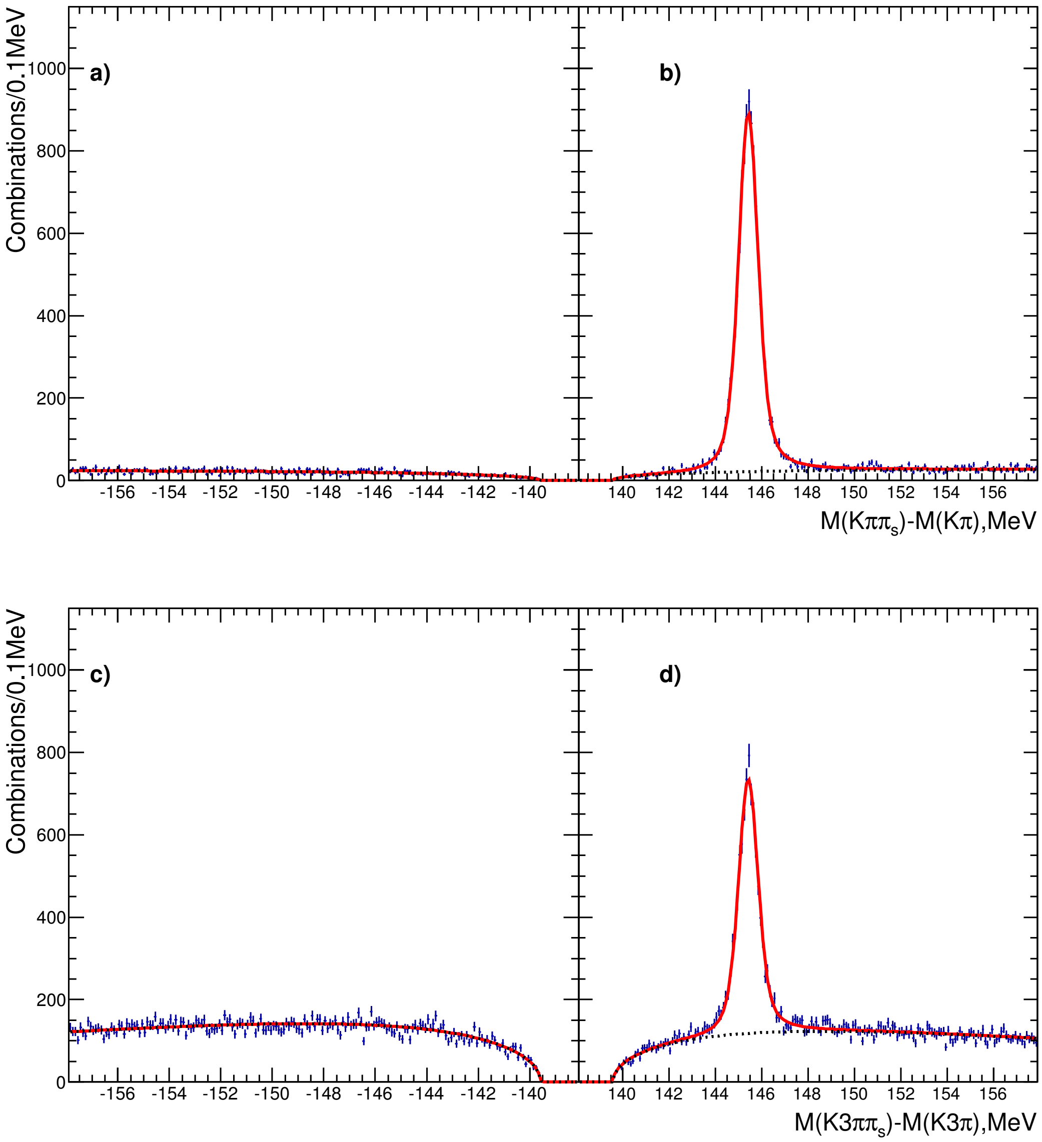

Figure 13.2: *The distribution of the mass difference in the MC sample: a),b) $\Delta M = M(K\pi\pi_s) - M(K\pi)$; c),d) $\Delta M = M(K\pi\pi\pi_s) - M(K\pi\pi)$. The negative values a),c) correspond to the wrong charge combinations. The curves are fits to the sum (solid line) of a relativistic Breit-Wigner function, convoluted with Gaussian resolution and a background function (dots).*

13.4 Corrections

To assure high quality of results, a validation of the MC simulation quality is needed. First of all, the reflections in the mass difference spectrum were studied with the MC simulated sample. It was found that, for the given selection, the most prominent reflection in the $M(K\pi\pi_s) - M(K\pi)$ mass spectrum comes from incomplete reconstruction of semileptonic decays of the D^0, when the muon or electron is misidentified as a pion. These decay modes of D^0 have similar branching fractions (see Tab. 13.1) to the studied hadronic mode $D^0 \to K\pi$, however, because of an incomplete reconstruction only a very tiny part of semileptonic decays will produce reflections in ΔM spectra (see Fig. 13.3). The relative contribution of the reflections to the signal peak is about 1.5%. To take into account reflections from the semileptonic decays and ensure a good peaking background description, their contribution to the MC signal was weighted to reflect the ratio of $\frac{\mathcal{B}(D^0 \to K\pi)}{\mathcal{B}(D^0 \to Kl\nu)}$ in PDG [1]. The only expected reflection in the $M(K3\pi\pi_s) - M(K3\pi)$ spectrum is the reflection from $D^0 \to K\pi K^0$ decay. The calculated branching ratio for this decay mode in the MC simulated sample was found to be consistent with the PDG value (see Tab. 13.1). The semileptonic decay modes that could cause another reflection have a negligible branching ratios (see Tab. 13.1). To check the description of data by the MC simulation, **background subtracted distributions** of $p_T(D^0)$, $p_T(D^{*+})$, $\eta(D^0)$, $p_T(D^{*+})$ for D^{*+} candidates from $D^0 \to K\pi$ and $D^0 \to K3\pi$ decays were studied. Those distributions were obtained from the distributions of right charge candidates with $144\,\mathrm{MeV} < M(K\pi\pi) - M(K\pi) < 149\,\mathrm{MeV}$ and $144\,\mathrm{MeV} < M(K3\pi\pi) - M(K3\pi) < 149\,\mathrm{MeV}$ with subtraction of weighted distributions of corresponding wrong charge candidates. The weighting coefficients were obtained from the fit as a ratio of wrong-charge background to the right-charge background. To ensure a good description of the data, the MC events with generated $D^{*+} \to D^0\pi_s^+$ decays were weighted to fit $p_T(D^0)$, $p_T(D^{*+})$, $\eta(D^0)$, $p_T(D^{*+})$ background subtracted distributions of data (see Fig. 13.4). The weight function was

$$W = \prod_i (1 + 0.2\eta(D_i^{*+}))e^{-0.1(p_T(D_i^{*+})[\mathrm{GeV}]-5.5)},$$

where the product runs over all generated D^{*+} in the event. For the events from $p_T(D^{*+})$ bins with the biggest discrepancy extra reweighting factors was applied: $W = 1.35$ for $3.5\,\mathrm{GeV} < p_T(D_i^{*+}) < 3.875\,\mathrm{GeV}$ and $W = 0.62$ for $4.625\,\mathrm{GeV} < p_T(D_i^{*+}) < 5.0\,\mathrm{GeV}$.

Name	Mode	PDG [1]	Pythia
Γ_{18}	$D^0 \to K^- \; e^+ \; \nu_e$	3.55 ±0.04 % S=1.2	
Γ_{19}	$D^0 \to K^- \; \mu^+ \; \nu_\mu$	3.30 ±0.13 % S=1.0	
Γ_{24}	$D^0 \to K^- \; \pi^+ \; \pi^- \; e^+ \; \nu_e$	$(2.8 \; ^{+1.4}_{-1.1}) \times 10^{-4}$	
Γ_{25}	$D^0 \to K_1(1270)^- \; e^+ \; \nu_e$	$(7.6 \; ^{+4.0}_{-3.1}) \times 10^{-4}$	
Γ_{26}	$D^0 \to K^- \; \pi^+ \; \pi^- \; \mu^+ \; \nu_\mu$	$< 1.2 \times 10^{-3}$ CL=90%	
Γ_{27}	$D^0 \to (\bar{K}^*(892) \; \pi \;)^- \; \mu^+ \; \nu_\mu$	$< 1.4 \times 10^{-3}$ CL=90%	
Γ_{27}	$D^0 \to K^0_S \; K^- \; \pi^+$	$(2.6 \pm 0.5) \times 10^{-3}$	0.08 %
Γ_{31}	$D^0 \to K^- \; \pi^+$	3.88 ±0.05 % S=1.2	7.30 %
Γ_{66}	$D^0 \to K^- \; 2\pi^+ \; \pi^-$	$8.07 \; ^{+0.21}_{-0.19}$ % S=1.3	15.43 %
Γ_{67}	$D^0 \to K^- \; \pi^+ \; \rho^0$ total	6.74 ±0.33 %	
Γ_{68}	$D^0 \to K^- \; \pi^+ \; \rho^0$ 3-body	$(5.1 \pm 2.3) \times 10^{-3}$	0.93 %
Γ_{69}	$D^0 \to \overline{K}^*(892)^0 \; \rho^0$,		
	$\overline{K}^*(892)^0 \to K^- \; \pi^+$	1.05 ±0.23 %	1.80 %
Γ_{70}	$D^0 \to K^- \; a_1(1260)^+$,		
	$a_1(1260)^+ \to 2\pi^+ \; \pi^-$	3.6 ±0.6 %	6.91 %
Γ_{71}	$D^0 \to \overline{K}^*(892)^0 \; \pi^+ \; \pi^-$ total,		
	$\overline{K}^*(892)^0 \to K^- \; \pi^+$	1.6 ±0.4 %	
Γ_{72}	$D^0 \to \overline{K}^*(892)^0 \; \pi^+ \; \pi^-$ 3-body,		
	$\overline{K}^*(892)^0 \to K^- \; \pi^+$	$(9.9 \pm 2.3) \times 10^{-3}$	1.85 %
Γ_{73}	$D^0 \to K_1(1270)^- \; \pi^+$,		
	$K_1(1270)^- \to K^- \; \pi^+ \; \pi^-$	$(2.9 \pm 0.3) \times 10^{-3}$	0.71 %
Γ_{74}	$D^0 \to K^- \; 2\pi^+ \; \pi^-$ non-resonant	1.88 ±0.26 %	3.23 %
$R = \frac{\Gamma_{66}}{\Gamma_{31}}$		2.08 ± 0.05	2.11

Table 13.1: *D^0 branching ratios according to PDG [1] The $\frac{\Gamma_{66}}{\Gamma_{31}}$ ratio takes into account correlations.*

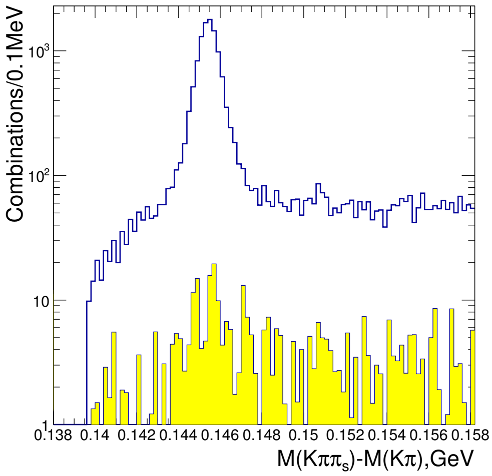

Figure 13.3: *The distribution of the mass difference* $\Delta M = M(K\pi\pi_s) - M(K\pi)$ *in the MC simulated events for all events (blue line) and events with* $D^{*+} \to D^0\pi_s, D^0 \to Kl\nu_l$ *decays only (yellow).*

From the previous studies [116] it is known that the relative efficiency of low p_T tracks to high p_T tracks is slightly higher in data than in MC. To correct for this effect, all reconstructed candidates in MC sample were given a weight (see Fig. 13.5(a)):

$$W = \prod_i \min(1, 1 + 0.526(p_T^i[\text{GeV}] - 0.26)),$$

where the product runs over all tracks in the decay. Effects related to the dependence of the track efficiency on the track multiplicity were corrected according to studies in Ref. [117] by giving a weight(see Fig. 13.5(b)) to each track in data and MC simulated sample as:

$$W = \prod_i 1/ \begin{cases} 1 - 0.0880(N_i - 3) & \theta < 21^\circ \text{ and } N_i > 3 \\ 1 - 0.0044\sqrt{N_i - 2} - 0.0379(N_i - 2) & \\ -0.0030(N_i - 2)^2 & 21^\circ < \theta < 169^\circ \text{ and } N_i < 2 \\ 1 - 0.1960(N_i - 5) & \theta > 169^\circ \text{ and } N_i > 5 \\ 1 & \text{otherwise,} \end{cases}$$

where θ is the track azimuthal angle and N stands for the number of tracks inside a cone $\sqrt{\Delta\phi^2 + \Delta\eta^2} < 0.3$ around i-th track.

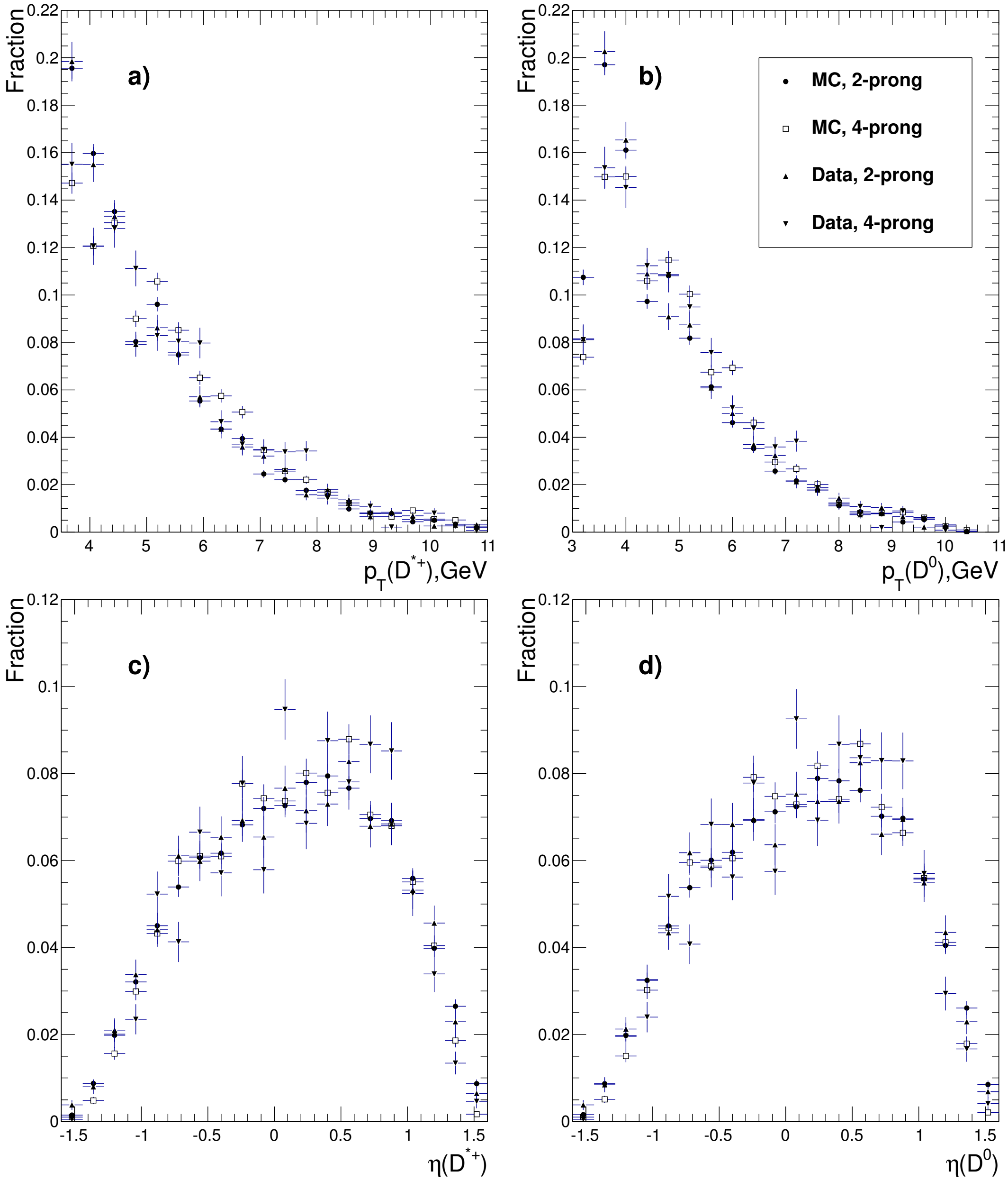

Figure 13.4: *The comparison of normalised background subtracted distributions: a) $p_T(D^{*+})$; b) $p_T(D^0)$; c) $\eta(D^{*+})$; d) $\eta(D^0)$; in the data and MC simulated samples for two reconstructed modes.*

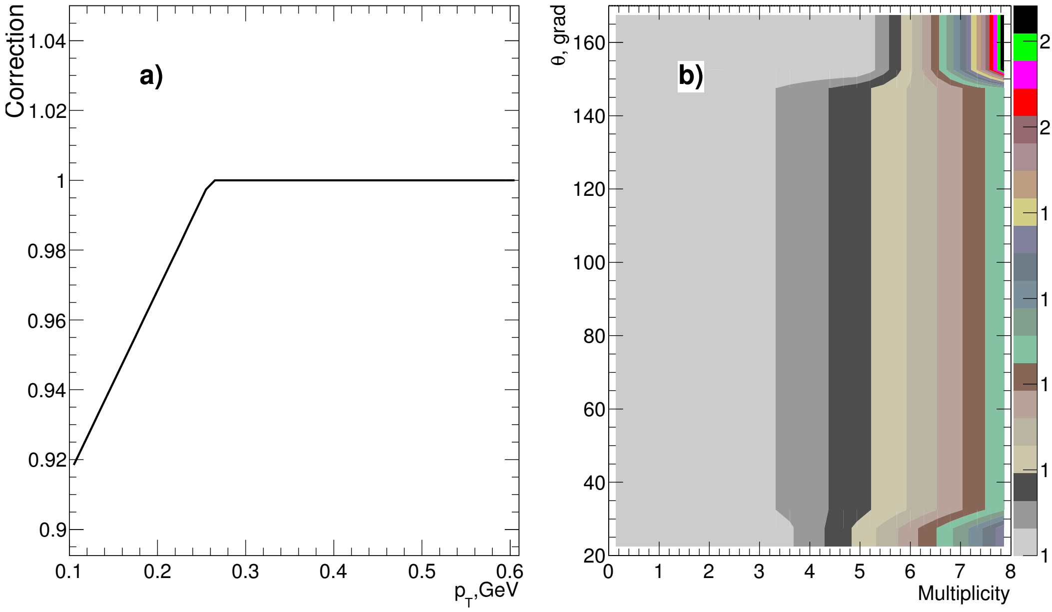

Figure 13.5: *Corrections of track efficiency: a) for track multiplicity in data and MC; b) for low p_T pions in MC.*

13.5 Results and conclusions

The fitted values of D^{*+} signals in data and MC sample are given in Tab. 13.2. Using the Eq. 13.9, the relative tracking efficiency for pions with $p_T > 0.45\,\mathrm{GeV}$ and $|\eta| < 1.6$ that passed at least three innermost CTD superlayers is:

Quantity	Data	MC
$N(D^{*+} \to D^0\pi_s; D^0 \to K\pi)$	3066 ± 87	10917 ± 127
$\frac{N(D^{*+}\to D^0\pi_s;D^0\to K\pi)}{N(D^*\to D^0\pi_s;D^0\to K3\pi)}$	0.626 ± 0.030	0.712 ± 0.013
R	2.08 ± 0.05 (PDG)	2.1188

Table 13.2: *The results of ΔM spectra fits in data and MC sample.*

$$\epsilon = 0.946 \pm 0.027,$$

or,

$$\epsilon = 0.946 \pm 0.024 \pm 0.011,$$

where the second error comes from PDG uncertainty on R.

The check with an independent method [118], which assumed a poor simulation of hadronic interactions in MC simulated samples, has shown that the tracking efficiencies should be at level of 98%, which is slightly higher that the obtained number.

List of Figures

List of Tables

References

[1] K. Nakamura et al. Particle Data Group, *Review of particle physics*, J. Phys. **G 37 (2010 and partial update for the 2012 edition)**, 075021, URL `http://dx.doi.org/10.1088/0954-3899/37/7A/075021`.

[2] N. Isgur and M.B. Wise, *Weak Decays of Heavy Mesons in the Static Quark Approximation*, Phys.Lett. **B232 (1989)**, 113, URL `http://dx.doi.org/10.1016/0370-2693(89)90566-2`.

[3] M.B. Wise, *Chiral perturbation theory for hadrons containing a heavy quark*, Phys.Rev. **D45 (1992)**, 2188, URL `http://dx.doi.org/10.1103/PhysRevD.45.R2188`.

[4] S.D. Drell and Tung-Mow Yan, *Massive Lepton Pair Production in Hadron-Hadron Collisions at High-Energies*, Phys.Rev.Lett. **25 (1970)**, 316, URL `http://dx.doi.org/10.1103/PhysRevLett.25.316`.

[5] A.F. Falk and M.E. Peskin, *Production, decay, and polarization of excited heavy hadrons*, Phys.Rev. **D49 (1994)**, 3320, URL `http://dx.doi.org/10.1103/PhysRevD.49.3320`.

[6] J.D. Richman and P.R. Burchat, *Leptonic and semileptonic decays of charm and bottom hadrons*, Rev.Mod.Phys. **67 (1995)**, 893, URL `http://dx.doi.org/10.1103/RevModPhys.67.893`.

[7] M. Neubert, *Heavy quark symmetry*, Phys.Rept. **245 (1994)**, 259, URL `http://dx.doi.org/10.1016/0370-1573(94)90091-4`.

[8] N. Isgur and M.B. Wise, *Spectroscopy with heavy quark symmetry*, Phys.Rev.Lett. **66 (1991)**, 1130, URL `http://dx.doi.org/10.1103/PhysRevLett.66.1130`.

[9] J.L. Rosner, *P Wave Mesons with One Heavy Quark*, Comments Nucl.Part.Phys. **16 (1986)**, 109, URL `http://ccdb5fs.kek.jp/cgi-bin/img/allpdf?198605131`.

[10] M. Di Pierro and E. Eichten, *Excited heavy - light systems and hadronic transitions*, Phys.Rev. **D64 (2001)**, 114004, URL `http://dx.doi.org/10.1103/PhysRevD.64.114004`.

[11] D. Ebert, R.N. Faustov and V.O. Galkin, *Heavy-light meson spectroscopy and Regge trajectories in the relativistic quark model*, Eur.Phys.J. **C66 (2010)**, 197, URL `http://dx.doi.org/10.1140/epjc/s10052-010-1233-6`.

[12] T. Matsuki et al., *New heavy-light mesons Q anti-q*, Prog.Theor.Phys. **117 (2007)**, 1077, URL `http://dx.doi.org/10.1143/PTP.117.1077`.

[13] K. Abe et al. BELLE Collaboration, *Study of* $B \to D^{**0}\pi^-(D^{**0} \to D^{(*)+}\pi^-)$ *decays*, in *Phys. Rev.* [15], 112002, URL `http://dx.doi.org/10.1103/PhysRevD.69.112002`.

[14] J.M. Link et al. FOCUS Collaboration, *Measurements of six body hadronic decays of the* D^0 *charmed meson*, Phys.Lett. **B586 (2004)**, 21, URL `http://dx.doi.org/10.1016/j.physletb.2004.02.038`.

[15] K. Abe et al. BELLE Collaboration, *Study of* $B \to D^{**0}\pi^-(D^{**0} \to D^{(*)+}\pi^-)$ *decays*, Phys. Rev. **D 69 (2004)**, 112002, URL `http://dx.doi.org/10.1103/PhysRevD.69.112002`.

[16] B. Aubert et al. BABAR Collaboration, *Observation of a narrow meson decaying to* $D_s^+\pi^0$ *at a mass of 2.32-GeV/*c^2, Phys.Rev.Lett. **90 (2003)**, 242001, URL `http://dx.doi.org/10.1103/PhysRevLett.90.242001`.

[17] D. Besson et al. CLEO Collaboration, *Observation of a narrow resonance of mass* 2.46 *GeV/*c^2 *decaying to* $D^{*+}(s)\pi^0$ *and confirmation of the* $D^*_{sJ}(2317)$ *state*, Phys.Rev. **D68 (2003)**, 032002, URL `http://dx.doi.org/10.1103/PhysRevD.68.032002,10.1103/PhysRevD.75.119908`.

[18] Xian-hui Zhong and Qiang Zhao, *Strong decays of heavy-light mesons in a chiral quark model*, Phys.Rev. **D78 (2008)**, 014029, URL `http://dx.doi.org/10.1103/PhysRevD.78.014029`.

[19] S. Godfrey, *Properties of the charmed P-wave mesons*, Phys.Rev. **D72 (2005)**, 054029, URL `http://dx.doi.org/10.1103/PhysRevD.72.054029`.

[20] A.F. Falk and M.E. Luke, *Strong decays of excited heavy mesons in chiral perturbation theory*, Phys.Lett. **B292 (1992)**, 119, URL `http://dx.doi.org/10.1016/0370-2693(92)90618-E`.

[21] P. Colangelo, F. Giannuzzi F. De Fazio and S. Nicotri, *New meson spectroscopy with open charm and beauty*, Phys.Rev. **D86 (2012)**, 054024, URL `http://dx.doi.org/10.1103/PhysRevD.86.054024`.

[22] Yi-Jin Pei, *A Simple approach to describe hadron production rates in e^+e^- annihilation*, Z. Phys. **C 72 (1996)**, 39, URL `http://dx.doi.org/10.1007/s002880050221`.

[23] F. Becattini, *A Thermodynamical approach to hadron production in e^+e^- collisions*, Z.Phys. **C69 (1996)**, 485, URL `http://dx.doi.org/10.1007/s002880050051`.

[24] F. Becattini, *Thermal hadron production in high-energy collisions*, J.Phys. **G23 (1997)**, 1933, URL `http://dx.doi.org/10.1088/0954-3899/23/12/017`.

[25] DESY, *Mediendatenbank*, URL `http://bilder.desy.de:9080/DESYmediabank/`.

[26] W. Bialowons, *Status of HERA*, Conf.Proc. **C960610 (1996)**, 3, URL `http://accelconf.web.cern.ch/AccelConf/e96/PAPERS/ORALS/MOX02A.PDF`.

[27] ZEUS Collaboration, *The ZEUS Detector*, Status Report (unpublished), DESY (1993), URL `http://zeusdp.desy.de/bluebook/bluebook.html`.

[28] G. Hemmie and J.R. Maidment, *DESY III, The New proton injector for HERA*, Conf.Proc. **C870316 (1987)**, 172, URL `http://accelconf.web.cern.ch/AccelConf/p87/PDF/PAC1987_0172.pdf`.

[29] ZEUS collaboration, *ZEUS evtake and lumi page*, URL `http://zeusdp.desy.de/physics/lumi/`.

[30] ZEUS, *ZEUS in pictures and posters*, URL `http://zeusdp.desy.de/pictures/zeus2d2.eps.gz`.

[31] V. Shoenberg, *Pictures Database*, URL `http://zeusdp.desy.de/~vschoenb/`.

[32] B. Foster et al. ZEUS Collaboration, *The Design and construction of the ZEUS central tracking detector*, Nucl.Instrum.Meth. **A338 (1994)**, 254, URL `http://dx.doi.org/10.1016/0168-9002(94)91313-7`.

[33] ZEUS Collaboration, *A Microvertex Detector for ZEUS*, *Technical report*, DESY (1997), URL `http://zeusdp.desy.de/ZEUS_ONLY/zeus_notes/ZEUS_NOTES/ZEUS-97-006.ps`.

[34] E. Maddox, *A Kalman filter track fit for the ZEUS microvertex detector*, *Technical report*, DESY (2003), URL `http://zeusdp.desy.de/ZEUS_ONLY/zeus_notes/ZEUS_NOTES/ZEUS-03-008.ps`.

[35] S. Goers, *The straw-tube tracker of the ZEUS-detector at HERA*, in Instrumentation and Measurement Technology Conference, 2004. IMTC 04. Proceedings of the 21st IEEE, volume 2, 1129 – 1134 Vol.2 (2004), ISSN 1091-5281, URL `http://dx.doi.org/10.1109/IMTC.2004.1351263`.

[36] ZEUS Collaboration, *The uranium scintillator calorimeter (CAL)* (2012), URL `http://zeusdp.desy.de/public/cal.php3`.

[37] J. Andruszkow et al., *Luminosity measurement in the ZEUS experiment*, Acta Phys.Polon. **B32 (2001)**, 2025, URL `http://th-www.if.uj.edu.pl/acta/vol32/ps/v32p2025.ps.gz`.

[38] M. Helbich et al., *The Spectrometer system for measuring ZEUS luminosity at HERA*, Nucl.Instrum.Meth. **A565 (2006)**, 572, URL `http://dx.doi.org/10.1016/j.nima.2006.06.049`.

[39] T. Sjöstrand et al., *PYTHIA 6.2: Physics and manual*, Comp. Phys. Comm. **135 (2001)**, 238, URL `http://arxiv.org/pdf/hep-ph/0108264.pdf`.

[40] H. Jung, The Rapgap Monte Carlo for Deep Inelastic Scattering, DESY (2004), URL `http://projects.hepforge.org/rapgap/rapgap.pdf`.

[41] L. Lönnblad, *ARIADNE version 4: A Program for simulation of QCD cascades implementing the color dipole model*, Comput.Phys.Commun. **71 (1992)**, 15, URL `http://dx.doi.org/10.1016/0010-4655(92)90068-A`.

[42] B. Brun et al., *GEANT3*, *Technical report*, CERN (Technical Report CERN-DD/EE/84-1, CERN, 1987).

[43] I. Antcheva et al, *ROOT: A C++ framework for petabyte data storage, statistical analysis and visualization*, Comput.Phys.Commun. **182 (2011)**, 1384, URL `http://dx.doi.org/10.1016/j.cpc.2011.02.008`.

[44] C.E. Vandoni R. Brun, O. Couet and P. Zanarini, *PAW: a general purpose portable software tool for data analysis and presentation.*, Comput.Phys.Commun. **57 (1989)**, 432, URL `http://dx.doi.org/10.1016/0010-4655(89)90257-9`.

[45] V. Chiochia, *The ZEUS Micro Vertex Detector*, Nucl.Instrum.Meth. **A501 (2003)**, 60, URL `http://dx.doi.org/10.1016/S0168-9002(02)02011-9`.

[46] G.F. Hartner, *VCTRAK Briefing: Program and Math*, *Technical report*, DESY (1998), URL `http://zeusdp.desy.de/ZEUS_ONLY/zeus_notes/ZEUS_NOTES/ZEUS-98-058.ps`.

[47] S. Chekanov et al. ZEUS Collaboration, *Search for a narrow charmed baryonic state decaying to $D^{*\pm}p^{\mp}$ in ep collisions at HERA*, Eur.Phys.J. **C38 (2004)**, 29, URL `http://dx.doi.org/10.1140/epjc/s2004-02042-9`.

[48] P. Avery, *Fitting Theory V: Track Fitting Using the Kalman Filter*, *Technical report*, CLEO (1992), URL `http://www.phys.ufl.edu/~avery/fitting/fitting5.pdf`.

[49] ZEUS tracking group, *Track resolution* (2012), URL `http://zeusdp.desy.de/ZEUS_ONLY/tracking/ZEUS_ONLY/info/resolution.html`.

[50] P. Billoir and S. Qian, *Fast vertex fitting with a local parametrization of tracks*, Nucl.Instrum.Meth. **A311 (1992)**, 139, URL `http://dx.doi.org/10.1016/0168-9002(92)90859-3`.

[51] H. Stadie, *tLite Home page* (2007), URL `http://zeusdp.desy.de/ZEUS_ONLY/tracking/ZEUS_ONLY/tools/tLite/index.html`.

[52] A. Spiridonov, *Evaluation of Beam Spot Size* (ZEUS Tracking Developers Group Meeting, 5 October 2009), URL `http://zeusdp.desy.de/ZEUS_ONLY/meetings/zems/group5/meet257/sess2552/pres11389/k091005.pdf`.

[53] A. Verbytskyi, *D meson reconstruction efficiencies* (ZEUS Tracking Group meeting, 29 July 2009), URL `http://zeusdp.desy.de/ZEUS_ONLY/meetings/zems/group15/meet242/sess2519/pres11260/mesonsvmcustudies.pdf`.

[54] U. Bassler and G. Bernardi, *On the kinematic reconstruction of deep inelastic scattering at HERA: The Sigma method*, Nucl.Instrum.Meth. **A361 (1995)**, 197, URL `http://dx.doi.org/10.1016/0168-9002(95)00173-5`.

[55] A. Blondel and F. Jacquet, *Proceedings of the Study of an ep Facility for Europe* **(1979)**, 391.

[56] S. Chekanov et al. ZEUS Collaboration, *Production of excited charm and charm-strange mesons at HERA*, Eur. Phys. J. **C 60 (2009)**, 25, URL `http://dx.doi.org/10.1140/epjc/s10052-009-0881-x`.

[57] H.L. Lai et al., *Global QCD analysis of parton structure of the nucleon: CTEQ5 parton distributions*, Eur.Phys.J. **C12 (2000)**, 375, URL `http://dx.doi.org/10.1007/s100529900196`.

[58] M. Gluck, E. Reya and A. Vogt, *Photonic parton distributions*, Phys.Rev. **D46 (1992)**, 1973, URL `http://dx.doi.org/10.1103/PhysRevD.46.1973`.

[59] M.G. Bowler, e^+e^- *Production of Heavy Quarks in the String Model*, Z. Phys. **C 11 (1981)**, 169, URL `http://dx.doi.org/10.1007/BF01574001`.

[60] B. Andersson et al., *A General Model for Jet Fragmentation*, Z. Phys. **C 20 (1983)**, 317, URL `http://dx.doi.org/10.1007/BF01407824`.

[61] L. Gladilin, *Private communication* (2010).

[62] P. del Amo Sanchez et al. BABAR Collaboration, *Observation of new resonances decaying to* $D\pi$ *and* $D^*\pi$ *in inclusive* e^+e^- *collisions near* $\sqrt{s}$ *=10.58 GeV*, Phys.Rev. **D82 (2010)**, 111101, URL `http://dx.doi.org/10.1103/PhysRevD.82.111101`.

[63] ZEUS HFL Group, *HFL Trigger* (2000-2012), URL `http://zeusdp.desy.de/physics/hfla/zeus/hfl_trig`.

[64] H. Abramowicz et al. ZEUS Collaboration, *Production of the excited charm mesons* D_1 *and* D_2^* *at HERA*, Nucl.Phys. **B866 (2013)**, 229, URL `http://dx.doi.org/10.1016/j.nuclphysb.2012.09.007`.

[65] K. Abe et al. BELLE Collaboration, *Observation of the* $D_1(2420) \to D\pi^+\pi^-$ *decays*, Phys.Rev.Lett. **94 (2005)**, 221805, URL `http://dx.doi.org/10.1103/PhysRevLett.94.221805`.

[66] P. Avery et al. CLEO Collaboration, *Production and decay of* $D_1^0(2420)$ *and* $D_2^{*0}(2460)$, Phys.Lett. **B331 (1994)**, 236, URL `http://dx.doi.org/10.1016/0370-2693(94)90968-7`.

[67] P.L. Frabetti et al. E687 Collaboration, *Measurement of the masses and widths of* $L = 1$ *charm mesons*, Phys.Rev.Lett. **72 (1994)**, 324, URL `http://dx.doi.org/10.1103/PhysRevLett.72.324`.

[68] P. Avery et al. CLEO Collaboration, *P wave charmed mesons in* e^+e^- *annihilation*, Phys.Rev. **D41 (1990)**, 774, URL `http://dx.doi.org/10.1103/PhysRevD.41.774`.

[69] H. Albrecht et al. ARGUS Collaboration, *Resonance decomposition of the* $D^{*0}(2420)$ *throught decay angular analysis*, Phys.Lett. **B232 (1989)**, 398, URL `http://dx.doi.org/10.1016/0370-2693(89)90764-8`.

[70] J.C. Anjos et al. TPS Collaboration, *Observation of Excited Charmed Mesons*, Phys.Rev.Lett. **62 (1989)**, 1717, URL `http://dx.doi.org/10.1103/PhysRevLett.62.1717`.

[71] A. Abulencia et al. CDF Collaboration, *Measurement of mass and width of the excited charmed meson states* D_1^0 *and* D_2^{*0} *at CDF*, Phys.Rev. **D73 (2006)**, 051104, URL `http://dx.doi.org/10.1103/PhysRevD.73.051104`.

[72] P. Abreu et al. DELPHI Collaboration, *First evidence for a charm radial excitation,* $D^{*\prime}$, Phys.Lett. **B426 (1998)**, 231, URL `http://dx.doi.org/10.1016/S0370-2693(98)00346-3`.

[73] J.M. Link et al. FOCUS Collaboration, *Measurement of masses and widths of excited charm mesons* D_2^* *and evidence for broad states*, Phys.Lett. **B586 (2004)**, 11, URL `http://dx.doi.org/10.1016/j.physletb.2004.02.017`.

[74] P. Aubert et al. BABAR Collaboration, *Measurement of Semileptonic B Decays into Orbitally-Excited Charmed Mesons*, Phys.Rev.Lett. **103 (2009)**, 051803, URL `http://dx.doi.org/10.1103/PhysRevLett.103.051803`.

[75] A. Kuzmin et al. BELLE Collaboration, *Study of anti* $- B^0 \to D^0\pi^+\pi^-$ *decays*, Phys.Rev. **D76 (2007)**, 012006, URL `http://dx.doi.org/10.1103/PhysRevD.76.012006`.

[76] P. Avery et al. CLEO Collaboration, *Production and decay of* $D_1^0(2420)$ *and* $D_2^{*0}(2460)$, in *Phys.Lett.* [66], 236–244, URL `http://dx.doi.org/10.1016/0370-2693(94)90968-7`.

[77] B. Aubert et al. BABAR Collaboration, *Dalitz Plot Analysis of* $B \to D^+\pi^-\pi^-$, Phys.Rev. **D79 (2009)**, 112004, URL `http://dx.doi.org/10.1103/PhysRevD.79.112004`.

[78] H. Albrecht et al. ARGUS Collaboration, *Observation of the* $D^{*0}(2459)$ *in* e^+e^- *Annihilation*, Phys.Lett. **B221 (1989)**, 422, URL `http://dx.doi.org/10.1016/0370-2693(89)91737-1`.

[79] A.E. Asratian et al. BBCNC Collaboration, *Study of* D^{*+} *and search for* D^{**0} *production by neutrinos in BEBC*, Z.Phys. **C68 (1995)**, 43, URL `http://dx.doi.org/10.1007/BF01579803`.

[80] H. Albrecht et al. ARGUS Collaboration, *Observation of the charged isospin partner of the* $D^{*0}(2459)$, Phys.Lett. **B231 (1989)**, 208, URL `http://dx.doi.org/10.1016/0370-2693(89)90141-X`.

[81] V.M. Abazov et al. D0 Collaboration, *Measurement of the* B_s^0 *semileptonic branching ratio to an orbitally excited* D_s *state,* *Br(*$B_s^0 \to D_{s1}^-(2536)\mu^+\nu X$*)*, Phys.Rev.Lett. **102 (2009)**, 051801, URL `http://dx.doi.org/10.1103/PhysRevLett.102.051801`.

[82] B. Aubert et al. BABAR Collaboration, *A Study of the* $D^*_{(sJ)}(2317)$ *and* $D_{(sJ)}(2460)$ *Mesons in Inclusive c anti-c Production Near* $\sqrt{s} = 10.6$ *GeV* , Phys.Rev. **D74 (2006)**, 032007, URL `http://dx.doi.org/10.1103/PhysRevD.74.032007`.

[83] A. Heister et al. ALEPH Collaboration, *Production of* $D^{**}(s)$ *mesons in hadronic Z decays*, Phys.Lett. **B526 (2002)**, 34, URL `http://dx.doi.org/10.1016/S0370-2693(01)01465-4`.

[84] A.E. Asratian et al. BBCNC Collaboration, *Observation of* $D_s^{**}(2536)$ *meson production by neutrinos in BEBC*, Z.Phys. **C61 (1994)**, 563, URL `http://dx.doi.org/10.1007/BF01552622`.

[85] J.P. Alexander et al. CLEO Collaboration, *Production and decay of the* $D^+_{(s1)}(2536)$, Phys.Lett. **B303 (1993)**, 377, URL `http://dx.doi.org/10.1016/0370-2693(93)91448-V`.

[86] H. Albrecht et al. ARGUS Collaboration, *Observation of the decay* $D_{s1}(2536) \to D^{*0}K^+$, Phys.Lett. **B297 (1992)**, 425, URL `http://dx.doi.org/10.1016/0370-2693(92)91282-E`.

[87] H. Albrecht et al. ARGUS Collaboration, *Observation of a new charmed-strange meson*, Phys.Lett. **B230 (1989)**, 162, URL `http://dx.doi.org/10.1016/0370-2693(89)91672-9`.

[88] T. Aushev et al. BELLE Collaboration, *Study of the decays* $B \to D_{s1}(2536)^+\bar{D}^{(*)}$, Phys.Rev. **D83 (2011)**, 051102, URL `http://dx.doi.org/10.1103/PhysRevD.83.059902,10.1103/PhysRevD.83.051102`.

[89] J.P. Lees et al. BABAR Collaboration, *Measurement of the mass and width of the* $D_{s1}(2536)^+$ *meson*, Phys.Rev. **D83 (2011)**, 072003, URL `http://dx.doi.org/10.1103/PhysRevD.83.072003`.

[90] A.E. Asratian et al. HLBC Collaboration, *Studiyng (anti-charm strange) spectroscopy in anti-neutrino N collisions*, Z.Phys. **C40 (1988)**, 483, URL `http://dx.doi.org/10.1007/BF01560218`.

[91] K. Ackerstaff et al. OPAL Collaboration, *Production of P wave charm and charm - strange mesons in hadronic* Z^0 *decays*, Z.Phys. **C76 (1997)**, 425, URL `http://dx.doi.org/10.1007/s002880050566`.

[92] T. Sjöstrand, *High-Energy Physics Event Generation with* PYTHIA 5.7 *and* JETSET 7.4, Comput.Phys.Commun. **82 (1994)**, 74, URL `http://dx.doi.org/10.1016/0010-4655(94)90132-5`.

[93] E. Lohrmann, *A Summary of Charm Hadron Production Fractions*, URL `http://arxiv.org/pdf/1112.3757.pdf`.

[94] H. Abramowicz et al. ZEUS Collaboration, *Measurement of charm fragmentation fractions in photoproduction at HERA*, In preparation **(2013)**.

[95] T. Bergfeld et al. CLEO Collaboration, *Observation of* $D^+_1(2420)$ *and* $D^{*+}_2(2460)$, Phys.Lett. **B340 (1994)**, 194, URL `http://dx.doi.org/10.1016/0370-2693(94)01348-9`.

[96] A.F. Falk and T. Mehen, *Excited heavy mesons beyond leading order in the heavy quark expansion*, Phys.Rev. **D53 (1996)**, 231, URL `http://dx.doi.org/10.1103/PhysRevD.53.231`.

[97] J.D. Jackson, *Remarks on the phenomenological analysis of resonances*, Nuovo Cim. **34 (1964)**, 1644, URL `http://dx.doi.org/10.1007/BF02750563`.

[98] J. Blatt and V. Weisskopf, Theoretical nuclear physics, Wiley (1952).

[99] Wolfram Research, *Wolfram Mathworld*, URL `http://mathworld.wolfram.com/Legendre-GaussQuadrature.html`.

[100] Wolfram Research, *Wolfram Mathworld*, URL `http://mathworld.wolfram.com/Newton-CotesFormulas.html`.

[101] F. James and M. Roos, *Minuit: A System for Function Minimization and Analysis of the Parameter Errors and Correlations*, Comput.Phys.Commun. **10 (1975)**, 343, URL `http://dx.doi.org/10.1016/0010-4655(75)90039-9`.

[102] The Linux man-pages project, *Linux Programmer's Manual*, URL `http://www.kernel.org/doc/man-pages/online/pages/man7/pthreads.7.html`.

[103] The EGI Foundation, *EGI – Europen Grid Infrastructure*, URL `http://egi.eu/`.

[104] The DataGrid Project, *EDG – European Data Grid*, URL `http://eu-datagrid.web.cern.ch/eu-datagrid/`.

[105] The EGEE Collaboration, *EGEE – Enabling Grids for E-sciencE*, URL `http://eu-egee.org/`.

[106] The NorduGrid Collaboration, *NorduGrid FAQ*, URL `http://www.nordugrid.org/documents/faq.html`.

[107] The gLite Open Collaboration., *gLite - Lightweight Middleware for Grid Computing*, URL `http://glite.cern.ch/`.

[108] The EMI Collaboration, *EMI – European Middleware Initiative*, URL `http://www.eu-emi.eu/`.

[109] The EGEE Collaboration, *gLite 3.2 User Guide* (2012), URL `https://edms.cern.ch/file/722398/1.4/gLite-3-UserGuide.pdf`.

[110] A. Parenti, *2009 Guide to Funnel: The ZEUS Monte Carlo Production Facility*, *Technical report* (2009), URL `http://www-zeus.desy.de/ZEUS_ONLY/zeus_notes/ZEUS_NOTES/ZEUS-09-002.pdf`.

[111] M. Lisovyi, *Measurement of charm production in deep inelastic scattering using lifetime tagging for $D^{\pm}$ meson decays with the ZEUS detector at HERA*, Ph.D. thesis, DESY (2011), URL `http://inspirehep.net/record/943511/files/desy-thesis-11-033.pdf`.

[112] Z. Akopov et al., *Status Report of the DPHEP Study Group: Towards a Global Effort for Sustainable Data Preservation in High Energy Physics* **(2012)**, URL `http://arxiv.org/pdf/1205.4667.pdf`.

[113] Scientific Linux, *S.L. Distribution Roadmap* (2012), URL `http://www.scientificlinux.org/distributions/roadmap`.

[114] The EMI Collaboration, *Releases, EMI – European Middleware Initiative*, URL `http://www.eu-emi.eu/releases`.

[115] R. Sinkus and T. Voss, *Particle identification with neural networks using a rotational invariant moment representation*, Nucl.Instrum.Meth. **A391 (1997)**, 360, URL `http://dx.doi.org/10.1016/S0168-9002(97)00524-X`.

[116] O. Behnke, *Track efficiency tests with K^0_S decays* (ZEUS Tracking Developers Group Meeting, 25 March 2010), URL `http://zeusdp.desy.de/ZEUS_ONLY/meetings/zems/group10/meet259/sess2643/pres11733/obehnke100325.pdf`.

[117] A. Spiridonov, *Mapping of tracking efficiency with VMCU utility (update)* (ZEUS HFL Group meeting, 4 March 2004), URL `http://zeusdp.desy.de/ZEUS_ONLY/meetings/zems/group10/meet284/sess2962/pres12909/h120404_Compatibility_Mode_.pdf`.

[118] V. Libov, *Tracking efficiency studies* (ZEUS HFL Group meeting, 25 January 2012), URL `http://zeusdp.desy.de/ZEUS_ONLY/meetings/zems/group10/meet284/sess2929/pres12799/29_HFL_25January2012.pdf`.

Acknowledgement

First of all I appreciate the work of many people that contributed to the building and operation of the Hera machine, Zeus detector and made all physics measurements possible. I would like to thank the people who provided a nice reconstruction, simulation and data analysis environments. A special thanks to Leonid Gladilin, who kindly agreed to share his simulation software.

I thank my supervisors – Olaf Behnke and Uri Karshon, who encouraged and led me through the analysis. I was always happy to work with Yuriy Onishchuk and Don Hochman.

I thank the members of the Offline, the Tracking and the HFL groups for their support in computing and analysis. I thank the DESY directorate for their strong support and encouragement.

Special thanks to people, who kindly agreed to be the referees of this thesis: Olaf Behnke, Brian Foster, Achim Geiser and Johannes Haller.